THÈSE POUR OBTENIR LE GRADE DE DOCTEUR
DE L'UNIVERSITÉ DE MONTPELLIER

En Physique

École doctorale Information Structures Systèmes (I2S)

Unité de recherche L2C, IATE

From Grain to Granule: The Biomechanics of Wheat Grain Fractionation with a Focus on the Role of Starch Granules

Présentée par Karsta M. Heinze
Le 24 Novembre 2017

Sous la direction de Jean-Yves DELENNE
Valérie LULLIEN-PELLERIN
et Matthieu GEORGE

Devant le jury composé de

Guy DELLA VALLE, Ingénieur de Recherche, INRA, Nantes, France	Rapporteur
Jean-Noël ROUX, Ingénieur Général des Ponts, des Eaux et Forêts, CNRS, Paris, France	Rapporteur
Evelyne KOLB, Maître de Conférences, ESPCI, Paris, France	Examinatrice
Philippe LECLÈRE, Senior Research Associate, University of Mons, Belgium	Examinateur
Laurence RAMOS, Directeur de Recherche, Université de Montpellier, France	Présidente du jury
Jean-Yves DELENNE, Directeur de Recherche, INRA, Montpellier, France	Directeur de thèse
Valérie LULLIEN-PELLERIN, Directeur de Recherche, INRA, Montpellier, France	Co-directrice de thèse
Matthieu GEORGE, Maître de Conférences, Université de Montpellier, France	Co-directeur de thèse

UNIVERSITÉ
DE MONTPELLIER

From Grain to Granule: The Biomechanics of Wheat Grain Fractionation with a Focus on the Role of Starch Granules

Karsta M. Heinze

Acknowledgements

I would like to thank CEPIA (INRA) and Labex NUMEV for providing the funding of this three-year project.

I thank **Guy Della Valle** and **Jean-Noël Roux** for being the rapporteurs, their detailed examination of this work and helpful comments.
I further want to thank the other members of the jury, **Evelyne Kolb**, **Philippe Leclère** and **Laurence Ramos** for accepting to examine the thesis and defence, for their questions, comments and interest in this work.

I want to thank my three supervisors, **Jean-Yves Delenne**, **Valérie Lullien-Pellerin** and **Matthieu George**, for all their guidance, ideas, enthusiasm and contributions to this work. Especially also for their determination to work together as a team on this multi-disciplinary project. In particular, I thank Valérie for her enthusiasm and incredible reactivity, Matthieu for his determination to find and develop a solution for doing CR-AFM on our samples, and Jean-Yves for his enduring positivity and help with the administrative side of things.

I thank **Olivier Arnould** for his continued involvement in the AFM work and interest in my thesis, for introducing us to CR-AFM in the first place, closely working with us on the correction method, his patient explanations and his help with sample preparations. I thank **Michel Ramonda** for performing the CR-AFM experiments on my not always easy samples, while always keeping a positive mood.

I want to thank **Farhang Rajdaï** for his helpful ideas and interpretations on the modelling results.

I wish to thank **Geneviève Carrière** for the uncomplicated administration, be it the simple printing of a poster or a conference visit abroad.

I thank **Thérèse-Marie Lasserre** for her help with the biochemical experiments, **George Maraval** for his help with the micromilling and all other members of the **UMR IATE**, with whom I have crossed paths.

I want to thank the "old" PhD students in my first office, the container: **Vincent**, **Santi**, **Adriaan**, **Vero** and **Lizeth** for welcoming me into the lab. I also thank the members of my later office, **Bettina**, **Karine**, **Amelie** and **Pierre-Alain**, for making this office a nice place to work at.
Chutima, Vero, Anaïs and **Justine**, thank you for the lunch times we shared and some unforgettable dinners and evenings.
Yannick, thank you for the coffee breaks, which truly deserved the name and our many discussions that made my work days more enjoyable and interesting.
I want to thank **Daniel** for being like-minded. I very much enjoyed our try in setting up a "PhD group", even though it did not work out, and our discussions in and out of the lab, usually starting off with a weird question from you.
Special thanks goes out to **Nicolas** for always having an open ear to my problems, helping whenever possible, always having nice tea ready to be consumed on our tea breaks, and becoming a good friend on the way.
I am also happy that I got to meet all the other PhD students, with whom I shared some or most

of my time in the last three years with: **Marianne, Gregoire, Aida, Ali, Fabien, Filippo, Oscar, Valentin, Céline**.
Rahila, thank you for your friendship and support, for all the good times we shared, also together with **Isabell**.

I am also grateful to all the members of the **COSY group** in Amsterdam that were there in 2013 and 2014, who helped me stepping into the world of scientific research. I learnt many things about succeeding in science in the time I spent there, which greatly helped me during the last three years. Special thanks go to **Douwe**, **Fabio**, **Felix** and **Pierre** for their continuing friendship.

Je tiens à remercier **Marie et Serge Girard** de me faire sentir chez moi dans votre maison et comme une membre de votre famille. Merci beaucoup aussi pour votre aide et soin, chaque fois que j'en avais besoin.

Ich danke meinen Eltern, **Stephanie und Burkhard Heinze**, für ihre ununterbrochene und bedingungslose Unterstützung, nicht nur in den letzten drei Jahren, sondern in all den Jahren meiner Ausbildung.

Jules, I thank you for bringing me to France, not only for the duration of this PhD, but possibly for a lifetime, for all your support, advice, encouragement and love.

Contents

List of Figures

List of Tables

Glossary

allele different forms of a gene on the same locus [1]. xvi, 3, 21, 29, 35, 146

allopolyploid polyploidy with distinct chromosome sets (from different species) [1]. xv, 9, 29

amyloplast an organelle in which starch is synthesised and stored [1]. xv, 15

anisotropic a property differs with the orientation within the material [2]. 80

apoptosis regulated cell death [3]. 15, 23

biomechanics the study of structure and functions of living systems with methods from mechanics. 2, 18

breeding the intentional creation of new varieties for wanted characteristics [1]. 2, 3, 18

C_3 the most common carbon fixation pathway in plants [1]. xv, 4, 48, 77, 78, 80

C_4 a carbon fixation pathway in plants less common than C_3, adapted to high temperatures and low water supply [1]. 4, 48, 77, 78, 80

cereal cereal grasses of the family Gramineae, include e.g. barley, wheat, millet, rice, maize [1]. 2, 4, 8, 11, 20, 48, 77, 78, 80, 82

common wheat *Triticum aestivum* subsp. *aestivum*, allohexaploid AA BB DD (see allopolyploid). 3, 9, 14, 16, 20, 23, 29, 32, 39, 82, 124

compound granule more than one starch granule is synthesised in the same amyloplast, leading to tightly packed starch granules [4]. 14, 20, 48, 77

cultivar a variety of a plant that is not normally found in wild populations, but resulted from agricultural techniques [1]. 12, 13, 18, 29, 30, 142

durum wheat *Triticum turgidum* subsp. *durum*, allotetraploid AA BB (see allopolyploid). 3, 4, 9, 16, 20, 23, 29–31, 39, 82, 124, 141

genotype the genetic constitution, results in the phenotype [1]. 17, 19–23, 39, 144, 146

glycolipid lipid that has a carbohydrate attached covalently [3]. 15

legume a plant, fruit or seed of the family Leguminosae; the fruit is a pod with usually several seeds [1]; dried legume seeds are known as pulses. 4, 48, 77, 78, 80, 83

lipid mostly of fully hydrophobic biological molecule [3]. 11, 15

locus the place on the chromosome where one or more specific genes are located [1]. xv, 3, 14, 23, 32, 37, 124

mealy opposite of vitreous; whitish appearance of the endosperm. 48

mutation a change in structure of the DNA or of a gene [1]. 3

NIL near-isogenic lines: (genetic) lines that differ only in one genomic location [5]. 18, 22, 29, 32, 35, 39, 82, 146

null allele or silent allele; the allele has no detectable product [1]. 14, 29

overexpression one or more populations, which can interbreed, but not exchange genes with other populations [6]. 20

phenotype increased expression of a gene beyond the normal expression level [1]. xv, 20, 29

polymer a molecule that consists of a number of smaller units of one or more types, which are connected; can be branched or linear [3]. xvi, 29

polypeptide a polymer made of amino acid residues that are linearly linked by peptide bonds [3]. 2

polyploidy organism possesses more than one set of homologous chromosomes, i.e. diploid - 2 copies, tetraploid - 4 copies, hexaploid - 6 copies [1]. xv, 9, 29

polysaccharide a polymer of monomeric carbohydrate chains linked by glycosidic bonds [3]. 2, 10, 11

primary structure sequence of amino acid residues [3]. 2

proteome the complete set of proteins within a cell [5]. 18

proteomics large-scale analysis of the proteins within an organism [5]. 18

QTL quantitative trait loci: region of chromosome associated with inheritable traits [5]. 18

quaternary structure spatial arrangement of the subunits of a macromolecule [3]. 2

secondary structure spatial arrangement of the atoms in the polypeptide backbone, commonly α-helices and β-sheets [3]. 2

species one or more populations, which can interbreed, but not exchange genes with other populations [1]. xv, xvi, 3, 8–11, 20

tertiary structure spatial arrangement of all the atoms of a polymer including backbone and side chains [3]. 2

trait visible phenotypic characteristic [1]. xvi

transgenic organism containing genetic material from different organisms [1]. 14, 18, 20

variety taxonomic rank below species and subspecies [7]. xv, 10, 13, 18, 31, 124

wild-type the most common allele of a certain gene [1]. 3, 20, 29, 33, 124

Acronyms

AFAM atomic force acoustic microscopy. 44
AFM atomic force microscopy. 3, 4, 12, 22–24, 39, 42, 44–49, 54, 77, 83, 124, 147, 150
AM amplitude modulation. 42, 45, 46, 52

B1 first break. 31–34
B2 second break. 31–34

CB coarse bran. 31
CR contact resonance. 4, 52, 53
CR-AFM contact resonance atomic force microscopy. xiii, 4, 39, 44, 46, 47, 49, 56, 77, 79, 80, 83, 99, 124, 147, 148, 150

DAF days after flowering. 15, 55
DEM discrete element method. 96, 126
DP degree of polymerisation. 10, 11, 80

FB1 first break flour. 31
FB2 second break flour. 31
FM frequency modulation. 42, 43, 52, 54, 56
FPDS fast Poisson disc sampling. 96, 126
FV force volume. 44, 52, 56

GSP grain softness protein. 14

HI hardness index. 30, 36

LEM lattice element method. 24, 25, 125

NIRS near infrared reflectance spectroscopy. 16, 19–21, 30, 36, 144, 146, 151

PIN puroindoline. 3, 14–16, 18–24, 29, 39, 124, 141, 147
PSD particle size distribution. 5, 86, 90, 92, 93, 100, 103, 104, 106, 109, 113, 116, 121, 148
PSI particle size index. 16, 19, 30–33

rpm rounds per minute. 31

SEM scanning electron microscopy. 12, 20, 22, 23, 39, 47, 54, 141, 142, 146, 151
SGAP starch granule associated proteins. 11, 13, 15
SGSD starch granule size distribution. 21, 22, 86, 121, 148

SKCS single kernel characterisation system. 16, 19–21, 30, 35, 36, 144

TKW thousand kernel weight. 17

TW test weight. 17, 30

1. General introduction and executive summary

> *"The grinding of wheat into flour is mankind's oldest continuously practised industry and the parent of all modern industry; all modern particle breakage operations have wheat milling in their ancestry."* [8]

Wheat is one of the most important cereal crops worldwide. In order to use wheat fractions, such as flour or semolina, for food or non-food purposes the grains need to be milled. Grain milling includes processes of grinding and separation of the fractions in order to isolate the inner grain parts from the peripheral tissues. For a better understanding of the wheat milling process knowledge of the mechanics of grain fragmentation is central. The wheat grain is a biological structure, and the question is therefore one of biomechanics, or more precisely plant biomechanics.

Milling involves a mechanical disruption of the grain's structure and therefore depends on the grain's mechanical behaviour, which depends on the mechanical properties of its components. These can potentially be studied by methods commonly used in the field of mechanics. Biomechanics research in general can make use of established methods of mechanics. One approach originating from the mechanics field with specifically great potential is numerical modelling as an addition to experimental research, especially when a complex interplay of mechanical and biological aspects is given. To the contrary, experimental methods for the investigation of the mechanics of samples were often developed for non-living materials and their application to biological subjects can require significant adaptions and modifications. Successful modifications and improvements are then however not limited to the specific object of interest only, but can be beneficial for the whole field of biomechanics. The challenges involved in biomechanics are therefore also an impulse for constant methodological improvement.

The part of the wheat grain, which is the major determinant of the milling behaviour is the starchy endosperm. The endosperm is a composite material [9] and its mechanical properties are therefore relatable to those of other known composites, as for example concrete. However, due to the endosperm's biological nature, the investigation of its mechanical properties is a complicated task.

There are numerous elements involved in building up the endosperm's structure: the two main components starch and gluten, with multiple levels of organisation respectively, and a number of minor components. Gluten is a network of proteins and a full description of its structure would include the primary structure, secondary structure, tertiary structure and quaternary structure of the molecules up to the network formed by the interaction of distinct proteins. About 1300 polypeptides alone were found in the wheat endosperm [10] and one of the protein types found in wheat (glutenins) form the largest proteins in nature [11].

The carbohydrate element of the endosperm, starch, is not less complex. Starch is composed of two major polysaccharides, one of them being highly branched. These polysaccharides are further organised into clusters, nanometer-sized lamellae and micrometer-sized granules. The structure of every one of the grain's biological components can depend on the genetic disposition, the environmental conditions during grain development or both.

Fortunately, humans have accumulated practical knowledge about wheat milling for the thousands of years since the first grains were crushed between stones by hand and even more so since the existence of industrial mills. A large amount of experimental research on the milling behaviour was and is done to observe the milling result of well characterised grain batches. By selective wheat breeding or genetic manipulations the variety of grains available for milling studies is increasing. However, extensive parametric studies can take years of preparation (including breeding, seeding and harvest of grains) and the micro-mechanical processes that happen within milliseconds between the milling rotors are not observable. But even though an efficient testing of hypotheses as to the origins of different milling behaviours is therefore challenging, significant knowledge has been accumulated by the large amount of experimental wheat milling studies.

The systematic study of wheat milling is overall an interdisciplinary field, including agronomy, genetics, biochemistry, botany, food engineering, bioinformatics and biomechanics. And only with a multi-disciplinary approach a comprehensive understanding of the grain fragmentation can be obtained.

The work presented in this PhD thesis is aiming to increase the knowledge of the biomechanics of wheat fragmentation by focussing on a small number of selected questions and methods.

In the following, a brief summary of each chapter is provided. This thesis combines three major approaches: experimental milling, experimental atomic force microscopy (AFM) assays and numerical simulations, which are organised in separate chapters and summarised hereafter.

Chapter 2 State of the art

This chapter provides a bibliographic review on wheat milling, the wheat grain and on the nature and structure of the major components of the grain. This is put into context for the understanding of grain fragmentation during wheat milling and the experimental and numerical approaches to investigate the involved micro- and nano-mechanical processes are summarised.

Chapter 3 The effect of puroindolines on milling behaviour

Puroindolines (PINs) are proteins of the wheat grain that are believed to cause differences in the adhesion between starch granules and gluten matrix in the endosperm and therefore to be one of the major factors influencing grain hardness [12]. PINs are encoded on a specific locus on chromosome 5D in common wheat *Triticum aestivum* [13]. When they are present in wild-type form, the grains classify as "soft" common wheat, whereas mutations on the puroindoline alleles lead to "hard" common wheat [13]. Durum wheat *Triticum durum*, does not possess the chromosome on which the puroindoline alleles are located and has the hardest grains of all wheat species [13]. Cross-breeding and recombination of wheat made it possible to translocate the puroindoline genes into durum wheat [14], which potentially greatly affects the way durum wheat is milled and which kind of products can be made from its milling products [14].

Puroindoline genes introduced into durum wheat reduce milling energy and change milling behavior similar to soft common wheats

(K. Heinze, A.M. Kiszonas, J.C. Murray, C.F. Morris, V. Lullien-Pellerin, *Published in Journal of Cereal Science, 2016 [15]*)

Grain physical characteristics and milling behavior of a durum wheat line in which both wild-type PIN genes were translocated and stabilised after backcrossing (*Svevo-Pin*) were compared with the parent line (*Svevo*). The only observed differences between grain characteristics were the mechanical resistance and starchy endosperm porosity revealed through vitreosity measurement. A significant increase of flour and a decrease of semolina yield and break milling energy were observed from *Svevo-Pin* in comparison with the non-recombinant parent line in accordance to the lower grain mechanical resistance and higher porosity measurements. Moreover, the particle size distribution shown for *Svevo-Pin* flour appeared consistent with a lower adhesion between starch granules and the protein matrix attributed to the presence of wild-type PINs. Coarse bran yield was conversely increased. This appeared to be due to a lower starchy endosperm recovery as a higher proportion of grain starch was found in this bran fraction. Flour from the durum parent line was inversely enriched in phytic acid, a cellular marker of the aleurone layer. Starch damage was also lower in *Svevo-Pin* flours in comparison with *Svevo*. All of the observed differences between translocation and parent lines were confirmed independent of the culture growth conditions (n = 12).

Chapter 4 Nano-mechanics of starch by AFM

Starch is one of the major components of the wheat endosperm [16]. In the grain it is deposited into micrometer-sized starch granules. Determination of the mechanical properties of starch is valuable for a better understanding of the fragmentation behaviour of the starchy endosperm. Atomic force microscopy (AFM) is a very utile tool, which can provide the required resolution for imaging and mechanical measurements and has great potential for investigation of the starch granule structure and surface.

AFM and starch

A brief review of the literature of AFM imaging on starch is provided with the focus on establishing a critical viewpoint on the observations due to the known limitations of the AFM technique. Furthermore, structural differences of starch depending on its botanical origin are illustrated, which can potentially affect the mechanical properties.

Contact resonance atomic force microscopy (CR-AFM) was chosen for the investigation and mapping of nano-scale mechanical properties. Starch granules can be observed in cut grain sections prepared by least-invasive techniques without resin embedding. However, these present challenging surfaces for AFM techniques, due to high topography variations.

On the effect of local sample slope during modulus measurements by contact-resonance AFM

(K. Heinze, O. Arnould, J.-Y. Delenne, V. Lullien-Pellerin, M. Ramonda, M. George, *Under review in Ultramicroscopy*)

CR-AFM is of great interest and very valuable for a deeper understanding of the mechanics of biological materials with moduli of a few GPa. However, sample surfaces can present a high topography range with significant slopes, where the local angle can be as large as ±50°. The non-trivial correlation between surface slope and contact resonance (CR)-frequency hinders a straight-forward interpretation of CR-AFM contact modulus measurements on such samples.

We aim to demonstrate the significant influence of the surface slope on the CR-frequency that is caused by the local angle between sample surface and the AFM tip and present a practical method to correct the measurements. Based on existing analytical models of the effect of the AFM set-up's intrinsic cantilever tilt on CR-frequencies, we compute the non-linear variation of the first two CR-frequency modes for a large range of surface angles. The computations are confirmed by CR-AFM experiments performed on a well-defined, curved, and mechanically homogeneous surface. Finally, the model is applied to directly correct contact modulus measurements on a durum wheat starch granule as an exemplary sample.

Mechanical properties of starches from different origins by CR-AFM

(*Article in preparation*)

Starch consists of the two major components amylose and amylopectin, whose proportion varies between 15 % to 30 % and 70 % to 84 %, respectively. Waxy (<15 %) and "high amylose" (>30 %) mutants make it possible to vary the amylose concentration more widely. The unique properties of starch are exploited by processing (cooking, baking ...) for food or for non-food products (paper, textiles, plastics, biofuel) after extraction.

Starch characteristic, such as the form and size of granule, the percentage of crystallinity, the swelling capacity and others, greatly depend on the botanical origin. However, very few studies are concerned with the in situ mechanical properties of starch, which play a role in the grinding behaviour of the grain and the amount of damaged starch afterwards.

A CR-AFM method was used to measure the contact modulus in cut starch granules on a size scale of some hundred nanometers and sections of grains from different botanical origin (C_3 and C_4 cereals, legumes) were evaluated. The results demonstrate the ability of AFM to measure the mechanical properties of starch and the results are discussed in the context of the current knowledge on starch structure and its physicochemical properties.

Chapter 5 Modelling endosperm as a cemented granular material

Numerical modelling is a valuable, complementary approach to experimental research, which can provide targeted testing of hypotheses. The endosperm can be seen as a cemented granular material and simulations on wheat fragmentation can therefore be performed in the framework of cohesive granular material research.

The effect of particle size distribution and porosity on the tensile properties of cemented granular materials

(*Article in preparation*)

The mechanical properties of a cemented granular material are expected to be influenced by the particle size distribution (PSD), because it influences the packing of the granules and consequently the distribution of the cementing matrix and the voids therein. To gain a comprehensive understanding of the effects of the granular packing on the mechanical behaviour a parametric study of particle size ratio and volumetric fraction of small particle is performed. Both parameters are shown to influence the packing density, the number of contact points per particle and the size of pores within the matrix. Furthermore, it is shown that these factors directly or indirectly influence the distribution of stresses within the composite and ultimately the Young's modulus and yield stress. We analyse in detail the relations between PSD, geometrical sample structure and mechanical behaviour and compare the numerical results to the theoretical prediction from the Mori-Tanaka model.

Investigation of the governing factors of particle damage in a cemented granular material

(*Article in preparation*)

The particle damage obtained by a cemented granular material under tensile or compressive forces depends on its structure and the mechanical properties of the constituting phases. We performed an extensive parametric of the effect of particle toughness and particle-matrix interface toughness on the fracture of a cemented granular material with bi-modal granule size distribution. As the mechanical response is known to be greatly influenced by the amount of cementing matrix, two matrix states were analysed: fully cemented and partly cemented with voids. The particle damage was traced separately in the large and small particles. In agreement with previous studies we observe that one parameter is governing the amount of particle, which is the relative toughness of particle to particle-matrix interface.

Chapter 6 Conclusion and Outlook

The main results of the three main chapters are summarised and discussed with a general viewpoint in an attempt to link the findings obtained from the different approaches and at different size-scales.

2. State of the art

Contents

The wheat genome has less chromosomes than the human genome, but contains at least six times more genes.

2.1. Wheat, milling and humans

The cultivation of seeds and the development of methods to extract the edible parts of the seeds by milling have been a challenge for mankind since the beginnings of civilisation [17]. Teague summarised the importance of wheat grain milling for human evolution and development aptly:

> *"The story is of how we men have learned to do these [milling] tasks better and better, devising improved tools and new skills as time passed; enlisting the forces of nature to help us; enlarging our mechanical arts and our mental capacities as we struggled with the twin problems of increasing the quantity and improving the quality of our product; adopting new ways of life, forming new social organisations as a result of a growing dependence on this increasing food supply. There is no other single thread of development that can be followed so continuously throughout all our history, and none which bears so constant a cause-and-effect relation to every phase of our progress in civilisation."* [18]

The first cultivation of wheat by humans dates back more than 10.000 years to the neolithic period [19]. The wheat subspecies, which makes up to 95 % of todays wheat production is part of the species *Triticum aestivum* and resulted from the hybridisation of *Triticum turgidum* and *Triticum tauschii* about 9.000 years ago [1][20]. All wheats of the species *Triticum aestivum* have since then only existed in cultivation[19, 21].
The great significance of wheat for humans is the result of its adaptability to a wide range of growing environments, its high yield, but for the most part due to its special storage proteins, which enable the production of doughs with unique properties [19].
Cereals are the most produced commodity of the world; wheat being one of the biggest three contributors, together with maize and rice [22]. The worldwide yearly wheat production reaches more than 700 Mt on an area of 220 Mha (Figure 2.1) [22]. More than 30 % of all produced wheats originate from Europe; France being the fifth largest wheat producing country of the world [22].

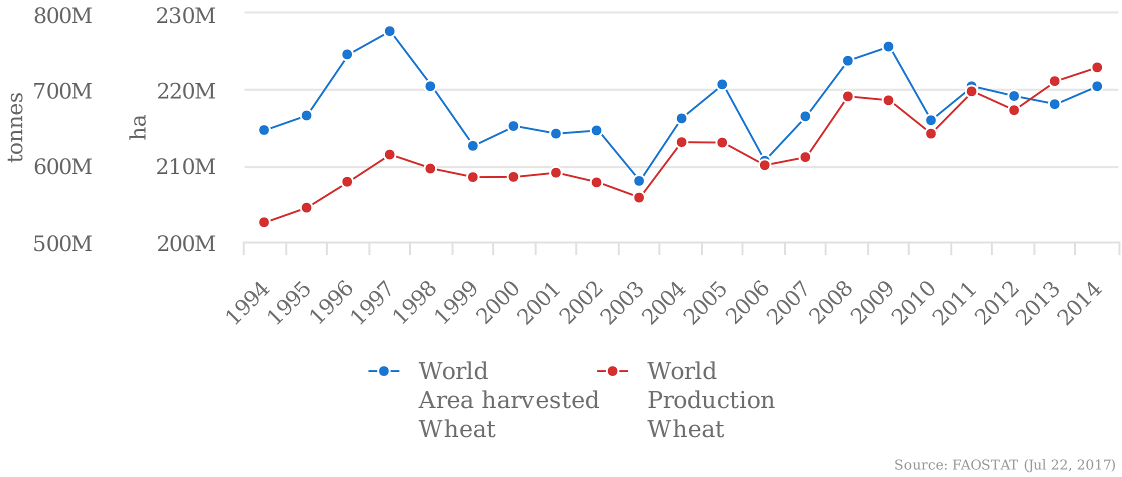

Figure 2.1. – Yearly world wheat production [Mt] (red) and area [Mha] (blue) over the past two decades [22].

---

[1] The tetraploid wheat species *Triticum turgidum*, which includes the subspecies *durum*, evolved earlier than the hexaploid *Triticum aestivum* from a natural hybridisation event, followed by domestication and diversification [21].

The two major subspecies of wheat grown today are the hexaploid[2] (genome AA, BB and DD) *Triticum aestivum* subsp. *aestivum*, also known as common wheat, and the tetraploid (genome AA and BB) *Triticum turgidum* subsp. *durum* or durum wheat. Whereas durum wheat is mainly used for pasta production, common wheat is used for a broad range of products, including cookies, cakes and bread [17].

2.2. The wheat grain

To understand the milling behaviour of wheat, it is necessary to know the morphology and histology of the single wheat grain (also termed kernel). A wheat grain contains three major tissues: the starchy endosperm and the germ, which are surrounded by the outer layers (Figure 2.2). The germ comprises only 2 to 3 % of the kernel weight. It contains the plant embryo and the scutellum [8, 16]. The tissue of the embryo is structurally separate from the rest of the kernel and can therefore disassociate readily during milling [16], depending however on the mill and the process. It is recovered in the "shorts" fraction[3].

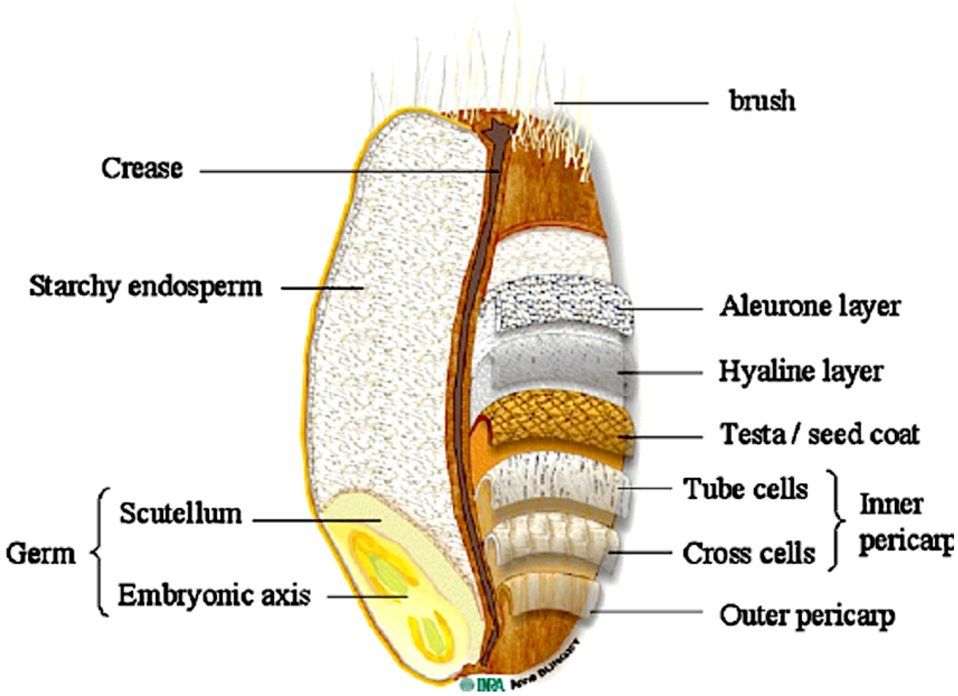

Figure 2.2. – Histology of the wheat grain. Figure from [23].

The aleurone layer is a single layer of living cells, which separates the starchy endosperm and the germ from the outer layers [8]. It is rich in nutrients, such as minerals, vitamin B and protein [24]. Though the aleurone layer is botanically a part of the endosperm, it usually separates from the starchy endosperm together with the outer layers during milling [16].

The outer layers include the pericarp (inner and outer), testa and hyaline layer. They enclose the starchy endosperm and germ and protect them against moisture and mold [8, 16]. In milling terminology, these tissues together with the aleurone layer are known as the "bran" [16]. The bran fraction comprises 14 to 16 % of the kernel weight [16]. An important structural property of the

---

[2] see allopolyploid and polyploidy

[3] For an overview of fractions obtained from wheat milling see Figure 2.7 on page 16.

wheat grain in relation to milling is the presence of a crease, which folds the bran layers towards the inner kernel (Figure 2.2) [8].
The major part of the grain (81 to 84 %) is the starchy endosperm. It is the storage compartment, intended as energy supply for the germinating plant [8]. Energy is stored as proteins and starch within the endosperm cells, resulting in a distinctive, very dense structure (Figure 2.3). Next to starch and protein the endosperm contains lipids. Additional minor components are contained in endosperm cell walls [25], which are however not part of this review.

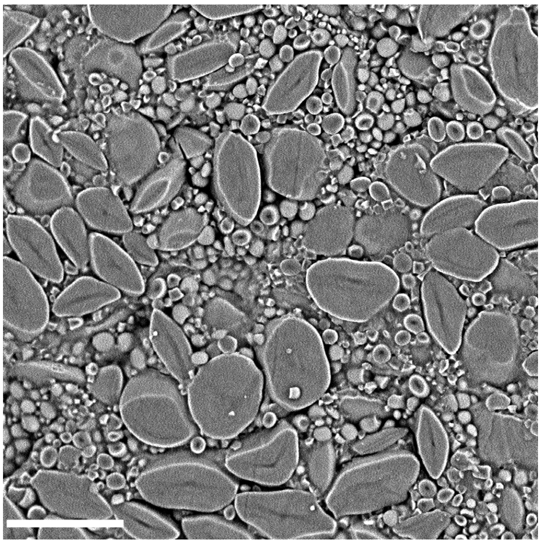

Figure 2.3. – SEM image of a sectioned wheat starchy endosperm showing the dense packing of starch granules. Scale bar: 30 µm.

2.3. Biopolymers of the starchy endosperm

2.3.1. Starch

Starch is a carbohydrate produced by green plants for energy storage [26]. It consists of the two major components amylose and amylopectin [27]. Starch structure and therefore its functional properties generally depend on the botanical origin. The following overview focusses on the properties common to all starches and more particularly on wheat starch.

Amylose

Amylose is a mainly linear polysaccharide containing glucose connected by mostly $(1\rightarrow4)$-α-linkages (Figure 2.4) [27]. Some molecules also have $(1\rightarrow6)$-α-linkages, resulting in a slight branching of the molecule [27, 28]. The specific size and structure of the amylose molecule (degree of polymerisation (DP), molecular weight, percent of branched amylose etc.) differ between plant species [28], but also between varieties [26]. For example, the DP (in number) between wheat varieties was found to range from 830 to 1570 [29].

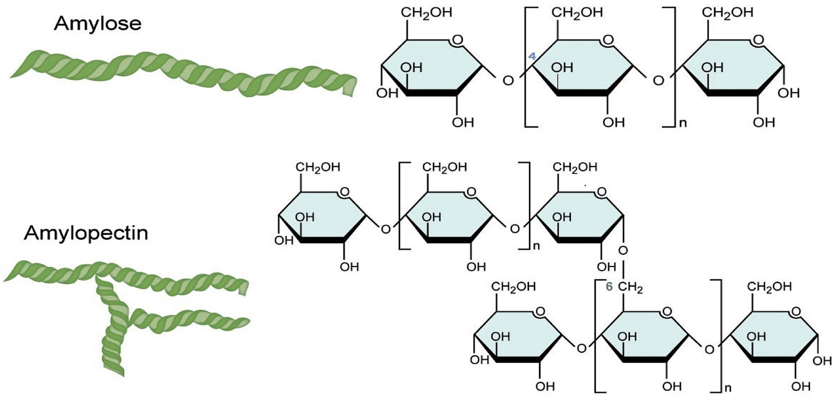

Figure 2.4. – Amylose (top) is a mainly linear polysaccharide with mostly (1→4)-α-linkages. Amylopectin (bottom) is highly branched with (1→6)-α-linkages between glucan chains. Image from [30]

Amylopectin

The structure of the amylopectin molecule is more complex than that of amylose [26]. It is a highly branched polysaccharide, formed by a high number of (1→4)-α-glucan chains that are connected through (1→6)-α-linkages (Figure 2.4) [27]. Similar to amylose, size and structure of amylopectin vary with its botanical origin [28].
The chains in an amylopectin molecule can be grouped into three categories: short chains (DP 14-18), long chains (DP 45-55) and chains of DP>60 [27]. The short chains form clusters (Figure 2.5) [27], which can be found as crystalline regions after acid-treatment of the starch [31]. Though the existence of clusters is generally accepted, the consequent arrangement of clusters in the amylopectin molecule is still unknown and several hypotheses co-exist [26, 27].

Other components of cereal starch

Starches also contain small amounts of non-carbohydrate components interiorly, the most important fraction for cereal starches being lipids in the form of free fatty acids and lysophospholipids [27, 32]. These lipids form complexes with a part of the amylose fraction [27, 32]. Another group of components are starch granule associated proteins (SGAP), which are described in subsection 2.3.2.

From molecule to granule

In the plant cells, amylopectin and amylose are deposited into starch granules [27]. The ratio of amylose to amylopectin in starch varies with the botanical origin. Most cereal starches consist of 70 to 80 % amylopectin and 20 to 30 % amylose [26]. However, starches with different percentage of amylose are known for a number of cereal species: waxy starches with <15 % of amylose and high-amylose starches (>40 % of amylose) [28].
Starch granules are semi-crystalline structures, whose crystallinity can be observed by X-ray diffraction [33, 34, 35, 36]. The percentage of crystallinity in starches can be measured and starches can be grouped by their crystallinity type, which is related to the packing density of the double helices [27, 28]. Most cereals, including wheat, show the so-called A-type crystallinity [26]. The crystallinity arises from the ordering of double helices in the amylopectin molecule, forming crystalline lamellae (Figure 2.5 right) [28]. The average orientation of the amylopectin double helices is perpendicular

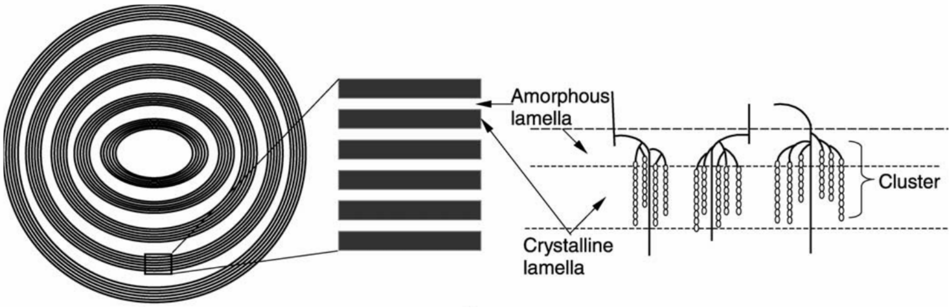

Figure 2.5. – The amylopectin molecules, with regions of ordered double helices (clusters) and branching regions, make up amorphous and crystalline lamellae within the starch granule. These lamellae form the concentric, alternating semi-crystalline and amorphous structures, which are known as growth rings. Image from [28].

towards the centre of the granule [37]. The branching points within the amylopectin molecule are mainly found within the amorphous lamellae (Figure 2.5 right) [26].
A pair of a crystalline and an amorphous lamellae alternates every 9 nm to 10 nm, creating crystalline shells [27]. The 9 nm repeat structure was found to be a universal feature for starch regardless of its origin [33]. A complementary scale of organisation of the double helices of amylopection into superhelices was proposed [38], but has yet to be confirmed. Such superhelices would form a continuous, crystalline network, constituting the granular backbone [26].
The amylose content is possibly related to the distribution of amorphous and crystalline lamellae [39]. Amylose itself is thought to not affect the crystallinity of normal starches, but might contribute for high-amylose starches [28]. It is believed to be randomly distributed in the granule in a radial orientation between amylopectin; its concentration being higher and the amylose chains smaller next to the granule surface than in the centre [26].
Concentric rings with thickness of some hundreds of nm can be observed by scanning electron microscopy (SEM) or atomic force microscopy (AFM) within opened granules (Figure 2.5 left) [27]. They are known as "growth rings" and are believed to be alternating semi-crystalline and amorphous regions [27]. Their precise structural organisation is still under debate [26]. Within the growth rings, structures of smaller sizes were observed by SEM and AFM and termed "blocklets" [40]. These "blocklets" were of sizes between 20 nm to 300 nm for wheat [41, 42, 43, 44]. A critical discussion of the observations on growth rings and blocklets by AFM is done in section 4.2 on page 47.

Granule shape, size and type

Starch granules have different shapes and sizes depending on the botanical origin [27]. Wheat has granules of two sizes (Figure 2.3): larger (diameter ≈30 µm), lenticular shaped granules, called A-type granules, and smaller (diameter ≈3 µm), round granules, called B-type granules[4][27]. Some authors distinguish a third granule type, C-type granules, with diameters <3 µm [45, 46]. The granule size distribution was found to vary between cultivars [47, 48, 49], but seems also influenced to a certain extent by environmental growing conditions [49].
The starch properties are different for both types of granules [36, 50, 51]. The structure and orientation of amylopectin was proposed be radial in the round B-type starch granules, but rather parallel (perpendicular to the granule surface) in the lenticular A-type granules (Figure 2.6) [52]. For the A-type granules this leads to an equatorial groove of less ordered molecules [53]. A- and

---

[4] This notation is not related to the type of crystallinity of starch (also noted A, B, etc.).

B-granules of wheat vary also in their amylose content, crystallinity and their functional properties (i.e. gelatinisation and pasting temperature, peak viscosity) [54, 55, 56]. A-type granules have higher amylose content [54, 56, 46]. Two studies found higher crystallinity in A-type granules than in B-type granules [54, 56], whereas a third study reported lower crystallinity in large granules [46]. It was suggested that the biosynthesis of these two granule types differs [52, 46].
Amylose content and crystallinity are also affected by cultivar and grain hardness [54, 57], amylose content being higher in soft grains and crystallinity higher in hard [54]. Additionally, amylose content can be affected by the environment, such as drought stress [55]. Kozlov et al. [58] hypothesised that the amylopectin cluster size and the thickness of crystalline lamellae remains unchanged and therefore would be a universal structural parameter of starch [58]. They also concluded that an increase of amylose content is related to an increase of defects in the crystalline lamellae [58].
It can be therefore hypothesised that starch granules of different type and from different varieties could have different mechanical properties.

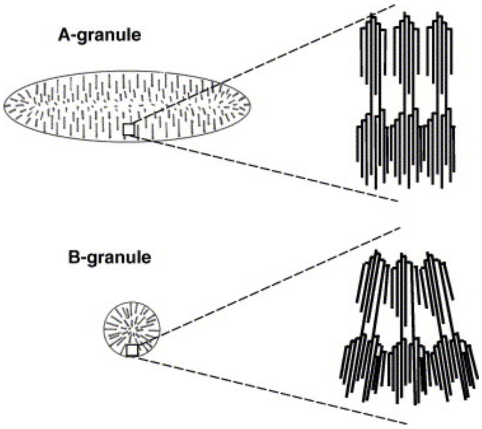

Figure 2.6. – The orientation of amylopectin molecules was proposed to be different for the A- and B-type wheat starch granules according to the granule shape. Image from [52].

Channels

Pores on the surface of starch granules were observed [59] and it has been suggested that these pores are openings of channels, which extend inside towards the centre of the granules [60] and contain proteins and phospholipids [61, 62, 63]. Such channels were found in both, the A- and B-type wheat granules [62]. Channels in A-type granules are large, originating from the equatorial groove or finer originating from the granule surface [62]. Channels in B-type granule are less defined, larger and more void-like [62]. It is believed that the channels facilitate the transport of chemical reagents into the granule interior [62] and on the other hand affect the susceptibility of starch granules to degrading enzymes [59].

2.3.2. Protein

The proteins in wheat endosperm can be divided into two large groups: starch granule associated proteins (SGAP) and storage proteins.

Storage Proteins

The storage proteins of wheat have been studied for more than 250 years and were one of the first proteins to be described by chemists [19, 64]. Two types of prolamins (glutenins and gliadins), interlinked together, form a matrix: the gluten [65]. Glutenins are the largest known proteins found in nature [11].

Puroindolines and grain softness protein

Puroindolines Greenwell and Schofield discovered in 1986 that a starch-bound protein fraction lies at the basis of low wheat grain hardness [66]. This protein fraction was later found to mainly consist of two proteins, which were called purodindolines [67]. Puroindolines (PINs) are basic proteins of 13 kDa with a tryptophan(Trp)-rich domain [67]. They show a strong affinity to polar lipids [68]. The two PINs, puroindoline A (PINA) and B (PINB), are 55 % identical [67] and have a similar secondary structure [68].
PINs are genetically encoded by the *pina* and *pinb* genes on the so-called hardness locus on the short arm of chromosome 5D in common wheat [13]. A number of allelic states exist, which differ from the wild-type form (*Pina-D1a* and *Pinb-D1a*) in the form of a null allele (*Pina-D1b*) or point mutations that lead to amino acid changes [69].
In the wheat grain, PINA and PINB have been reported to be in the aleurone layer and in the starchy endosperm [70, 71, 72]. On extracted starch, PINs are found bound to the starch granule surface [73]. In transgenic rice endosperm, PINs were also found between compound granules and between starch granules [74].
The Trp-rich region is crucial for the starch binding ability [75]. Whereas Capparelli et al. [76] stated that the expression of *pina* might control the binding of both PINs to starch, Feiz et al. [73] concluded that both PINs bind to starch granules independently and other authors observed that PINB limits the binding of PINA to starch [77, 78] . Wanjugi et al. concluded that PINs can indeed act together or separately, but high amounts of starch-bound PINs were only found, if PINA and PINB were present [79]. Ziemann et al. [80] reported findings on *in vivo* interactions between PINA and PINB. PINB was found to interact with itself and with PINA, whereas PINA was a interacting less [80].
The exact biological function of PINs in the grain is still under debate [12], but PINs were shown to have antimicrobial effects [70, 71, 81, 82, 83, 84]. This antimicrobial function is likely to be related to the lipid-binding capacity [85]. PINs bind to lipids, likely via the Trp-rich domain [68, 86], can stabilise lipid monolayers [87] and therefore prevent polar lipid breakdown in the endosperm [88]. Mutations can lead to changes of the lipid binding capacity [89]. In the endosperm, PINs are linked to the lipid content at the starch granule surface [73, 90]. It was shown that PINs require lipids to be able to bind to starch [90, 91].
Though the biological function of PINs may be antimicrobial, it is indisputable that they form the biochemical basis of grain hardness, which is discussed in detail in subsection 2.6.1.

Grain softness protein Another protein, which is encoded on the hardness locus is the grain softness protein (GSP). But opposite to PINs, which are encoded solely on the hardness locus on chromosome 5D, GSP is also encoded on other chromosomes [13]. The GSP does not interact with lipids *in vitro* [92] and was found to have no significant influence on grain hardness [93].

2.3.3. Lipids

The endosperm contains a small amount of lipids (0.75 % to 2.2 %), which can be separated into starch-associated and non-starch lipids [94]. The lipids are believed to have an important role in determining grain hardness together with PINs [12].
Starch lipids are either located inside starch granules, where they are possibly complexed with amylose [94, 95] or on the surface of starch granules (SGAP) [95]. The latter ones are for the most part lysophospholipids and are hypothesised to be remnants of the amyloplast membrane [96]. Starch bound glycolipids and phospholipids content on the starch granule surface was found to correlate with the occurrence of PINs [90, 97].
Non-starch lipids show greater variation, as they include triglycerides, non-polar lipids, glycolipids and phospholipids [96].

2.3.4. Development, genetic and environmental influences

Starch and gluten accumulate in the endosperm at roughly the same rate, first rapidly from 10 to 21 days after flowering (DAF) and then slightly slower from 21 to 42 DAF [98]. Large A-type starch granules are deposited separately within large amyloplasts from 4 to 12 DAF [46]. B-type starch granules develop in the time between 12 to 18 DAF [46]. Eventually, the amyloplast membrane degrades and starch granules are released into the endosperm cells [46], which undergo apoptosis at later stages of grain development [99].
Proteins are deposited into vacuoles (protein bodies), which start to fuse around 17 DAF to form the protein matrix [100].
Environmental factors during endosperm development such as light intensity, temperature, water availability and fertilizer can influence the starch and protein accumulation and therefore the grain and flour yield [101].

2.4. Industrial wheat milling

Wheat milling or grinding is a dry fragmentation process. It is a part of the wheat processing chain, which starts with the breeder, seed producer and farmer, and then continues with the buyer, miller, and the baker for further processing into food- or non-food products [8]. The goal of wheat milling is to recover as much starchy endosperm as possible, while damaging the bran as little as possible [8]. The morphology of the wheat grain with the presence of a long crease (see Figure 2.2 on page 9) presents a technical challenge for that, because in order to separate bran and endosperm the grain has to be broken open first [16]. This initial breakage of the grain ("first break") is crucial for further processing [8]. Due to this, wheat milling is different to for example the milling of rice grains, which do not have a crease and can therefore be easily de-branned before milling [16].

2.4.1. Wheat grading and quality

Prior to milling, wheat grains are assessed to determine their quality and facilitate the proper processing and milling. However, the grading assessments and classes for wheat are not internationally standardised [16]. Only methods relevant for this thesis are mentioned here.

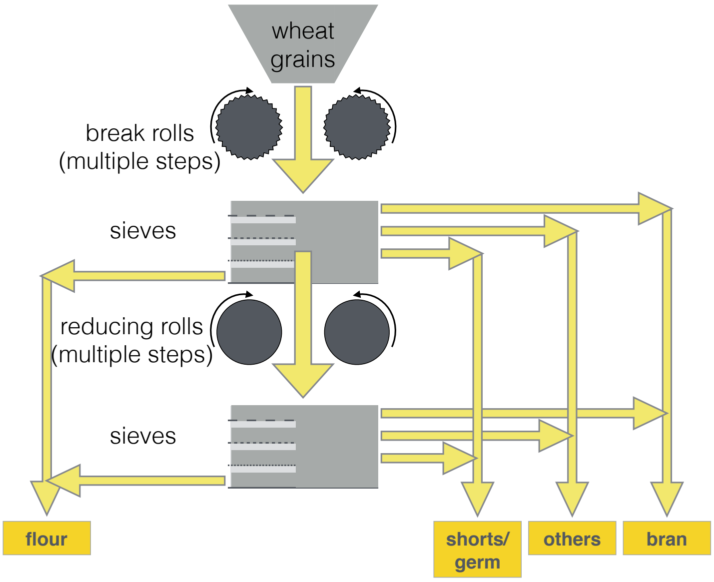

Figure 2.7. – The wheat milling process is shown schematically. The first step is the breaking open of the grains with the break rolls, which is followed by sieving and separation of the fractions. In the reduction step the particle size is further reduced and more starchy endosperm is disassociated from the bran tissues. Adapted from [102].

Grain grading

Hardness Kernel hardness is an important factor that directly influences the milling of grains and the end-uses of the obtained products (Figure 2.8) [103, 104]. It is for a large part determined by the mechanical properties of the starchy endosperm, because of its major contribution to the grain tissues (>80 %). A common classification for wheat is into three categories: soft and hard common wheat and extra-hard durum wheat, which is based on the allelic state of the genes encoding the PINs [13].
From a purely mechanical point, hardness is defined as the resistance of grains to crushing [105]. Different grain-scale measurements for hardness exist. Particle size index (PSI) [106, 107] and near infrared reflectance spectroscopy (NIRS) [108, 109] measure the particle size distribution of ground grains by either sieving or spectroscopy. Another method is the single kernel characterisation system (SKCS) [110], which measures the crushing force of individual kernels [111]. Because of their different methodology, these measurements give different information about the grain and are not interchangeable [112]. Another approach is the measurement of the mechanical properties of endosperm blocks [113], which is however difficult to apply on a large scale, because preparation and mechanical testing is time-consuming.
The biomechanical mechanism of grain hardness is discussed in detail in section 2.6.

Protein content Soft common wheat grains have usually the lowest protein content of wheat cultivars (8 % to 11 %). Hard common wheat grains have a higher (10 % to 14 %) protein content and durum wheat grains have the highest protein content (9 % to 18 %) [114].

Vitreosity Vitreosity (or vitreousness) describes the glassy and translucent appearance of kernels [115] and is determined optically. Vitreosity is to some extent related to protein content [112, 115, 116, 117] and is controlled by both genetics [118] and environment [112, 116, 117].

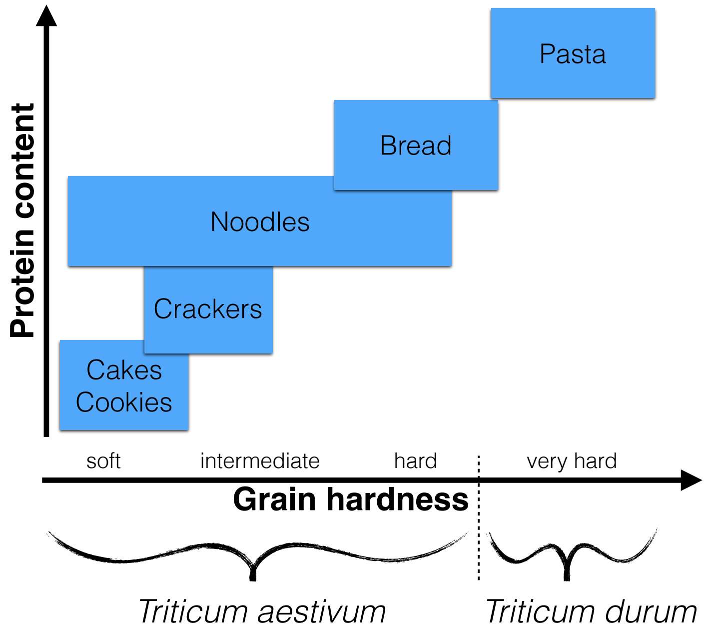

Figure 2.8. – The end use of wheat flour depends on the flour's protein content and the hardness of the grains. Adapted from [104].

Test weight The test weight (TW) is the weight of 1 hL of wheat grains, which is sensitive to measuring conditions (moisture level, grain shape, amount of broken kernels) [16].

Thousand Kernel Weight The thousand kernel weight (TKW) gives the weight of one thousand grains of wheat and is an indicator of millability and highly correlated with flour yield [16]. (However, disagreeing reports exist, too [119].)

Flour grading

Break flour yield The recovery of as much flour as possible is the main goal of the milling of wheat grains [16]. The first step in the milling process is the breaking open of the kernel, which also fragments the endosperm and produces the so-called break flour [8]. It is followed by "reduction" steps (Figure 2.7 on page 16), in which the different fractions are milled further to produce more flour by separating more endosperm from the grain envelopes [8]. Wheats of the soft genotype produce higher break flour yields than hard genotype wheats [120].

Protein content and functionality Protein content and functionality are important for the further use of the flour (Figure 2.8) and therefore the quantity and quality of the protein in the flour is an important parameter for the baker [16, 114].

Starch damage During milling a percentage of starch granules is damaged. The amount of starch damage is depending on the wheat genotype [121, 122]. Damaged starch absorbs more water and is more susceptible to enzymatic degradation [123]. It influences the dough handling properties [124] and is therefore an important factor for the baker [125].

2.5. Wheat milling research general

Research on wheat grain milling is an interdisciplinary field that combines different specialties. The general goals are the accurate prediction of milling behaviour from a known set of grain characteristics and the development of grains with better quality or higher suitability for specific end-uses. At the basis of this has to be the aim for a comprehensive understanding of the determinants of milling behaviour and end-product quality.

The foundation of grain milling research is the milling of a low, but sufficient number of grains under conditions that replicate the industrial milling conditions. Such tests can serve best to predict milling behaviour [126]. Experimental milling is done on commercially available laboratory [5]or pilot wheat mills or home-built mills, such as the one described by Pujol et al. [126]. The grain properties of interest (hardness, vitreousness, protein content etc.) are determined on grains before milling and the characteristics of the end product (starch damage, protein content, flour yield, biochemical marker for tissue dissociation) are evaluated after completion of the milling process. Analysis of the relationships between grain properties, milling behaviour and product properties helps to clarify the underlying mechanisms of milling behaviour and consequently its prediction. Some authors also focus purely on the prediction of milling behaviour by a mathematical equation, called the breakage or milling function [127, 128].

A crucial point for milling experiments is the need for specific samples to test distinct hypotheses. Milling experiments therefore go hand in hand with wheat breeding and wheat cultivation in different environments. Breeding in general is done with the aim to improve grain quality for milling or the nutritional quality of the milling products [129]. Breeding led for example to the creation of NIL, which allow to study the effect of specific QTL [112, 130, 131, 132, 133, 134, 135]. Genetic manipulation methods or cross-breeding also enabled gene transfer, for example *pina* and *pinb*, in between species leading to the creation of transgenic rice [82, 136], maize [137], durum wheat [14, 138] or common wheat [122, 139, 140]. The grains from these transgenic plants can have very different properties and milling behaviour compared to the parent plant. The analysis of their milling behaviour does therefore contribute to the understanding of the effects of the translocated genes on one hand [78, 82, 129, 122, 136, 137, 140] and, on the other hand, can result in the creation of new constituents for bakery products [141, 142].

Genetics is also applied to determine the genetic diversity between plants [143, 144, 145] and genetic mapping can find QTL of grain properties [146, 147].

Other methods help to close the gap between genetics and grain properties. Proteomics was used to identify the proteins in specific grain tissues (germ [148], aleurone layer [149]) or components (proteins [10, 133, 150], starch [151]). Not only can the protein functions be identified, but the proteomes can also be compared, making it possible to analyse differences and similarities at different stages of grain development [10, 133], between different cultivars and varieties [149, 150, 151] or for different environmental conditions during grain growth [149].

With microscopy, spectroscopy and biochemical assays the localisation of specific components within the grains can be determined [70, 71, 74, 72] and the composition, structure and functional properties of the separate endosperm components are studied in great detail (proteins reviewed in [152], starch reviewed in [26], lipids reviewed in [153], PINs reviewed in [154]).

And finally, the milling behaviour is analysed by the means of biomechanics. The approach has to be "bio"-mechanical, because in order to obtain meaningful knowledge, the mechanical approach needs to be linked with methods from biology [2], such as the ones described above. The contribution of biomechanics to grain milling research lies in the explanation of the milling behaviour, which can for example aid the genetic selection of lines with properties leading to the wanted milling product.

---

[5] For example the labmill by Chopin technologies, French Patent Chopin, INRA, ARVALIS, No. 0905572

2.6. Biomechanics of grain fragmentation

The central question of (biomechanical) research on grain fragmentation is the understanding of processes and properties, which determine the breaking behaviour. This is approached by investigating the influence of grain properties on the milling behaviour (Figure 2.9). Most of the grain properties of interest are structural properties, such as grain protein content or starch granule size distribution. Vitreousness is an optical property, but related to porosity and therefore structural properties. Grain hardness is a mechanical property of the whole grain [155] and therefore already depends on the structural properties.

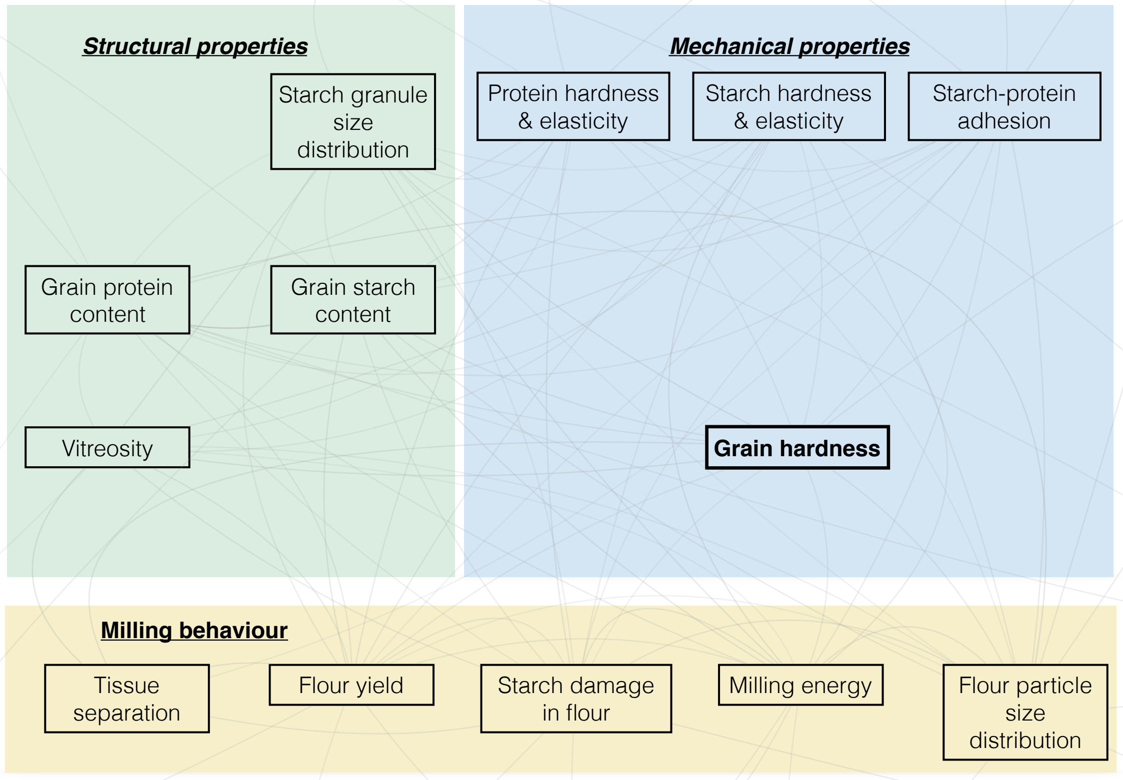

Figure 2.9. – Milling behaviour and product properties are the result of a complex network of factors, including the grain's structural properties and the mechanical properties of its components. (This overview is non-exhaustive, as it focusses only on the properties discussed in this thesis.)

The question for the basis of milling behaviour can be separated in two parts:

1. How do the structural and mechanical properties affect each other?
2. How do the structural and mechanical properties affect the milling behaviour?

As expected for the complicated structure of the wheat grain, no single grain property can explain all the differences of the milling behaviour, but it has to be a combination of different properties. The two seemingly most important grain properties are hardness and vitreousness. Grain hardness can be defined as the resistance of grains to crushing [105]. Different experimental methods for the determination of grain hardness have been developed, but they are based on different measurements (particle size distribution after crushing or crushing force, see subsection 2.4.1). Therefore, depending on authors, the term hardness corresponds to NIRS, PSI or SKCS measurements. Additionally, hardness can be referring to the genotype in terms of the allelic state of PIN genes (section 2.3.2), which can create confusion [156].

2.6.1. Genotype, puroindolines and hardness

Grain hardness as measured on the phenotype is strongly correlated to the genotype, specifically to the allelic state of both PINs. This correlation is so strong that a large number of authors use the terms "soft" and "hard" common wheat to refer to the genotype. The hardness locus, where both PINs are encoded (on the genes *pina* and *pinb*), is certainly the major genetic cause for grain hardness. Though the exact biochemical mechanism through which PINs change grain hardness is not yet completely understood, the knowledge of the relation between genotype and phenotype is substantial.

It is known that a soft phenotype (measurable by SKCS or NIRS) needs the presence of both PIN genes in the wild-type allelic state (*Pina-D1a* and *Pinb-D1a*) [12]. The configuration of *Pina-D1a* and *Pinb-D1a* is therefore the (genetically) soft wheat. A number of mutations are known for both, *pina* and *pinb* [157] and result in a hard or medium-hard phenotype [13, 158]. Any allelic configuration differing from the (genetically) soft wheat with *Pina-D1a* and *Pinb-D1a*, would be termed (genetically) hard wheat.

Though the mechanism by which PINs change grain hardness is not yet fully understood, their effects on grain and milling properties are rather well documented, especially through studies of transgenic plants, where one or both PIN genes were introduced. In transgenic rice with *pina* and/ or *pinb* the rice grain hardness was reduced, the starch obtained less damage during milling and the flour particles were finer [82, 136]. When the grain structure was studied more in detail in transgenic rice with *pinb*, air spaces between the compound granules were observed. PINs were found to be located between the compound granules and between the single starch granules within compound granules [74]. Similarly, in transgenic durum wheat with *pina*, grains had a medium (SKCS) hardness value, which correlated with the level of PINA, and even more closely with the level of starch-bound PINA [78]. SEM observations of the endosperm showed that the protein in the transgenic grains was adhering less to the starch granules [78]. The transfer of both wild-type puroindoline genes, *pina* and *pinb*, into durum wheat resulted in mechanically soft (SKCS) grains [14].

The overexpression of PINs in (genetically) soft or hard common wheat also reduced grain hardness (SKCS) and resulted in smaller flour particle size [8, 79]. This agrees with the hypothesis of Nirmal et al. [159] that it is not only the presence of genes, but also the expression level, which is different in (genetically) soft and hard common wheat.

Therefore, there seems to be a general mechanisms by which PINs influence grain hardness, regardless of the cereal species. The effect seems to be only locally, because grain properties such as protein content, amylose content in starch or grain diameter were not affected. Changes in the structure could be observed qualitatively for the adhesion between starch and protein [78, 136].

2.6.2. Grain scale mechanical and milling experiments

Relations amongst grain properties A number of authors investigated the relationship between the measurable grain properties. Protein content is only weakly correlated to SKCS and NIRS hardness [112, 131], but rather strongly to vitreousness [112]. SKCS hardness was found to be correlated with vitreousness [112, 160]. Relations were also found for SKCS hardness and starch granule size and starch properties. Harder (SKCS) wheats have a higher amylose content and higher starch crystallinity [54, 57]. Softer wheats (determined by milling) were found to have larger granules by Gaines et al. [161], whereas Singh et al. [57] observed more granules with sizes >25 µm for harder (SKCS) grains. On the contrary, harder (NIRS) wheat were also observed to have a higher number of small granules [146] and for genetically hard wheat a lower number of large granules was observed [48]. However, greater B-type granules were observed in genetically hard wheats [48]. Due to the number of factors involved when mechanical hardness is measured, it is still difficult to relate starch granule size distribution (SGSD) to the mechanical grain hardness.

Grain properties and milling behaviour Grain hardness correlates with the most important milling characteristics (break flour yield, starch damage, milling energy and others) [112, 120, 126, 131, 162, 163, 164, 165]. Harder grains (NIRS, SKCS) require more energy to produce the same amount of flour like soft grains [126, 131] and the break flour yield is higher for lower SKCS hardness values [112, 120, 162, 163, 164]. Harder grains (SKCS) produce flours with a higher amount of damaged starch [122, 121, 164], whereas softer grains (NIRS) produce finer flour particles [131]. Flours produced from softer grains can also be clearly distinguished from those from hard grains as they display a bimodal particle size distribution profile compared to the unimodal one found for flours from harder grains [131].

Vitreousness was found to be correlated to the ability of the endosperm for size reduction, the energy to produce flour [131, 160] or the amount of first break flour [131]. The flour yield was also found to be higher, if starch granules are larger [161] or large granules are higher in numbers [166, 167]. Interestingly, the effect of vitreousness on hardness [112] and milling behaviour [131] was found to vary for different PIN alleles, indicating different mechanics between grains with different genotypes.

Tissue dissociation The dissociations of the different grain tissues happening during the milling process can be evaluated by biochemical characterisation of milling products [168]. Phytic acid was found to be a good tracer for the fate of the aleurone layer in the breaking step [169]. Differences in phytic acid content between millings of grains of different (genetical) hardness showed that hardness also affects the way of separation between outer layers and starchy endosperm [169]. Harder wheats seem to have a more efficient separation between starchy endosperm and bran, but the bran is also more damaged, which leads to higher contamination of the flour with bran [169].

Knowledge on these tissue dissociation and the properties of the outer layers is therefore also important for predicting grain milling.

2.6.3. Endosperm bricks

When whole grains are milled for experiments, the number of properties that could possibly lead to observed differences in milling behaviour is large. And the application of uni-directional mechanical tests to whole grains is difficult because of the morphological differences of the kernels, as for example the depth of the crease [126]. Furthermore, Pujol et al. [126] discussed that the stress field between the milling rotors is highly complex. The behaviour observed in milling experiments is therefore expected to be caused by a complex interplay of many factors (Figure 2.9), which are difficult to disentangle.

Because the grain consists of more than 80 % of endosperm, it can be assumed that most of the grain's mechanical properties are determined by the endosperm's mechanical properties. A suitable system for experimental mechanical measurements are well-defined volumes of starchy endosperm, because they eliminate difficulties caused by the other grain tissues or the grain shape, but conserve the structure and interaction of the components within the starchy endosperm.

A number of authors generated endosperm blocks or bricks and tested them in compression or tension to obtain the Young's modulus, yield stress and to observe the fracture surface [14, 131, 155, 170, 171]. Most authors test endosperm volumes in compression, except for Glenn et al. [170] who also included tension tests. The absolute values or Young's modulus and yield stress obtained from such experiments vary significantly between laboratories [14] and instruments [172]. Generally, non-vitreous, (genetically) soft wheat has the lowest yield stress and Young's modulus. Non-vitreous wheats also have significantly lower yield stress than vitreous ones [131, 155, 170]. The Young's modulus is affected to a lesser degree than yield stress by vitreousness [131, 155, 170]. However, not only the absolute values are different, but also the relative change of Young's modulus between vitreous and non-vitreous varies for the different studies. Similarly, the change of the reported Young's modulus between (genetically) hard and soft wheats is different between authors, which hinders qualitative conclusions.

Fracture surface Glenn et al. [170] and Wang et al. [171] imaged the fracture surfaces of the endosperm blocks with SEM. In (genetically) soft, non-vitreous wheat not much adhesion of the protein to the starch granules was observed after both tension and compression tests [170]. Whereas no cavities in the shape of starch granules were observed in the protein matrix in compression for soft non-vitreous wheat, such cavities were present after tensile failure. Contrary to the crack pattern of soft non-vitreous wheat, in soft vitreous and durum wheat cavities of dislodged starch granules were observed on the fracture surface after compression, whereas tensile failure created mostly broken starch granules [170]. Wang et al. [171] stated that the crack pattern in compression goes around the starch granules. The differences mostly highlight that the fracture patterns depends on the testing direction. An additonal observation related to starch granule fracture is that broken starch granules are showing an angular slope towards the centre of the granule [170].

2.6.4. Nano-mechanics

To understand the mechanical behaviour of a composite structure, it is also necessary to know the mechanical properties of the structural components separately and their interaction. The major components of wheat endosperm are starch granules and the protein matrix (section 2.2). The properties of interest are their hardness and elasticity (Figure 2.9 on page 19). The structural level of starch, which is mostly relevant for endosperm mechanics is the highest level of starch organisation - the starch granule. Similarly, for proteins it is the network of polypeptides. Mechanical properties at this micro- to nanometer-scale can be resolved with specific AFM approaches, but only a limited number of studies on starch exists so far.
Salerno et al. [44] used a number of different techniques on resin embedded starch and reported an indentation modulus of ≈ 1.5 GPa and contact modulus (1.8 ± 0.3) GPa for wheat starch. Chichti et al. [135] performed AFM abrasion tests to determine the hardness of common wheat starch and protein in cut grains without resin embedding. They report an abrasive hardness of (2.4 ± 0.6) GPa and (2.5 ± 0.3) GPa for hard and soft common wheat starch, respectively. Protein hardness was reported to be (0.64 ± 0.17) GPa [173] Furthermore, differences at the starch-protein interface between NILs of common wheat differing in the allelic state of the PIN genes could be demonstrated [135]. In (genetically) soft lines, a behaviour indicating a lubricating interface between starch and protein was observed [135].

2.6.5. The biomechanical mechanism of hardness

Despite the accumulated knowledge of wheat grain structure, PINs and milling behaviour, the biomechanical basis of grain hardness is still not fully understood and greatly debated. From the mechanical viewpoint the cause of significant differences wheat hardness could lie in the properties of the storage proteins, starch, the adhesion at the interface between protein and starch or the porosity of the protein matrix (related to vitreousness). The protein content was observed to not change due to the presence of the PIN genes [78], but vitreousness seems to be partly influenced by the hard or soft genotype. The effect of SGSD on (mechanical) grain hardness is still under debate.

The most widely accepted hypothesis is that differences in hardness are caused by changes of the starch-protein interface adhesion due to PINs, which are encoded on the hardness locus on chromosome 5D. The adhesion hypothesis was brought forward by Barlow et al. [174], who observed a similar protein composition, which indicates similar protein mechanical properties, but differences in a starch-bound extractable fraction. In agreement with that, Arena et al. [175] also observed no proteomic changes between common wheat and durum wheat, except for the proteins encoded on chromosome 5D. The differentially expressed proteins are largely involved in metabolism, but also in protein destination and storage, defence, protein synthesis and cell structure [175]. This is in accordance with the results of Lesage et al. [133] in common wheat, who also found differentially expressed protein involved in starch metabolism, protein synthase and assembly, stress defence and cell structure. Lesage et al. [72, 133] observed changes of the polymer size and polydispersity of albumins and globulins during grain development for different genotypes. Their results showed that the protein matrix is formed earlier in (genetically) hard wheat than in soft and that the apoptosis of endosperm cells occurs earlier in hard wheat [133]. Lesage et al. hypothesised that PINs contribute to the folding of storage proteins or prevent early aggregation of those. From their experiments it is however not possible to separate the effect of PINs from other possible causes of protein changes, such as vitreousness.

Turnbull et al. [176] observed that the timing of PIN accumulation in the developing grain and the possible distinction between mechanically soft and hard grains do not fully coincide and therefore concluded that hardness is most likely not only the result of starch-protein adhesion (caused by PINs).

In 1977, Stenvert et al. [177] proposed that hardness is caused only by differences in the state (porosity) of the protein matrix and not by adhesion. Though by now the adhesion hypothesis is supported by indirect proof (i.e. SEM observations [170] and AFM abrasions [135]), some of Stenverts arguments might be worth being reconsidered. They observed that within a single cultivar, hardness changes with the amount of protein and that the quantity of protein that is required to create a full matrix (vitreous grain) is depending on the genotype. This implies that the same protein content can lead to more or less vitreous grains. These arguments do in fact integrate well with what is known to date about the relationship of vitreousness and hardness. For hard and soft wheat, vitreousness was found to be correlated to grain hardness (SKCS) [112]. But the protein content alone was also not sufficient to explain all observed differences in vitreousness and hardness [112]. This is also supported by for example the different hardness found for transgenic durum wheat without a change of protein content [78].

It therefore seems evident, that hardness is the result of at least the two factors: starch-protein adhesion and vitreousness. Vitreousness could possibly be linked to the genotype indirectly through changes of the starch-protein adhesion. However, vitreousness is also strongly affected by the growth conditions.

Another possible factor for grain hardness could be the starch properties and Budny et al. [178] observed that starch was the main factor for changes in the mechanical resistance of endosperm models. They therefore concluded that a non-protein mechanism is involved in the determination of the mechanical resistance, which could be the composition or structure of starch. In barley, Yu et al. [179] observed differences in the activity of starch synthase correlated to different protein content. However, nano-mechanical measurements of starch and protein in wheat found no differences in the starch and protein hardness between soft and hard genotype so far [135].

In summary, grain hardness is at the first instance caused by the allelic state of the PIN genes, but also the expression level [159]. In the further instances however, a complicated network of different direct and/ or indirect interactions follow, which we are only beginning to understand.

2.7. Mechanical modelling of endosperm fragmentation

Numerical modelling is an approach from the mechanics field, which can be very helpful for biomechanical questions, especially when a complex interplay of mechanical and biological aspects is present, which is undoubtedly the case for wheat grain hardness.

The starchy endosperm can be considered as a cemented granular material, where the harder starch granules are embedded in a softer protein matrix. A small number of numerical studies investigated the strength properties of endosperm as a cemented granular material [180, 181, 182, 183]. Among the investigated parameters were the effect of matrix volume fraction [180, 181, 182, 183], which relates to matrix porosity and therefore vitreousness, and particle-interface strength [180, 181, 182, 183], according to the strach-protein adhesion hypothesis for PINs. The influence of particle volume fraction was also investigated [183], which relates to differences in starch content.

A first model two-dimensional modelling approach was presented by Delenne et al. [184] based on the micro-mechanics of cohesive granular material. In a geometrical model, rigid spheres of two different sizes (Figure 2.10a) were connected to different percentages by bonds with a set failure criterion. With this simple approach the breaking behaviour observed in experiments on endosperm bricks [185] could be reproduced. Based on these first promising results, more complex approaches were developed to model wheat endosperm. With a two-dimensional lattice element method (LEM) model (Figure 2.10b), Topin et al. [181] performed a parametric study for particle-matrix adherence and matrix volume fraction on the stiffness, yield strength and crack propagation in tension. They showed an almost linear evolution of the effective stiffness with the matrix volume fraction and resolved the dependency of the tensile strength on both parameters. Furthermore, the particle damage was shown to scale with the relative toughness between particles and the particle-matrix interface and three distinct regimes of particle damage were distinguished based on matrix volume fraction and particle-matrix adhesion (Figure 2.10c) [181]. The findings were also confirmed for compression [182]. In the continuation of this work, Chichti et al. [183] (Figure 2.10d), refined the model with values obtained from AFM nano-mechanical measurements for the elastic properties of starch and protein. They confirmed the strong dependence of the elastic modulus on the porosity of the matrix and the strong dependence of the yield stress on the particle-matrix adhesion.

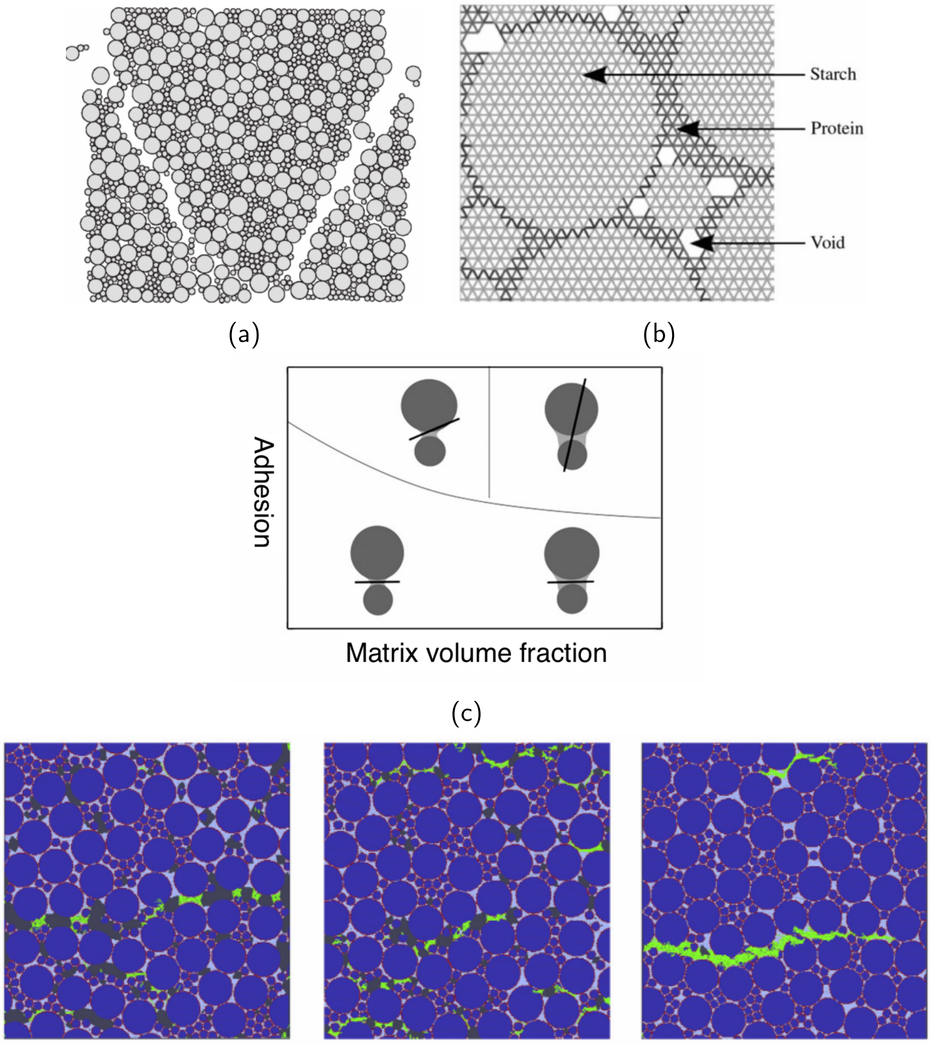

(a) (b)

(c)

(d)

Figure 2.10. – (a) A volume element after compressive failure in the simple geometrical model by [184], (b) The LEM used by [181, 182, 183] distinguishes between the phases starch, protein and voids, (c) The three cracking regime found by Topin et al. [181, 182] depending on matrix (protein) volume fraction and starch-protein adhesion, (d) Sample volumes after fracture under tension with increasing matrix volume fraction (left to right) [183].

3. Puroindolines and milling behaviour

Contents

Millers used to ask the "Millwright" - the craftsman who carved the surfaces of the millstones - to show them "their metal": while carving the millstones, pieces of stone and metal would embed in the forearms of the millwright and more "metal" revealed more experience.

3.1. Puroindoline genes introduced into durum wheat reduce milling energy and change milling behavior similar to soft common wheats

Abstract

Grain physical characteristics and milling behavior of a durum wheat line in which both wild-type puroindoline genes were translocated and stabilised after backcrossing (*Svevo-Pin*) were compared with the parent line (*Svevo*). The only observed differences between grain characteristics were the mechanical resistance and starchy endosperm porosity revealed through vitreosity measurement. A significant increase of flour and a decrease of semolina yield and break milling energy were observed from *Svevo-Pin* in comparison with the non-recombinant parent line in accordance to the lower grain mechanical resistance and higher porosity measurements. Moreover, the particle size distribution shown for *Svevo-Pin* flour appeared consistent with a lower adhesion between starch granules and the protein matrix attributed to the presence of wild-type puroindolines. Coarse bran yield was conversely increased. This appeared to be due to a lower starchy endosperm recovery as a higher proportion of grain starch was found in this bran fraction. Flour from the durum parent line was inversely enriched in phytic acid, a cellular marker of the aleurone layer. Starch damage was also lower in *Svevo-Pin* flours in comparison with *Svevo*. All of the observed differences between translocation and parent lines were confirmed independent of the culture growth conditions (n = 12).

3.1.1. Introduction

Wheat grain hardness is a key parameter that influences its mechanical properties, milling behavior, and end-uses [103, 104]. Grain hardness was found mainly related to the genetic background and more precisely to the Hardness locus, *Ha*, on the short arm of chromosome 5D, which encodes the so-called puroindolines (PINs) a and b [143]. The allotetraploid [1] *Triticum durum* ($2n = 28 =$ AABB), which does not contain the D genome and thus no PINs, displays the hardest grain texture and essentially produces coarse semolina at milling, which is used primarily for pasta and couscous. The allohexaploid *Triticum aestivum* (or common wheat, $2n = 42 =$ AA BB DD) can be divided in two distinct grain hardness types [13] depending on the presence of wild-type alleles of both puroindoline genes (= soft type) or the presence of a null allele or mutated allele of one of the two puroindoline genes (= hard type). Differences between hard and soft common wheat texture were found to be only related to changes at the interface between starch granules and the protein network in the wheat endosperm due to the distinct nature and amount of PINs, which appeared to affect the adhesion between the constituent polymers [174, 186]. Mechanical changes at the interface had only been recently demonstrated by Chichti et al. [135] using near-isogenic lines (NILs) differing only by the wild-type or mutated version of one of the puroindoline genes.

Evidence for the direct effect of both wild-type puroindolines on the mechanical properties of the endosperm also results from complementation of the null allele or mutated allele with the wild-type allele to restore a soft phenotype [122, 139]. Conversely, silencing of puroindoline genes led to an increase in grain hardness [140, 187]. Removal of the Hardness locus results in grains with mechanical properties similar to durum wheat [118].

Comparison of the milling behavior of near-isogenic common wheat lines indicates that soft grain texture results in a reduction of milling energy, the production of a higher amount of small particles recovered as flour and an increase in the coarse bran fraction at the breaking stage in comparison with hard grains [131]. Concomitantly, the soft wheat break flours showed lower levels of ash, which likely result from the greater extensibility of the corresponding grain outer layers [188]. Moreover, flours produced from soft grains can be clearly distinguished from those from hard grains as they display a bimodal particle size distribution profile rather than a unimodal one. Presence of wild-type puroindolines was also associated with a lower level of starch damage in flours [121, 122]. This difference in particle size distribution and starch damage probably results from differences in adhesion between starch granules and the protein network, which appears to be weaker in soft wheats. Construction of a numerical model of the endosperm structure confirmed the importance of adhesion between the constituent polymers on the grain mechanical resistance differences and starch damage level [181, 182]. A lower adhesion, as expected from the presence of wild-type PINs, leads to a reduction of overall mechanical resistance and starch damage. Due primarily to starch damage and water absorption/ batter and dough viscosity, hard common wheats are mainly used for common making whereas soft wheats are better for cake and biscuit making [189].

Recently, both of the wild-type alleles of the puroindoline genes were successfully introduced in a durum wheat background providing the possibility to obtain wheat grains with expected changes in their milling behavior and product properties in comparison with the durum parent cultivar [14, 141, 142, 190].

The present study analyses in detail the grain characteristics, milling behavior, and energy required to grind a recombinant Italian durum cultivar in which puroindoline genes were introduced (*Svevo-Pin*) in comparison with the parent cultivar (*Svevo*) grown together in distinct locations.

---

[1] see allopolyploid and polyploidy

3.1.2. Material and methods

Wheat samples and grain physical characteristics

Grains from the Italian durum wheat *Svevo* cultivar and a translocated wheat line, *Svevo-Pin*, where the puroindoline genes from chromosome 5D of the soft common wheat cultivar *Chinese Spring* were introduced, were collected in 2014 in one location in the South of France (Maugio) and in 11 different locations in the U.S. All U.S. locations were in Eastern Washington State, ranging between 117°3′ W to 120°14′ W longitude, and 46°0′ N to 47°40′ N latitude. In each of the U.S. locations, two field plot replications of *Svevo* and *Svevo-Pin* were analyzed.

Morphological measurements (length, width, thickness) and weight of each of approximately 300 grains of *Svevo* and *Svevo-Pin* samples, grown in France, were performed with a micrometer and a micro-precision balance as described in [191].

Particle size index (PSI) was measured to evaluate hardness according to internationally approved method (AACCI N° 55-30.1). At least three determinations were performed and the results presented as means and standard deviation.

Grain vitreousness was evaluated after cutting the grains with a Pohl grain cutter (Versuchs- und Lehranstalt, Brauerei, Berlin, Germany) with three repetitions of 50 grains each to determine the sum of percentage of totally or partly non-vitreous grains.

For the U.S. grown samples, hardness index (HI) and grain weight were determined with the single kernel characterisation system (SKCS) 4100 apparatus (Perten Instruments, Inc., Springfield, IL) according to approved method (AACCI N° 55-31.01).

Test weight (TW) was determined with AACCI N° 55-10.01 method.

Biochemical analysis

Moisture content was determined using a standardized international method (ISO 712:2009) on ground grains and milling fractions. Grain protein content was measured directly on grains using near infrared reflectance spectroscopy (NIRS) (AACCI N° 39-25.01) or using the Kjeldahl International Standard Method (ISO20483, 2013) using a nitrogen-to-protein ratio of 5.7, with at least two measurements performed on ground grain samples. Phytic acid content of ground grains or flours was measured at 500 nm from acidic extracts according to a colorimetric method, in comparison with a standard curve obtained with corn phytate (P-8810, Sigma-Aldrich, St. Quentin Fallavier, France) solutions of known concentrations, as detailed in [168]. Total starch concentration was determined in duplicate on ground grains or on milling fractions using a Megazyme kit "Amyloglucosidase/alpha-Amylase method" according to AACCI 76-13-01 method (K-TSTA assay kit, Megazyme International Int., Ireland). Before analysis coarse bran fractions were ground with a ball grinder (MM400, Retsch, Haan, Germany) after being frozen in liquid nitrogen. Damaged starch was determined on milling flours with a Megazyme kit (K-SDAM starch damage assay kit, Megazyme Int., Ireland) according to method AACCI N° 76-31.01.

Wheat grain processing

Two replications per U.S. location and the French samples were used to study the milling behavior of *Svevo-Pin* in comparison to *Svevo*. The French sample was analyzed twice independently.

Grain moisture content before milling was adjusted to $(16.8 \pm 0.4)\,\%$ by adding water to grain during a time period of (19 ± 2) h, including an initial 2 h of constant mixing. Milling was performed with around 200 g of grain using a laboratory micromill, which is instrumented to measure torque between

the two rotating cylinders [126], and thus measured the milling energy in kJ kg^{-1} at the breaking step (corrugated rolls, dull to dull orientation). The first break (B1) occurred with roll speeds of the fast and slow rolls adjusted to 500 and 200 rounds per minute (rpm), respectively, a roll gap and length of 0.70 mm and 0.50 mm respectively, and a constant grain feed rate of 2 g s^{-1}.
Milling fractions were then classified by sieving on a rotary screen (Rotex, Tripette et Renaud, Paris, France) for 5 min on square-mesh sieves (200, 500, 710, 1000, 1400 and 2500 mm). The recovered fractions with particle size superior to 1000 mm were subjected to a second break (B2) with roll speeds of 1000 and 285 rpm, and gap of 0.10 mm, at the same feed rate as B1. B2 fractions were then sieved (same sieves as B1 without the sieve of 2500 mm).
Flours were the finest fractions recovered under the 200 mm sieve after B1 and B2 (first break flour (FB1), second break flour (FB2)). Particles of fine semolina were passing through the 500 mm sieve and overs 200 mm whereas coarse semolina were passing through the 710 mm and over 500 mm. They were recovered after B1 and B2 and pooled for further analysis. coarse bran (CB) corresponds to fractions larger than 1000 mm obtained from B2. The fractions were weighed at each step, and stored separately at 4 °C before biochemical analysis. Flour particle size was determined by laser granulometry (Malvern Mastersizer 2000, Malvern Instruments SARL, Orsay, France).
The energy required to produce one kilogram of total flour was calculated from the micromill data and is represented by the K0 index (in kJ kg^{-1} of flour).

Statistical analysis

XLSTAT (Addinsoft SARL, Paris, France) or R software (www.r-project.org) were used to perform box plots, one-way ANOVA or wilcoxon rank sum tests or comparison between means with Student t-test and linear correlation analyses. Differences between sample values were marked in the Tables as either non-significant (*n.s.*), or with asterisks depending on their level of significance 95 % (*), 99 % (**), superior to 99 % (***).

3.1.3. Results and discussion

Introduction of wild-type puroindolines in durum wheat markedly changed the grain mechanical properties

Length, width, thickness and weight of individual grains from *Svevo* and *Svevo-Pin* grown in France were measured in order to compare their morphological and grain filling characteristics (Table 3.1).
No significant differences were observed, except grain thickness which appeared slightly lower for *Svevo-Pin* in comparison with *Svevo*. Both wheat samples exhibited typical durum wheat grain features as identified by Mabille and Abecassis [191], i.e., a higher ratio of grain length by width compared with common wheat grains (Table 3.1). Similar grain weight was observed and both varieties displayed similar biochemical composition of the main compounds as starch (65 %), protein (15 %), and ash 1.8 % (grain dry mass basis).
In contrast, the PSI value of *Svevo-Pin* was five-fold greater than that of *Svevo* (Table 3.1), reflecting a softer texture in accordance with the known effect of wild-type puroindoline introduction in the changes of grain's mechanical properties [14, 122, 139]. Moreover, the *Svevo-Pin* grain texture was also found to be affected as the number of non-vitreous grains was greater than that observed for *Svevo*. Indeed, the number of totally vitreous grains was less than 1 %. Therefore, the presence of puroindolines also appeared to increase grain porosity as the samples were grown in the same location and cultivation conditions. These results were in agreement with previous studies undertaken on

Table 3.1. – Means and standard deviations (in brackets) for grain morphological traits and weight (water content 11.5 %) of *Svevo* and *Svevo-Pin* (grown in France). Mechanical (PSI) and textural (vitreousness) characterization of the same grain samples. Differences of significance between values for an identical parameter were marked depending on their level in the last column.

Grain characteristics	*Svevo*	*Svevo-Pin*	
Length [mm]	7.9 ± 0.5	7.9 ± 0.6	*n.s.*
Width [mm]	2.9 ± 0.3	3.0 ± 0.3	*n.s.*
Thickness [mm]	3.0 ± 0.3	2.9 ± 0.3	*
Weight [mg]	49.7 ± 11.8	48.3 ± 10.8	*n.s.*
PSI hardness	3.0 ± 0.5	15.0 ± 1.6	***
Non-vitreous grains [%]	26.0 ± 2.0	99.3 ± 1.2	***

common wheat NILs differing only in the allelic form of puroindoline b or presence/absence of the Hardness locus, and thus on grain hardness [112, 118]. Indeed, grains carrying the wild-type puroindoline alleles generally did not display vitreosity levels above 60 % to 70 %. Therefore, these differences in texture and mechanical resistance of grains between *Svevo* and *Svevo-Pin* must have an impact on their milling behavior.

Puroindolines in durum wheat affected the grain milling behavior

An instrumented micromill previously developed to measure the energy (E_t in kJ kg^{-1}) at grinding [126] was used to investigate differences in milling behavior of the two wheat samples. After identical tempering, a first grinding step (B1) was undertaken on grains as described in Pujol et al. [126] and the recovered larger fractions from 2500 mm to 1000 mm were subjected to a second grinding operation (B2) with a higher roll speed and narrower roll gap to mimic the grinding step of a mill processing diagram. The corresponding grinding energies are reported in Table 3.2.

Table 3.2. – Milling energies at each grinding step for 1 kg of *Svevo* or *Svevo-Pin* grains (E_t), or corresponding produced flour (K') and yield of each recovered milling fractions in percentages of total grain weight. Values are the means of three independent millings on two distinct tempered grain batches. The standard deviation is given in brackets. Differences of significance between values for an identical parameter were marked depending on their level in the last column.

Milling data	*Svevo*	*Svevo-Pin*	
E_t B1 [kJ kg^{-1}]	17.4 ± 0.5	13.9 ± 0.2	***
E_t B2 [kJ kg^{-1}]	29.8 ± 0.2	19.4 ± 0.8	***
K' B1 [kJ kg^{-1} flour]	780 ± 62	153 ± 6	***
K' B2 [kJ kg^{-1} flour]	288 ± 2	103 ± 9	***
B1 flour [%]	2.0 ± 0.0	7.9 ± 0.8	***
B2 flour [%]	6.7 ± 0.4	9.8 ± 1.3	***
Total flour [%]	8.7 ± 0.4	17.7 ± 2.1	***
Total fine semolina [%]	40.2 ± 2.4	29.6 ± 0.7	***
Total coarse semolina [%]	44.2 ± 1.6	31.8 ± 2.5	***
Coarse bran [%]	7.0 ± 1.2	21.0 ± 0.3	***

At each milling step, *Svevo-Pin* was shown to require significantly less grinding energy, E_t, than *Svevo* (Table 3.2). The second break (B2) was found to require more energy than the first break (B1) for both samples, but they differed in their response. The energy increase between first and second break was around 40 % for *Svevo-Pin*, whereas it was around 71 % for *Svevo*. Taking into account the milling diagram, this difference reveals greater resistance to reduce the size of the largest particles from *Svevo* grain sample, and potentially to separate the starchy endosperm from the outer bran layers. In comparison with results of Pujol et al. [126], the energy consumption at first break for the *Svevo* sample was in the order of those found with a hard common wheat or a durum wheat, whereas the energy of *Svevo-Pin* was clearly in the order of those obtained for a soft common wheat.

Differences in flour yield at each step also clearly distinguished the two grain samples. *Svevo-Pin* produced 4 and 1.5 fold greater flour yield in comparison with *Svevo*, depending on the grinding step. Flour yield at the first break for *Svevo* was in the same range as already observed for a durum wheat, whereas that of *Svevo-Pin* was increased to a level similar to that for a softer grain, i.e. a hard common wheat [126]. Finally, the total flour yield for *Svevo-Pin* was found to be higher than that of *Svevo*, which is consistent with the changes observed in the grain mechanical properties estimated through the PSI measurement. Therefore, the introduction of wild-type puroindolines into a durum wheat leads to a drastic reduction of the mechanical resistance of the grain and to a significant increase (around two fold) of flour production. These results are in accordance with previous studies on *Svevo-Pin* behavior using different milling devices [190, 192]. The observations are also similar to the changes in milling behavior observed with another recombinant durum wheat line possessing both wild-type puroindolines [142]. It was furthermore shown that the energy required to produce the same amount of flour was significantly reduced by a factor of 5 to 3, depending on the grinding step. Indeed, the required energies to obtain 1 kg of *Svevo* flour (K') were in the range of values observed previously for durum wheat, whereas those measured for *Svevo-Pin* were closer to what was observed for a soft common wheat [126].

Additionally, a distinct particle size distribution profile of flours produced from *Svevo* and *Svevo-Pin* was observed following measurement by laser granulometry. Flour from *Svevo* appeared mainly mono-modal with a peak centred around 155 µm to 160 µm corresponding to D50, whereas flour from *Svevo-Pin* was clearly bi-modal (Figure 3.1). The first observed peak, around 20 mm to 25 mm, is known to correspond to isolated starch granules [193]. The other peak was observed around 110 mm to 130 mm leading to a total D50 value of 80 mm to 88 mm.

These differences in particle size distribution were clearly related to wheat grain hardness [193] and thus linked to the nature of the puroindoline alleles (wild-type or mutated) as demonstrated in [131]. Moreover, introduction of wild-type puroindolines appeared thus to increase the starch granule dissociation from the protein matrix in accordance with their potential role in reducing adhesion [13].

Related to the increase of flour production during milling from *Svevo-Pin* in comparison with *Svevo*, the coarse and fine semolina amount was reduced as expected. However, this reduction was not only explained by the corresponding increase of the flour amount, but also by the three fold increase in coarse bran production from *Svevo-Pin* in comparison with *Svevo*. This milling behavior appeared to be related to differences in grain hardness, as previously observed with near-isogenic common wheats differing in the wild- type or mutated form of Puroindoline b gene [131]. This result could reveal differences in the starchy endosperm-outer layers separation efficiency or distinct mechanical properties of the grain outer layers as already shown with near-isogenic common wheat lines [188].

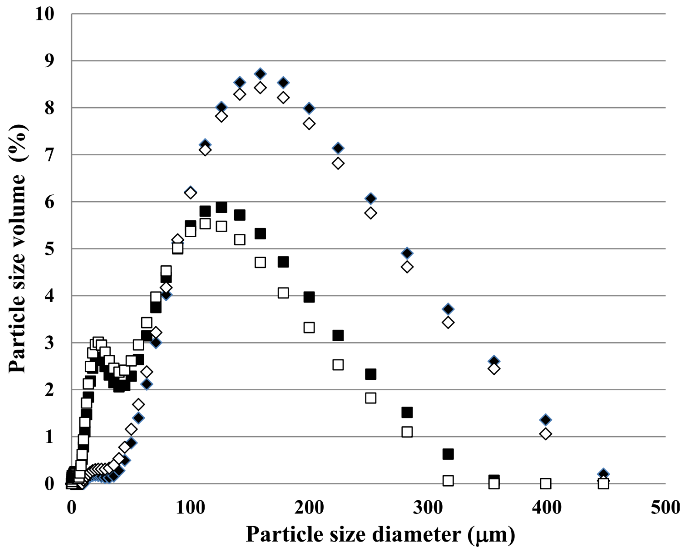

Figure 3.1. – Particle size distribution of flours, determined by laser granulometry and obtained after milling from the first break rolls (B1, closed symbols) or the second break rolls (B2, open symbols) of *Svevo* (diamonds) and *Svevo-Pin* (squares) grains.

Puroindolines in durum wheat affect the grain tissue distribution at break and the level of starch damage

In order to further analyze how the introduction of wild-type puroindolines affected the durum wheat grain milling behavior, biochemical markers, i.e. starch and phytic acid, already found to correctly monitor the starchy endosperm and the aleurone layer [168], were quantified in grains and in coarse bran and flours, respectively (Table 3.3) .

Table 3.3. – Starch content in grains and coarse bran and proportion of grain starch found in coarse bran, phytic acid content in grains and total break flour and proportion of grain phytic acid recovered in flour and level of damaged starch. Results were means and standard deviation from two independent milling repetitions of the same sample. All the values were reported in dry mass. Differences of significance between values for an identical parameter were marked depending on their level in the last column.

Biochemical composition	*Svevo*	*Svevo-Pin*	
Starch content in grains [%]	64.8 ± 1.0	65.6 ± 2.4	*n.s.*
Starch content in coarse bran [%]	28.2 ± 0.8	33.9 ± 1.2	*
Starch proportion in coarse bran [%]	2.9 ± 0.5	10.7 ± 0.1	***
Phytic acid in grains [mg g^{-1}]	15.8 ± 2.5	18.8 ± 2.0	*n.s.*
Phytic acid in flour [mg g^{-1}]	10.2 ± 1.4	3.5 ± 0.0	*
Phytic acid proportion in flour [%]	5.7 ± 0.2	3.3 ± 0.2	***
Damaged starch in flour [%]	11.0 ± 1.2	2.4 ± 0.2	**

Although starch content did not differ between the two wheat grain samples (Table 3.3), starch content as well as proportion of grain starch recovered in coarse bran was found to be significantly higher in *Svevo-Pin* in comparison with *Svevo*. Therefore, a higher proportion of the starchy endosperm was not efficiently isolated in the flour or semolina fractions from *Svevo-Pin* and was instead recovered in the bran fraction. This could account for the increase in the total coarse bran production from *Svevo-Pin* in comparison with *Svevo*. Concomitantly, while no difference in phytic acid content was observed between the two grain samples (around 1.7 %), flour from *Svevo* displayed a higher concentration of this biochemical marker in comparison with flour from *Svevo-Pin* suggesting a difference in the separation of the aleurone layer in the harder grains as already pointed out when comparing hard and soft common wheat cultivars [169]. Therefore, separation between the starchy endosperm and the outer grain layers appeared to differ between the two wheat samples probably as a consequence of the observed grain mechanical property changes linked with the wild-type puroindoline alleles introduction. The aleurone content enrichment of the harder sample in comparison with the one possessing the wild-type puroindolines could be related to the higher flour ash content observed previously [190].

Examination of the percentage of damaged starch in flours from *Svevo* and *Svevo-Pin* revealed a four to five fold higher amount in the former in accordance with the differences in hardness between the corresponding grains. These differences in damaged starch content were consistent with previous data comparing starch damage from *Svevo* and *Svevo-Pin* obtained with different milling devices [190, 192]. Differences in starch damage could explain differences in flour water absorption between a different durum wheat line possessing both wild-type puroindolines and its parent line [142]. These differences in level of damaged starch are also similar to those observed between hard and soft common wheat grains, which differ in the nature of the puroindoline alleles [103], and relate well with the mechanical role of wild-type puroindolines in adhesion impairment. Indeed, reduction of the adhesion between starch granules and the protein network in a numerical model mimicking the starchy endosperm structure clearly showed an impact on the level of starch damage [181, 182].

Milling of Svevo and Svevo-Pin grown from distinct locations strengthen the findings

Svevo and *Svevo-Pin* were also grown at 11 locations in the U.S. and two independent replicate samples of each were analyzed with the instrumented micro-mill. Even though the protein content was shown to vary from 14 % to 20 % depending on location, *Svevo* and *Svevo-Pin* were not found to differ significantly (Figure 3.2). Grain weight and test weight were also not different with means of (43.6 ± 4.6) mg and (42.6 ± 5.1) mg, and (78.0 ± 2.9) kg hl^{-1} and (77.6 ± 3.0) kg hl^{-1}, respectively, for *Svevo* and *Svevo-Pin*. Grain hardness, measured using the SKCS, however, was shown to vary both among locations and between the two genotypes, with *Svevo-Pin* being significantly softer than *Svevo* (Figure 3.2). Hardness Index values of *Svevo-Pin* varied between 2.1 to 40.8 (mean 17.2 ± 9.7), whereas *Svevo* varied between 46.3 to 84.2 (mean 66.6 ± 10.7). Similar variation across locations, but greater effect of the genotype on SKCS values was in accordance with the results obtained by [112] when comparing common wheat NIL differing only in the Puroindoline b allele (wild-type or mutated). Similar significant differences in milling behavior between *Svevo* and *Svevo-Pin* wheat samples, regardless of whether they were grown in U.S. or in France, were observed. The milling energies were (13.5 ± 2.2) kJ kg^{-1} and (11.6 ± 1.1) kJ kg^{-1} of grains at the first break, for *Svevo* and *Svevo-Pin* grains, respectively, and (27.9 ± 3.0) kJ kg^{-1} and (19.1 ± 1.9) kJ kg^{-1} of grains at the second break. Differences in the K' energies needed to produce the same amount of flour from the two wheat grain samples were even greater with mean and standard deviations of (624 ± 200) kJ kg^{-1} and (146 ± 20) kJ kg^{-1} of flour for Svevo and Svevo-Pin grains, respectively, at the first break, and (254 ± 47) kJ kg^{-1} and (95 ± 12) kJ kg^{-1} of flour at second break (Figure 3.2). Therefore, the introduction of wild-type puroindolines in durum wheat dramatically reduced the energy required to produce flour on the first and second break rolls. Indeed, if the specific energy to produce one kilogram of flour from *Svevo* was found to be on the order of that already observed for a durum wheat cultivar [126], that of *Svevo-Pin* was found to be closer to that of a soft common wheat cultivar. Scattering (variation across locations) of the K' values for *Svevo-Pin* was also

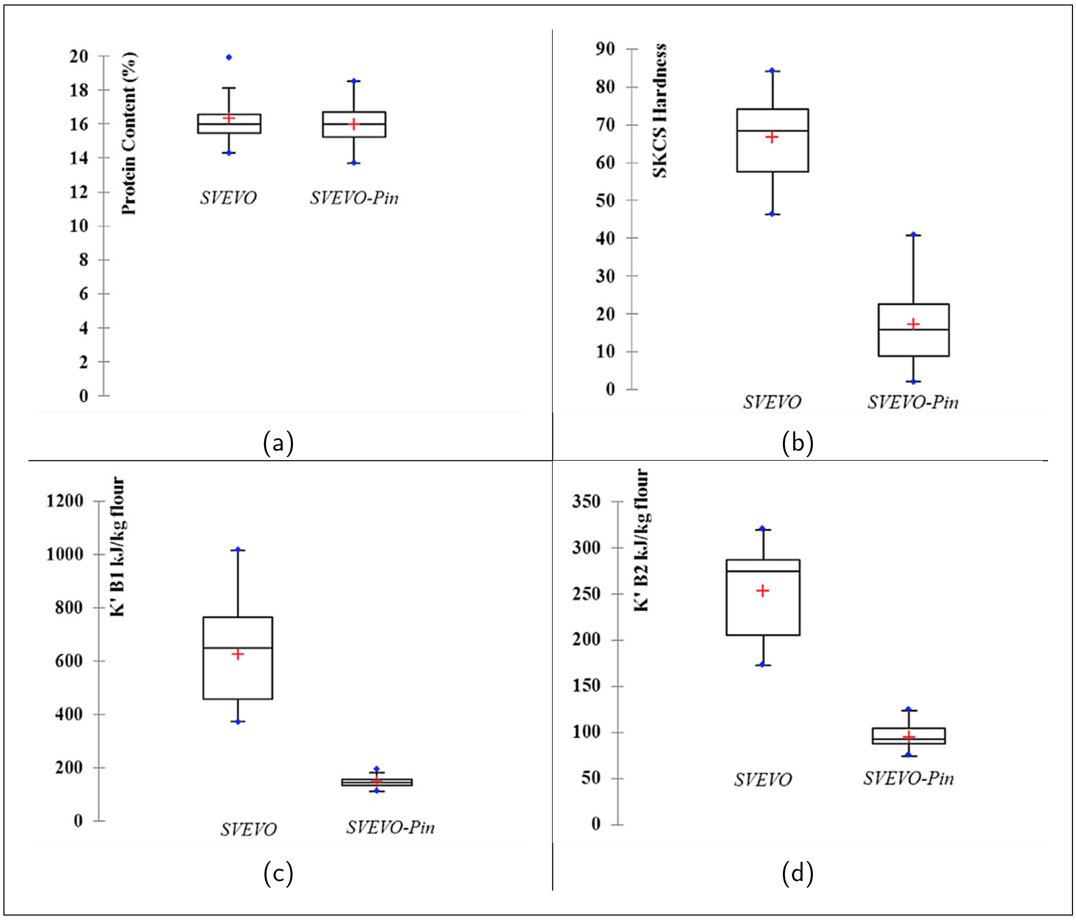

Figure 3.2. – Distributions of (a) grain protein content measured with NIRS and (b) SKCS HI for *Svevo* and *Svevo-Pin* cultivated in different U.S. locations (n = 22 for each boxplot, 11 sites, two replications). Distribution of milling energy (in kJ) required at first break (c, K'B1) or at second break (d, K'B2) to produce one kg of flour from *Svevo* and *Svevo-Pin* cultivated in the different French and U.S. locations.

found to be less than for *Svevo* suggesting a lower effect of the variation in grain texture due to the different growing location when wild-type puroindolines are present. This lower variation appears consistent with the low adhesion within the starchy endosperm between the starch granules and the protein network, and the lower mechanical resistance found in these grains.
Moreover, differences in the yield of the different milling fractions were also found to reveal a softer texture in *Svevo-Pin* in comparison with *Svevo* with an increase in flour yield (around 2-fold) and coarse bran yield (almost 3-fold) with a concomitant decrease (1.4-fold) in semolina yield (Figure 3.3a, Figure 3.3b, Figure 3.3c). Biochemical analyses were also in accordance with the former observations made on grains produced in France. Indeed, total starch content in the coarse bran of the overall sample set was significantly higher (Figure 3.3d) in *Svevo-Pin* ($(33.7 \pm 2.0)\,\%$) than in *Svevo* ($(26.2 \pm 2.4)\,\%$), whereas starch damage ($(1.9 \pm 0.3)\,\%$ versus $(8.3 \pm 1.8)\,\%$, Figure 3.3e), and phytic acid content in total flour ($(3.1 \pm 0.7)\,\mathrm{mg\,g^{-1}}$ versus $(8.9 \pm 1.7)\,\mathrm{mg\,g^{-1}}$, Figure 3.3f) were lower. These biochemical differences were similar to those observed between soft and hard common wheats carrying wild-type or mutated puroindoline alleles [103, 169].

Further analysis between milling and biochemical data showed a clear correlation between the quantity of coarse bran ($R^2 = 0.89$ and 0.71 for *Svevo* and *Svevo-Pin* samples, respectively), revealing a clear effect on the starchy endosperm difference in extraction rate between the two wheat samples, which affects the amount of coarse bran production.
Therefore, the introduction of wild-type puroindolines into durum wheat clearly leads to an increase in grain softness resulting in a higher production of flour with less damaged starch, but potentially a less efficient separation between the starchy endosperm and the outer layers. The energy required to produce flour from *Svevo-Pin* was on the order of one-quarter to one-third that of the hard durum *Svevo*, illustrating the profound and technologically transformative effect of the Hardness locus on durum wheat kernel characteristics and milling.

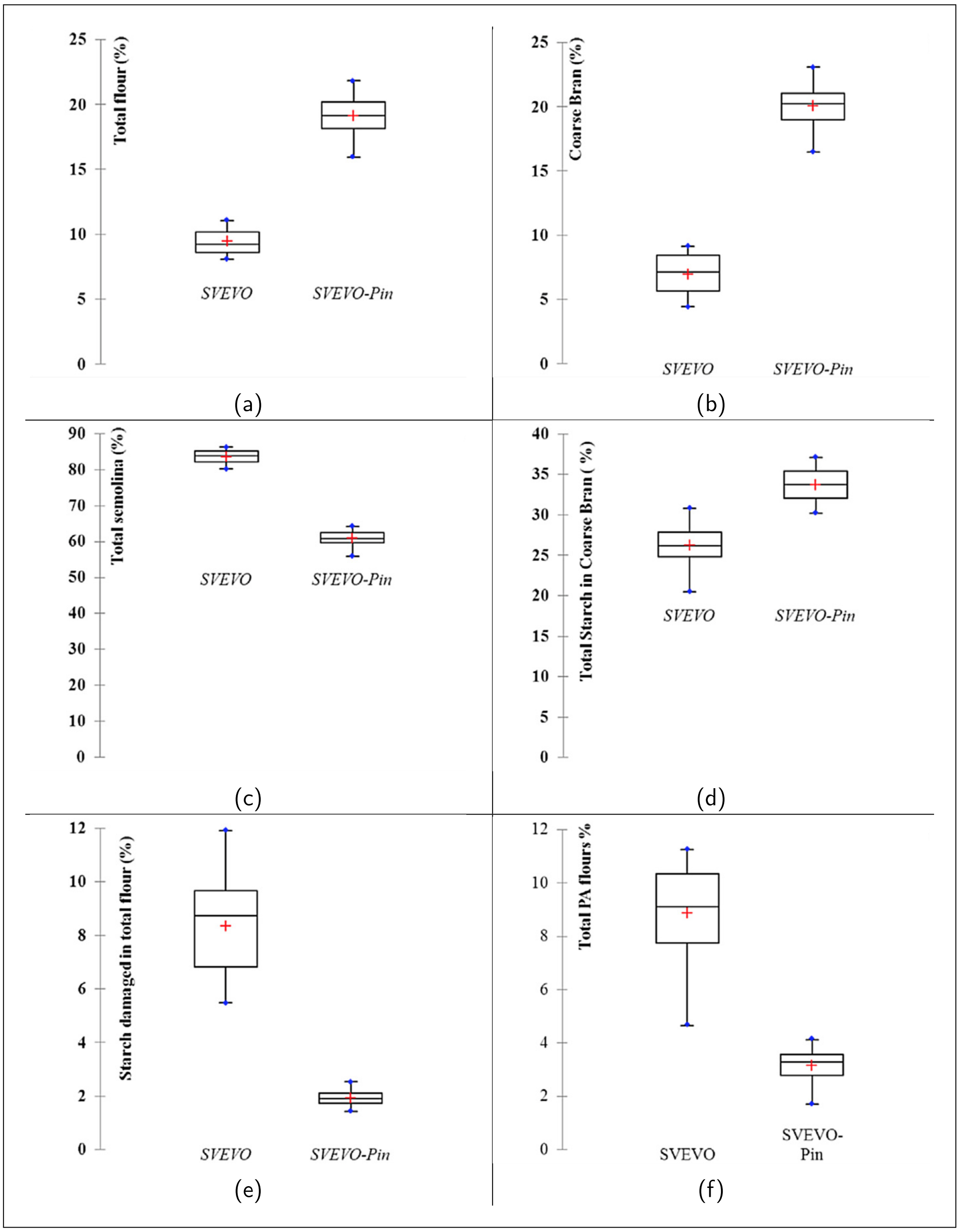

Figure 3.3. – Total milling flour (a), coarse bran (b), and total semolina (c) yields from *Svevo* and *Svevo-Pin* cultivated in the different French and U.S. locations. Total starch content in coarse bran (d), content of damaged starch (e), and phytic acid (f) in total flour from the same wheat grain samples.

3.2. Conclusion

This study clearly pointed out that PINs change the grain's mechanical properties and therefore milling behaviour, without changing changing structural properties like grain size and protein content, with the exception of vitreousness. Scanning electron microscopy (SEM) observations by Li et al. [78] in transgenic durum wheat with *pina* showed that the adhesion between starch granules and protein matrix was affected. Furthermore, Chichti et al. [135] demonstrated differences in the starch-protein interface of NILs of common wheat by atomic force microscopy (AFM)-based nano-mechanical measurements, which indicated the presence of a "lubricating interface". The protein and starch hardness were not affected by the genotype [135].
The presence of puroindolines seems to also affect the porosity of the grain, as was observed in the above presented study by vitreousness measurements and by Wada et al. [136] in rice. Such an effect is also observable for common wheat, where (genetically) soft grains are limited to lower vitreousness values in comparison with (genetically) hard lines [112].
It can therefore be concluded that puroindolines, regardless of the genetical background they are expressed in, drastically influence grain hardness and milling behaviour, possibly directly through starch-protein adhesion, and indirectly through vitreousness changes.

Setting out for experimental confirmation Based on the previous nano-mechanical results obtained by Chichti et al. [135] the performance of AFM abrasion on the *Svevo* and *Svevo-Pin* grain samples of the above presented study seemed a promising experimental approach to confirm changes at the starch-interface level. Such abrasion experiments are performed on cut grain sections by "digging" into the surface. Interface properties can potentially be observed, if first a layer of protein is removed and an uncut starch granule is revealed underneath [135].
Abrasion experiments performed on *Svevo* and *Svevo-Pin* did however not give the expected results. The reason, why no conclusions could be drawn from the abrasion experiments is probably due to the differences in grain properties between common wheat (studied by Chichti et al.) and durum wheat. Durum wheat has a higher protein content than common wheat. In *Svevo* this caused the protein layers on starch granules to be rather thick, which made it difficult to reach the starch granule surface by "digging" (Figure 3.4a). In *Svevo-Pin* on the other hand, most uncut starch granules seemed to have no protein layer on top (Figure 3.4b). This was probably caused by the removal of chunks of the protein network during the cutting process.
The nano-mechanical properties are however an important clue to the understanding of grain mechanical properties and milling behaviour and therefore another AFM-based nano-mechanical method was taken up: contact resonance atomic force microscopy (CR-AFM), which is the main focus of the following chapter.

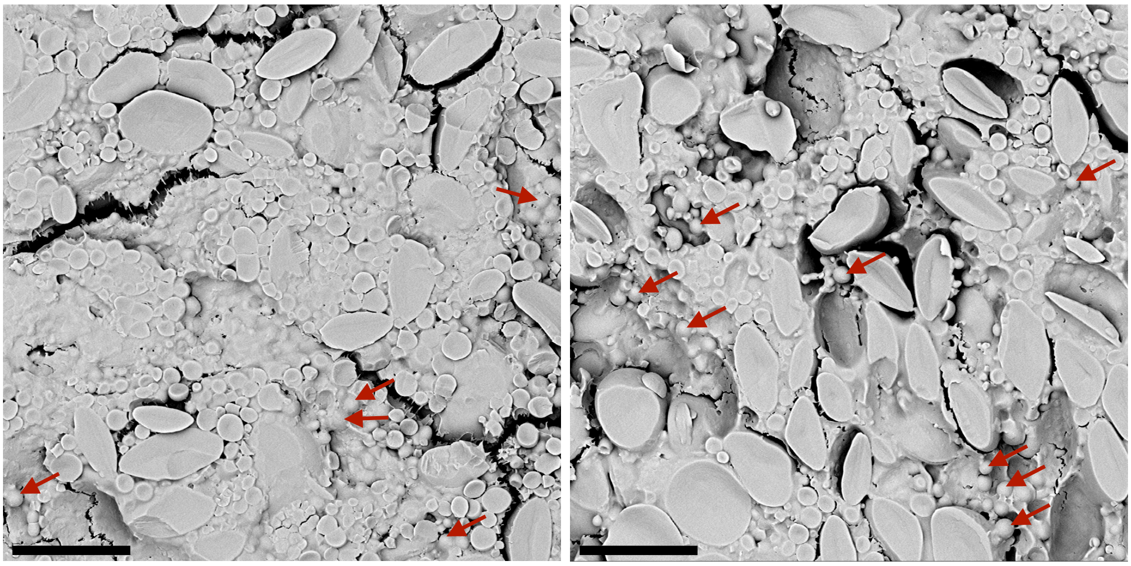

(a) *Svevo*

(b) *Svevo-Pin*

Figure 3.4. – SEM images of coated, cut grain section of *Svevo* and *Svevo-Pin*. Arrows indicate uncut starch granules. Scale bar: 30 µm (a) Uncut starch granules are most of the time covered by a protein layer of unknown thickness. Uncut starch granules are not very abundant. Scale bar: 30 µm (b) Uncut starch granules are more abundant than in *Svevo*, but they seem "naked", not covered with protein.

4. Nano-mechanics of starch by AFM

Contents

The Romans are the first people reported to having sieved the milling products through linen to separate the very fine, white fraction. The term "flour" originates from the latin word "flos", meaning "blossom", "flower" (the best part of the plant) or more generally "the best part of something".

4.1. Introduction

Atomic force microscopy (AFM) is a microscopy method, which is increasingly applied in life sciences, food sciences or biomedical engineering [194, 195, 196], due to its high versatility. AFM offers a number of advantages in comparison with other microscopy techniques, additionally to providing high magnification and high resolution [194]. No pre-treatment (i.e. staining) of the samples is necessary. Samples can be imaged in physiologically relevant conditions due to the ability to image under liquid. The acquired images offer three-dimensional information [194, 196]. Very interesting for life sciences are also high-speed AFM setups, which can potentially illuminate biological reactions in real time [196]. Next to imaging, the ability to characterise the mechanical properties of nano-sized structures or to perform molecular manipulations is of great interest for many researchers [194, 195, 196, 197].

4.1.1. AFM principle and operation modes

AFM is a microscopy technique that is able to supply three-dimensional surface imaging with nanometre resolution. AFM is a very versatile tool, because it can be operated in air, under liquid, in vacuum or in enclosures with controlled environmental conditions.
The technique is based on tracing the position of a sharp tip in close proximity to a surface, while scanning this surface in x- and y-direction with the help of a piezo-electric element [198] (Figure 4.1). The tip is mounted on a beam, called cantilever. While scanning, the interaction between tip and sample is monitored through the deflection of a laser on the back of the cantilever. The deflection depends on the forces between tip and sample, which can then be calculated with the knowledge of the cantilever stiffness and the z-position. Via feedback loops the z-distance between tip and sample is adjusted to meet a defined set point condition. From these adjustments a three-dimensional, topographical map is created. Different imaging modes with different parameters used as feedback exist. The modes relevant for the discussion in this chapter are briefly described in the following.

Contact mode As the name suggest, tip and sample are in contact for this mode. Most commonly, measurements are done at constant force, which is achieved by using the deflection as feedback parameter [199]. Because tip and sample are in contact and the tip is moving laterally, the force is the sum of normal and lateral forces. Therefore, shear forces can cause significant image distortions. The surface can also sustain damage if the forces between tip and sample are too high [199]. Whereas contact mode imaging is therefore not the method of choice for very soft or fragile samples, the damaging of the surface under high forces can be exploited for nanomechanical tests, such as scratch testing.

Non-contact modes In non-contact (or dynamic) modes the tip is very close to the surface, yet not in contact with it. Two non-contact modes exist: amplitude modulation (AM) and frequency modulation (FM), which are detailed hereafter.

Amplitude modulation or tapping In amplitude modulation (AM), the cantilever is excited with a frequency near or at its resonance frequency at a small amplitude (20 nm to 100 nm) [199, 200]. Due to the oscillating tip, tip-sample contacts are kept short and the issues of lateral forces or shear are avoided. The tip-sample forces cause a change in amplitude and/or phase of the cantilever's oscillation [199, 200]. The amplitude of the cantilever oscillation is used as the feedback parameter.

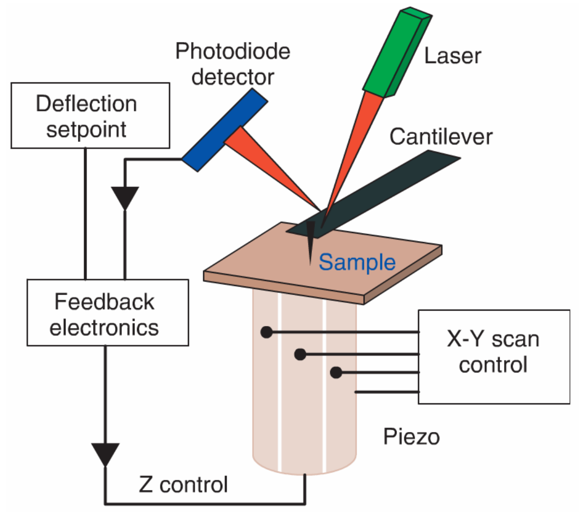

Figure 4.1. – The basic setup of an AFM is shown. A very sharp tip is attached on the cantilever and scanned in x- and y-direction across the surface. The cantilever deflection is traced by the reflection of a laser on the cantilever and measured on a photodiode detector. Through at least one feedback loop, the z-distance between tip and sample is controlled. Image from [196]

The phase changes during a scan in tapping mode can reveal qualitative changes of the viscoelastic properties of the surface.

Frequency modulation In frequency modulation (FM) the cantilever is also oscillated in close proximity to the surface with a constant amplitude at its resonance frequency. The tip-surface forces cause a changes of the resonance frequency of the tip-sample system. This frequency shift is used as the feedback parameter [200]. FM is able to measure the tip-surface forces with great accuracy, but is to day only applicable in ultra-high vacuum of liquid [200].

AFM nanomechanics

The fact that the AFM method is based on the interaction between tip and sample, makes it possible to investigate surface mechanical properties with the advantage that imaging can be done simultaneously (or within a very short time frame) on the same region.

Nanoindentation Nanoindentations can be performed by decreasing the z-distance between tip and sample while x-y scanning is disabled. The deflection of the cantilever, d, is recorded and translated into force by applying Hooke's law $F_z = d \cdot k_c$, where k_c is the cantilever spring constant. This leads to so-called force-distance (FZ) curves, from which the stiffness of the sample can be obtained. Nanoindentations are an easy way to obtain quantitative measurements on homogeneous materials and thin films or thin structures on a hard substrate. Nanoindentations can also be done on thick, inhomogeneous materials, but the interpretation of the measured stiffness is difficult. Depending on the depth of the indentation, the measured stiffness will result also from the material well below the surface, for which no structural information can be obtained.

Force volume Force volume (FV) measurements are based on the nanoindentation principle. At every imaging point a FZ curve is performed, which can then be processed into two-dimensional maps of surface properties [201]. But this approach has high acquisition time and large data volumes to be processed and the resolution of the acquired maps is usually not very high (64x64 pixel) [201]. Furthermore, the disadvantage of having no information about the actual indented material on thick samples still holds.

Abrasion/ Scratch assays As mentioned above, the fact that the sample surface can be damaged in contact mode by scanning it with high forces can be used to test the mechanical properties of the surface. One approach are abrasion assays (also called scratch assay). A two-step approach is needed: first, the region of interest is imaged under normal scanning forces (low enough to not damage the sample) and second, a smaller region within the imaged area is scanned with high forces with the intent to abrade this area. Finally, the region of interest is re-imaged with normal scanning force to evaluate the damage in the abraded zone [173, 202, 203]. With these assays the abrasive hardness of the material can be obtained [173].

Acoustic AFM Atomic force acoustic microscopy (AFAM) combines AFM with ultrasonics to obtain quantitative information on the surface viscoelastic properties. One approach is contact resonance atomic force microscopy (CR-AFM).

Contact resonance AFM In CR-AFM the the surface is scanned in normal contact mode. Additionally, the sample is being subjected to a sinusoidal vibration of low amplitude and the elastic and viscous properties of the sample are inferred from the oscillatory response of the cantilever to the surface vibrations [204, 205]. CR-AFM is explained in detail in subsection 4.3.2.

4.1.2. Limitations of AFM

As with all microscopy techniques, AFM images are only a representation of the surface, but never show the “true” surface. For a correct interpretation of such representations a sufficient understanding of the underlying process, which creates the image, is necessary.
Specifically relevant for the observations of small surface features is the lateral resolution of AFM, because it directly determines how their size can be measured.

Lateral resolution Lateral resolution is on one hand limited by the image resolution in terms of number of pixels. Resolution can never be higher than the size of one image pixel: $size_{x,y}^{image}/n_{pixel}$ [200]. Typically, the number of pixels per line is minimally 256, most often 512. Exemplarily, on a 2 µm × 2 µm image with 512 points per line, this would still lead to a resolution of <10 nm. Because an increase of pixels is always accompanied by a significant increase in imaging time, usually the size of the image is reduced to achieve better resolution.
A more crucial point with regards of lateral resolution is that the image will be significantly distorted, if surface features are smaller or of similar size to the apex of the AFM tip (see Figure 4.2) [200]. Then the image will display only an approximation of the specimen surface [206]. This effect is known as tip dilation. Therefore the lateral resolution is also limited by the size of the tip apex [200]. For the most commonly used AFM tips the tip radius is ≈30 nm, but it can vary largely and for exact knowledge of size and shape a calibration on specifically designed calibration samples is needed. Sharper AFM tips are commercially available, but are also more fragile. AFM tips with

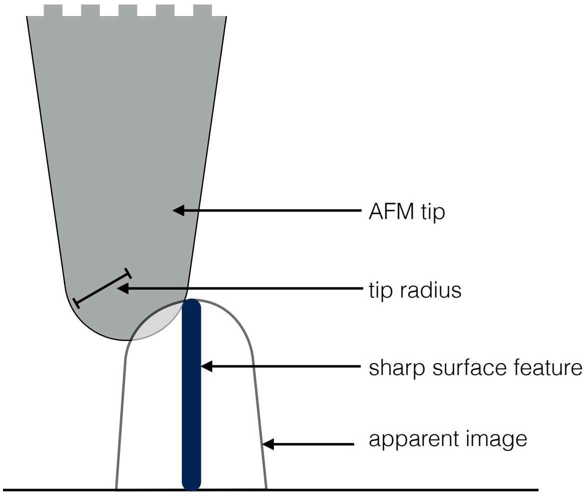

Figure 4.2. – The figure illustrates the effect of tip dilation during AFM imaging. Surface features that are sharper than the tip apex are not imaged with their true size, but the apparent image shows the inverted tip shape.

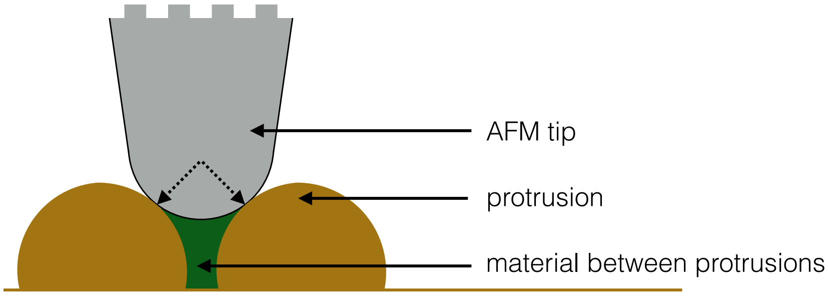

Figure 4.3. – The peaks of surface grains prevent the AFM tip to enter the inter-grain valley.

specially rounded apex are also commercially available. The rounding of the tip results in lower variation of size and shape of the tip apex.

Tip dilation is an issue for all types and modes of AFM measurements and therefore a lot of research has been and is undertaken to take it into account and to correct for it. A straight-forward solution is to take size measurements from the height distances instead of lateral distance, though this is also not free of possible distortions. The sample might get compressed under the scanning force and in deep regions (holes or valleys) the tip might not actually reach the bottom. Otherwise, if the tip geometry is precisely measured on specific calibration surfaces, the true features of the image can be back-calculated [206]. Surface reconstruction is an available option in most commercial AFM softwares, given that tip radius and shape are known.

Furthermore, the size of the tip apex can complicate the measurements on granular surfaces. If inter-grain spaces are smaller than the tip size, multiple asperity contacts will arise (Figure 4.3), which lead to significant variation in the contact area [207].

Origin of phase contrast in amplitude modulation mode In AM mode qualitative information on the mechanical properties can be obtained from the phase image. However, the origin of phase contrast depends greatly on the tapping regime [208] and artefacts can also be caused by surface curvature [209]. Magonov [208] demonstrated the importance of the ratio of driving amplitude A_0 to set-point amplitude A_{sp}. To measure phase information that is related to surface stiffness, measurements should be done at "moderate" tapping with $A_0/A_{sp} \approx 0.5$. If the ratio is higher an inversion of phase contrast is possible.

Furthermore, the AM phase can be influenced by the tip geometry, especially so if the surface features are smaller than the tip apex [209]. Mazeran et al. [209] demonstrated a direct correlation between phase images and the surface curvature and therefore the phase contrast has to be interpreted as being due to surface topography and not due to local sample properties. Only if a high change in contrast does not directly correlate with surface curvature can it be concluded that it is reflecting a physical contrast [209].

AFM mechanical measurements A number of AFM methods to quantitatively measure the mechanical properties of the surface exist, each with their own limitations. For CR-AFM, Stan et al. [207] demonstrated that granular topographies with small surface features $<$100 nm cause significant changes of contact area, which then leads to an inversion of contrast of the measured resonance frequency. The CR-AFM frequency in the inter-grain spaces is measured to be higher than on top of the centre of grains, which would suggest a higher modulus in the inter-grain spaces. But after consideration of the effect of contact area changes, the contact modulus in the inter-grain spaces was found to be lower [207]. We demonstrate that also large scale surface slopes (hundreds of nanometres) can have a significant effect on the measurements in CR-AFM (detailed in section 4.3).

4.2. AFM and starch

4.2.1. Introduction

Starch is a complex molecule that is organised on multiple levels. The two major molecules of starch, amylose and amylopectin, are deposited into starch granules [27], whose shape and size of these granules depends on the botanical origin [210].
Starch granules are semi-crystalline structures. The ratio of amylose to amylopectin, the percentage and type of crystallinity vary within starches from different botanical origin [26, 27, 28]. Concentric rings of thicknesses of some hundred nanometer can be observed by microscopy techniques with high µm-scale resolution such as scanning electron microscopy (SEM) or AFM [27]. They are known as "growth rings" and are believed to be alternating semi-crystalline and amorphous regions (Figure 4.4) [27]. Structures smaller than growth rings were observed by SEM and AFM and termed "blocklets" [40]. Whereas the molecular organisation and the crystalline ultrastructure are more or less known, the structural organisation of the growth rings and blocklets is less well understood [211]. AFM, with its ability to provide nanometer resolution, is seen as the optimal tool to provide more insight into this level of organisation and the number of AFM studies on starch from different botanical origins is constantly increasing. Certain AFM-based methods, such as CR-AFM (see section 4.3) can potentially provide quantitative information on the mechanical properties on the nano-scale, which is particularly interesting for understanding the biomechanics of endosperm fractionation.

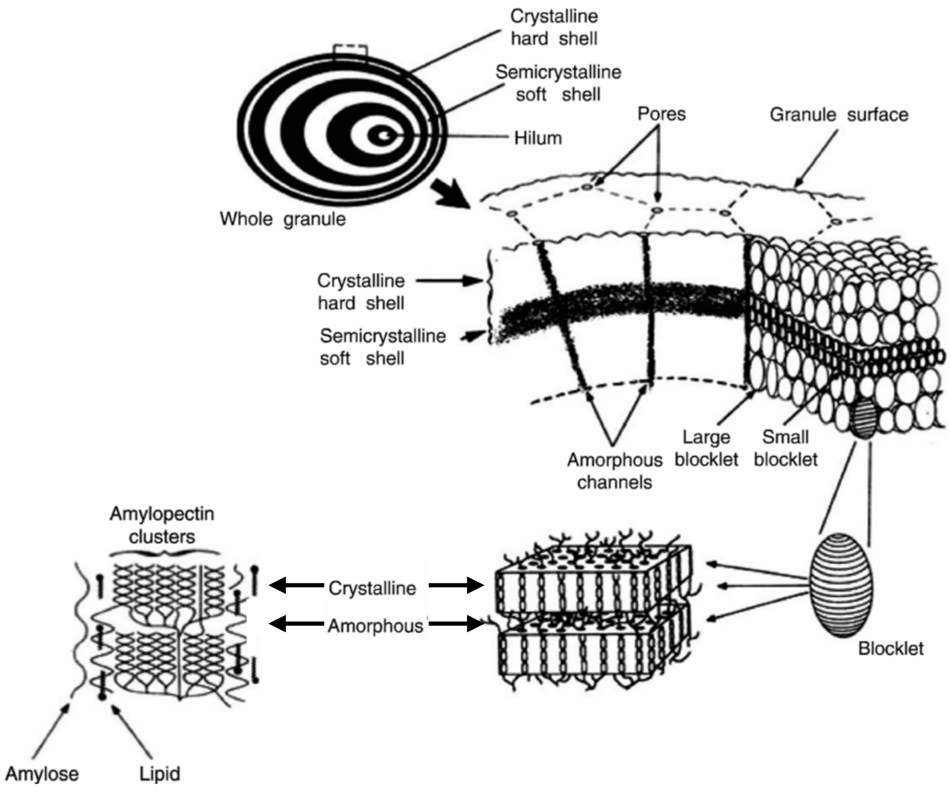

Figure 4.4. – The different levels of starch structure proposed by Gallant et al. [40] are shown. Image adapted from [40]

The potential of useful information from AFM studies on starch is therefore immense. However, AFM is also a very delicate method with a number of known limitations, which can cause artefacts in the acquired data. Such limitations should especially be considered when imaging a biological material, such as starch, which, compared to the flat and smooth surfaces of for example semi-conductor surfaces, is a rather challenging object of study.

4.2.2. Starch granule shape and size

Starch granule shape and size can be observed on extracted starch granules, in cut grain sections (Figure 4.5 on page 50) or sections of embedded starch granules.

Botanical differences It is well known that the shape and size of starch granules varies with the botanical origin. The grains, which will be discussed in this chapter are from cereal and legume (pea, lentil, chickpea) plants. The cereals can further be separated into C_3 (wheat, barley, rice) and C_4 (corn, sorghum) plants, depending on their carbon fixation cycle. An extensive study of starch granule shape on extracted starch granules was done by Jane et al. [210]. Interestingly, for some plants (corn, pea) the starch granule shape seems to resemble the shape of the grain itself [210].
Wheat and barley (C_3 cereals) have a bi-modal granule size distribution of large, disk-shaped granules and small, more round granules (Figure 4.5a, Figure 4.5b and Figure 4.5c) [210]. Rice (Figure 4.5d) is a C_3 cereals with compound granules. The starch granules are unimodal, smaller, irregularly shaped and polygonal [210]. Sorghum (C_4 cereals) also has a bi-modal granule size distribution with irregularly shaped granules [210]. Corn (C_4 cereals) has irregularly shaped, polygonal starch granules (Figure 4.5e) [210] in the vitreous part of the grain, and apparently slightly less sharp-edged in the mealy part (Figure 4.5f). Waxy corn shows granules with more shape irregularities and rougher surfaces, whereas high-amylose corn starch displays smoother surfaces [210]. Differences in edginess and granule roughness are however also observed between the vitreous and mealy region and unfortunately, in the experiments of Jane et al. the original location of the granules is not known.
Of the legume starches, chickpea has more irregularly shaped granules, but with round edges [210]. Pea (Figure 4.5g) has rather disk-shaped granules with an indentation in the middle and lentil has smooth, ellipsoidal granules [210].

4.2.3. Opening the starch granule

Certain structures, such as the growth rings, can only be observed in the granule interior.
Even though AFM does not require any specific sample preparations, it does require the surface to be as flat as possible. To achieve this, most authors perform micro- or cryo-cutting. For the experimental approaches of this thesis, samples were also cut in a cryotome at $-20\,^{\circ}\mathrm{C}$. The samples therefore undergo freezing and unfreezing, followed by possible drying or humidification of the created surface. During cutting, the starch granules are opened with force and the forces during the cutting process should also be considered for the subsequent interpretation of both, topographical and mechanical measurements on the cut surface.
A general observation amongst many authors is that cut starch granules have a depression in the granule centre, which is visible in SEM images as well as in AFM topography images. It is likely that the depression in the middle is the result of a bulging of the outer granule regions and it has been suggested to be caused by the release of internal stresses of the granule [212]. For corn, sorghum, rice granules and small granules of wheat and barley this depression is just in the centre of the granule, whereas in large granules of wheat and barley, a stretched equatorial groove can be observed. The groove is likely to show the centre of the granule, the hylum, and the differential shape between large and small wheat starch granules would be the result of the different orientation

of the amylopectin molecules (Figure 2.6 on page 13). Interestingly, a groove was also observed by Glenn et al. [170] in fractured starch granules after endosperm failure in tension. There seems to be a preferential fracture mechanism of starch granules, which draws the fracture towards the centre of the granule.

However, it is not sure, if all parts of the granule undergo exactly the same fracture mechanism during microtome sectioning. A part of the granule might experience high yielding, whereas other parts might fracture due to brittle crack propagation. Therefore, the mechanical properties could already play a role in the creation of the surface, which should be kept in mind for potential differences observed with AFM.

Visible growth rings Growth rings become visible/ observable after the opening of starch granules. Following the above discussion, the topographical and mechanical contrast between the rings could result from the cutting process itself, where different layers could respond differently to the forces, but also from the subsequent unfreezing, drying or humidification. Some authors observed an increase in contrast after humidification of the surface [213, 214], and we observed that growth rings are less contrasted, if starch is embedded and cut with a very fine diamond knife in a microtome at room temperature (data not shown).

4.2.4. Growth rings

Growth rings can be observed in all kinds of cut granules, without any treatment of the surface. They are topographical features with a certain periodicity and are therefore most likely the result of a structural periodicity of the starch structure. Different shapes can be observed for different types of grains (Figure 4.6). For example growth rings in rice (Figure 4.6b) are of the same shape like the starch granules and not actual "rings". In large wheat starch granules (Figure 4.6a) the equatorial groove can be seen.

Certainly, interesting information could be obtained from quantitative investigation by AFM of the growth rings in cut granules, if the above discussed limitations are kept in mind. Such information might aid the understanding of starch granule growth.

The imaging of growth rings is theoretically affected by tip dilation, but due to their size (hundreds of nanometres) tip dilation has less impact. Distances can be measured peak-to-peak for better accuracy, because of the absence of tip dilation on the top of a peak. One aspect that needs to be considered is the missing knowledge of where exactly the starch granule was cut. Figure 4.7 illustrates that depending on the level of the cut relative to the granule centre, the measured growth ring distance would vary. However, with a large enough number of measurements and careful consideration of distance measurements, AFM could provide relevant information on growth ring size.

A number of authors reported quantitative values for growth ring distances, which are in the range of 100 nm to 800 nm (see Table 4.1 on page 52) [215, 216, 217, 218]. Unfortunately, most authors do not specify their distance measurement procedure in detail. Furthermore, the interpretation of what structures are observed, concerning the nature of the bands and the cause of contrast, varies. Theoretically, the size of growth rings would allow for the measurement of mechanical properties with AFM. However, caution should still be taken due to the possible effects of surface curvature. For demonstration, a data series acquired on a cut corn starch granule is shown in Figure 4.8 on page 53. The corn grain was cut in a cryo-microtome without any addition of resin or other modifications and imaged in contact mode with a SD-R30-CONT AFM tip (Nanosensors^{TM}), which has a rounded tip apex of 30 nm, in a Bruker Dimension AFM with Nanoscope V controller. The surface's resonance frequency was measured by CR-AFM. The details of this AFM method are described in detail in

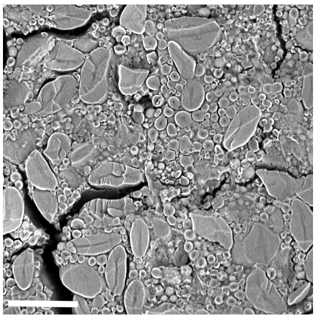

(a) Durum wheat

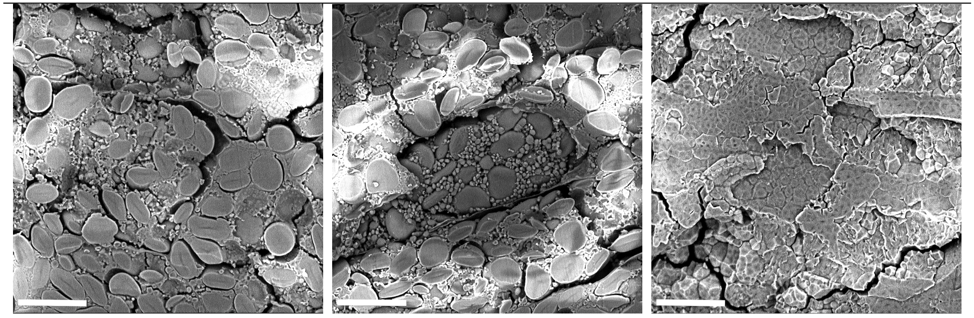

(b) Barley (c) Barley - opened cell (d) Rice

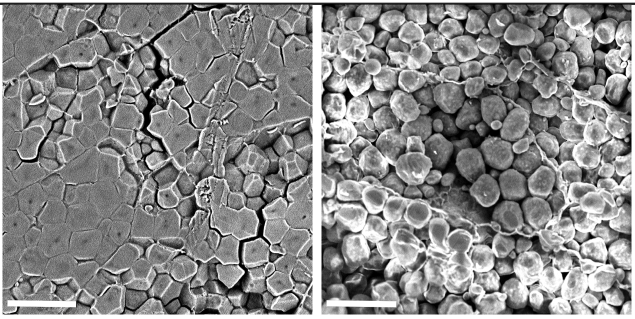

(e) Corn - vitreous part (f) Corn - mealy part

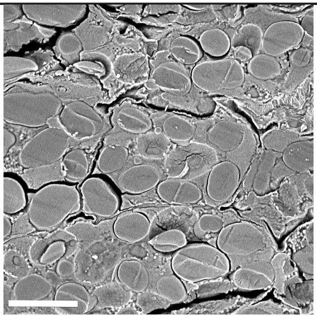

(g) Pea

Figure 4.5. – Scale bar: 30 µm. (a-g) SEM images in uncoated, cut grains, taken with Phenom ProX SEM from Phenom-World, 10 kV. Black and white contrasts result from charging of the uncoated surface around the centre of the beam and are therefore not representing any real surface property.

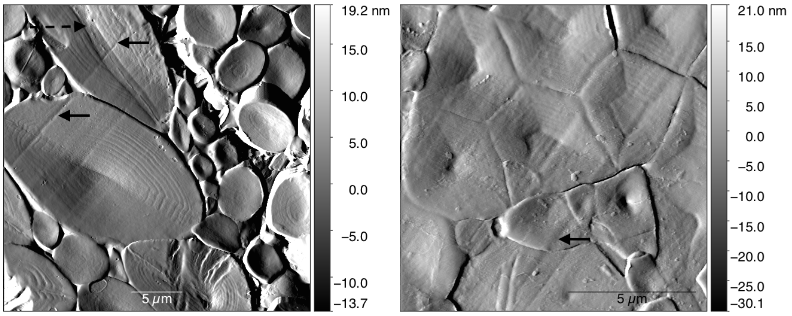

(a) Durum wheat (b) Rice

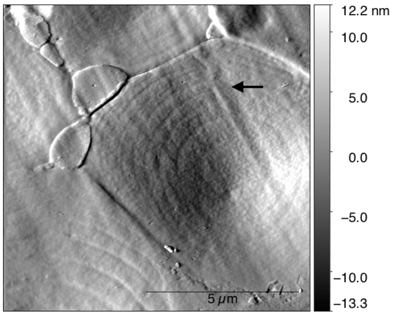

(c) Sorghum

Figure 4.6. – (a-c) The deflection error images from AFM imaging in cut grain sections is shown to illustrate the appearance of growth rings. Arrows indicate marks from the cryotome knife. The dashed arrow in (a) points to the equatorial groove.

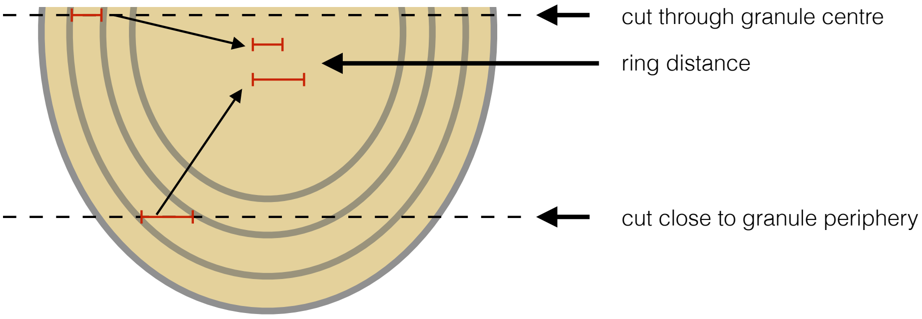

Figure 4.7. – Depending on the level of the cut in the starch granule, the measured growth ring size would vary.

Table 4.1. – Overview of results on the interior of starch granules

Interior Starch

Author, Year	Starch origin	AFM setup			Results	
		cantilever stiffness k [N/m]	Imaging mode	Scan rate [Hz]	**Blocklet size** [nm]	**Growth ring distance** [nm]
Ohtani, 2000 [219]	rice	n.s.	tapping, contact	n.s.	30	
Baker, 2001 [215]	corn	0.06	contact, tapping, FM, AM, lateral force	n.s.		100 (finer rings) and 450
Ridout, 2002 [220]	corn, potato	0.38	contact, FM	1-2	45-85	
Ridout, 2003 [216]	pea	0.38	contact, FM	2-2.5	128	300-800
Dang, 2003 [217]	rice	13	?	n.s.	100	400
Ridout, 2004 [213]	pea	0.38	contact, FM	2-2.5	130	"contrast arises solely due to preferential swelling of certain regions"
Ridout, 2006 [221]	pea	0.38	contact, FM	2-2.5		"selective swelling of the amorphous region [...] reveals a periodic banding (growth ring) structure"
Neethirajan, 2008 [222]	Durum wheat	0.06-0.12	contact	n.s.		
Parker, 2008 [212]	pea	0.38	contact, tapping	3, 1		"alternating bands with different levels of crystallinity rather than amorphous and crystalline growth rings"
Neethirajan, 2012 [223]	buckwheat	42	intermittent contact	0.2-0.3		
Tsukamoto, 2012 [214]	corn	42	intermittent contact	n.s.	30	"growth rings showed shrinkage during drying", no alternating layers but "only one layer"
Salerno, 2014 [44]	potato, wheat	n.s.	contact, tapping, FM, FV	n.s.	100-450	350-370
Okita, 2015 [218]	banana	7, 0.2	intermittent contact, FM	n.s.	30-200	200

section 4.3. Here, the images only serve a demonstrative purpose. Growth rings are clearly present on the surface and can be seen in the topography (Figure 4.8a) and error signal images (Figure 4.8b). The acquired contact resonance (CR) frequency (Figure 4.8c) appears to show interesting contrasts between growth rings, which is however rather strongly correlated with the sample topography (discussed in detail in section 4.3) and the average curvature (Figure 4.8d). The average curvature was calculated with the equations from [209] and it shows some significant arrangement of contrast. Whereas the major parts of the growth rings have a rather homogeneous curvature, the valleys in between growth rings are in strong contrast to that. Observations on possible stiffness or mechanical differences between peaks and valleys of growth rings on such an area would therefore have to be considered with caution, because such differences could be potentially caused by curvature instead of physical properties.

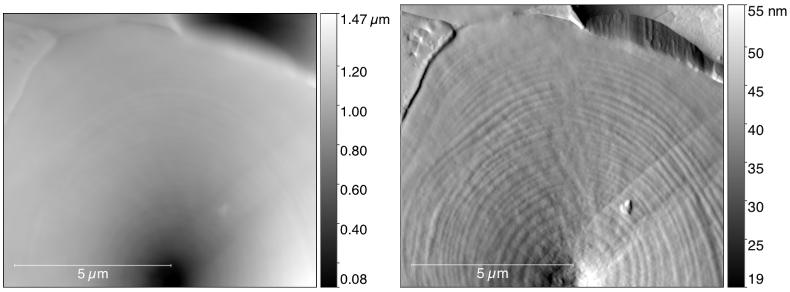

(a) Topography (b) Deflection error

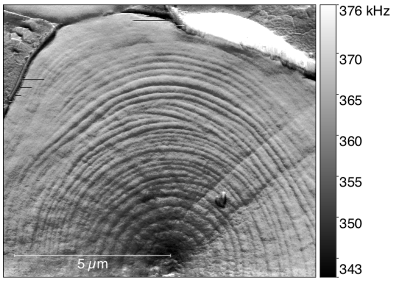

(c) CR frequency

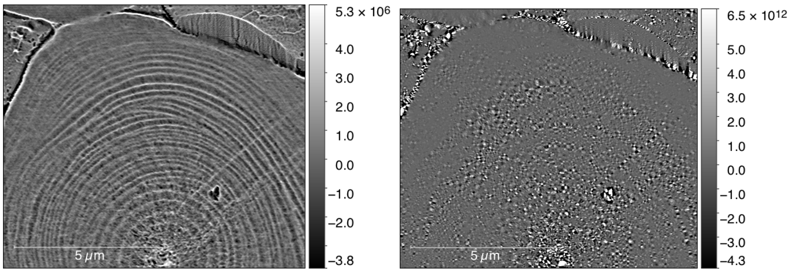

(d) Average curvature (e) Gaussian curvature

Figure 4.8. – (a-e) A set of AFM data acquired on a cut corn starch granule with clear growth ring structure is shown to demonstrate that possible correlations between observed mechanical properties and sample curvature need to be considered, when interpreting AFM data.

4.2.5. Starch blocklets

Gallant introduced the blocklet concept on the basis of SEM measurements on the surface of starch granules[1][224], which was followed by AFM observations reporting protrusions on the granule surface [40, 225, 226]. Gallant et al. [224] proposed that blocklets are "packs of crystals composed of small crystalline sheets, stacked tangentially to the granule surface". Blocklets were observed to be 20 nm to 50 nm large, semi-spherical structure and assumed to be of carbohydrate nature [226]. They also observed that blocklets have different sizes in the crystalline or amorphous regions, though more recent studies are contradicting this [212, 220]. These first AFM studies on starch granules mark the beginning of many researchers using AFM to gain insight into the nano- and microlevel of starch organisation, between growth rings and molecular chains.

There are two major lines in this research collection: investigating the granule surface and the interior of starch granules. The last one requires a more delicate sample preparation procedure, since the granule has to be opened to study its interior. Table 4.1 and Table 4.2 summarise the results of AFM studies on blocklet on the granule surfaces and interior, respectively. The aim of the following arguments is not to question the blocklet concept of starch, but to point out why care should be taken when interpreting the AFM data, especially when determining the sizes of blocklets and the qualitative and quantitative mechanical properties.

Common to all studies is the conclusion of the authors to confirm of the blocklet model of starch structure, based in the observation of protrusions on the granule surface. Most authors also report an approximate blocklet size, some report very specific values (Table 4.1, Table 4.2). Blocklets were reported to have sizes between 20 nm to 450 nm for example for wheat [41, 42, 43, 44]. For the size range of some tens of nanometers, the tip dilation effect is expected to be significant and non-negligible. Unfortunately, the exact way how blocklet sizes were measured from the AFM images is often not specified. If blocklet size is measured on the x- and y-direction and from valley-to-valley, a significant distortion due to tip dilation is to be expected. Unsurprisingly, the lowest reported value for blocklet size is 20 nm [42, 228, 229], which is the limit of lateral resolution with the most common commercial AFM tips. Unfortunately, none of the authors performed calibrations for tip shape and size. The large range of values could also be caused by the very different cantilever stiffnesses and different imaging modes.

Furthermore, all of these studies base their argumentation on an early hypothesis of Baldwin et al. [226], who believed that the observed protrusions are of carbohydrate nature and represent the ends of amylopectin side chain clusters. The chemical nature of surface structures can however not be determined by AFM imaging.

To image blocklets in the interior of the granules, the granules need to be necessarily destroyed by breaking or cutting them open. The most commonly adapted solution is embedding of the granules into resin, followed by microtome cutting. Ridout et al. [220] demonstrated the importance of selecting the right embedding material, because only with a non-penetrating resin the observed features can be interpreted as starch features. Ridout et al. [216] were the first to report "hard blocklets dispersed in a softer matrix material" based on FM measurements. As discussed in subsection 4.1.2, such measurements are prone to artefacts caused by surface curvature. Furthermore, if the "matrix" is assumed to be located in the valleys between blocklets, it is not evident that the AFM tip does actually measure the properties of this material, since the peaks of the blocklets might prevent the tip from reaching the valley (Figure 4.3 on page 45).

---

[1] An earlier mention of a "Blöckchen", engl. blocklet, structure was by Hanson and Katz in 1934 and Badenhuizen in 1937 [227]. For Badenhuizen the blocklets were structures of about 1 µm that are not preformed in the granule and only created after hydration and swelling of the starch granules [227]. Today's concept of blocklets is different from that and essentially originated from Gallant and Baldwin's descriptions.

Table 4.2. – Overview of studies on starch granule surface (n.s. - not specified)

Starch Granule Surface

<table>
<tr><th rowspan="2">Author, Year</th><th rowspan="2">Starch origin</th><th colspan="3">AFM setup</th><th>Results</th></tr>
<tr><th>cantilever stiffness k [N/m]</th><th>Imaging mode</th><th>Scan rate [Hz]</th><th>Blocklet size [nm]</th></tr>
<tr><td>Juszczak, 2003a [230]</td><td>barley, maize, oat, waxy maize, wheat</td><td>2.1</td><td>tapping</td><td>n.s.</td><td>below 200</td></tr>
<tr><td>Juzsczak, 2003b [231]</td><td>potato, tapioca</td><td>2.1</td><td>tapping</td><td>n.s.</td><td>some 100</td></tr>
<tr><td>Szymonska, 2003 [232]</td><td>oat, potato, wheat</td><td>n.s.</td><td>non-contact</td><td>n.s.</td><td>40-50</td></tr>
<tr><td>Simao, 2008 [233]</td><td>mango</td><td>40</td><td>tapping (moderate)</td><td>n.s.</td><td>60</td></tr>
<tr><td>Sujka, 2009 [228]</td><td>corn, potato</td><td>n.s.</td><td>tapping</td><td>n.s.</td><td><table><tr><td>corn</td><td>121</td></tr><tr><td>potato</td><td>20</td></tr></table></td></tr>
<tr><td>Waduge, 2010 [41]</td><td>wheat</td><td>48</td><td>tapping (slightly repulsive)</td><td>1-2</td><td>30</td></tr>
<tr><td>Park, 2011 [229]</td><td>corn, potato</td><td>0.06-0.12</td><td>tapping</td><td>n.s.</td><td>20-30</td></tr>
<tr><td>Jiranuntakul, 2013 [234]</td><td>corn, potato, rice, waxy corn, waxy potato, waxy rice</td><td>42</td><td>tapping</td><td>0.1-1</td><td><table><tr><th></th><th>normal</th><th>waxy</th></tr><tr><td>corn</td><td>33.80±8.38</td><td>44.27±6.95</td></tr><tr><td>potato</td><td>56.02±10.53</td><td>51.26±10.80</td></tr><tr><td>rice</td><td>27.87±5.85</td><td>26.96±5.34</td></tr></table></td></tr>
<tr><td>Waduge, 2013 [42]</td><td>wheat</td><td>48</td><td>tapping</td><td>1-2</td><td><table><tr><th>Time</th><th>small granule</th><th>large granule</th></tr><tr><td>7 DAF</td><td colspan="2">(68x97)-(98x154)</td></tr><tr><td>14 DAF</td><td>(32x36)-(49x82)</td><td>(20x25)-(45x55)</td></tr><tr><td>28 DAF</td><td>(25x42)-(45x84)</td><td>(20x36)-(25x51)</td></tr><tr><td>49 DAF</td><td>(20x40)-(26-60)</td><td>(21x38)-(36x56)</td></tr></table></td></tr>
<tr><td>Barrera, 2013 [43]</td><td>wheat</td><td>n.s.</td><td>tapping</td><td>n.s.</td><td>40-100</td></tr>
<tr><td>Hong, 2016 [235]</td><td>cassava</td><td>n.s.</td><td>tapping</td><td>2.441</td><td>/</td></tr>
</table>

4.2.6. Quantitative mechanical measurements

The amount of studies on quantitative determination of starch granule mechanical properties is very limited (Table 4.3). Salerno et al. [44] performed a number of different modes of AFM imaging (tapping, contact, force volume, force modulation) on resin embedded starch granules. They report an indentation modulus of ≈1.2 GPa for wheat and ≈1.5 GPa for potato and a contact modulus (from force modulation) of (1.8 ± 0.3) GPa for wheat and (2.2 ± 0.5) GPa for potato [44].
Chichti et al. [135] performed AFM abrasion tests to determine the hardness of common wheat starch in cut grains without resin embedding. They report an abrasive hardness of (2.4 ± 0.6) GPa and (2.5 ± 0.3) GPa for hard and soft common wheat, respectively.
We recently applied CR-AFM on cut starch granules in grains and concluded that a significant correlation between the acquired contact modulus and surface slope and curvature exists (section 4.3). Such quantitative measurements of the nano-mechanical properties of starch are however of very great interest. Therefore, an approach to calculate a more correct modulus from the data was developed by taking into account the local surface curvature, which allows to extract relevant information on the contact modulus of starch granules.

Table 4.3. – Overview of results on mechanical properties of starch

Mechanical Properties

Author, Year	Starch origin	AFM setup		**Results**
		cantilever stiffness k [N/m]	Imaging mode	Mechanics (modulus E, hardness H) [GPa]
Salerno, 2014 [44]	potato,	n. s.	contact,FM, force modulation, FV	$E_i = 1.5$, $E_{FM} = 2.2 \pm 0.5$
	wheat			$E_i = 1.2$, $E_{FM} = 1.8 \pm 0.3$
Chichti, 2013 [173]	wheat	1-5	contact	$H = 2.4 \pm 0.6$
Chichti, 2015 [135]	wheat	1-5	contact	similar to [173]

4.3. On the effect of local sample slope during modulus measurements by contact-resonance atomic force microscopy

Abstract

Contact-resonance atomic force microscopy (CR-AFM) is of great interest and very valuable for a deeper understanding of the mechanics of biological materials with moduli of at least a few GPa. However, sample surfaces can present a high topography range with significant slopes, where the local angle can be as large as ±50°. The non-trivial correlation between surface slope and CR-frequency hinders a straight-forward interpretation of CR-AFM indentation modulus measurements on such samples. We aim to demonstrate the significant influence of the surface slope on the CR-frequency that is caused by the local angle between sample surface and the AFM cantilever and present a practical method to correct the measurements. Based on existing analytical models of the effect of the AFM set-up's intrinsic cantilever tilt on CR-frequencies, we compute the non-linear variation of the first two CR-frequency (eigen)modes for a large range of surface angles. The computations are confirmed by CR-AFM experiments performed on a curved surface. Finally, the model is applied to directly correct contact modulus measurements on a durum wheat starch granule as an exemplary sample.

Table 4.4. – Nomenclature used in this section

α		angle between tip and surface
α_0		fixed inclination angle of cantilever in AFM instrument
β_n	$n = 1, 2, 3$ ...	wavenumber; solution of vibrational equation
γ_{lat}		lateral damping
γ_N		normal damping
λ	$= k_{lat}/k_{lat}$	stiffness factor
η		fitting parameter
μ		factor in dispersion relation
ν		Poisson ratio
ϕ		local angle due to surface curvature
ω_n	$n = 1, 2, 3$ ...	pulsation
a		cantilever thickness
f_n	$n = 1, 2, 3$ ...	resonance frequency
E		Young's modulus
$E*$		reduced modulus
F_{adh}		adhesive force
F_N		normal force
h		AFM tip height
k_c		cantilever stiffness
k_{lat}		lateral stiffness
k_N		contact stiffness
L		cantilever length
L_1		(effective) cantilever length
M_S		indentation modulus sample
M_T		indentation modulus tip
r		radius
R_t		AFM tip radius
x_0, y_0		centre of sphere in x- and y-axis

4.3.1. Introduction

The mapping of the mechanical properties of micrometer- and sub-micrometer-sized structures has become available in the recent years by the technological advancement of a number of methods based on atomic force microscopy (AFM). Due to the unlimited scope of applications, such techniques have already been applied in very different areas, such as cell wall stiffness in plants [236, 237, 238] or material science research on composites from natural polymers [239, 240, 241]. Wheat grains are another natural composite material, for which the knowledge of the micro-scale elastic properties of its components would greatly benefit the understanding and accurate simulation of the grains' milling behaviour [184].

One of the AFM-based nano-mechanical characterization methods is contact-resonance atomic force microscopy (CR-AFM). The elastic and viscous properties of the sample are inferred from the modal response of the AFM cantilever, which is in contact with the surface through the AFM tip, while the sample is subjected to a sinusoidal ultrasonic vibration of low amplitude [204, 205]. This technique has especially been of great interest since it was shown that vibrational mode frequencies were very sensitive to changes in the indentation modulus of the sample [242]. Despite the great potential of the technique, one has to be aware of the limitations before relevant information on the sample's mechanical properties can be extracted. The difficulties linked to the topography of the surface and the badly known geometry of the contact area are probably the most substantial and the most hindering, especially since the delicacy and the heterogeneous nature of the samples can limit the preparation of truly flat surfaces. Mazeran et al. [209] pointed out, for phase interpretation in tapping mode, how cautious one should be if the mechanical measurements are correlated with the sample's topography. In CR-AFM in particular, the resonance frequencies of the cantilever-tip-sample system are highly dependent on its exact geometry. Stan et al. [207] studied for instance, how roughness can be taken into account for a granular material at the nanometric scale based on accurate Scanning Tunnelling Microscopy acquisitions of the sample topography and a model which takes into account multiple asperity contacts. Such a level of resolution is necessary when one hopes to get quantitative determination of the mechanical properties at the nanometric scale, but is rarely possible to reach. For most samples, the amplitude and wavelength of the roughness over a micron-sized area are fortunately smaller than the local radius of the AFM tip, so that such precise measurements are not necessarily needed. However, the samples often present long range variations of the local slope, which constitute an important and easily measurable parameter of the contact geometry that should be addressed to improve the mechanical measurements. Passeri et al. [243] demonstrated the significant influence of the angle between the cantilever-tip and the surface on the frequency modes in CR-AFM. Yet, the only angle, which is usually taken into account, is the one directly resulting from the tilt of the cantilever in AFM devices. A possible slope of the surface is generally neglected, although it can induce local changes of the tip-surface angle, which can easily reach several tens of degrees. The non-trivial correlation between surface slope and CR-frequency then hinders a straight-forward interpretation of CR-AFM indentation modulus measurements.

In this paper we study the influence of the local surface slope on nano-mechanical measurements by CR-AFM. We propose a practical method to correct the measure by taking into account the topography, which is acquired simultaneously to the CR-frequencies. This correction method is based on a simplified model of the vibrating cantilever to emphasize the effect of the local slope. It can easily be implemented using more advanced models of the vibrating cantilever and should also be easily adaptable to other experimental techniques, i.e. acoustic and ultrasonic AFM [244, 245, 246, 247, 248, 249], PeakForce$^{\text{TM}}$ QNM$^{\text{TM}}$ [250] or QI$^{\text{TM}}$ [251], force modulation (FMM) [252] or any other force volume (FV) and force distance (FD) like modes, which are very likely exposed to the same problem.

The correction method was successfully applied to mechanical measurements on a biological surface, whose high surface slopes so far inhibited the correct interpretation of CR measurements: a cut starch granule within the sectioned endosperm of a wheat grain.

4.3.2. Theory

Analytic determination of the vibration eigenmodes

The key principle of CR-AFM is that the resonance frequencies of the cantilever are strongly dependent on the stiffness of the contact between the AFM tip and the surface and thus on the mechanical properties of the sample surface. Frequency shifts can therefore reveal even small changes in the mechanical properties of the scanned surface, provided that a good compromise between stability of the tip-surface contact, sensitivity of the frequency measurement and sensitivity of the frequency shift response to contact stiffness changes are reached. The vibrational response of the cantilever can be modelled with the elastic equation of motion of a rectangular beam in the frame of the Euler-Bernoulli theory, with boundary conditions depending on the geometry of the cantilever-tip-surface system. It is a well-studied problem, resulting in a series of resonances corresponding to the different vibrational eigenmodes of the cantilever. Numerical solutions have been developed to obtain the amplitude and phase of the cantilever's vibrational response as a function of the angle and considering the entire complex geometry of the tip-cantilever system during contact-resonance measurements. Such in-depth theoretical analysis of the system can be found in the literature [204, 205, 207, 242, 243].

Due to the numerous parameters that have a strong non-linear influence on the vibrational response of the cantilever, the application of these works to correctly analyse CR-AFM measurements is not straight-forward. The present study focuses on the influence of the local slope of the surface on the measured CR-frequencies. We thus take benefits from the above mentioned global studies to provide a way to practically obtain quantitative measures on samples with surface angles as high as $50°$. The overall geometry of the cantilever-tip system in contact with a surface is schematically presented in Figure 4.9, along with a simplified version, which focuses on the effect of local slope angle. We will demonstrate hereafter that these simplifications allow to soundly fit the experimental results. Damping of the cantilever is not taken into account in the model, as we focus only on the determination of the resonance frequencies of the different vibration modes. They are sufficient for the determination of the indentation modulus, and the effect of damping of the cantilever on the resonance frequencies is assumed to be negligible. Similarly, damping γ (Figure 4.9a) of the material of the sample is assumed to have a negligible effect on the measured frequencies and is also not taken into account. Rabe et al. [204] have shown that the position of the tip along the cantilever length strongly influences the vibrational frequencies during contact and that the correct analytical model should involve both the total length L of the cantilever and the real distance L_1 between the base of the cantilever and the exact tip location (Figure 4.9a). A sound simplification can be made, taking into account only the base-tip distance L_1 in the calculation assuming that the cantilever extension after the tip has a negligible effect on the resonance frequencies (Figure 4.9b). One of the main difficulties in the analysis is the description of the normal and lateral forces that constitute the contact between the tip and the surface. While the normal stiffness k_N of the tip-surface contact is always present and can be usually described with the well-documented models available in contact theory, the lateral stiffness k_{lat} depends on the type of contact (free sliding, friction, pinning) that occurs between the tip and the surface, and is difficult to anticipate. A general way to address the lateral forces is to express the lateral stiffness as proportional to the normal one, $k_{lat} = \lambda k_N$, and to confront the model's results with increasing values of the coefficient factor λ, from 0 (free-sliding contact) to more than 1 (pinning) [204], to actual experimental results. Describing the vibrations with an elastic beam model and the specific boundary conditions, one obtains a system of equations, whose non-trivial solutions are obtained independently of the excitation amplitude when the system's determinant is equal to 0. This leads to solve the characteristic equation [204]:

$$\begin{aligned} &(\beta L_1)^4\ [1+\cos(\beta L_1)\cosh(\beta L_1)] \\ &+ (\beta L_1)^3\ C_1\ [\sin(\beta L_1)\cosh(\beta L_1)+\cos(\beta L_1)\sinh(\beta L_1)] \\ &+ 2(\beta L_1)^2\ C_2\ \sin(\beta L_1)\sinh(\beta L_1) \\ &+ (\beta L_1)\ C_3\ [\sin(\beta L_1)\cosh(\beta L_1)-\cos(\beta L_1)\sinh(\beta L_1)] \\ &+ (C_1C_3 - C_2^2)\ [1-\cos(\beta L_1)\cosh(\beta L_1)] = 0, \end{aligned} \tag{4.1}$$

$$\begin{aligned} \text{with } C_1 &= \left(\frac{h}{L_1}\right)^2 \frac{3k_N}{k_c}(\sin^2\alpha + \lambda\cos^2\alpha) \\ C_2 &= \frac{h}{L_1}\frac{3k_N}{k_c}\sin\alpha\ \ \cos\alpha\ (\lambda - 1) \\ C_3 &= \frac{3k_N}{k_c}(\cos^2\alpha + \lambda\sin^2\alpha). \end{aligned}$$

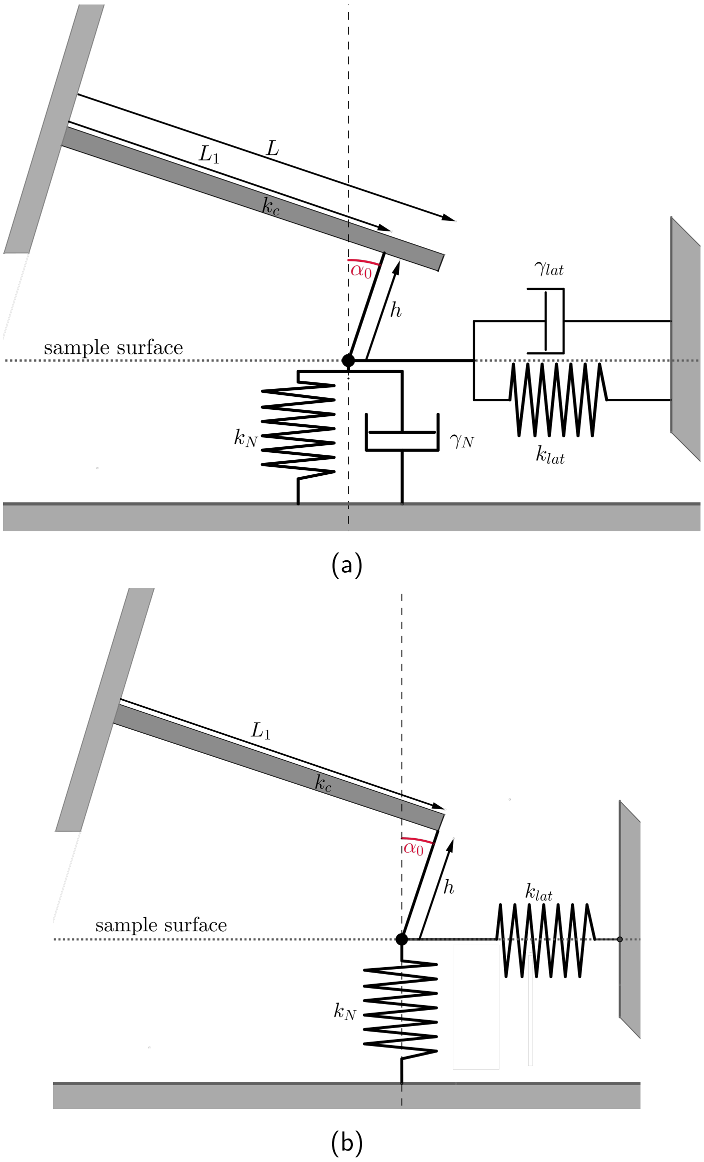

Figure 4.9. – Simplified elastic beam model of the cantilever and AFM tip in contact with a sample surface. (a) The full system is characterized by the cantilever length L and stiffness k_c, the AFM tip height h, the surface's normal stiffness k_N and lateral stiffness k_{lat}, the normal and lateral damping, γ_N and γ_{lat}, and the angle α between tip and surface. (b) The simplified model does not take into account damping, lateral forces, and the cantilever part extending the centre of the tip.

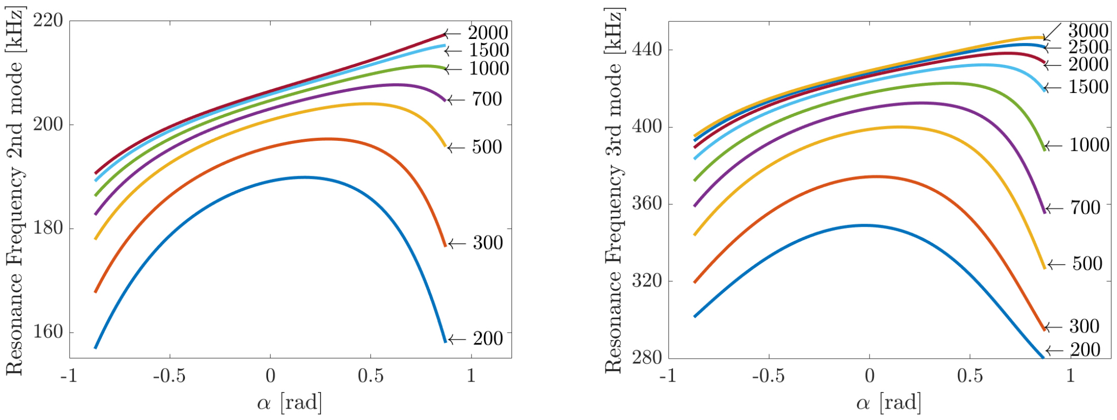

(a) (b)

Figure 4.10. – Influence of the tip-surface angle on the (a) 2nd and (b) 3rd resonance frequency from Equation 4.1 with $L_1 = 432\,\mu\text{m}$ and $h = 12.5\,\mu\text{m}$ is shown for different ratios k_N/k_c (values next to lines). Assuming a low cantilever stiffness of $k_c = 0.27\,\text{N}\,\text{m}^{-1}$ these ratios correspond to a range of indentation modulus M_S of 1 GPa to 100 GPa. The second mode saturates for values of $k_N/k_c > 1000$, the third mode for $k_N/k_c > 2000$.

The solutions β_n of this equation can be obtained numerically as a function of the geometrical parameters cantilever length L_1, tip height h, angle α between tip and surface, of the ratio λ between normal and lateral stiffness, and of the ratio k_N/k_c between normal contact stiffness k_N and cantilever stiffness k_c. The solutions are the wavenumbers β_n of the spatial vibration modes ($n \in \mathbb{N}^*$). Wavenumber β_n and pulsation ω_n are linked by the dispersion relation:

$$\beta_n^4 = \frac{\omega_n^2}{\mu^2}, \tag{4.2}$$

with $\mu = \sqrt{\frac{EI_x}{\rho A}}$ where E is the Young's modulus of the cantilever material along its axis, ρ its density, I_x the moment of inertia of the cantilever in bending, and A the cantilever's cross-section. The resonance frequencies associated to each mode are then:

$$f_n = \frac{\omega_n}{2\pi}. \tag{4.3}$$

Figure 4.10 shows the non-linear influence of the angle α on the 2nd and 3rd resonance frequencies obtained from Equation 4.1 for the parameters and range of ratio k_N/k_c corresponding to our experimental conditions in the absence of friction or pinning ($\lambda = 0$). It is interesting to note how different the influence is for these two modes and how strongly it is dependent on the ratio k_N/k_c. The asymmetry related to the sign of the tilt angle arises from the asymmetry of the torque acting on the tip (projected normal force in the direction parallel to the cantilever times the height h of the tip, $\sin\alpha$ term in the C_2 coefficient in Equation 4.1 that cancels if $\lambda = 1$, see subsection 4.3.6. The measure of the 3rd mode frequency enables us to study in good experimental condition the effect of the angle up to ratio $k_N/k_c \geq 2000$ (this would correspond to a contact modulus of about 50 GPa in our experimental conditions).

Tip-surface contact mechanics

In this work, we modelled the tip-surface contact within the classical frame of elastic sphere-plane contact geometry. Assuming small amplitude excitation of less than a few nanometers, as it is the case in CR-AFM, and considering the rather stiff material with limited adhesion, contact was described by the DMT model [253]. The small modulation around the interaction force, which is the sum of the normal load F_N and of the adhesive force F_{adh}, allows then to express the normal stiffness as a function of this sum, of the tip radius R_t and of the reduced modulus of the contact E^*, according to [254]:

$$k_N = \sqrt[3]{6R_t(F_N + F_{adh})E^{*2}}, \tag{4.4}$$

where the reduced modulus can be written as:

$$E^* = \left(\frac{1}{M_S} + \frac{1}{M_T}\right)^{-1}. \tag{4.5}$$

where M_S and M_T are the indentation moduli of the sample and tip, respectively. The indentation modulus of the silicon tip, oriented in (001) crystallographic direction, used in the model was $M_T = 163\,\mathrm{GPa}$.

For the investigation of the influence of the local slope, the interaction force has to be projected along the normal to the surface so that Equation 4.4 is modified as:

$$k_N = \sqrt[3]{6R_t(F_N + F_{adh})\cos\phi E^{*2}}, \tag{4.6}$$

where ϕ is the local angle as described later in Figure 4.12.

4.3.3. Experimental measurements

All measurements were performed with a SD-R30-CONT probe (Nano-sensors$^{\mathrm{TM}}$). This type of probe has the advantage of having an initially rounded tip apex of a well-defined radius $R_t = (30 \pm 5)\,\mathrm{nm}$ obtained through manufacturing by ion beam melting. The cantilever is rectangular, which is necessary to apply the developed model. Its spring constant was determined by thermal noise calibration [255] to be $k_c = 0.27\,\mathrm{N\,m^{-1}}$, which is within the range of $0.02\,\mathrm{N\,m^{-1}}$ to $0.77\,\mathrm{N\,m^{-1}}$ given by the supplier. The cantilever length L and tip height h are supplied by the manufacturer as $L = (450 \pm 10)\,\mathrm{\mu m}$ and $h = (12.5 \pm 2.5)\,\mathrm{\mu m}$.

The resonance frequencies of the three first modes in free vibration were determined to be $f_1^{free} = 13\,\mathrm{kHz}$ (supplier: 6 kHz to 21 kHz), $f_2^{free} = 86\,\mathrm{kHz}$ and $f_3^{free} = 243\,\mathrm{kHz}$. These free vibration modes were used to determine experimentally the parameter $\mu = \sqrt{\frac{EI_x}{\rho A}}$ that is used in the calculation. We ensured that our values fitted very nicely the dispersion relation Equation 4.2 relatively to the known theoretical wavelength of a cantilever of length L. We found $\mu = 0.005\,\mathrm{m^2\,Hz}$, which is very close to the estimation ($\mu_{est} = 0.0049\,\mathrm{m^2\,Hz}$) that can be obtained from the cantilever characteristics.

CR-AFM was performed on a Bruker Dimension AFM with Nanoscope V controller with an averaged vertical force of $F_N + F_{adh} = (200 \pm 10)\,\mathrm{nN}$. Sample holder discs containing the sample were

polystyrene (PSFILM-12M, Bruker)	acrylic resin (LR-White, Polysciences) [238]	epoxy based adhesive (Hysol EA9394) [259]	PMMA [260]	mono-crystalline sulphur (100) [260]	aluminum [259]	Silicon (100) [260]
3 GPa	3.5 GPa	4.5 GPa	6.5 GPa	20 GPa	65 GPa	163 GPa

Table 4.5. – Samples used for calibration of the resonance frequencies and their indentation moduli as determined by nano-indentation or from literature data.

placed on a small amount of acoustic coupling gel on top of a contact transducer (Olympus V 103-RM), which generated an ultrasonic sinusoidal oscillation. Resonance frequencies were tracked via dual-resonance frequency tracking [256] using an H2FLI lock-in amplifier from Zurich instruments, which serves as a signal generator for the transducer excitation, too.

Calibration of resonance frequencies

The resonance frequencies of the tip-sample system are highly dependent on the exact geometry of the system. However, an accurate description of the contact mechanics of the tip surface system is difficult, if not unreachable, and analytical equations describing the whole range of geometry and mechanical properties are not available. In practice, most users avoid this problem by calibrating the resonance frequencies on surfaces with known mechanical properties for each cantilever [243, 257]. We performed the calibration of the cantilever by measuring resonance frequencies of the 2nd and 3rd modes of the cantilever on a number of rather flat surfaces at a constant scanning speed of 12 µm s^{-1}. To obtain an accurate calibration the use of samples with not only a known indentation modulus, but also a surface with limited change of local angles and low roughness is important. The calibration samples were chosen so that their indentation moduli, determined by nano-indentation and/or using known elastic properties in the literature and anisotropic indentation model [258] if required, were in a range of 3 GPa to 163 GPa. The samples and their respective indentation moduli are listed in Table 4.5.

The calibration points were then fitted with Equation 4.1 and Equation 4.6 for the 2nd and 3rd modes simultaneously. Only the case where the lateral stiffness is null ($\lambda = 0$, free-sliding contact) is described here and represented in Figure 4.11. The cases with $\lambda \neq 0$ are shown and discussed in appendix (subsection 4.3.6), because it is shown in section 4.3.3 that, with the present experimental conditions, only a free sliding contact describes well the experimental data. The best fit of the measured resonance frequencies versus the respective indentation modulus was obtained for the following parameters: $L_1 = 431$ µm, $h = 12.5$ µm, $\alpha = 9.7^\circ (:= \alpha_0)$ and $R_t = 101$ nm.
The fitting values for L_1 and h are in very good agreement with the supplier information on the cantilever and tip geometry, considering that the tip is generally located at a distance of 10 µm to 20 µm from the end of the cantilever. The inclination angle of the cantilever is known to be about 10° in the Bruker Dimension AFM and is thus also in very good agreement with the fitting value found for the angle α on the horizontal samples. The radius found for the tip is three-times larger than the nominal tip radius. This can be due to usual flattening of the far end of the tip apex that can be either the original state of the tip or caused by wear. The tip radius was verified by an AFM measurement of the tip topography after CR measurements on a calibration grid (PA01, μmash). We found an equivalent radius of the ellipsoidal far end of the tip (down to 0.5 nm depth corresponding to the maximal indentation depth on the different reference materials) equal to (92 ± 15) nm which is in good agreement with the value $R_t = 101$ nm obtained with the fit.
One should notice that, even if the fit is not perfect compared to the experimental data (especially

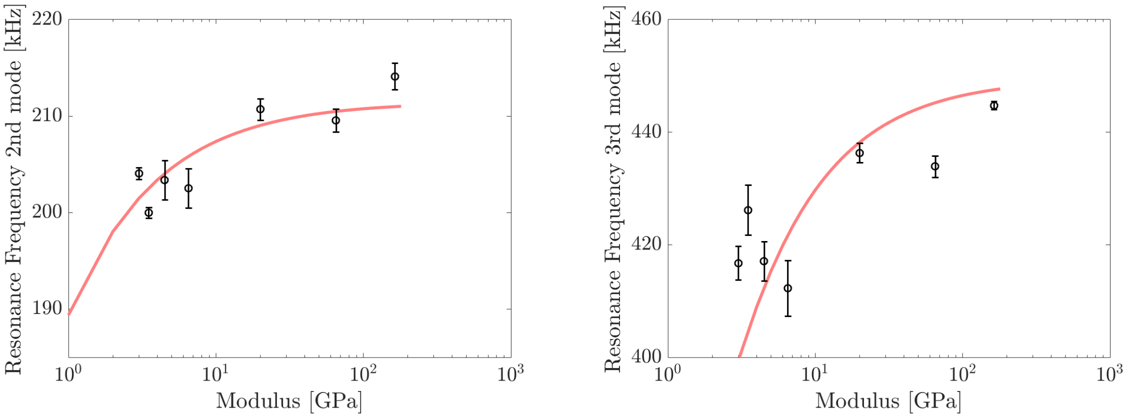

(a) (b)

Figure 4.11. – Calibration curves for (a) 2^{nd} and (b) 3^{rd} CR-frequencies measured on samples with known indentation modulus. Black circles: experimental data; Red: fit with Equation 4.1 to 2^{nd} and 3^{rd} mode simultaneously.

for the stiffest samples), simultaneously fitting with the same set of parameters, which are sound when confronted to the known geometry of the tip/cantilever system, allows to describe well the level of the plateau and the position of the curving point for the two modes. Large discrepancies between the model curve and the experimental data for the stiffest materials probably arise from the invalidity of the perfectly free sliding assumption in this case. It has been shown that free sliding, friction and pinning contact would change drastically the shape of the curve in the plateau regime [204, 260, 261].

Noise in the resonance frequency determination was measured to be of the order of 1 kHz. Considering the calibration curves, we can thus infer that in our experimental conditions, frequency measurement will allow for determining contact moduli differences when these moduli are below 50 GPa using the 3^{rd} mode (respectively 30 GPa using the 2^{nd} one). From the local slope of the curves, the sensitivity in terms of modulus determination can be evaluated to be around 0.1 MPa at moduli of the order of 1 GPa and of around 10 GPa when we reach the limit of discrimination.

Effect of local angle

A curvature or slope of the sample surface changes the overall angle between tip and surface. As illustrated in Figure 4.12, it must be considered as the sum of the inclination angle of the cantilever relative to the horizontal (α_0) and of the local angle of the surface towards the horizontal (ϕ). To study the effect of this local surface slope, CR-AFM was performed on spherical beads, which were assumed to be mechanically homogeneous. Silica hollow spheres with diameters of 10 µm to 30 µm (Polysciences, Inc.) were selected for their high sphericity. They were spread onto double-sided sticky tape on a sample disc and sputter-coated with about 5 nm of gold for fixation of the beads. Topographical AFM scans were performed to select a bead with very good spherical appearance. Figure 4.13 shows a three-dimensional view of the topography of the selected bead on the 12 µm × 12 µm imaging area. The surface can be well fitted by a spherical cap of radius $r = 13$ µm, whose centre is very close to the centre of the image ($x_0 = 6.02$ µm, $y_0 = 5.98$ µm). The root mean square difference between the fitted spherical cap and the real surface is 60 nm.

The local angle ϕ, defined in Figure 4.12, can be obtained from any untreated topographical AFM

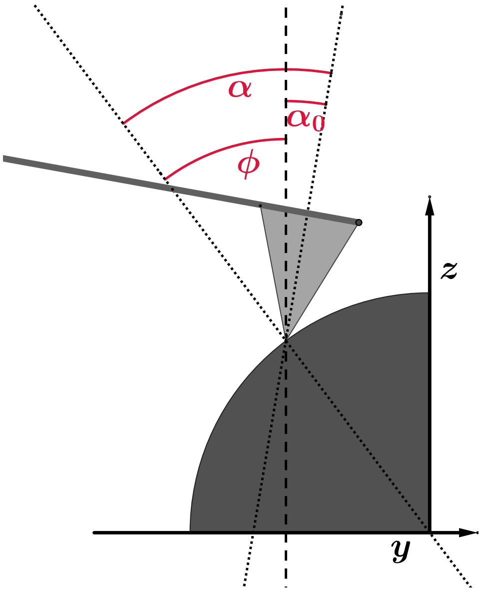

Figure 4.12. – Definition of angles in the direction parallel to the cantilever. α_0 is resulting from the cantilever tilt in the AFM instrument and therefore constant. ϕ depicts the local angle. The resulting overall angle α is the sum of α_0 and ϕ.

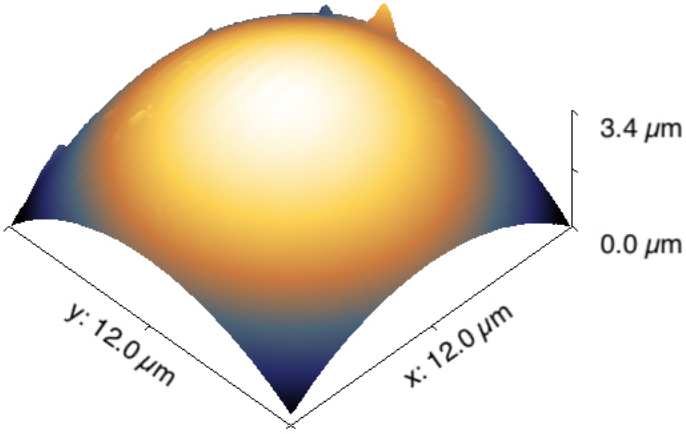

Figure 4.13. – 3D view of the topography of a silica glass bead measured by AFM. The surface can be well fitted to a sphere of radius $r = 13\,\mu\text{m}$ centred at $x_0 = 6.02\,\mu\text{m}$, $y_0 = 5.98\,\mu\text{m}$.

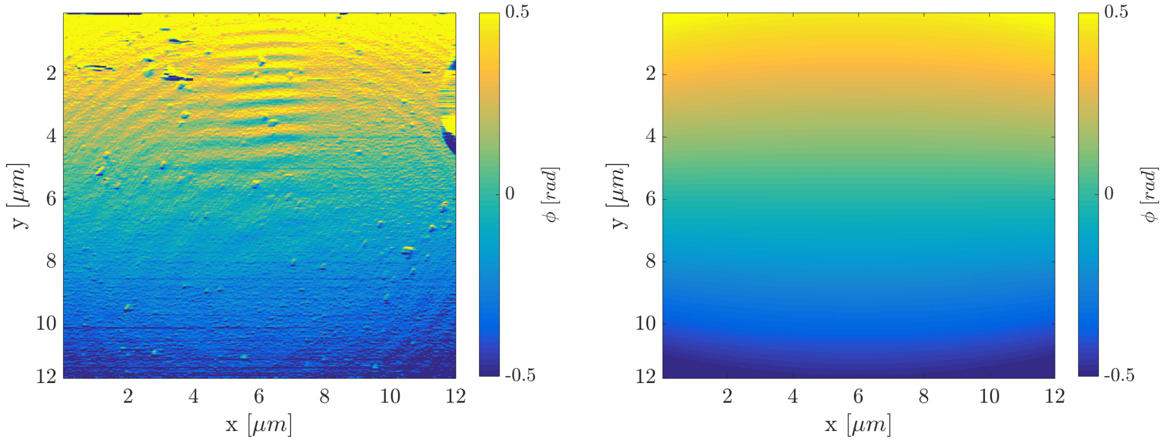

(a)

(b)

Figure 4.14. – (a) The local angle ϕ between surface and AFM tip calculated from AFM topography data on silica glass bead by Equation 4.7. (b) The angle ϕ^{Th} calculated for a perfect sphere of the size of the measured silica glass sphere according to Equation 4.8.

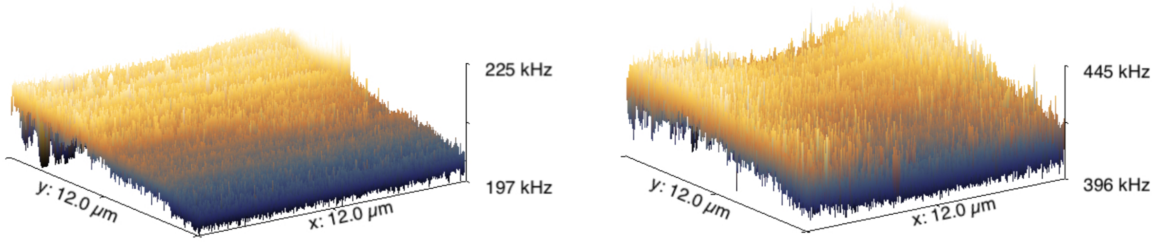

(a)

(b)

Figure 4.15. – Recorded CR-AFM frequencies for (a) 2nd and (b) 3rd mode on a silica glass bead.

image by calculating the partial derivative of the height z with respect to the y-direction:

$$\phi = \arctan \frac{\partial z}{\partial y} \tag{4.7}$$

The angle measured by Equation 4.7 on the selected bead can be compared to the theoretical value ϕ^{Th} calculated from the spherical fit according to:

$$\phi^{Th} = -\arcsin \frac{y - y_0}{r \ \cos\left(\arcsin \frac{x - x_0}{r}\right)} \tag{4.8}$$

The local angle determined by both methods is presented in Figure 4.14. The very good agreement between the two maps shows that the calculation of the partial derivative to obtain ϕ is reasonable.

Images of the 2nd and 3rd resonance frequency modes on the silica bead are presented in Figure 4.15. In spite of the expected homogeneity of the surface in terms of mechanical properties, the measured frequencies are not constant and present a significant variation in the y-direction (along the cantilever axis, Figure 4.12), whereas much fewer variations are observed in the x-direction (perpendicular to the cantilever axis, Figure 4.12). This is the expected manifestation of the change of local angle relatively to the cantilever direction.

For each pixel of the image the 2nd and 3rd eigenmodes are measured independently, as well as the topography and therefore the local angle of the surface relatively to the cantilever. Such a set of

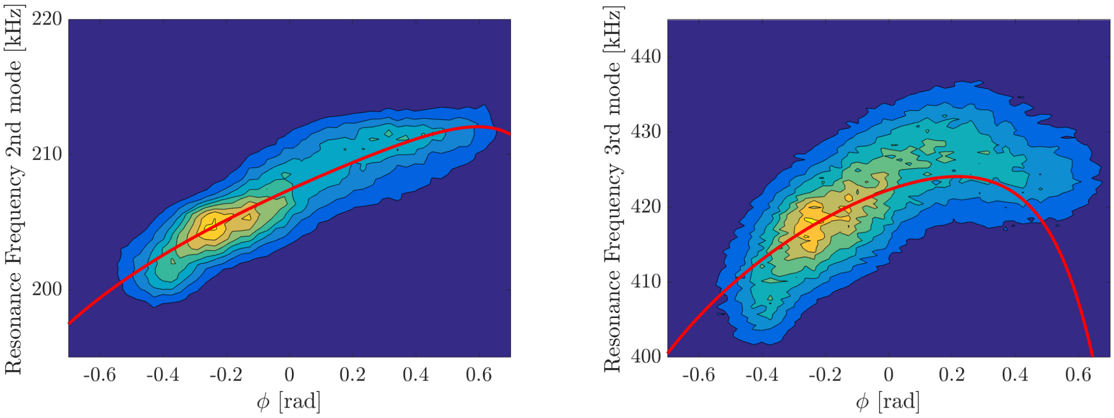

(a) (b)

Figure 4.16. – Point density maps of the recorded CR-AFM frequencies plotted as a function of angle ϕ for (a) 2nd and (b) 3rd vibrational eigenmode on the silica glass bead. Densest areas are represented in yellow, least dense in dark blue. The result of a least square fit of Equation 4.1 to the data is shown in red.

images can thus be considered as an array of measurements of both frequencies as a function of the local angle on a material with homogeneous contact modulus M_S. Both frequency measurements are plotted as a function of the angle ϕ in Figure 4.16. Due to the high number of pixels (512×512) and unavoidable scattering, iso-values of different point density are represented by a colour code. Regions of highest density are shown in yellow, lowest density in dark blue.

Both sets of data were fitted simultaneously with a least square optimization method, entering the values of L_1, h, α_0 and R_t that were determined during calibration (section 4.3.3) as fixed parameters and using the sample contact moduli as the only fitting parameter for the model. Such fits were performed for increasing values of the lateral stiffness ($\lambda = 0,\ 0.3,\ 0.5,\ 1$). The results are given in subsection 4.3.6. We observed that only in the case where the lateral stiffness is equal to zero, the fit was able to capture the main trend of the experimental data for both vibrational modes. This could be due to the fact that, in the present study contrary to what is generally done in the literature, all the measurements and calibrations are done while scanning. It has been shown that ultrasonic vibrations lead to a reduction of friction even at the nanoscale [262, 263, 264] and, thus, the pinning effect is assumed to be reduced while scanning too. In consequence, the following part will be discussed in the frame of free-sliding contact between the tip and the surface. The scattering of the data might be due not only to impurities at the surface, but also to geometrical effects such as the lateral angle and the variation of the contact area, which are not taken into account in the model. It should also be noted that the assumption of homogeneous mechanical response of the sample over the scanning area is not accurate since we worked on an hollow sphere, detailed hereafter. All these effects are likely to be the origin of the second order variation of the 3rd mode frequency observable along the x-axis in Figure 4.15b. In any case, the model, even though it is simplified, captures the major trend of the data in both modes and can thus be used to correct the local slope artefact on the experimental measurements.

On the sphere, an apparent contact modulus of $M_a = (11 \pm 5)$ GPa was found to provide the best simultaneous fit for the variation of the two frequency modes as a function of the local angle. This contact modulus, which corresponds to an apparent contact stiffness $k_a = (245 \pm 76)\,\mathrm{N\,m^{-1}}$, does not correspond to the glass indentation modulus (i.e., $M_{\text{glass}} = 73$ GPa) as it results from the contact stiffness k_N of the 5 nm gold layer in series with the stiffness k_S of the hollow silica/glass

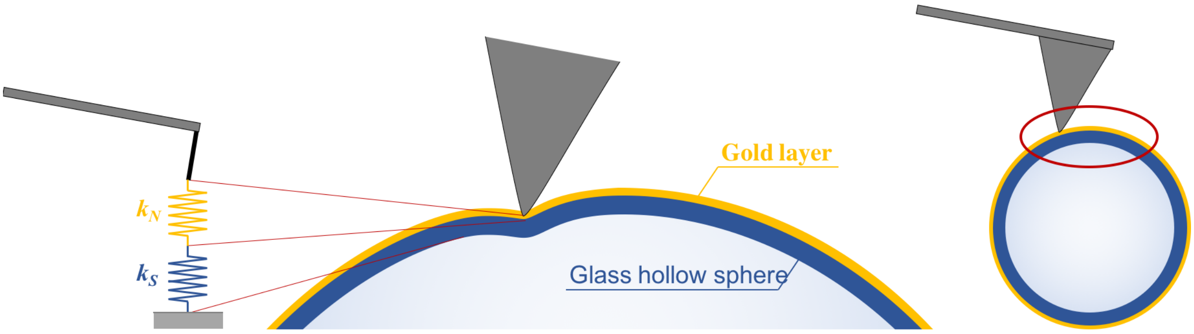

Figure 4.17. – Scheme of the measurement configuration on the glass hollow sphere (radius $R_S =$ 13 µm, thickness h_S) coated with a 5 nm gold layer: indentation of the tip in the gold layer, stiffness k_N, in series with the sphere elastic membrane deformation, stiffness k_S, leading to an apparent contact stiffness k_a.

sphere, that behaves like a linear elastic membrane (Figure 4.17). The sphere's exact shell thickness h_S is unknown, but its order of magnitude was optically roughly estimated to be some hundreds of nm. The theoretical stiffness k_S of a thin hollow sphere, of radius R_S and thickness h_S loaded centrically, is available in the literature [137]:

$$k_S = \frac{4E_{\text{glass}}h_S^2}{\sqrt{3(1-\nu_{\text{glass}}^2)}R_S}, \tag{4.9}$$

where $E_{\text{glass}} = 71$ GPa and $\nu_{\text{glass}} = 0.17$ for silica/glass elastic properties. In our case, quite high off-centre loading (up to 6 µm) occur during the scanning. Linear elastic finite elements modelling, using *Cast3M 2017*[2], of such a case yields an increase of $\approx 12\%$ of the stiffness for an off-centred loading of 6 µm, which is therefore negligible here. Thus, using Equation 4.9, the indentation stiffness of the pure gold layer (Equation 4.4 with $E_{\text{gold}} = 77$ GPa and $\nu_{\text{gold}} = 0.42$, $M_{\text{gold}} = 94$ GPa, $F + F_{adh} = 200$ nN and $R_t = 101$ nm) and the apparent contact stiffness of (245 ± 76) N/m, it is possible to back calculate an estimate of the sphere shell thickness $h_S = (156 \pm 32)$ nm. This theoretical shell thickness agrees with the expected order of magnitude and validates the experimental measurements. One should note that the contribution of the gold layer and of the glass sphere are well decorrelated, as the indentation depth in the gold layer is estimated to be ≈ 0.3 nm in the worst case, which is at least ten times smaller than the gold layer thickness.

Whole image correction

From a complete set of data containing the frequencies (2^{nd} and 3^{rd} modes) and the local angle calculated from the topography via Equation 4.7, a map of a corrected modulus can be calculated by solving Equation 4.1 for each pixel separately. Figure 4.18 compares the uncorrected estimation of the indentation modulus on the silica bead as obtained from both frequencies and constant cantilever tilt (Equation 4.1 with $\alpha = \alpha_0$) to the corrected indentation modulus (Equation 4.1 with $\alpha = \alpha_0 + \phi$ for each pixel). Scatter excluded, the expected homogeneity of contact modulus on the scanned area is recovered after the correction. The average line profiles (Figure 4.18c shows that the correction removes the inhomogeneities in the y-direction and that the corrected modulus value is more even throughout the whole image.

---

[2] http://www-cast3m.cea.fr/

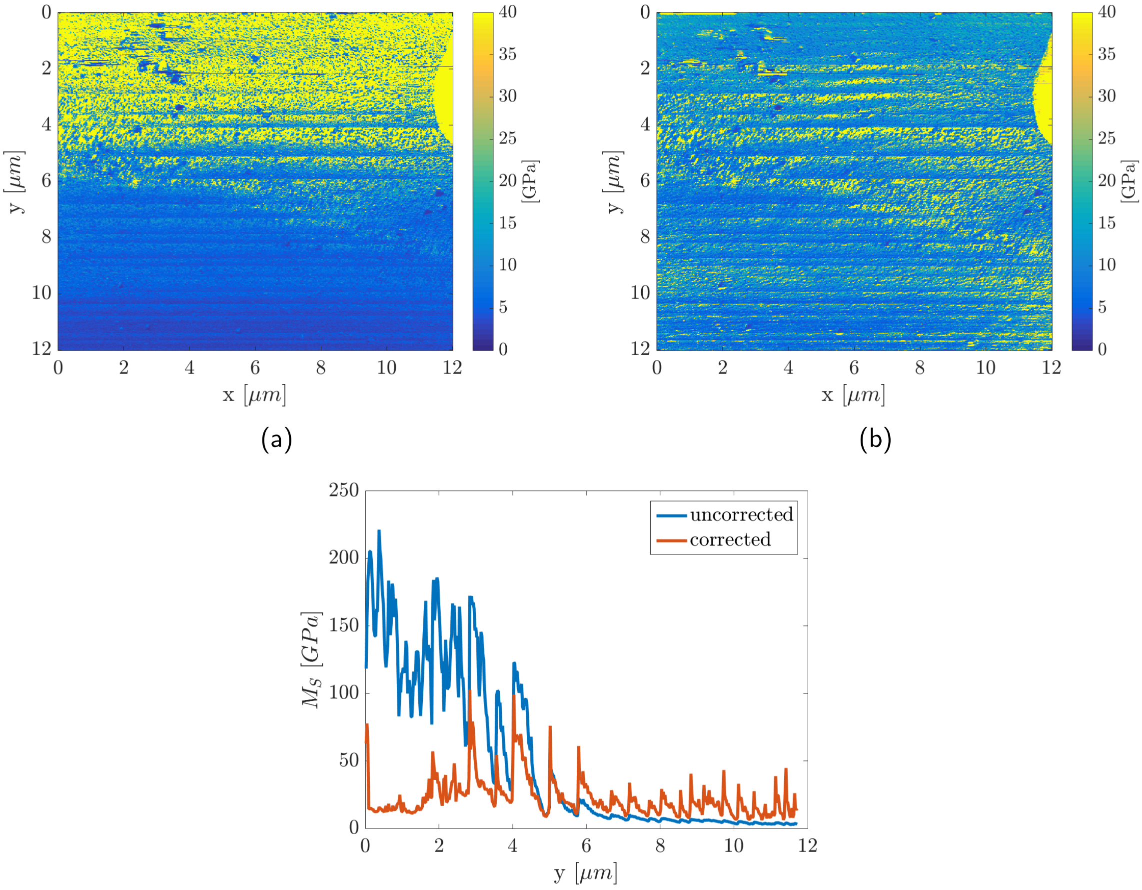

(a)

(b)

(c)

Figure 4.18. – (a) Uncorrected and (b) corrected maps of the indentation modulus on hollow silica bead are shown. The modulus is obtained by Equation 4.1 for (a): $\alpha = const = \alpha_0$ and (b): $\alpha = \alpha_0 + \phi$, for each pixel respectively. The color range is the same for both images. (c) shows the average line profile for both the uncorrected (blue line) and corrected (orange dashed line) modulus maps.

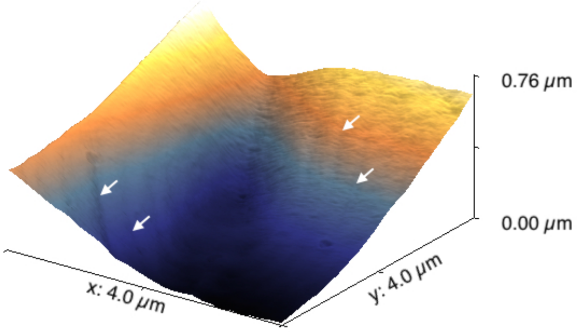

Figure 4.19. – Three-dimensional view of the topography on a cut starch granule in a sectioned wheat grain. Arrows are pointing out the valleys between growth rings.

4.3.4. Application

The correction method was applied to the measurement of a biological surface, whose high surface slopes inhibit the interpretation of CR measurements so far: a cut starch granule within the sectioned endosperm of a *durum* wheat grain. Starch consists mainly of amylose and amylopectin, which together form spherical to elliptical granules in the grain [27]. Starch granules are, next to protein, one of the main components of wheat grains. Wheat grains are a natural composite material and the mechanical properties of the separate constituents are of interest in order to better understand the fragmentation behaviour during the milling process. Indentation modulus information on starch can provide insight into the elastic properties, which would complement other nano-mechanical measurements of for example the abrasive hardness of starch [135]. Nano-scale abrasion tests were able to reveal the overall differences in the abrasive hardness of starch ((2.0 ± 0.6) GPa) and protein ((0.64 ± 0.17) GPa) [173], but they are limited to measuring only the global properties on an area of ∼1 μm × 1 μm. Both types of mechanical properties, elasticity and hardness, are necessary to accurately simulate the mechanical behaviour of the whole grain [184].

The sample was obtained by sectioning an intact wheat grain in a cryotome (Microm HM520, $-20\,^{\circ}\mathrm{C}$). Both distal regions of the grain (containing the brush and the germ [265]) were removed with a scalpel. The grain was then placed vertically on a cryotome sample holder, covered in freezing medium (Richard-Allan Scientific Neg-50TM) and placed in the cryotome for about 5 minutes to freeze fully. Sectioning was performed at slow speed using a carbon steel blade (Feather C35). The sectioning thickness was gradually reduced from 50 μm to 2 μm until a mirror-like surface was obtained.

As can be seen in Figure 4.19 the starch granule exhibited high topography changes of several hundred nanometers within a small imaging area of 4 μm × 4 μm. Due to the centre of the granule being lower than the edges, both granule halves are strongly inclined at opposite angles and an additional overall inclination is present. Contact-resonance measurements on this sample are therefore greatly influenced by the surface slope and the correction is necessary to remove the artificial variation of the indentation modulus and to obtain the one of the actual material.

CR-AFM measurements were performed on the same set-up as described in subsection 4.3.3 and with the same cantilever probe. The indentation moduli calculated without surface angle correction is shown in Figure 4.20a. It shows a strong contrast between the left and right side of the granule, which is caused artificially by the opposite surface slopes of the granule halves. To obtain a meaningful modulus of the CR-AFM measurements on this area, the correction method for the whole image was applied on the data. The map of the modulus obtained after correction is shown in Figure 4.20b and the histograms of the modulus before and after correction are shown in Figure 4.20c. These figures show that our method allows for efficiently correct the asymmetry

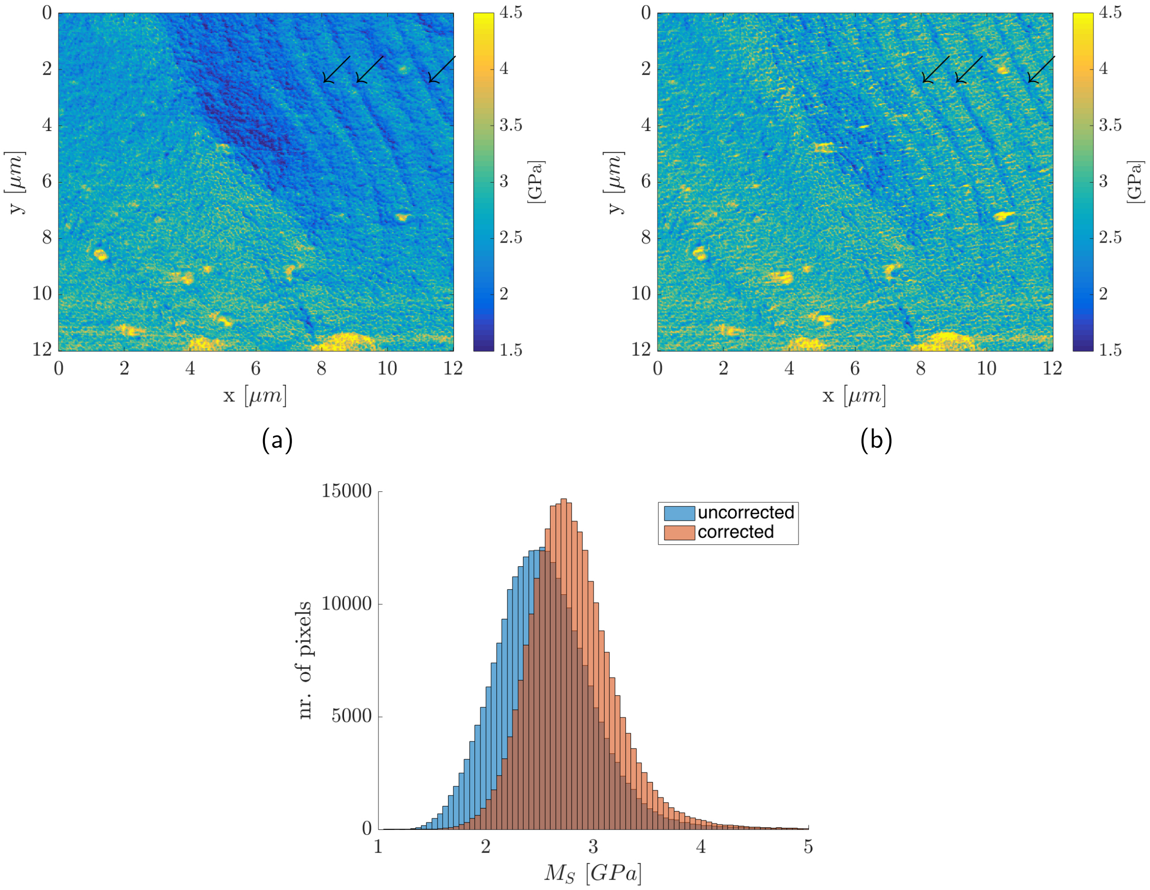

(a)

(b)

(c)

Figure 4.20. – (a) Uncorrected and (b) corrected maps of the indentation modulus on a cut starch granule are shown. Arrows are pointing out regions of lower modulus correlating to valleys between growth rings. (c) shows the modulus histograms of the uncorrected and corrected maps of the modulus.

of the measured modulus induced by the different slopes of the opposing halves of the granule. The average value of indentation modulus obtained for this cut starch granule after correction was (2.8 ± 0.4) GPa. Within the granules itself, starch also exhibits nano-scale substructures, whose exact mechanical properties are still unknown. One of these substructures are growth rings, which originate from different states in the crystallinity of the starch polymers [27]. The rings' thickness is in the range of a few hundred nanometers and they are often already observable in topography images, the regions in-between two rings usually forming small valleys. It is possible that the regions of different crystallinity have different mechanical properties, but no direct evidence exists so far. One of the advantages of CR-AFM is the possibility to investigate the mechanical properties of such sub-micrometer structures. In the examined starch granule, growth rings were observed in the topography image (Figure 4.19). They were also recovered with contrast in the modulus maps without and, to a lesser extent, with surface slope correction (Figure 4.20). The regions between the rings were slightly lower in modulus and the different crystallinity of the polymers could be the cause of these differences. However, the valleys between the rings are sharp ($\sim$100 nm in width) and possibly lead to changes of the contact area, which are not corrected with our model.

The crystalline structure of starch and its deposition into circular growth rings result in an anisotropy of the material. Therefore, the measured mechanical properties are depending on the testing direction with regard to the orientation of the crystalline layers. This effect must also be taken into account in the interpretation of contact modulus measurements. Therefore, the real mechanical properties of the starch's growth rings cannot be determined yet by this method.

4.3.5. Conclusion

In this article we demonstrated the non-negligible effect of the surface angle, caused by high topography of the samples, on the mechanical measurements by CR-AFM. This effect is so pronounced that the obtained maps of the mechanical properties of curved surfaces become meaningless due to an artificial broadening of the moduli that can be measured, which has nothing to do with the actual mechanical properties of the sample. A simplified theoretical model, without damping, was shown to be able to predict the relation between surface angle and measured cantilever vibrational frequencies. The validity of the model was confirmed by comparison with experimental measurements on a spherical surface. Successful correction of the measurements on this surface demonstrated that the model is suitable to correct the mapping of the contact modulus on surface with local angles ranging from $-50\,^{\circ}\mathrm{C}$ to $50\,^{\circ}\mathrm{C}$. Furthermore, this model was successfully used to correct the experimental data on a surface of biological origin with high surface slopes. After correction, a first value of the indentation modulus of a starch granule in situ in a sectioned wheat grain was obtained. This opens the way to investigate possible differences in modulus of starch granules depending on the botanical origin.

We proposed thus a practical way to account for the local slope of the surface in the CR-AFM measurements. In our experimental conditions and for our sample, contact was likely to occur in free-sliding mode (i.e., with negligible lateral forces). We nevertheless show how these lateral forces can be accounted for and what is their influence on the relation between the local angle and the frequencies (subsection 4.3.6). It should be noticed that the proposed correction is likely to be effective only on topography with in plane typical length-scales of several hundreds of nanometers. Smaller curvatures caused by structures approaching the size of the tip diameter ($<$100 nm) might change the contact area in ways that are not corrected with this model [207].

The present study highlights in any case that extreme caution should be applied when interpreting nano-mechanical measurements by AFM, as the interactions between tip and sample on the nanometer scale are highly complex and often non-linear. Similar effects are strongly expected to occur for other nano-mechanical AFM techniques, which rely on the effect of tip-sample contact on the cantilever behaviour, such as ultrasonic and acoustic AFM, PeakForce$^{\mathrm{TM}}$ QNM$^{\mathrm{TM}}$ or QI$^{\mathrm{TM}}$, FMM and other force-distance like modes.

λ	0	0.3	0.5	1
R_t (nm)	101	403	279	76
L_1 (µm)	431	438	438	436
α_0 (°)	9.7	8.6	6.9	14.2

Table 4.6. – Fitting parameter of the calibration data as a function of stiffness ratio λ

4.3.6. Appendix: Effect of the lateral forces

The whole analysis of the measured 2nd and 3rd modes resonance frequencies, from calibration to determination of the local angle effect on the spherical sample was performed for different values of the lateral/normal stiffness ratio $\lambda = 0,\ 0.3,\ 0.5$ and 1. Fits of calibration data for the two modes with increasing ratio λ are presented in Figure 4.21. The accuracy of the calibration is not sufficient to allow for the discrimination between the different fits.

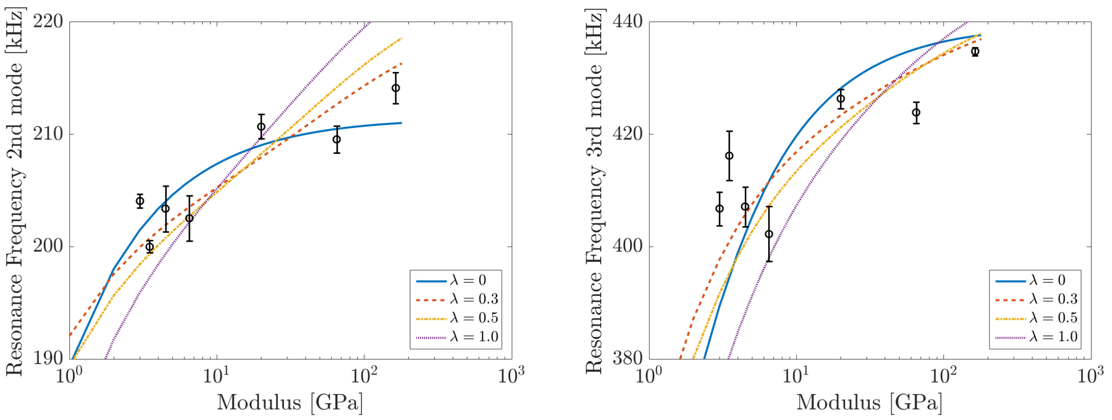

(a) (b)

Figure 4.21. – Calibration curves for (a) 2nd and (b) 3rd CR-frequencies measured on samples with known modulus for values of λ between 0 and 1 is shown. Blue circles show the experimental data with error bars.

It is yet interesting to consider the fitting parameters which are calculated for each value of λ and reported in Table 4.6. It is in particularly interesting to notice that for the intermediate cases, the fitting value of the tip radius, are very large, out of the range of the expected values.

For increasing value of the lateral/normal stiffness ratio λ and consequent values of the geometrical parameters obtained from the calibration fit, we tried to adjust the experimental data obtained on the hollow sphere as a function of the local angle. The corresponding fitting curves are represented on Figure 4.22. We can remark that with the ratio λ has a strong influence on the variation of the frequency as a function of the local angle. It was expected, since this ratio change drastically the torque applied on the cantilever/tip system. Moreover, the stronger the lateral forces are set in the model, the less the fit is able to capture the global trend of the data. In our experimental conditions this leads us to think that the tip/surface contact while scanning was in free sliding mode. It would nevertheless be interesting to systematically investigate the influence of the lateral force when correcting the data, especially if adhesive surfaces are tested.

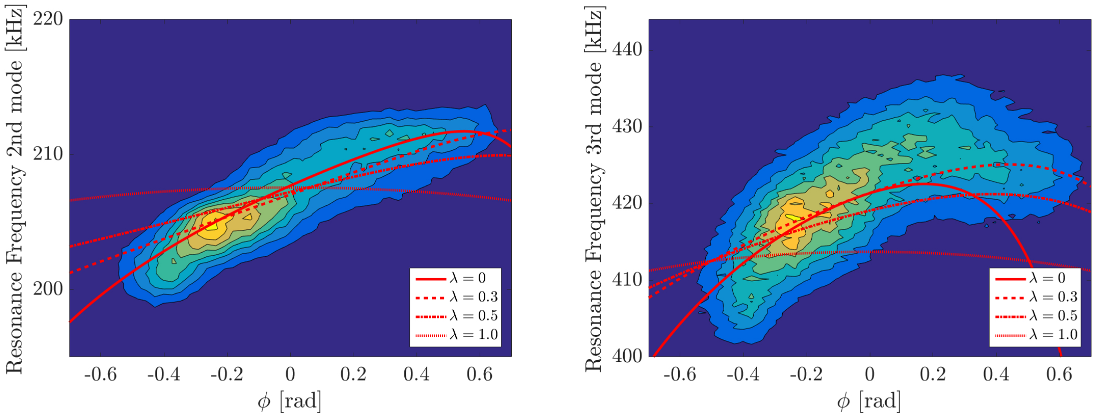

(a) (b)

Figure 4.22. – Point density maps of the recorded CR-AFM frequencies on the silica glass bead plotted as a function of angle α for (a) 2^{nd} and (b) 3^{rd} vibrational mode. Results of least square fits for values of λ between 0 and 1 are shown in red.

4.4. Mechanical properties of starches from different origins by CR-AFM

Abstract

Starch is a major compound of grains (cereal and others), which serves as an energy storage for plants. It consists of the two major components amylose and amylopectin, whose proportion varies between 15 % to 30 % and 70 % to 85 %, respectively. Waxy (<15 %) and "high amylose" (>30 %) mutants make it possible to vary the amylose concentration more widely. The unique properties of starch are exploited by processing (cooking, baking ...) for food or for non-food products (paper, textiles, plastics, biofuel) after extraction.

Starch characteristics, such as the form and size of granule, the percentage of crystallinity, the swelling capacity and others, greatly depend on the botanical origin. However, very few studies are concerned with the *in situ* mechanical properties of starch, which play a role in the grinding behaviour of the grain and the amount of damaged starch afterwards.

A CR-AFM method was used to measure the contact modulus in cut starch granules on a size scale of some hundred nanometers and sections of grains from different botanical origin (C3 and C4 cereals, legumes) were evaluated. The results demonstrate the ability of AFM to measure the mechanical properties of starch and the results are discussed in the context of the current knowledge on starch structure and its physicochemical properties.

4.4.1. Introduction

Starch is a major compound of grains (cereal and others), which serves as an energy storage for plants. It consists of the two major components amylose and amylopectin, whose proportion varies between 15 % to 30 % and 70 % to 85 %, respectively. Waxy ($<$15 %) and "high amylose" ($>$30 %) mutants make it possible to vary the amylose concentration more widely. Starch characteristics, such as the form and size of granule, the percentage of crystallinity, the swelling capacity and others, greatly depend on the botanical origin [266, 267]. However, very few studies are concerned with the *in situ* mechanical properties of starch, which play a role in the grinding behaviour of the grain and the amount of damaged starch afterwards.

In this study a range of cereal and legume starches are investigated with an AFM nano-mechanical assay *in situ* in cut grain sections. The grains of cereals and legumes (pea, lentil, chickpea) plants were studied. The cereals can further be separated into C_3 (wheat, barley, rice) and C_4 (corn, sorghum) plants, depending on their carbon fixation cycle. The shape and size of most of these starch granules differ from each other. Wheat and barley (C_3 cereals) have a bi-modal granule size distribution of large, disk-shaped granules and small, more round granules [210]. Rice is a C_3 cereal with compound granules. The starch granules are unimodal, smaller, irregularly shaped and polygonal [210]. Sorghum (C_4 cereal) also has a bi-modal granule size distribution with irregularly shaped granules [210]. Millet (C_4 cereal) has smaller, but also irregularly shaped, polygonal granules [210]. Corn (C_4 cereal) also has irregularly shaped, polygonal starch granules [210]. Of the legume starches, chickpea has more irregularly shaped granules, but with round edges [210]. Pea has rather disk-shaped granules and lentil has smooth, ellipsoidal granules [210].

Due to these significant differences in structure, possible differences in mechanical properties could be expected.

4.4.2. Material and methods

The starch samples are summarised in Table 4.7.

Grain sample preparation Sample preparation was done similar to the method described in [135] by cutting grain sections in a cryotome (Microm HM520, $-20\,^{\circ}\mathrm{C}$). The distal regions of the grains were removed with a scalpel until an $\approx$5 mm big slice of the central grain part was obtained. The sections were placed vertically onto separate cryotome sample holders and covered with freezing medium (Richard-Allan Scientific Neg-50TM). The holders with the slices were placed in the cryotome. Sectioning was commenced after 5 minutes, when medium and slice were fully frozen. Sectioning thickness was gradually reduced from 50 µm to 2 µm at slow sectioning speed until the sections had a mirror-like surface. The sample holders were removed from the cryotome and left to unfreeze at ambient temperature, before the grain sections were recovered. The sections were stored between two microscopy glass slides, sealed with parafilm, at $8\,^{\circ}\mathrm{C}$ until atomic force microscopy (AFM) experiments. For contact resonance atomic force microscopy (CR-AFM) measurements the grain sections were fixed on AFM sample holder discs with a small drop of Araldite Rapid resin (Huntsman Advanced Materials, UK).

CR-AFM AFM experiments were performed on a Bruker Dimension AFM with Nanoscope V controller with an averaged force of $F_N + F_{adh} <$ 200 nN at ambient conditions. The AFM sample holder discs with the fixated sections were placed on a drop of acoustic coupling gel on a contact transducer (Olympus V 103-RM). Resonance frequencies were tracked via dual-resonance frequency

Table 4.7. – Starch samples

Sample	Specification
C_3 Cereals	
Wheat:	
Durum wheat *Svevo*	[141]
Common wheat *Triticum aestivum* near-isogenic lines	[131, 112]
Waxy wheat (Waximum)	from F.X. Oury, UMR GEDEC, Clermont Ferrand, France (2015)
High-amylose wheat *Triticum aestivum* cultivar Cadenza	from D. Lafiandra, C. Morris, V. Tascia, Viterbo, Italy
Barley *Pirona*	from VTT, Finland (2015) [268]
Brown Rice *Camargue cv Arelate*	from BIOSUD, Arles, France (2015)
C_4 Cereals	
Corn	from Limagrain (2014)
Millet	
Sorghum *Macia*	from S. Joseph, UMR Qualisud, Montpellier, France (2016)
Legumes	
Pea	from Sotexpro (2015)
Green lentil *Anicia*	from CELNAT, St Germain Laprade, France (2015)
Chickpea	from CELNAT, St Germain Laprade, France (2015)

tracking [256] using an H2FLI lock-in amplifier from Zurich instruments. Experiments were performed with two cantilevers of the type SD-R30-CONT (from Nanosensors^{TM}). This type of tip has a specially rounded apex of a well-defined radius $R_t = (30 \pm 5)$ nm and a rectangular shaped cantilever. Their spring constant were determined by thermal noise calibration [255]. The cantilever was calibrated according to the method described in section 4.3. The second mode of the cantilever's resonance frequency was measured in contact with selected surfaces of known contact modulus at the constant scanning speed of 12 µm s^{-1}. The calibration samples with contact modulus and measured contact-resonance frequencies are summarised in Table 4.9. Fitting the data to the model developed in section 4.3, resulted in the fitting values given in Table 4.8.
Imaging regions were selected from the build-in light microscope. In grains with cheeks (barley, wheat) the centre of the cheek was chosen. In rather homogeneous grains (rice, pea, chickpea, lentil) a region in the middle between the centre and periphery was chosen. Corn and sorghum grains had a gradient of vitreousness from the centre of the grain (very mealy) to the periphery (very vitreous). In these grains, only the vitreous regions could be imaged. Two types of grains of the selection could not yet be tested due to the unavailability of the setup and samples: millet and high-amylose wheat.
Images of 10 µm × 10 µm were collected and the data treated via the method described in section 4.3, calculating the contact modulus while correcting for the local surface slope. The image size and speed was kept constant among all samples for better inter-sample comparison. In grains with larger granules, i.e. lentil and pea, this lead to only parts of the granules being imaged. To obtain the average contact modulus value for each botanical origin, the modulus values for each pixel of all images from that origin were counted in a histogram and then fitted with a normal distribution to obtain mean and standard deviation.

Table 4.8. – Spring constant k, resonance frequencies of free vibration f_i^{free}, and best fit parameters after tip calibration are given for the different tips used for CR-AFM.

	k	f_1^{free}	f_2^{free}	f_3^{free}	L	h	α	μ
tip A	0.746 N m^{-1}	13 kHz	84 kHz	235 kHz	429 µm	12.5 µm	9.9°	0.0047 m^2 Hz

Table 4.9. – The indentation moduli of the calibration samples and the measured CR-AFM frequencies for tip A are summarized.

	polystyrene (Bruker)	resin (kevlar) [241]	HOPG	monocrystalline sulphur	kevlar fiber [241]	fused silica	Silicon $<100>$
Indentation mod.	3 GPa	5 GPa	18 GPa	20 GPa	22 GPa	70 GPa	163 GPa
tip A F2	192 kHz	193 kHz	199 kHz	199 kHz	200 kHz	206 kHz	206 kHz

4.4.3. Results and discussion

The contact modulus values are summarised in Figure 4.23 and one contact modulus map of the surface is shown for each sample in Figure 4.24 and Figure 4.25. To our knowledge, this is the first study quantitatively measuring the nano-scale modulus in all of these starches, with the exception of common wheat. In general, we did not observe large differences between any of the samples, except for sorghum starch.

Values in C_3 cereals centre around 4 GPa. This is twice the value reported by Salerno et al. [44] for wheat. Within the wheats, waxy wheat does not differ from normal common wheat, despite its different amylose/ amylopectin ratio. This could be partly expected from the fact that amylose might not significantly contribute to the crystallinity of normal starches [28] and therefore also of low-amylose (waxy) starches. However, an increase of amylose was suggested to increase defects in the crystalline lamellae [58]. High-amylose wheat is therefore of great interest, but could unfortunately not be examined yet.

C_4 cereals seem to differ from C_3 cereals. Sorghum has a significantly higher contact modulus than any other of the tested starches. Sorghum starch was reported to have one of lowest digestibilities of cereal starches [269]. However, great variability of starch properties between sorghum cultivars was reported in terms of crystallinity and amylose content [269, 270]. Unfortunately, none of these properties were yet determined for the examined sorghum cultivar. Our results show a clear trend, but no general conclusions on the mechanical properties of sorghum starch can be drawn yet. It needs also yet to be determined, if sorghum is an exception in the group of C_4 cereals. The preliminary contact modulus of corn is also slightly higher than any of the C_3 cereals. Additionally to the confirmation of the modulus of corn, the examination of millet is expected to provide greater insight. Millet has, like sorghum, less digestible starch than other cereals [271].

The modulus of legume starches does not differ to the one of C_3 cereals.

A certain intra-sample variability is visible, which is between 8 % to 17 %, but significantly larger for sorghum with 27 %. The origin of this larger variability still needs to be investigated, but it partly results from differences between the imaged regions.

Though the presented results are preliminary, some trends are observable. Despite the known differences in starch properties (percent of crystallinity, gelatinisation behaviour, degree of polymerisation (DP) of amylopectin, ratio amylose/amylopectin) [210, 266, 267], the contact modulus measurements are not able to depict striking differences between different starches (except sorghum). To confirm these first observations, additional experiments are necessary. A larger number of imaged regions in parts of the cut grains and in different grains are needed for each grain type. If it can be confirmed that the average modulus is maintained throughout grain regions and grains, an interesting point of investigation would be possible differences between large and small granules in samples with bi-modal granule size distributions (wheat, barley).

However, a general question raised by the similarity in contact moduli is, if this CR-AFM approach is able to detect differences of mechanical properties in this particular structure. CR-AFM on a cut grain will always measure the modulus in the normal direction to the surface, which is rather tangential to the growth rings. The structure of starch is known to be anisotropic and the same should be expected of the mechanical properties. For another biological anisotropic structure, wood cell walls, the significance of differences in longitudinal and transversal modulus on nano-mechanical was reported [272]. A similar anisotropy is most certainly expected for starch and the lack of difference in the contact moduli reported here might only reflect that in the tested direction the mechanical properties are not much influenced by the composition and structure.

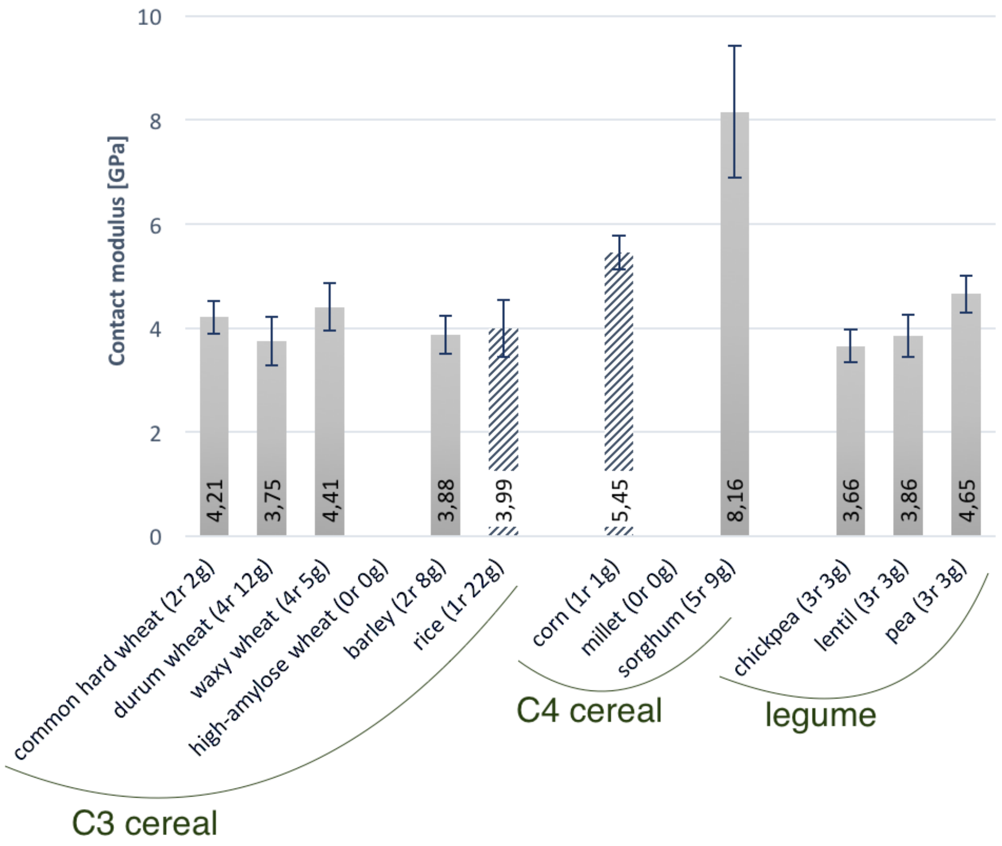

Figure 4.23. – The contact modulus value for starches from different botanical origin is shown. Values in brackets report the number of imaged regions (r) and approximate sum of starch granules (g). Values for rice and corn are preliminary.

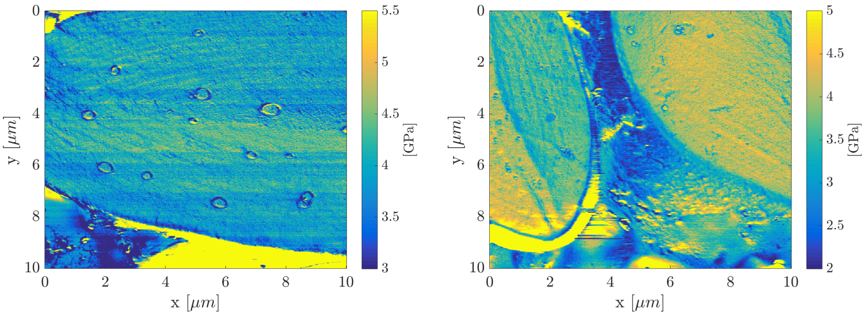

(a) Common wheat, hard NIL (b) Durum wheat

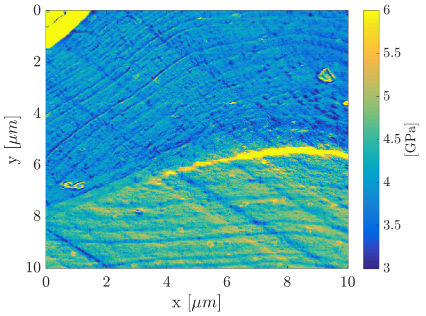

(c) Waxy common wheat

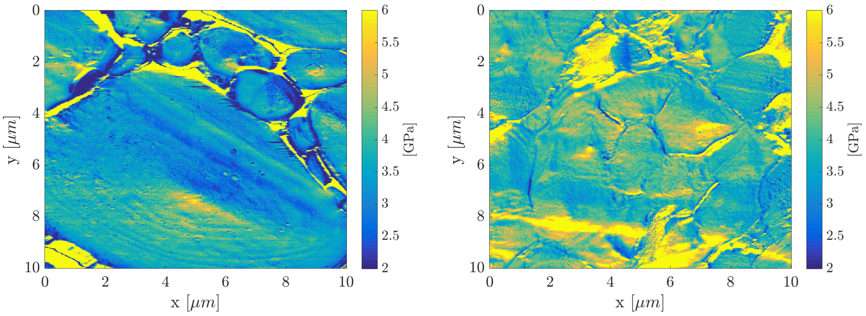

(d) Barley (e) Rice

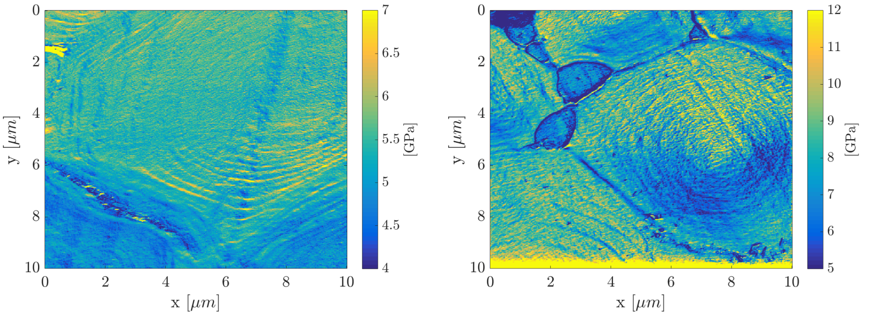

(f) Corn (g) Sorghum

Figure 4.24. – (a-g) Contact modulus maps of cut grain sections in cereals.

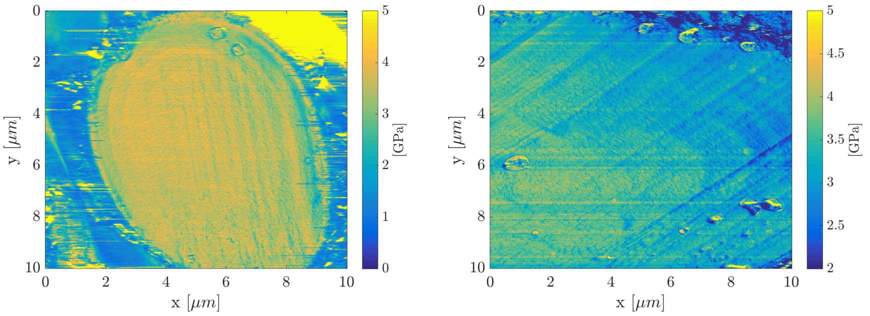

(a) Chickpea (b) Lentil

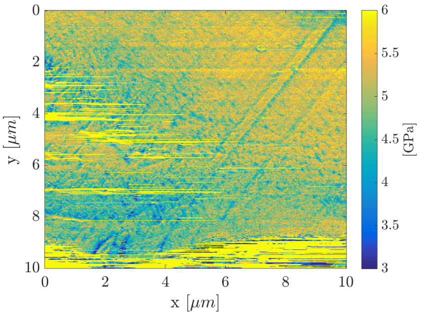

(c) Pea

Figure 4.25. – (a-c) Contact modulus maps of cut grain sections in legumes.

4.5. Conclusion

This chapter was concerned with the application of AFM to investigate the structure and mechanical properties of starch granules. Taking into account the limitations of the AFM method, the results reported in the existing literature were discussed critically. It was pointed out that tip dilation effects are very relevant for the measurement of blocklet size and for the qualitative or quantitative determination of mechanical properties.

Larger scale effects, such as micrometer-range surface slopes, can also cause significant artefacts during AFM measurements, which was demonstrated for CR-AFM nano-mechanical measurements. A correction procedure based on the cantilever vibration mechanics was developed. Some first results from the application of CR-AFM in combination with the correction assay on cut starch granules from different botanical origin revealed no large differences in the measured contact modulus, even between starches with very different compositions, with the exception of sorghum starch. These results should be confirmed by additional experiments with sufficient measurements in different location on the cut grain sections as well as different grains.

Despite the limitations of the CR-AFM method and the awaiting confirmation of results, this method has great potential for the study of starch granule properties.

5. Modelling endosperm as a cemented granular material

Contents

Ceres is the Roman goddess of agriculture. "Cerealis" carries the meaning of "devoted to Ceres" or is referring to the cultivation of land or grain. During the seven days-long festival "Cerealia", ripe ears of wheat were offered to Ceres. The term Ceres became a metonym for grain, corn, fruit, bread and food.

5.1. Introduction into numerical simulations on biological materials and wheat

The starchy endosperm can be considered as a cemented granular material (see Figure 2.3 on page 10). It consists of a multi-modal distribution [45, 166] of harder starch granules that are embedded in a softer protein matrix [135]. The milling behaviour of wheat is to a great part determined by the starchy endosperm's mechanical properties. These properties are the result of the interplay different factors, which can be determined both by genetics and environmental conditions during grain development. The main genetic component, the allelic state of proteins called puroindolines, is directly linked to whole grain hardness. These proteins are hypothesised to cause differences in the starch-protein adhesion strength [13, 135]. The environmental conditions impact, amongst others, the porosity of the protein matrix, commonly measured as endosperm vitreosity [112].
The effects of adhesion, porosity and mechanical properties have been studied by experimental [131, 155] and numerical approaches [180, 183]. Other possible sources for differences in milling behavior, such as the starch granule size distribution (SGSD), are less well studied and understood. Experimental studies on the connection of SGSD and endosperm hardness are not numerous and not convergent [146, 273], and studies on the milling performance as a function of SGSD are also contradicting [166, 167]. Given the contradicting experimental findings, the application of numerical modelling can aid to better understand the influence of SGSD separately and in combination with other factors on the fragmentation behavior of wheat. Such insights would give important information for the directed breeding of wheat towards improved milling properties. Additionally, the study of particle size distribution (PSD) and its impact on the mechanical properties is also of interest for other granular materials, such as the study of sands [274, 275], cement [276, 277], or polymer composites [278, 279].

The mechanical response of a cemented granular material is the result of an interplay of several factors. These can be separated into factors of geometrical and mechanical origin (Figure 5.1). The basic geometrical or structural properties are the volume fractions of the granular phase (particles) and the cementing phase (matrix). The matrix can further be porous or non-porous. The particle phase also has an extra level of structure concerning particle size, shape and packing. Similarly, the voids in the matrix are characterised by pore size and shape, and their spatial distribution. In dense granular packings the particle phase is dominating the arrangement (distribution of matrix around particles, rather than distributing particles in a matrix) and the three phases (particles, matrix, voids) are not independent of each other. For example the granular packing affects the maximally possible amount of matrix (demonstrated in section 5.2) and the maximally possible pore size and the pore location.
The mechanical properties affecting the mechanics of a cemented granular material are the elasticity and strength of the particle and matrix phase and, additionally, of the particle-matrix interface (Figure 5.1). A small number of studies used numerical simulations to investigate the interplay of these factors and their effect on the mechanical properties of the cemented granular structure [180, 181, 182, 183]. Among the investigated parameters were the effect of changing particle volume fraction [183], matrix volume fraction [180, 181, 182, 183] and particle-interface strength [180, 181, 182, 183].
Motivated by the unclear influence of SGSD on the milling behaviour of wheat, we continue this line of study to investigate the effect of the particle size distribution on the structure (particle volume fraction, matrix volume fraction and pore size and distribution) and consequently on the mechanical behaviour (section 5.2). In this first series of simulations, the granules are assumed to be spherical and to optimise calculation times and due to the complexity of the algorithms, simulations are

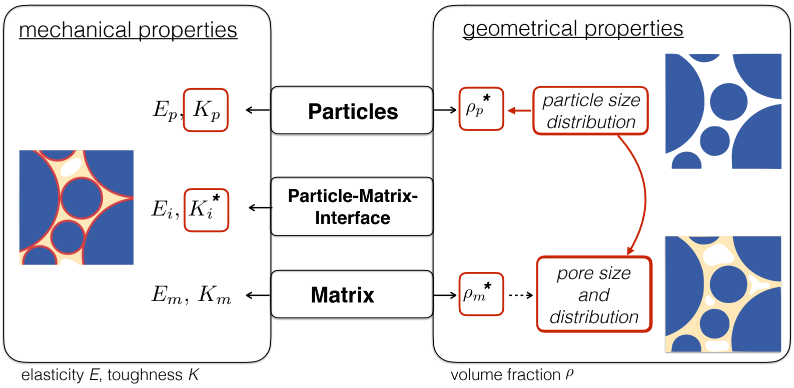

Figure 5.1. – Summary of the mechanical and structural properties affecting the mechanical behaviour of a cemented granular material. Properties marked with * were investigated by other authors [180, 181, 182, 183]. Red squares mark the parameters investigated in this chapter.

performed in two dimensions.
In the second part of the chapter (section 5.3) the influence of two mechanical parameters on the fracture path and therefore the particle damage is investigated in an attempt to determine the factors that influence starch damage during wheat fractionation.

5.2. The effect of particle size distribution and porosity on the tensile properties of cemented granular materials

Abstract

The mechanical properties of a cemented granular material are expected to be influenced by the particle size distribution, because it influences the packing of the granules and consequently the distribution of the cementing matrix and the voids therein. To gain a comprehensive understanding of the effects of the granular packing on the mechanical behaviour a parametric study of particle size ratio and volumetric fraction of small particle is performed. Both parameters are shown to influence the packing density, the number of contact points per particle and the size of pores within the matrix. Furthermore, these factors directly or indirectly influence the distribution of stresses within the composite and ultimately the Young's modulus and yield stress. We analyse in detail the relations between particle size distribution, geometrical sample structure and mechanical behaviour and compare the numerical results to the theoretical prediction from the Mori-Tanaka model.

Table 5.1. – Nomenclature used in this section

α		perimeter coverage factor
γ	$= r_L/r_S$	radius ratio
γ^*	$= r_L^*/r_S^*$	effective radius ratio
ϵ		strain
μ		friction coefficient (DEM)
ν	≈ 0.3	Poisson coefficient
θ	$= \rho_L/\rho_S$	area ratio
θ^*	$= \rho_L^*/\rho_S^*$	effective area ratio
ρ		volume fraction
ρ_L		volume fraction large discs
ρ_L^*		effective volume fraction large discs
ρ_m		volume fraction matrix
ρ_m^*		effective volume fraction matrix
ρ_p	$= \rho_L + \rho_S$	particle solid fraction
ρ_p^*	$= \rho_L^* + \rho_S^*$	effective particle solid fraction
ρ_S		volume fraction small discs
ρ_S^*		effective volume fraction small discs
ρ_v		volume fraction voids
ρ_v^*		effective volume fraction voids
σ		stress
σ^y		yield stress
ζ		bridge width factor
B		bulk modulus
d		coefficient
E		Young's modulus
G		shear modulus
K		toughness
k_n		particle stiffness (DEM)
l_{xy}		size sample in x- and y-direction
L_{nn}	$= l_{xy}/N_p$	node to node distance
n_L		number large discs
n_S		number small discs
N_p	=1024	number of mesh points per line
P		confining pressure (DEM)
r		radius
r_{equ}	$= r_L + r_S$	perimeter radius
r_L		radius large discs
r_L^*		effective radius large discs
r_S		radius small discs
r_S^*		radius small discs
S_m	$= \rho_m/(1-\rho_p)$	matrix saturation
S_m^*	$= \rho_m^*/(1-\rho_p^*)$	effective matrix saturation
w	$= \zeta \cdot r$	bridge width
Z		coordination number

5.2.1. Introduction

The mechanical properties of a cemented granular material are expected to be influenced by the particle size distribution (PSD), because it influences the packing of the granules and consequently the distribution of the cementing matrix and the voids therein. So far only a small number of studies was concerned with a systematic investigation of the mechanical properties of dense granular material in relation to the PSD. The mechanical behaviour of cement (cemented granular material) [276], non-cohesive sands [275], cohesive polymer-glass bead mixtures [279] and assemblies of frictional steel beads [280] were studied experimentally, whereas non-cohesive 2D [281] and frictional 3D [280] particle assemblies were investigated numerically. To our knowledge no extensive parametric numerical study of the effect of PSD on the mechanical behaviour of a cemented granular material exists.
The mechanical behaviour of a granular material is the result of its granular structure and an understanding of the mechanical properties has to originate from the understanding of the underlying structure. Several parameters were investigated for their effect on the tensile behaviour and on the fracture pathways: the PSD, the porosity of the matrix, and granule-matrix interface toughness. The results are presented in two parts: first an evaluation of the changes in granular structure related to PSD is given (subsection 5.2.3) and second, the mechanical behaviour is analysed (subsection 5.2.4 and following).

5.2.2. Numerical method

Bond-based peridynamics

The peridynamic approach uses integral equations instead of partial differential equations, which makes it interesting for mechanistic simulations involving cracks and fracture [282]. It assumes that particles within a continuum interact with their neighbours within a neighbourhood of limited size. The spherical neighbourhood is defined by the radius δ, the so-called horizon (Figure 5.2). A point at time $t = 0$ is located at $\mathbf{x}$ and at $\mathbf{x} + \mathbf{u}$ at time t. The equation of motion for a point $\mathbf{x}$ within the body is [282]:

$$o\ddot{\mathbf{u}}(\mathbf{x}, t) = \int_{\mathcal{H}_x} \mathbf{f}(\mathbf{u}(\mathbf{x}', t) - \mathbf{u}(\mathbf{x}, t), \mathbf{x} - \mathbf{x}')dV_{x'} + \mathbf{b}(\mathbf{x}, t) \tag{5.1}$$

with the mass density o, the neighbourhood $\mathcal{H}_x$ around $\mathbf{x}$, the displacement field $\mathbf{u}$ and the body force $\mathbf{b}$. $\mathbf{f}$ is a pairwise force function with the value of the force that $\mathbf{x}'$ exerts on $\mathbf{x}$ [282]. It depends on the distance $\xi = \mathbf{x} - \mathbf{x}'$ and the relative displacement with time $\eta = \mathbf{u}(\mathbf{x}', t) - \mathbf{u}(\mathbf{x}, t)$, because the deformed bond state is the sum of both: $\xi + \eta$ [283]. The interaction between point $\mathbf{x}$ and $\mathbf{x}'$ is called a bond [282]. Assuming a micro-elastic material, bonds can be thought of as springs [282]. For heterogeneous media with different phases λ the force function $\mathbf{f}$ depends on both points that form the bond [283]:

$$\mathbf{f}(\xi, \eta, \mathbf{x}) = \begin{cases} c_{\lambda(x)\lambda(x')}\ s(\xi, \eta) & \|\xi\| \leq \delta \\ 0 & \|\xi\| > \delta \end{cases} \tag{5.2}$$

with the elastic micro-modulus c and the bond elongation s. Bond elongation is defined as:

$$s(\xi, \eta) = \frac{\|\xi + \eta\| - \|\xi\|}{\|\eta\|} \tag{5.3}$$

Failure is introduced by breakage of the bonds, when they are stretched more than the critical bond elongation s_0 [282].
Micro-modulus c, Young's modulus E, critical bond elongation s_0 and fracture energy G in 2D can be related via [284]:

$$c_{\lambda(x)\lambda(x')} = \frac{6E}{\pi\delta^3(1-\nu)} \tag{5.4}$$

$$s_0 = \sqrt{\frac{4\pi G}{9E\delta}} \tag{5.5}$$

with the Poisson's ratio $\nu = 1/3$ [283].

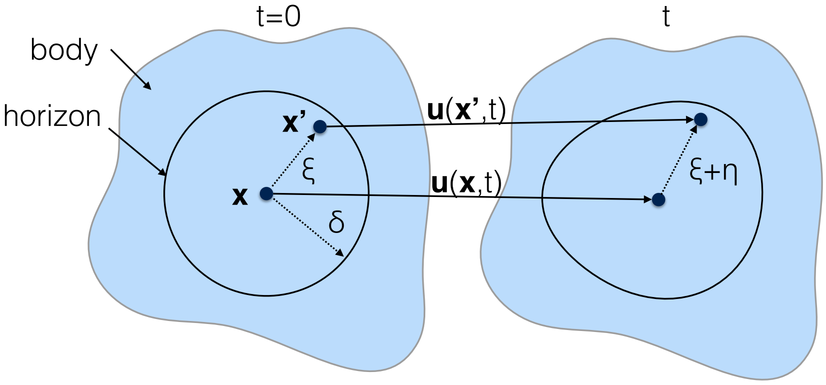

Figure 5.2. – A point $\mathbf{x}$ at any time t is subjected to interaction forces with all points $\mathbf{x}'$ within the horizon δ. Adapted from [283].

For numerical simulations, bodies are discretised on a two-dimensional rectilinear grid with the points $\mathbf{x_i}$ having the mass $m_i = (\delta x)^2 o(\mathbf{x_i})$ [283]. The horizon was chosen to be 3, because this is a good compromise between computation time and resolution [283]. This horizon leads to a total of 28 bonds per node (Figure 5.3). The evolution of the system with time is computed with the velocity-Verlet algorithm [285].

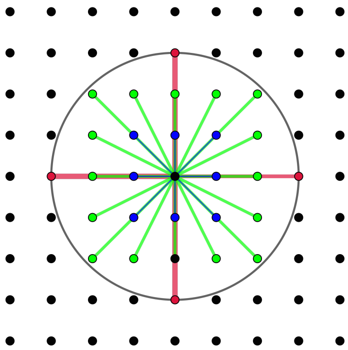

Figure 5.3. – A horizon of 3 on a orthonormal grid results a total of 28 bonds per node. All bonds for the central node are illustrated. Colours only serve for better visualisation.

Meshing effect An unavoidable effect when using the discretised peridynamics method with a horizon of $\delta > 0$, is a "blurring" of the edges of phases (Figure 5.4). As a result of the different types of bonds connected to a node at the border between two phases, these nodes are acting not fully as nodes of their respective phase. This effect is especially pronounced on smaller particles.

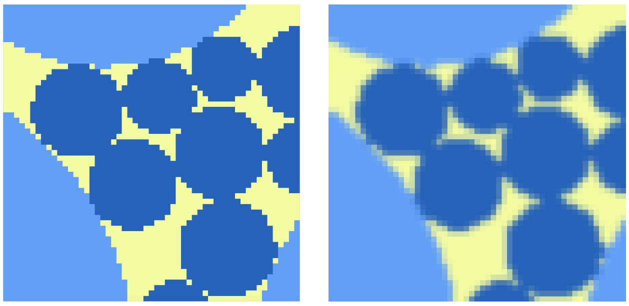

(a) No blur for $\delta = 0$: 0 bonds per node

(b) Blur for $\delta = 1$: 4 bonds per node

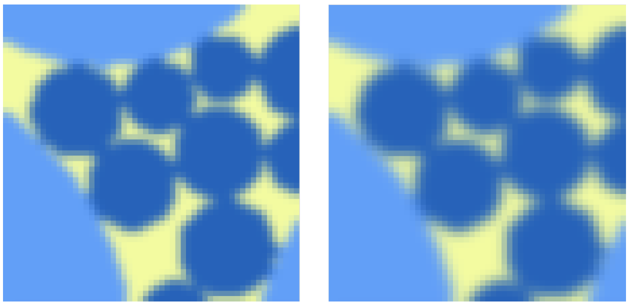

(c) Blur for $\delta = 2$:13 bonds per node

(d) Blur for $\delta = 3$: 28 bonds per node

Figure 5.4. – A zoom into a discretised sample shows (a) the discretisation of the round discs due to the rectangular meshing and (b-d) the blurring that occurs with increasing horizon radius δ. Blue and yellow colour represent different phases and therefore different mechanical properties of the nodes of particle and matrix. One pixel represents one node. The integration of the bonds with all nodes within the horizon then "blurs" the properties leading to less defined borders between mechanical phases.

Damage zone Damage in peridynamics manifests as a zone of a finite width (Figure 5.5 on page 93), in which a certain percentage of the bonds of the nodes are broken. The maximum damage that can be obtained by a node is 28, if the horizon is 3.

Sample construction

Two-dimensional, square sample volumes were used as volume elements. Samples consisted of three bulk phases with the volume fractions ρ_{phase}: particles in the shape of round discs (ρ_p), a matrix (ρ_m), and a void phase (ρ_v), so that $\rho_p + \rho_m + \rho_v = 1$. The discs were chosen to be of a bi-modal size distribution with larger discs (ρ_L) and smaller discs (ρ_S), so that $\rho_p = \rho_L + \rho_S$.

Variation of particle size distribution One parameters defining the PSD is the ratio between the radii of larger and smaller discs:.

$$\gamma = r_L/r_S \tag{5.6}$$

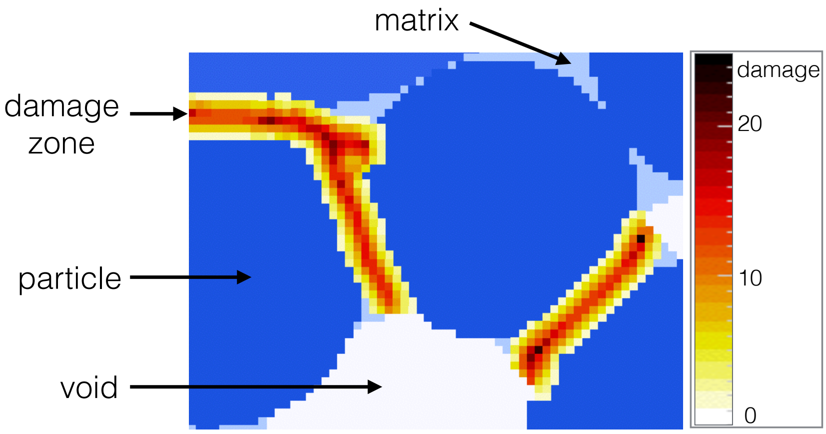

Figure 5.5. – A zoom into a damaged sample is shown. The phases (particle, matrix, voids) are overlaid with the damage. One pixel represents one node. The damage value gives the number of broken bonds per node (minimum 0, maximum 28).

with r_L and r_S being the radius of the larger and smaller discs, respectively.

In order to change the PSD in a controlled way, r_L was kept constant, while r_S was varied from $r_S^{min} = 0.2r_L$ to $r_S^{max} = r_L$ in steps of $0.1r_L$. The resulting nine investigated ratios γ were [5.00, 3.33, 2.50, 2.00, 1.67, 1.43, 1.25, 1.11, 1.00]. The higher the value of γ, the larger is the difference between r_L and r_S.

Another parameter defining the PSD is given by the volume fractions of large discs ρ_L and small discs ρ_S, which is related to the number of discs for both sizes respectively. The important value is the ratio of both volume fractions:

$$\theta = \frac{\rho_L}{\rho_S} = \sum_{n_L} \pi r_L^2 \Bigg/ \sum_{n_S} \pi r_S^2 \tag{5.7}$$

$n_{L,S}$ being the respective total number of discs per type.

From a simplified, two-dimensional point of view, θ represents the amount of "coverage" of a large particle by small particles (Figure 5.6). The number of small discs n_S of radius r_S in the perimeter around the large disc at the radius $r_{equ} = r_L + r_S$ can be estimated by assuming a "coverage" of α (Figure 5.7):

$$n_S = \alpha \cdot \frac{2\pi\, r_{equ}}{2r_S} = \alpha\pi \left(1 + \frac{r_L}{r_S}\right) \tag{5.8}$$

From Equation 5.7 and Equation 5.8 it follows that

$$\theta = \frac{\pi r_L^2}{n_S \pi r_S^2} = \frac{1}{\alpha\pi} \frac{r_L^2}{(r_L r_S + r_S^2)} \tag{5.9}$$

Several values for α were investigated: [1.00, 0.83, 0.65, 0.50, 0.25] (examples in Figure 5.6) from theoretically full ($\alpha = 1.00$) to low ($\alpha = 0.25$) coverage. For $\alpha = [1.00, 0.83, 0.65, 0.50, 0.25]$ it follows that $\theta = [1.32, 1.59, 1.65, 2.65, 5.31]$, given that $\gamma = 5.00$.

The schematic assumption of coverage of the large granule is only a mean to define θ. To keep samples comparable to each, the above values of θ were used for all values of γ. For every combination of γ (9 values) and θ (5 values) 5 samples were created independently.

Numercial sample construction consisted of five consecutive steps: disc packing, sample densifying, matrix filling, cropping and meshing.

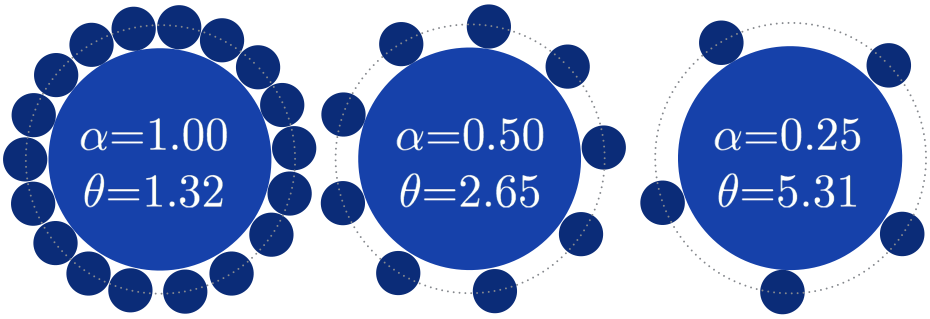

Figure 5.6. – Schematic representation of different coverage of a large particle by a number of small particles for $\gamma = 5.00$, where α denotes the amount of coverage. θ is calculated by Equation 5.9.

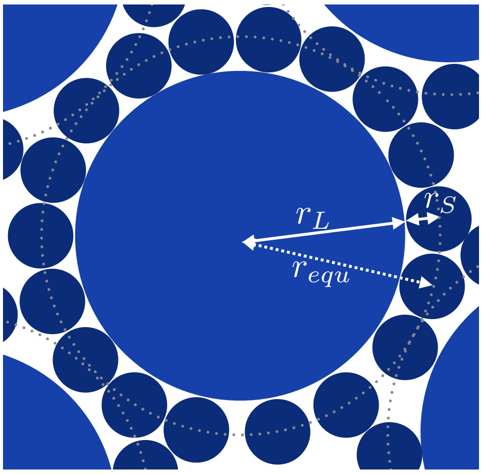

Figure 5.7. – The schematic of a large disc of radius r_L surrounded by small discs of radius r_S at the radius $r_{equ} = r_L + r_S$ is shown.

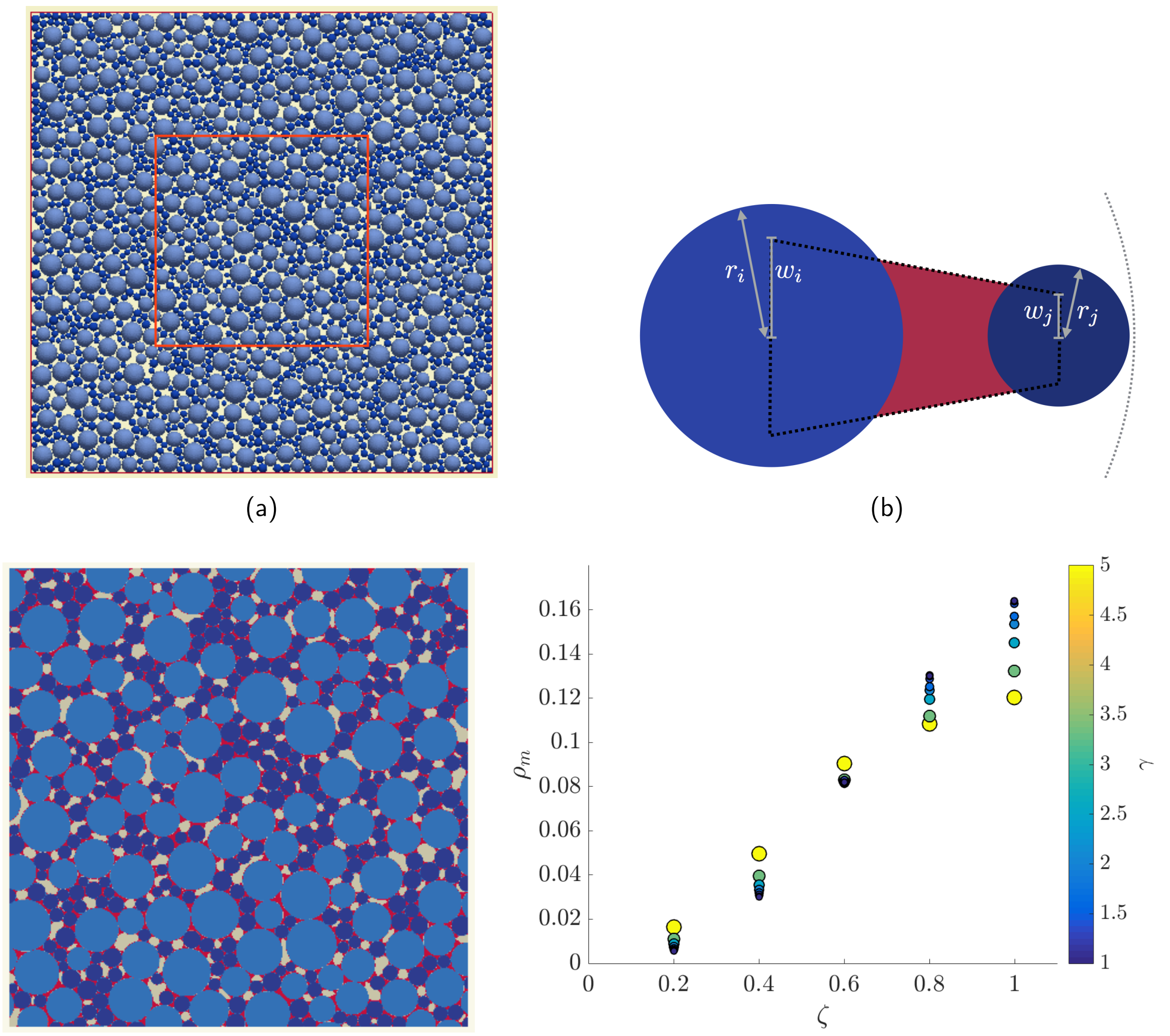

(a)

(b)

(c)

(d)

Figure 5.8. – Sample preparation steps are shown: (a) The sample box after Fast Poisson disc sampling and densifying. The central red square marks the area of the crop. (b) The matrix filling for porous samples is calculated by establishing bridges between neighbouring two particles of radius with bridge width $w_{ij} = \zeta \cdot r_{ij}$ depending on the width factor ζ and particle radius of both particles in the pair, r_i and r_j respectively. The matrix filling is shown in magenta. (c) The cropped sample after matrix filling and meshing. The matrix is shown in magenta, particles in blue and pores in grey. (d) The increase of matrix volume fraction ρ_m with the increase of the bridge width factor ζ is shown. For different γ the same factor ζ results in different ρ_m.

Disc packing Round discs were packed in square boxes. In order to represent the variability typical for a biological system and to avoid local crystallisation, the disc sizes followed a normal distribution for each disc type respectively. Large discs followed a normal distribution around the mean radius $r_L = 5$ (a.u.) with the standard deviation $\sigma_{r_L} = 0.25 r_L$, and small discs followed a normal distribution around the mean radius $r_S \leq r_L$ with the standard deviation of $\sigma_{r_S} = 0.25 r_S$. The ratio of the mean radii $\gamma = r_L / r_S$ was varied as is described above. Due to the finite resolution of the mesh applied to the sample for the peridynamic method (section 5.2.2), a cutoff of sizes $c_L^{+,-} = r_L \pm 1.5\sigma_L$ and $c_S^{+,-} = r_S \pm 1.5\sigma_S$ had to be applied to avoid the occurrence of very small discs, which could not be meshed sufficiently, or very large discs. Consequently, the smallest allowed disc would still be meshed by about 10 nodes along its diameter.
Disc packing was performed in two consecutive steps. First, a square box of the area $A_{box} = 900\pi {r_L}^2$ and length $L = \sqrt[2]{A_{box}}$ was filled with large discs using a fast Poisson disc sampling (FPDS) method [286]. The first disc with a random radius within the normal distribution around r_L was placed at a random position within this box. Then, a high number of preliminary large discs were randomly placed in the periphery of the first disc. All preliminary discs were tested consecutively for overlap with all existing discs. If no such overlap existed and a minimum distance d_{min} between discs was maintained, the preliminary disc was permanently placed into the sample volume. Then, one disc from the sample box was randomly selected and the steps of creating preliminary large discs, validating the no-overlap and minimum distance conditions and adding the new discs to the sample volume, were repeated. If, after a finite number of iterations, no more large discs could be permanently placed, the sample box was regarded as being filled to the maximum with large discs. In the second step, small discs with a random radius within the normal distribution around radius r_S were placed into the free spaces remaining in-between the large discs. The same FPDS approach as for the large discs was used, only that no minimum distance between discs was required, which therefore enabled a dense packing of small discs into the interspaces.
To guarantee homogeneous packing and achievement of the specific value of the area ratio θ for each radius ratio γ, a sufficient number of small discs needed to fit in the spaces between the large discs. Therefore, the minimum distance d_{min} between large discs had to be increased for a decrease in γ. Iterations of a step-wise increase of d_{min} were implied in the disc packing computations, until the required area ratio θ was met for every γ.

Sample densifying With a limited computation power and time, the described FPDS method was able to achieve only a medium dense packing of discs, especially with the rapidly increasing number of discs accompanying a decreasing γ. Therefore, a classical discrete element method (DEM) approach [184] was used to apply a slight, bi-axial compression to the sample volumes after disc packing (Figure 5.8a). In this DEM step, the contact law of a classical linear spring-dash pot model was used. The relation of normal stiffness of the discs k_n to the confining pressure P was $\frac{k_n}{P} \approx 10^4$. As a consequence the overlap of the stiff discs during the compression was smaller than the size of the applied mesh [287]. Coulombs law of friction was applied with a sliding friction coefficient of $\mu = 0.3$. The confining pressure was set to achieve dense packing and the number of time steps was chosen sufficiently high to result in a mechanical equilibrium.

Matrix filling and voids Several variations of matrix filling were investigated. For $\rho_v = 0$ all free spaces that were not occupied by discs, were considered to be filled with matrix. This case is referred to as "full". For all combinations of γ and θ five full samples were tested. For $\theta = 1.59$ and $\gamma = 1.00 ... 5.00$ sample volumes containing void spaces were created ($\rho_v > 0$). The matrix filling was computed following the procedure described by Topin et al. [180]. For each discs trapezoidal bridges were established to all neighbouring discs within a certain distance. Bridge width $w_{ij} = \zeta \cdot r_{ij}$

depended on the width factor ζ and the radius of each disc, respectively (schematic in Figure 5.8b). Through variation of between $\zeta = [0.2 \; ... \; 1]$ bridges are wider or thinner and therefore more or less matrix is present in the sample (Figure 5.8d). The resulting void fractions varied between $\rho_v = 0 \; ... \; 0.2$ (Figure 5.8d).

Sample cropping and meshing A square box of the length $l_{x,y} = 24 r_L = 0.12$ was cropped out of the centre of the sample box to avoid boundary effects during the simulations. The cropped, matrix-filled sample volumes were meshed onto a rectilinear grid of 1024 × 1024 nodes[1]. A certain discretisation of the round discs is unavoidable (Figure 5.4a on page 92). The volume fractions were therefore calculated after meshing by summing the number of nodes of each phase: $\rho_{phase} = n^{nodes}_{phase} / n^{nodes}_{total}$. The area ratio $\theta = \rho_L / \rho_S$ was also re-calculated exactly for each sample volume after meshing. The exact values varied slightly compared to the attempted values of θ due to effects of cropping and meshing.

Pore size and number Pore area after meshing was determined using a floodfill routine [288]. This image processing algorithm allows to determine the number of pores and the area of each pore by counting the number of nodes within each pore. The floodfill routines colours void spaces one after another by evaluating for every void node, if neighbouring nodes are of the type "void" or not. Neighbouring void nodes are assigned the same colour (Figure 5.9) . Voids connected to the image border were not taken into account.

Mechanical properties of the phases

Nodes were connected via brittle linear springs within a horizon of three nodes in each direction. Discs were considered as distinct elements, whereas the matrix was considered as a single element. The bonds were classified to three cases: (I) connecting two nodes of the same material within the same element (node in $disc^X$ to node in $disc^X$, all nodes within matrix to each other), (IIa) connecting two nodes of the same material in different elements (node in $disc^X$ to node in $disc^Y$) or (IIb) connecting nodes of different material phases (node in matrix to node in disc). Whereas bonds of case (I) belong to either the particle of matrix phase, all bonds of case (IIa) and (IIb) represent interfaces. No bare contacts were allowed between discs, because due to (IIa) an interface layer was present around all discs.
Bonds were characterised by an elastic modulus E_p, E_m, E_{pm} and toughness K_p, K_m, K_{pm} (particle, matrix, interface). The values of E and K depend on the type of the bond.
A correction of the volume fractions was done to account for the reduction of the mechanically effective volume fractions due to the meshing effect (Figure 5.4 on page 92). The radius r of a particle is reduced by the length of one node-to-node distance L_{nn}. In the case of a horizon of 3, a meshing resolution of 1024 × 1024 and a sample size of $l_{xy} = 12$ (a.u.) the node-to-node distance is:

$$L_{nn} = l_{xy} / N_p = 12/1024 \tag{5.10}$$

The effective radius (radius reduced by one node-to-node distance) is then:

$$r^*_L = r_L - L_{nn} \tag{5.11}$$
$$r^*_S = r_S - L_{nn} \tag{5.12}$$

---

[1] A mesh of 1024 × 1024 nodes with 28 links per node leads to a total of ≈30 000 000 links. One simulation of this size takes ≈12 h on 16 processors in parallel computing.

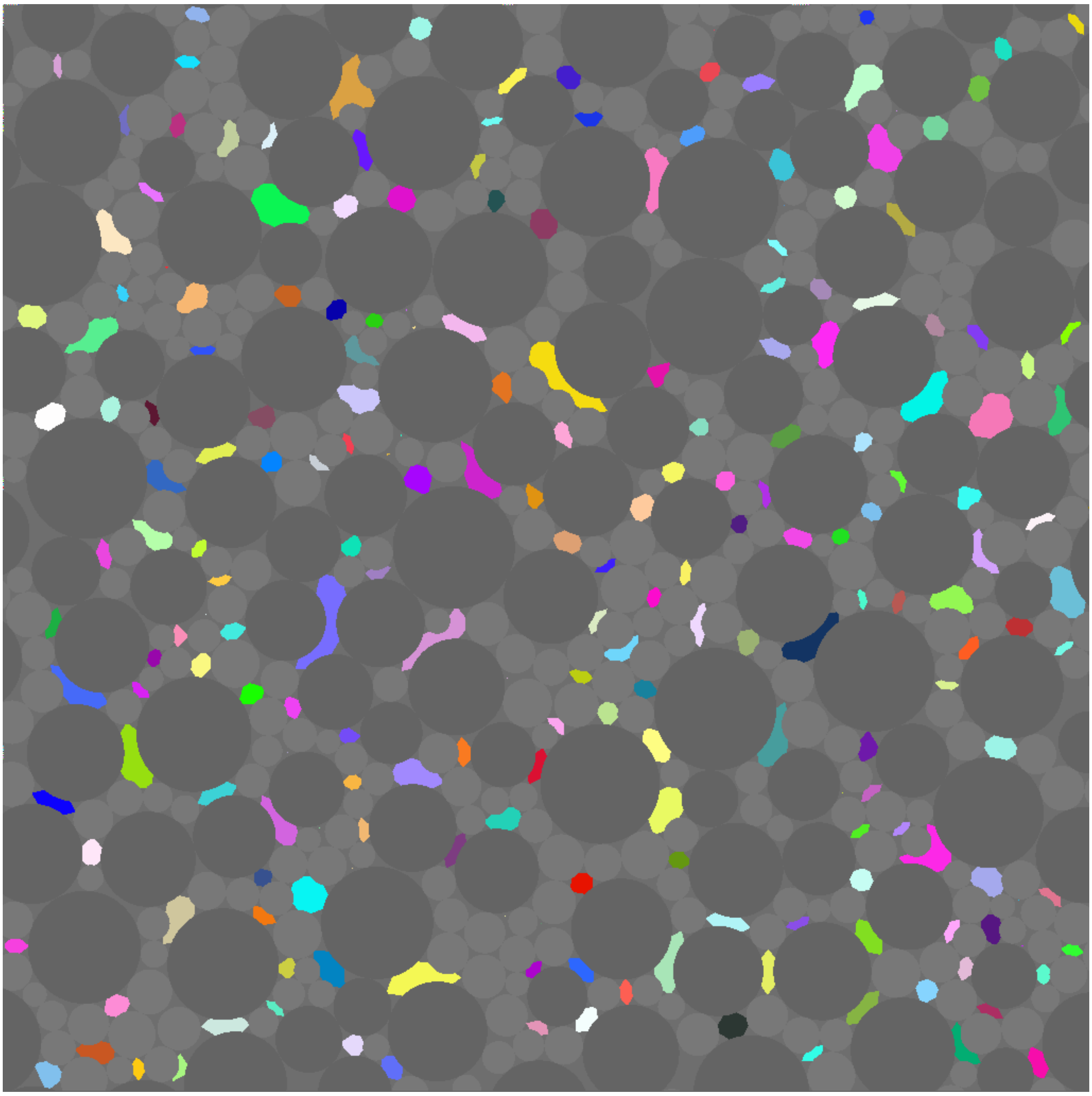

Figure 5.9. – Void spaces were coloured individually with a floodfill algorithm, which allows the evaluation of pore size and number. Particles and matrix are coloured in grey. Void spaces connected to the borders are not taken into account and also coloured grey.

Samples with the corrected radii were meshed once more and the effective volume fractions ρ_p^*, ρ_m^*, ρ_v^*, ρ_L^* and ρ_S^* were calculated after the meshing. The effective area ratio θ^* was calculated from:

$$\theta^* = \frac{\rho_L^*}{\rho_S^*} \tag{5.13}$$

The radius ratio was corrected to γ^*:

$$\gamma^* = \frac{r_L^*}{r_S^*} = [5.53, 3.53, 2.59, 2.05, 1.69, 1.44, 1.26, 1.11, 1.00] \tag{5.14}$$

Parameter choice For toughness and elasticity parameters, the ratio between particle and matrix phase is relevant in the simulations, but not the absolute values. All discs were assumed to have the same elastic and toughness properties, regardless of their size. The parameters were chosen to be similar to the values reported in [183], taking into account nano-mechanical measurements of starch and protein inside wheat endosperm by atomic force microscopy [173]. The hardness of starch and gluten reported in [173] were 2.4 GPa and 0.6 GPa, respectively, giving a ratio of ≈ 3.5. The measured hardness can be interpreted as an indicator for the toughness K. The contact modulus measurements described in section 4.3 can be seen as an indicator of the elasticity. Though experimental values for the elasticity of the protein matrix are scarce, a preliminary modulus ratio of ≈ 4 between starch and protein could be extracted from the contact resonance atomic force microscopy (CR-AFM) measurements. This value is not yet fully verified, but it is the most relevant, experimental information available so far. The ratios between the different phases are summarised in Table 5.2.

For two values of θ ($\theta = 1.59$ and $\theta = 2.65$) the effect of interface toughness K_{pm} was investigated. Two different cases of interface toughness were studied: the strongest possible adhesion between disc and matrix, where matrix and interface have the same toughness ($K_m = K_{pm}$) and a low adhesion for which the toughness of the interface K_{pm} was decreased by 50% (see Table 5.2). All other simulations were performed with the strong interface properties.

Table 5.2. – The model parameters elasticity E $[Pa]$ and toughness K $[Jm^{-3}10^{-4}]$ for the three phases and different interface properties are summarised.

	Matrix	Particle	Interface
strong interface	E_m K_m	$E_p = 4E_m$ $K_p = 3.5K_m$	$E_{pm} = E_m$ $\mathbf{K_{pm} = K_m}$
weak interface			$E_{pm} = E_m$ $\mathbf{K_{pm} = 0.5K_m}$

Evaluation of the mechanical behaviour

Samples were submitted to quasi-static, uniaxial tension or compression in the y-direction. The lower boundary was fixed, the side boundaries were free. Tension and compression were achieved by displacing the uppermost line of nodes at constant displacement speed. Tests were carried out until integrity failure of the sample volume occurred, indicated by a drastic decrease in stress amplitude (Figure 5.10a). The behaviour was elastic linear with a brittle failure.

The yield stress σ_y and the strain at maximum yield stress ϵ_{σ_y} were obtained from the stress-strain curves (example in Figure 5.10a). Yield stress was normalised by the yield stress of pure matrix: $\sigma_y^{norm} = \frac{\sigma_y}{\sigma_y^{matrix}}$. The Young's modulus E was calculated from the stress-strain curves: $E = \frac{\sigma}{\epsilon}$.

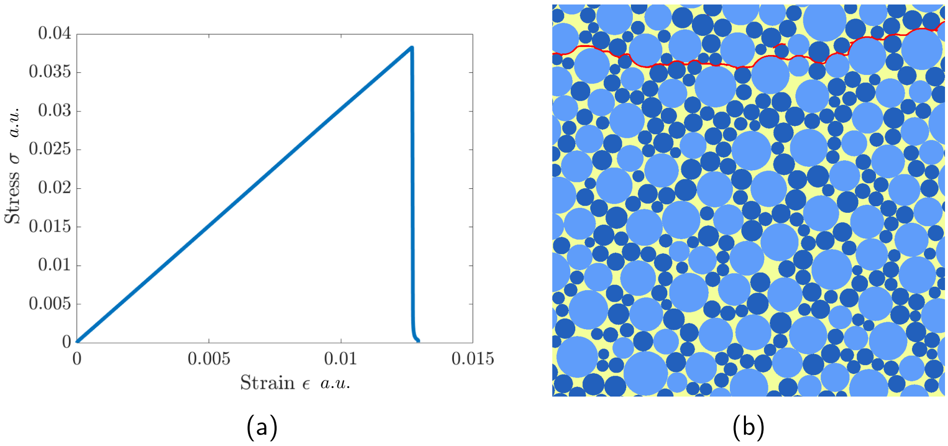

(a) (b)

Figure 5.10. – (a) An exemplary curve of tensile behaviour until failure and (b) a sample after failure in tension are shown. Nodes with broken bonds are highlighted in red.

5.2.3. Structural changes with particle size distribution

Changing γ and θ resulted in major changes of the disc packing, which affected the number of discs, their arrangement (Figure 5.11 and Figure 5.12), and the particle volume fraction ρ_p. Therefore, it also affects the matrix volume fraction of full samples directly through $\rho_m = 1 - \rho_p$ and the distribution of matrix in porous samples. Before interpreting the mechanical response of the samples, it is important to understand the structural changes linked to PSD.

Particle volume fraction

The particle volume fraction ρ_p increases almost linearly with γ, shown in Figure 5.13a on page 103. This is in accordance with other studies that investigated the packing of bi-dipserse discs experimentally [274] or numerically [289, 290, 291, 292, 281, 293, 280]. This increase was reported to be less steep for size ratio of $\gamma > 7$ [289, 281], but such high values of γ were not part of this study.

Compared to the radius ratio γ, the value of area ratio θ is of less importance for ρ_p (Figure 5.13b and Figure 5.13c), especially for $\gamma < 3$. However, it should be noticed that contrary to the influence of γ, it is not the highest θ that gives the highest particle volume fraction. For the five investigated values of θ, a clear maximum of ρ_p is reached for $\gamma = 5.00$ at $\theta = 2.65$ (Figure 5.13b). The true maximum of the curve might lie somewhere between $2.65 < \theta < 5.00$, but unfortunately with the selected values of θ no better distinction is possible.

The ratio of small to large discs, for which the densest packing is reached, has been observed experimentally [289, 274] and numerically [290, 292]. The densest packing is reached if large particles make up about 70 percent of the whole particle fraction [289, 274, 290, 292]. This corresponds to an area ratio of $\theta \approx 2.3$ in this study. At this state, large particles are packed densest and all spaces in-between the large particles are filled with small particles [274, 290]. A further increase of the volume of small particles leads to an increase of large-large particle distances and therefore reduces ρ_p by reducing the packing density of large particles (see Figure 5.12 on page 102). Efforts have been undertaken to estimate this critical packing of polydisperse discs by modelling [291]. The peak particle volume fraction was reported to increase with increasing size ratio [289, 274, 290, 292, 291], in accordance with our observations that the maximum is clearest for the highest γ.

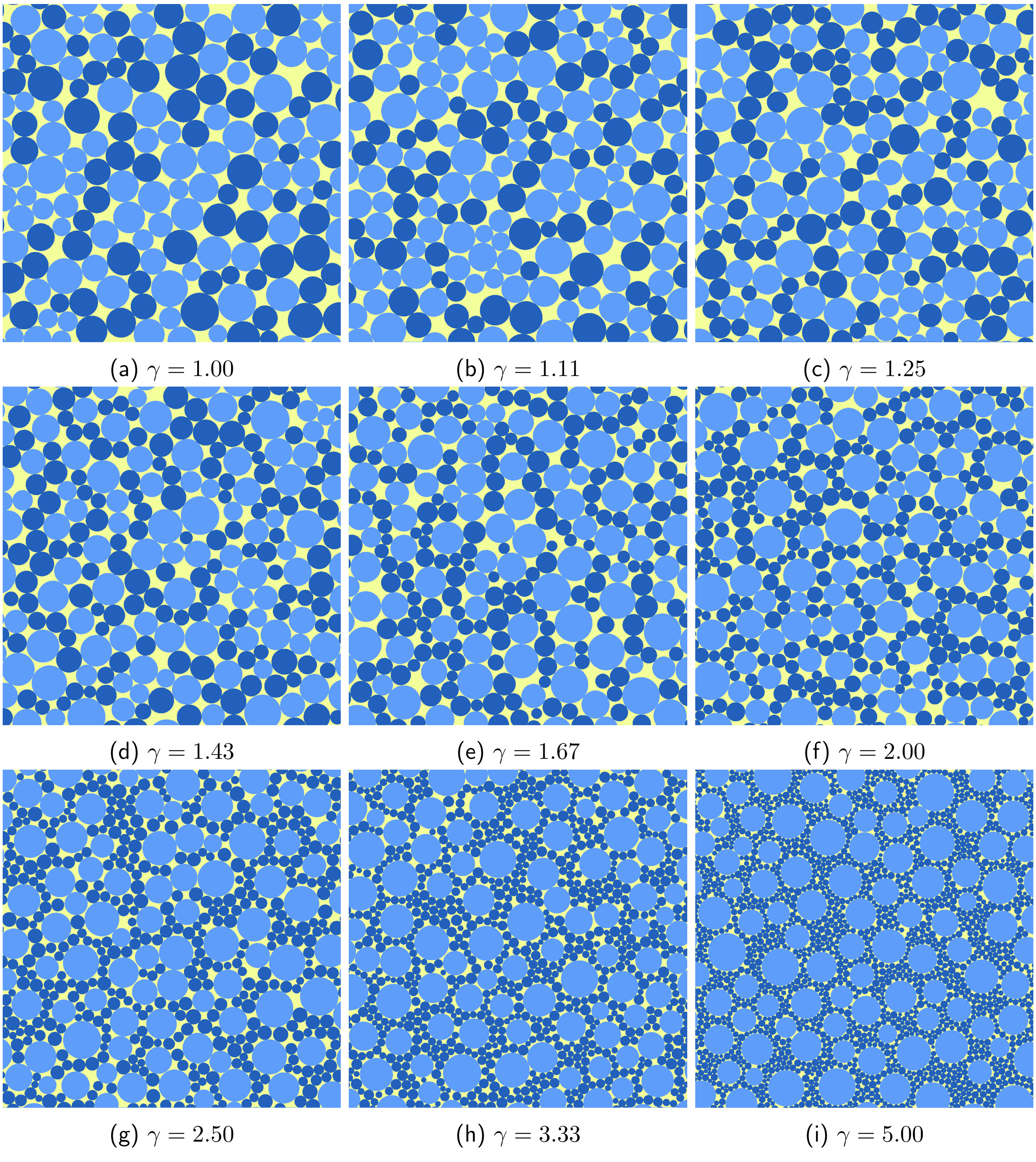

(a) $\gamma = 1.00$ (b) $\gamma = 1.11$ (c) $\gamma = 1.25$

(d) $\gamma = 1.43$ (e) $\gamma = 1.67$ (f) $\gamma = 2.00$

(g) $\gamma = 2.50$ (h) $\gamma = 3.33$ (i) $\gamma = 5.00$

Figure 5.11. – One example volume is shown for constant area ratio $\theta = 1.32$ with increasing radius ratio $\gamma = r_L/r_S$. Large particles are coloured in light blue, small particles in dark blue and matrix in yellow.

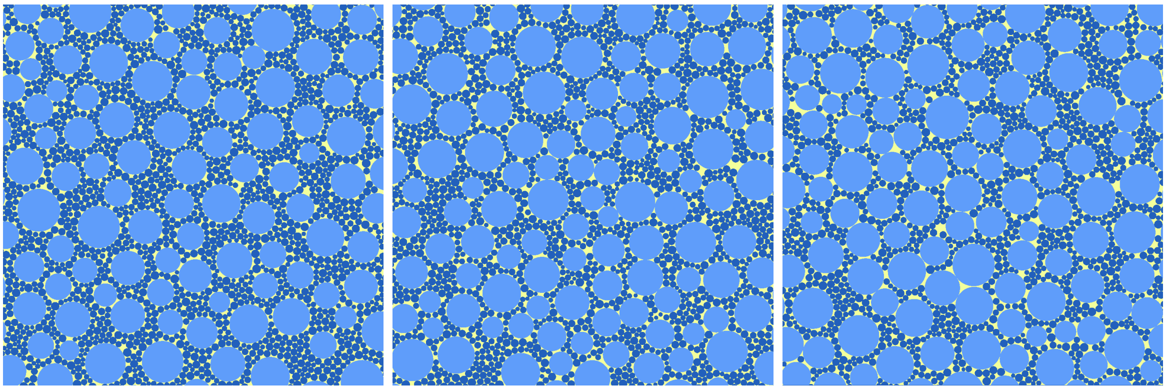

(a) $\theta \approx 1.32$ (b) $\theta \approx 1.59$ (c) $\theta \approx 2.04$

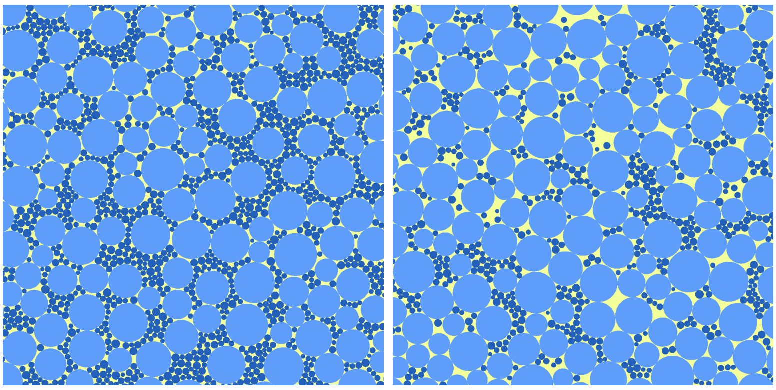

(d) $\theta \approx 2.65$ (e) $\theta \approx 5.31$

Figure 5.12. – One example volume is shown for constant radius ratio $\gamma = 5.00$ with increasing area ratio ratio $\theta = \rho_L/\rho_S$. Large particles are coloured in light blue, small particles in dark blue and matrix in yellow.

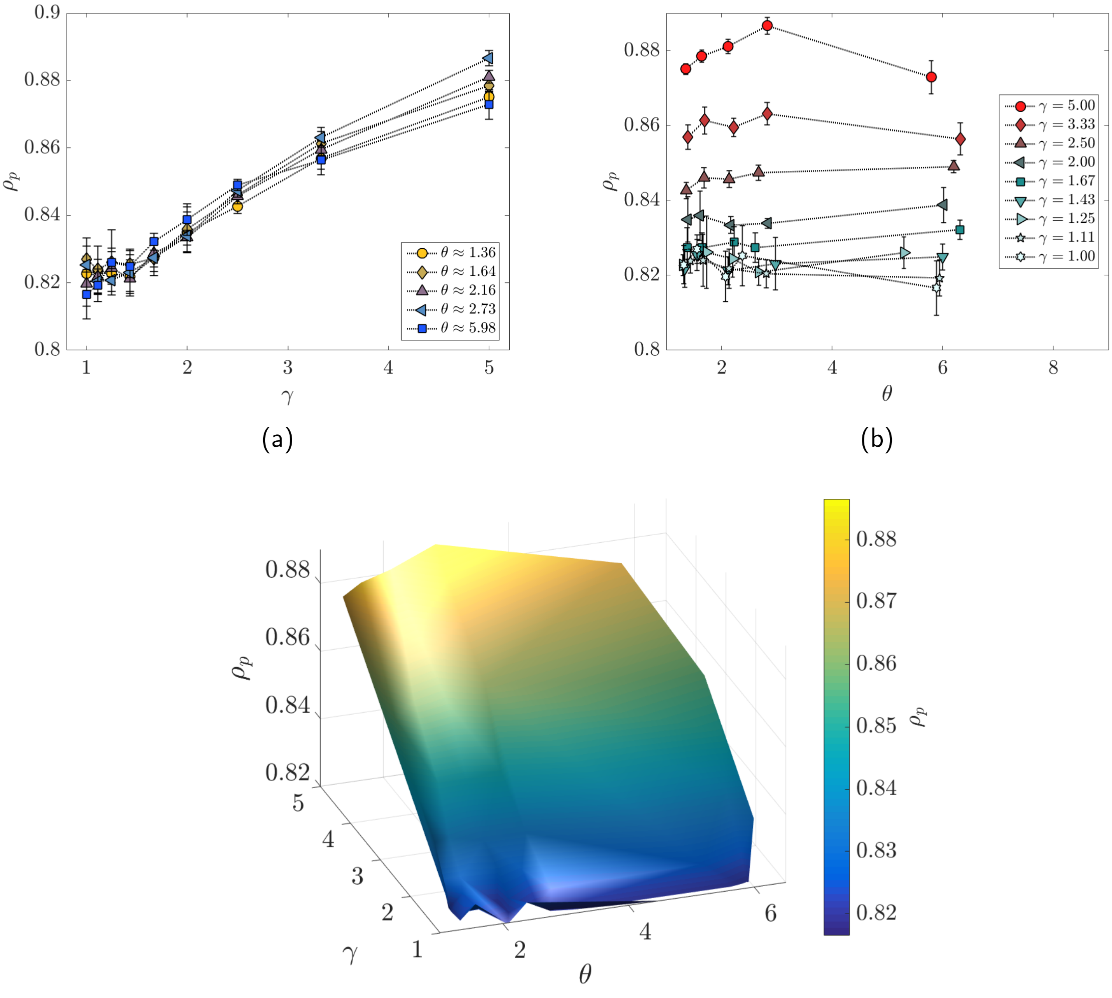

(a)

(b)

(c)

Figure 5.13. – The evolution of particle volume fraction ρ_p with the two parameters defining PSD is shown separately for (a) γ and (b) θ. Values are given as the average over 5 samples and error bars represent standard deviations. (c) shows the dependency of ρ_p on both parameters combined.

Coordination number

The coordination number gives the average number of contacts per particle with other particles and therefore important structural information of the packing. Coordination numbers were calculated assuming that two particles are in contact, when their distance is less or equal to the length of the horizon (3 nodes):

$$Z_{\lambda\lambda'} = \sum_{\lambda_i=1}^{n\lambda} \sum_{\lambda'_j=1}^{n\lambda'} z \Big/ n_\lambda \tag{5.15}$$

$$z = \begin{cases} 1 & \sqrt{(x_{\lambda_i} - x_{\lambda'_j})^2 + (y_{\lambda_i} - y_{\lambda'_j})^2} \leq 3L_{nn} \\ 0 & \sqrt{(x_{\lambda_i} - x_{\lambda'_j})^2 + (y_{\lambda_i} - y_{\lambda'_j})^2} > 3L_{nn} \\ 0 & \lambda_i = \lambda'_j \end{cases} \tag{5.16}$$

Because of the large size differences between particles, we focus on the partial coordination numbers [294] of large and small particles separately with the following denotations: Z_{ll} for large-large contacts, Z_{ls} for the small particle contacts of large particles, $Z_l = Z_{ll} + Z_{ls}$ for all contacts of large particles, Z_{sl} for the the large particle contacts of small particles, Z_{ss} for small-small contacts and $Z_s = Z_{sl} + Z_{ss}$ for all contacts of small particles.

The coordination numbers for large and small particles change significantly with the PSD. The overall Z_l increases with increasing with γ (Figure 5.14a), which is mainly due to Z_{ls} increasing with γ (Figure 5.14e). Because the number of small particles rapidly increases (qualitatively visible in Figure 5.11 on page 101) the coverage of the surface of large particles and consequently Z_{ls}, increases.

θ should be directly related to the amount of small particles surrounding a large particle for $\gamma = 5.00$. In Figure 5.14g an almost linear decrease of Z_{ls} with θ can be observed. The effect is less important for lower γ, because lower γ implies larger radii of small particles and therefore less numerous particles.

It is also possible to observe, for which values of γ and θ the large particles are completely separated from each other by small particles. This is indicated by $Z_{ll} < 1$ (Figure 5.14c). It can be observed that $Z_{ll} < 1$ for $\gamma \gtrapprox 1.75$ if $\theta \approx 1.36$, $\gamma \gtrapprox 2.00$ for $\theta \approx 1.64$ and $\gamma \gtrapprox 4.00$ for $\theta \approx 2.16$. In the same graph it is also visible that γ has almost no influence on Z_{ll} for $\theta \approx 5.98$, which shows that for these samples the volume fraction of small granules is not large enough to disturb the packing of large granules, but that small particles will simply fill the spaces between large particles (visible qualitatively in Figure 5.12e on page 102). These observed trends on the partial coordination numbers are in accordance with other studies in 2D [281] and 3D [292].

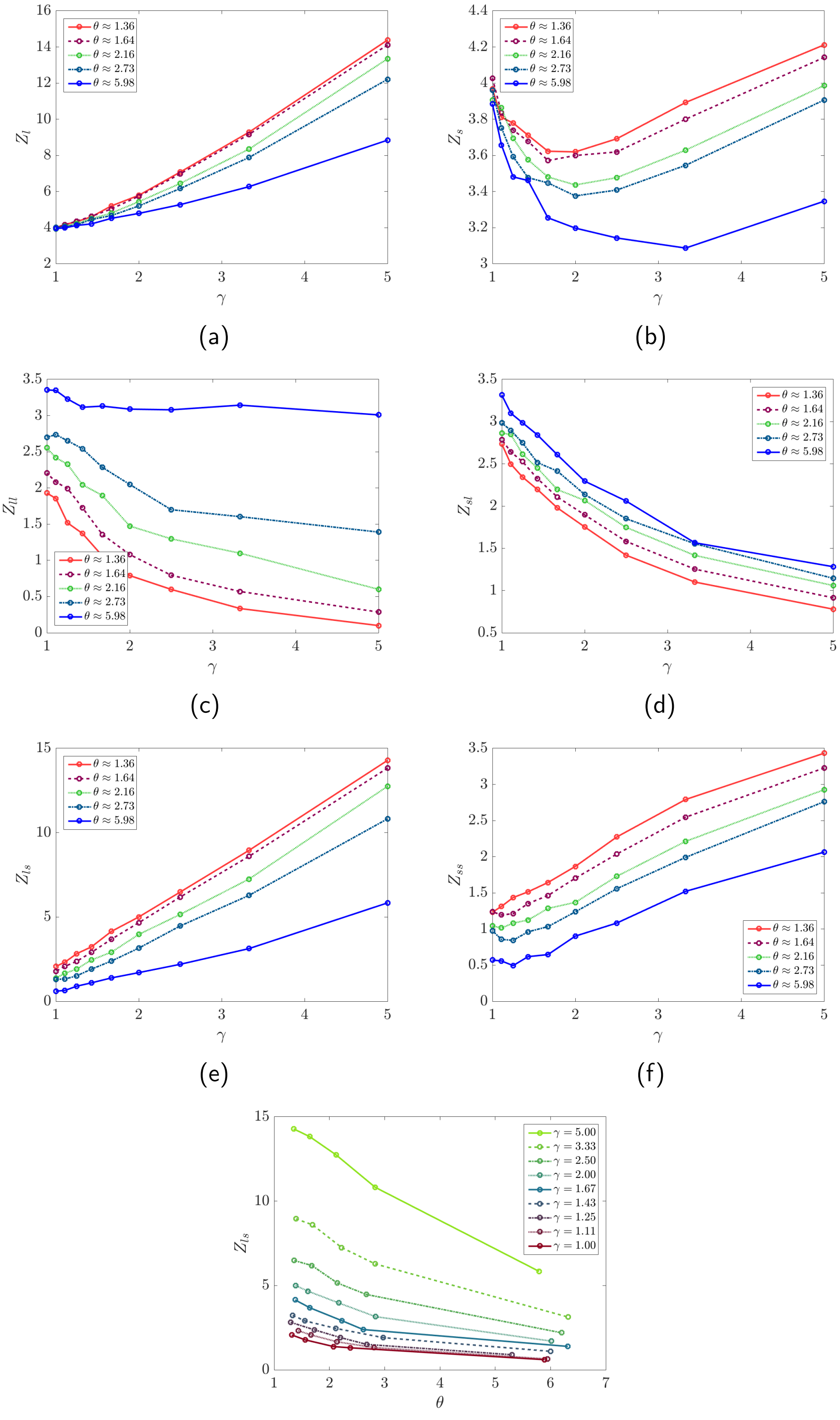

(a) (b) (c) (d) (e) (f) (g)

Figure 5.14. – Coordination numbers are given as the average over five samples. No error bars are shown for better clearness, but the standard deviations were verified to be not higher than 5 %. (a) All contacts of large particles, (b) all contacts of small particles, (c) large-large contacts, (d) small-large contacts, (e) large-small contacts, (f) small-small contacts in dependency of γ and (g) large-small contacts in dependency of θ.

Two behaviours for the small particle fraction Z_s shows a particular evolution with γ (Figure 5.14b). At first, Z_s decreases with increasing γ, but after reaching a minimum it increases almost linearly. The value of γ for which the minimum is reached is different for varying θ, being larger for larger θ. This behaviour is due a competition of two different effects in the small particle phase.

For $\gamma = 1.00$ small particles are exactly the same as large particles and $Z_s = Z_l$. As γ increases, small and large particles are not of a homogeneous size distribution anymore and, due to their lower volume fraction, small particles are "disturbing" the packing of the large particles (also reflected in decreasing Z_{ll}). Z_{ss} is however constantly increasing with γ, while Z_{sl} is decreasing, due to the increasing number of particles. After $\gamma \approx 2$, a minimum of Z_s is reached. For $\gamma > 2$ the increase of Z_{ss} is more important than the decrease of Z_{sl}, and Z_s is increasing. This indicates that the small particles now behave like a separate "phase". The "onset" of the separate phase behaviour is at $\gamma \approx 2$ with a trend to shift to slightly larger values for higher θ.

These differences of the contact network in the samples are likely to affect their mechanical properties.

Pore spaces

Porous samples were studied only for a subset of PSD. For $\theta \approx 1.36$ and $\gamma = 1.00$ ... 5.00 the series of 9 samples was studied for five different bridge sizes ζ. With the matrix-bridge-method it is not possible to exactly control the resulting ρ_m. Therefore, for inter-sample comparison the matrix saturation S_m is used:

$$S_m = \frac{\rho_m}{1 - \rho_p} \tag{5.17}$$

The matrix saturation describes the percent of non-particle space that is filled by matrix. A full sample would give $S_m = 1.00$, a sample without any matrix $S_m = 0$. An example set of sample volumes with matrix saturation between 0.75 to 0.97 ($\zeta = 0.8$) is shown in Figure 5.15. Differently from the full samples, whose structure could be described by three parameters (γ, θ and ρ_p), for porous samples the matrix saturation S_m is needed additionally. It should be noted that samples with different ρ_p and ρ_m can have the same matrix saturation.

In Figure 5.15 it is easily observable that the pores are very different for different PSD, concerning their size and spatial distribution. Some analysis of pore area and size distribution is given in Figure 5.16a[2]. The average pore size increases with decreasing γ, because the inter-grain spaces are smaller for smaller particles. For $\gamma > 3.00$ the probability density function (pdf) has one peak with an extensive "tail" towards higher pore sizes. Figure 5.16b shows that for smaller γ a second, smaller peak at higher pore area exists, which becomes more pronounced for lower γ. The most probable pore size is linked to the regions of locally very dense packing and therefore linked to the particle size and γ. However, not all sample regions are locally very densely packed, which leads to the existence of larger pores and the less polydisperse the particles are, the larger are these pores.

Pore size alone is however not supplying sufficient information. Pores act as defects in the material and next to their size it is also the homogeneity of defects, which governs the fracture behaviour of a material. An indication of the homogeneity of pore size can be taken from the excess kurtosis $kurt$ of the size distribution [295], shown in Figure 5.16c. The excess kurtosis is rather large for all samples and no clear general trend is visible, but two observations can be made: Kurtosis is lowest for the most homogeneous particle size distribution at $\gamma = 1.00$ and highest for the highest $\gamma = 5.00$. This shows that even though the pore size distribution for $\gamma = 1.00$ has two peaks, pore sizes are still more homogeneous than for $\gamma = 5.00$, where some larger pore sizes induce a

---

[2] The size distribution for the case of no matrix is shown in the appendix in Figure A.1 on page 179.

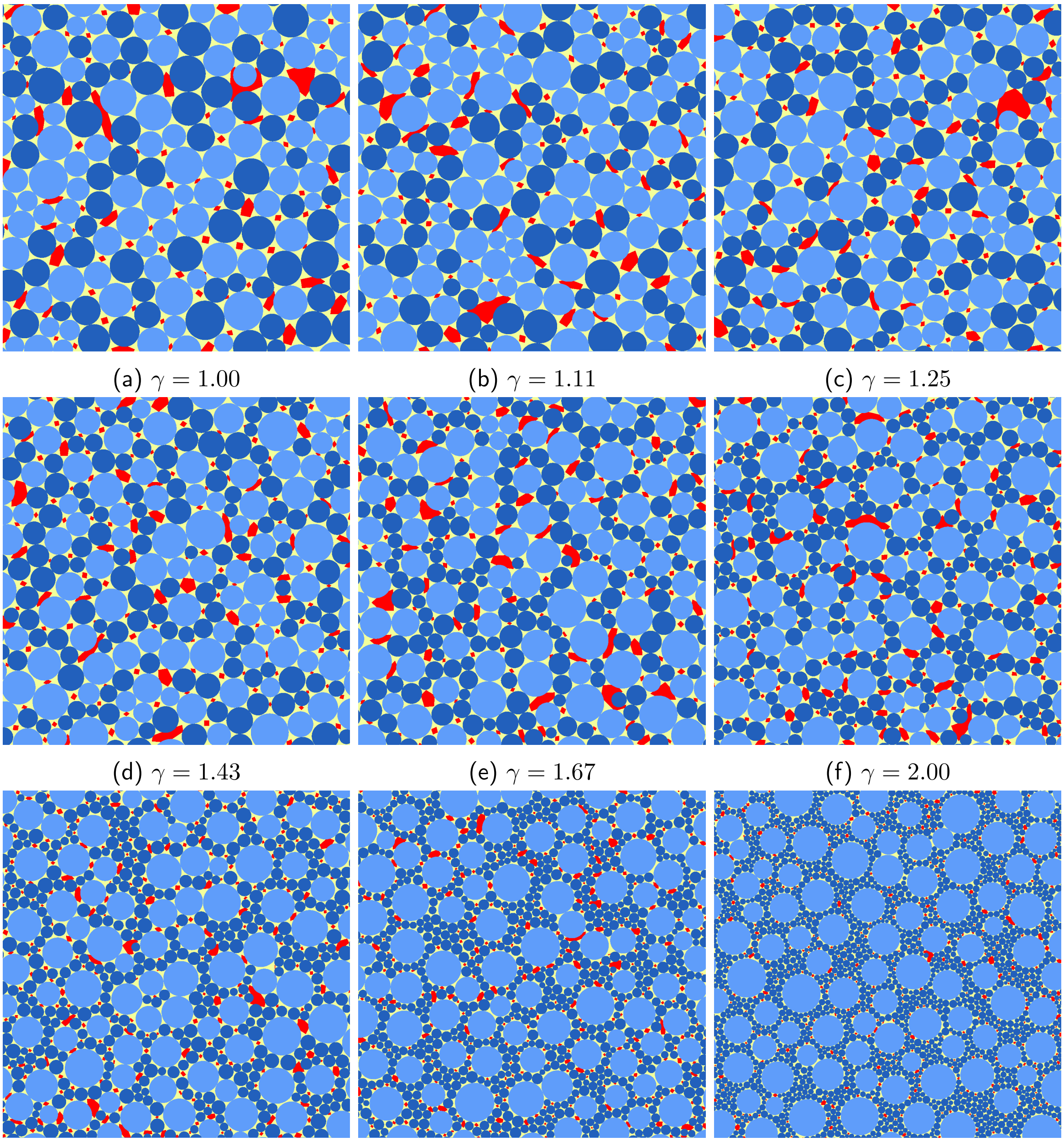

(a) $\gamma = 1.00$ (b) $\gamma = 1.11$ (c) $\gamma = 1.25$

(d) $\gamma = 1.43$ (e) $\gamma = 1.67$ (f) $\gamma = 2.00$

(g) $\gamma = 2.50$ (h) $\gamma = 3.33$ (i) $\gamma = 5.00$

Figure 5.15. – One example porous sample is shown for $\theta \approx 1.36$ with increasing γ. Large particles are coloured in light blue, small particles in dark blue, matrix in yellow and voids in red.

lot of inhomogeneity in the distribution. This can also be linked to the "phase" behaviour of the small particles observed by the coordination numbers. Locally, small particles act as a separate volumetric "phase" with only small inter-grain spaces and consequently small pore spaces in the matrix. However, small particles are still confined to the spaces in between large particles and at the small-large particle contact area larger pores exist, which create the long tail of the pore size distribution. The significance of this tail manifests in the larger excess kurtosis for pores in samples with radius ratio $\gamma = 5.00$.

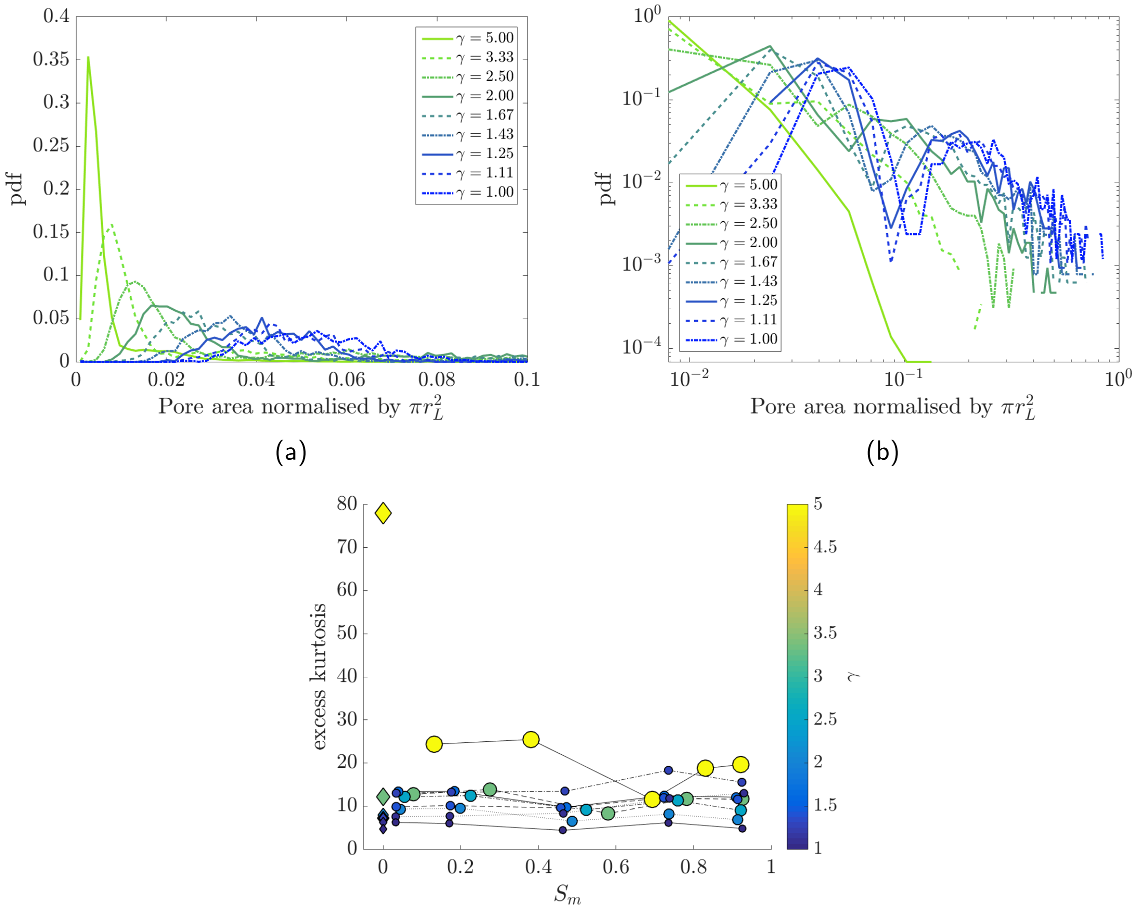

(a) (b)

(c)

Figure 5.16. – The pore size distribution for samples of $\theta \approx 1.36$ and varying γ is shown. (a) The largest peak for every γ is found at smaller pore sizes. (b) For smaller γ a second peak is present at larger pore sizes. (c) The excess kurtosis of pore size distribution is shown versus S_m. Circle size and colour show ρ_p. Diamonds show the kurtosis of inter-grain spaces, which is equivalent to $S_m = 0$.

5.2.4. Tensile properties of full samples

We studied the influence of PSD on the mechanical properties, measured as Young's modulus Y and yield stress σ^y, in tension. The PSD was characterised by the two effective parameters γ^* and θ^*, which have a direct, non-linear effect on the sample structure, as was discussed in the previous section (subsection 5.2.3). The effective volume parameters, which are likely to be important for the mechanical properties are ρ_p^*, ρ_m^* and ρ_v^*. In this first results section, only "full" samples are considered ($\rho_v = 0$). For these samples, only one volume fraction, ρ_p^*, is relevant, because ρ_m^* is defined immediately by $\rho_m^* = 1 - \rho_p^*$. However, the PSD is only fully described by the combination of all three parameters γ^*, θ^* and ρ_p^*.

Young's modulus

Young's modulus in dependence of both θ^* and γ^* is shown in Figure 5.17 on page 109. It is visible that E increases with γ^* and θ^* and some specific trends can be observed for γ^* and θ^*. There appears to be a threshold value for which γ^* gains importance around $\gamma^* \approx 2$. This threshold

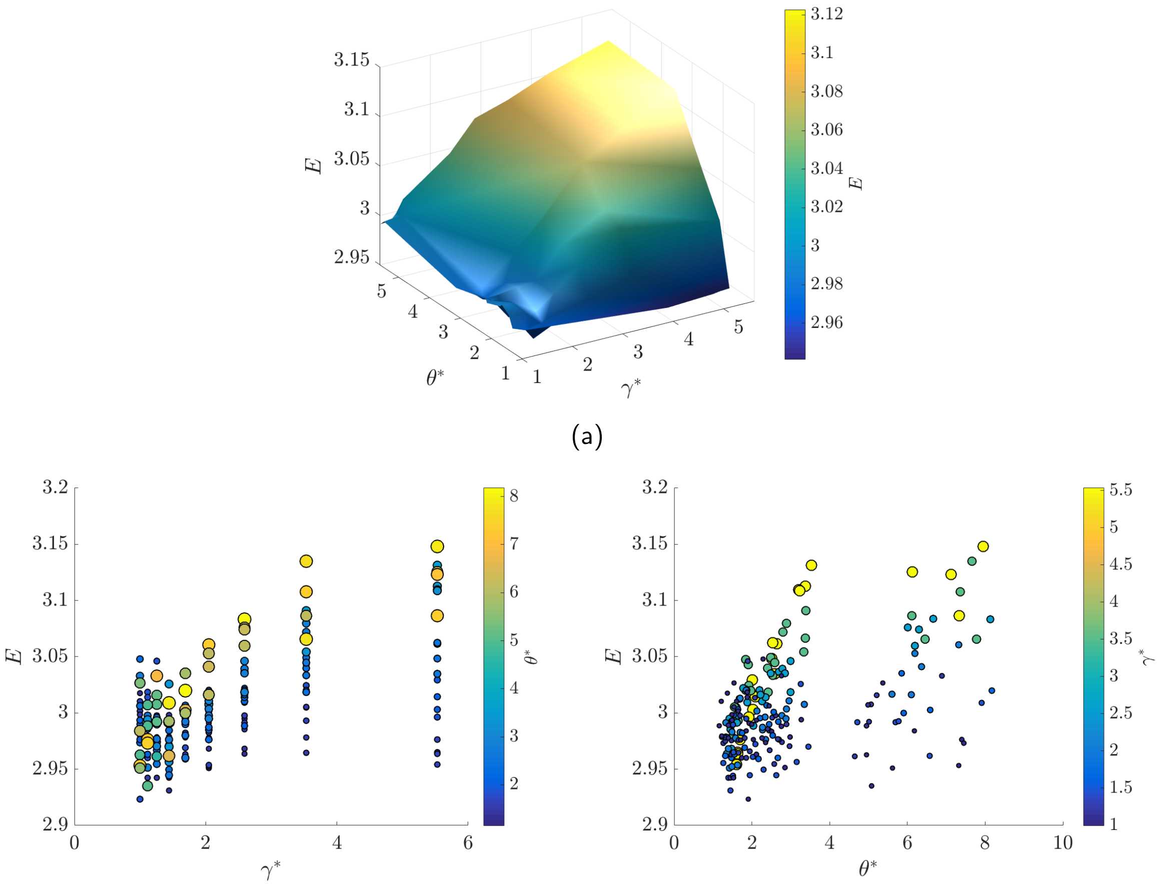

(a)

(b)

(c)

Figure 5.17. – (a) The evolution of the Young's modulus E in tension is shown depending on radius ratio γ^* and area ratio θ^*. The surface connects the average values of five simulations for each combination of γ^* and θ^*. (b) The Young's modulus dependence on γ^* is shown. Circle size and colour show the value of θ^*. (c) The Young's modulus dependence on θ^* is shown. Circle size and colour show the value of γ^*.

corresponds well with the threshold after which the coordination number Z_s increases (Figure 5.14b on page 105) and which indicates the small particles acting as a separate phase. Once that threshold is passed, the Young's modulus increases with γ^*, but interestingly only if θ^* is also of high value. This can also be seen in Figure 5.17b as the increasing vertical sorting of circles by size (level of θ^*) with increasing γ^*. Therefore, the modulus is highest, if the size difference between particle types is largest, but only if the amount of such small particles is not too high [3]. For higher θ the number of large-large contacts Z_{ll} is decreasing less steep with increasing γ (Figure 5.14c on page 105). The trend for θ^* by itself is however less clear (Figure 5.17c).
These observed relations of the Young's modulus point towards the importance of the granular backbone formed by large particles.

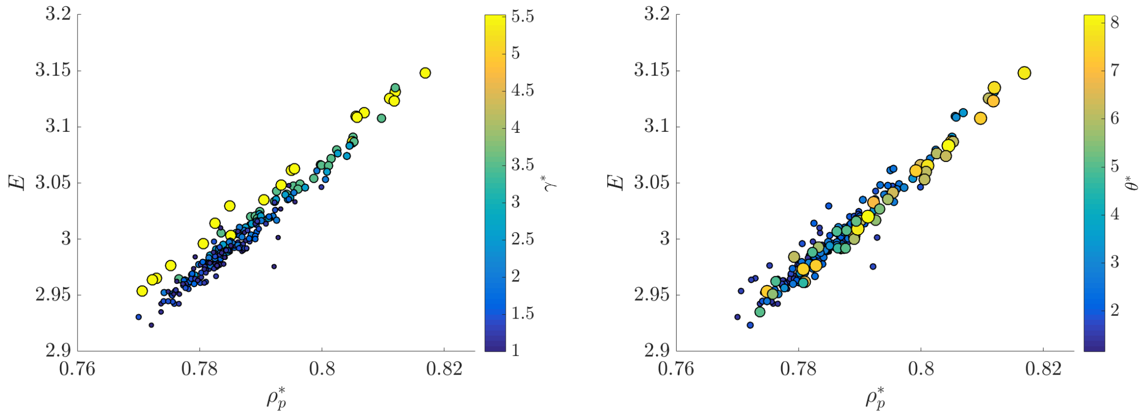

(a) (b)

Figure 5.18. – (a) The Young's modulus dependence on ρ_p^* is shown. Circle size and colour show the value of γ^*. (b) The Young's modulus dependence on ρ_p^* is shown. Circle size and colour show the value of θ^*.

A theoretical prediction of the bulk modulus B of a composite can be obtained from the Mori-Tanaka method [296]. The bulk modulus of a composite of isotropic matrix (bulk modulus B_0, shear modulus G_0 and volume fraction ρ_0) and two populations of isotropic spherical inclusions (B_1, B_2, ρ_1 and ρ_2) is then given by [297]:

$$B = \frac{d_1 + d_2 B_1 + d_3 B_3 + d_4 B_1 B_2}{d_5 + d_6 B_1 + d_7 B_3 + d_8 B_1 B_2} B_0 \tag{5.18}$$

with

$$d1 = 16\rho_0 G_0^2 \tag{5.19}$$
$$d2 = 4G_0[3\rho_0 + \rho_1(3 + 4G_0/B_0)] \tag{5.20}$$
$$d3 = 4G_0[3\rho_0 + \rho_2(3 + 4G_0/B_0)] \tag{5.21}$$
$$d4 = 3[3 + 4(1 - \rho_0)G_0/B_0] \tag{5.22}$$
$$d5 = 12(1 - \rho_0)G_0 B_0 + 16G_0^2 \tag{5.23}$$
$$d6 = 9\rho_2 B_0 + 12(1 - \rho_1 G_0) \tag{5.24}$$
$$d7 = 9\rho_1 B_0 + 12(1 - \rho_2 G_0) \tag{5.25}$$
$$d8 = 9\rho_0 \tag{5.26}$$

---

[3] $\theta^* = \rho_L^*/\rho_S^*$ and therefore larger if ρ_S^* is lower.

The Young's modulus E can be obtained for our samples from the relations of the different moduli in 2D: [298]

$$E = 2B(1-\nu) \tag{5.27}$$

$$G/B = (1+\nu)(1-\nu) \tag{5.28}$$

assuming a Poisson coefficient $\nu \approx 0.3$.
For full samples the two populations of spherical inclusions are assumed to be large and small particles. In this study $E_L = E_S$ and it follows:

$$G_0 = E_m/2(1+\nu) \tag{5.29}$$

$$B_0 = E_m/2(1-\nu) \tag{5.30}$$

$$\rho_0 = \rho_m^* \tag{5.31}$$

$$B_1 = E_L/2(1-\nu) = B_2 \tag{5.32}$$

$$\rho_1 = \rho_L^* \tag{5.33}$$

$$B_2 = E_S/2(1-\nu) = B_1 \tag{5.34}$$

$$\rho_2 = \rho_S^* \tag{5.35}$$

$$\tag{5.36}$$

This model describes the observed evolution of modulus with the particle volume fraction $\rho_p^* = \rho_L^* + \rho_S^*$ well (Figure 5.19). This indicates that the particles act as inclusions in a continuous matrix even for rather high particle volume fractions. However, a deviation between the Mori-Tanaka prediction and numerical results can be observed for $\rho_p > 0.8$.

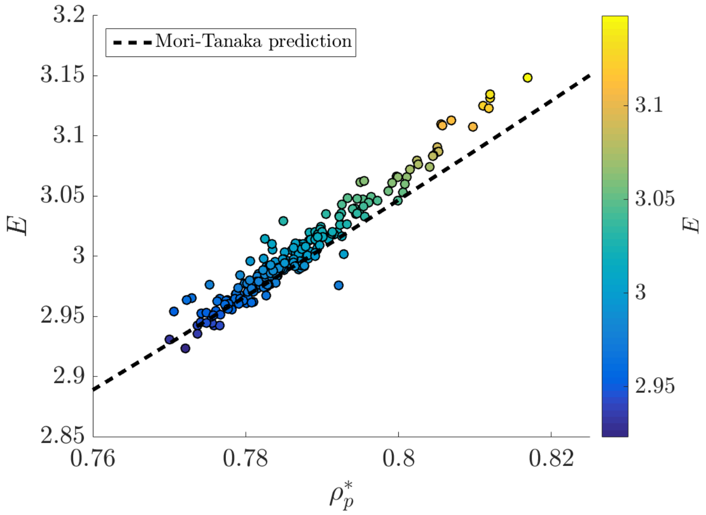

Figure 5.19. – The Mori-Tanaka prediction (Equation 5.18) fits well to the numerical results. The error between prediction and simulation is 3.5 %.

Yield stress

The yield stress increases with γ^* (Figure 5.20a), but the scatter of values for a fixed γ^* is rather large. Also, no obvious trend regarding θ^* can be observed. Opposite to the Young's modulus, the yield stress depends more on γ^* than on ρ_p^* (Figure 5.20b). The yield stress depends more on the defects of the material and their distribution. In a cemented granular sample filled with matrix and high particle-matrix adhesion, the most important defaults will be the grain-grain contacts. With increasing radius ratio γ^* and decreasing area ratio θ^* the number contacts for large Z_l and small Z_s particles increases (Figure 5.14a and Figure 5.14b on page 105). An increase in contacts on the same area likely results in a more homogeneous spatial distribution of grain-grain contacts and therefore a more homogeneous spatial distribution of the "defaults". Additionally, this implies a more homogeneous distribution of the stresses within the material, discussed in the next paragraph.

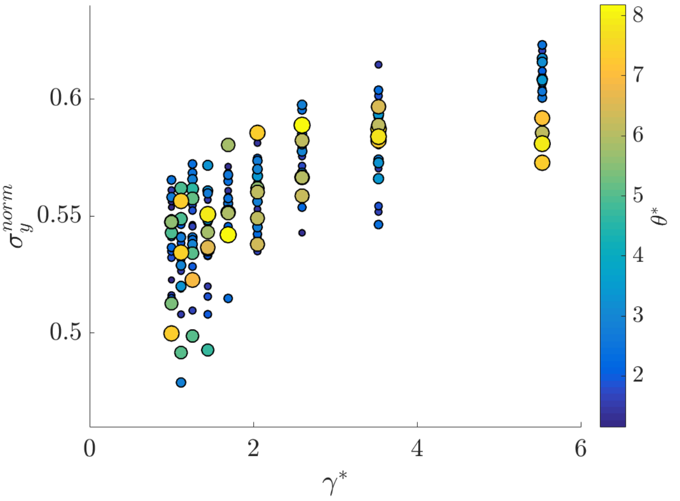

(a)

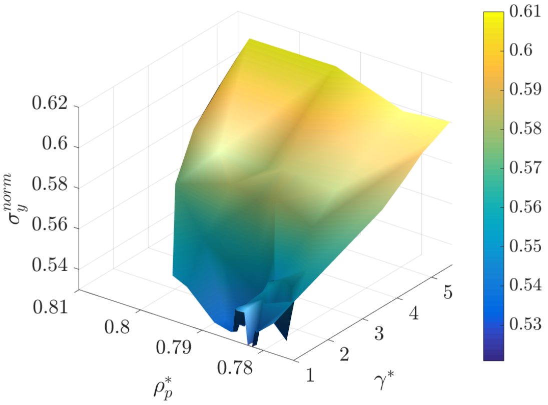

(b)

Figure 5.20. – The normalised yield stress of full samples is shown in dependence of (a) γ^* (circle size and colour show the value of θ^*) and (b) ρ_p^* and γ^*. The surface connects the average values of five simulations for each pair of ρ_p^* and γ^*.

Stress distributions

The distribution of stresses in a material is important for its mechanical behaviour. The transfer of stresses was found to be highly dependent on the PSD for cohesionless materials [281, 299]. Examples of stress distribution[4] are shown in Figure 5.21. It is visible that the stresses concentrate at the grain-grain contacts and that the distribution is more homogeneous for larger radius ratios γ^*.

The distribution of stresses within the different phases is shown in Figure 5.22a on page 115. The vertical stresses are normalised by the average stress of the whole sample: $\sigma_{yy}^{norm} = \sigma_{yy}/\overline{\sigma_{yy}}$. Lower than average stresses are found in the matrix, higher than average stresses in the large particles and average stresses within small particles. The stress distributions in small particles and matrix are Gaussian making the stress distribution in small particles more similar to the one in matrix than in large particles. Stress distributions in matrix do not vary with γ^* (Figure 5.22b). The distribution in small particles (Figure 5.22d) shifts slightly towards higher stresses for smaller[5] γ^* to the values of σ_{yy}^{norm} found in large granules. This indicates that the smaller particles become more involved in the stress bearing force chains the closer the size distribution is to a monodisperse granular material. The stresses in large particles vary significantly with $\gamma^* = 1.0$ (Figure 5.22c). They are least distributed in large particles for $\gamma^* = 5.53$. The distribution is even narrower than a Gaussian distribution, indicating that the stresses are very homogeneous within large particles. The different spread of stresses in large particles for the monodisperse and bidisperse ($\gamma^* = 5.53$) PSD are visible in Figure 5.21e and Figure 5.21f. For $\gamma^* = 5.53$ and this particular $\theta^* \approx 1.36$, the coordination number $Z_{ll} < 1$ and therefore the force chains have to pass through small particles. The average number of small particles in contact with one large particle is also very high at $Z_{ls} \approx 14$. Therefore, stresses are likely to pass through more than one small particle in parallel in between large particles (see Figure 5.21f), which results in the very homogeneous distribution of stresses within the large particles. For lower γ^* the number of contacts between large and small particles decreases (Z_{ls} in Figure 5.14e on page 105) and stresses within large particles become more widely distributed.

---

[4] Stress distribution maps for all γ^* are shown in the appendix in Figure A.5 on page 183.

[5] $\gamma^* = 1.0$ is the monodisperse particle size distribution.

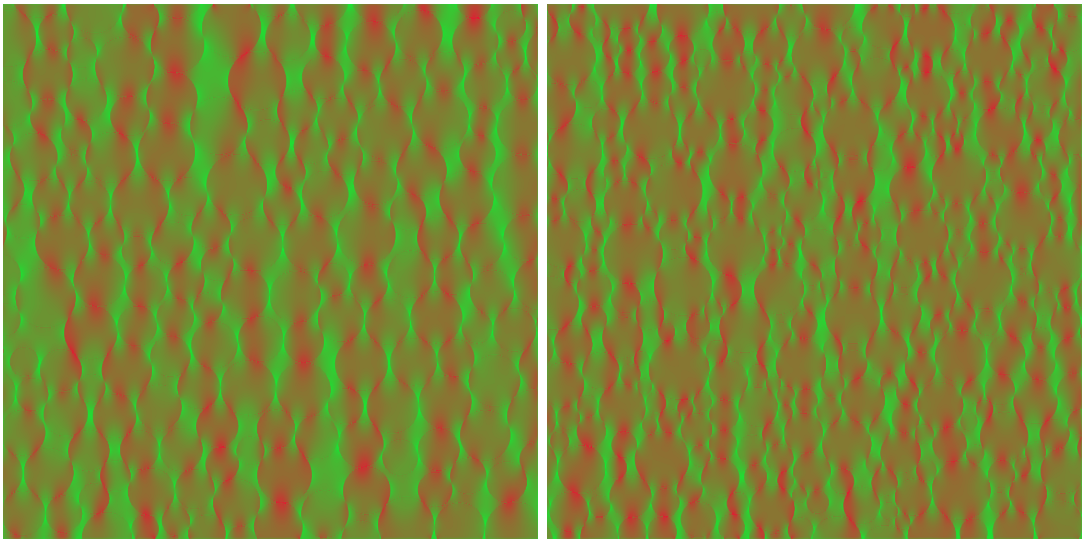

(a) $\gamma^* = 1.00$ (b) $\gamma^* = 2.05$

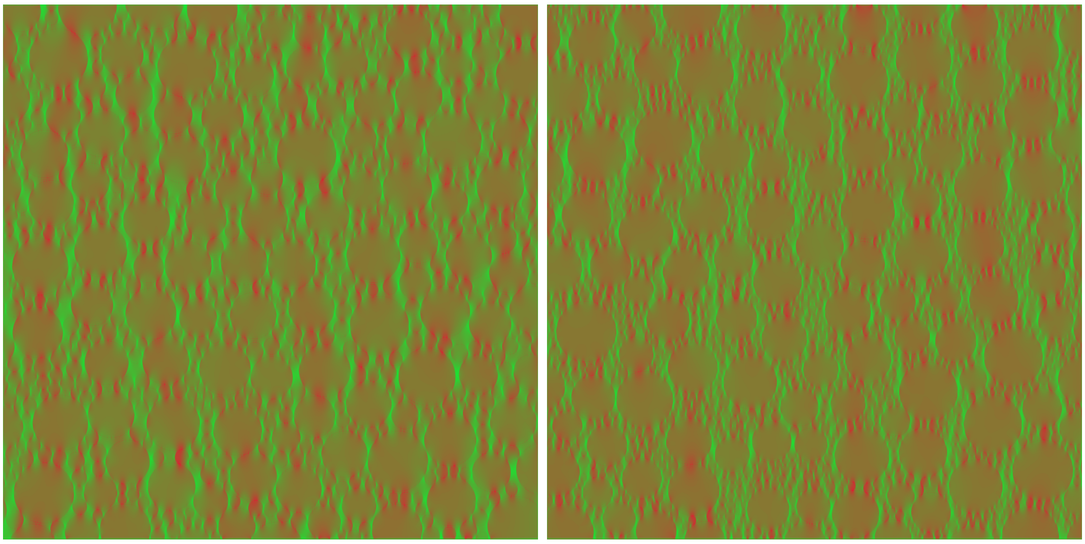

(c) $\gamma^* = 3.53$ (d) $\gamma^* = 5.53$

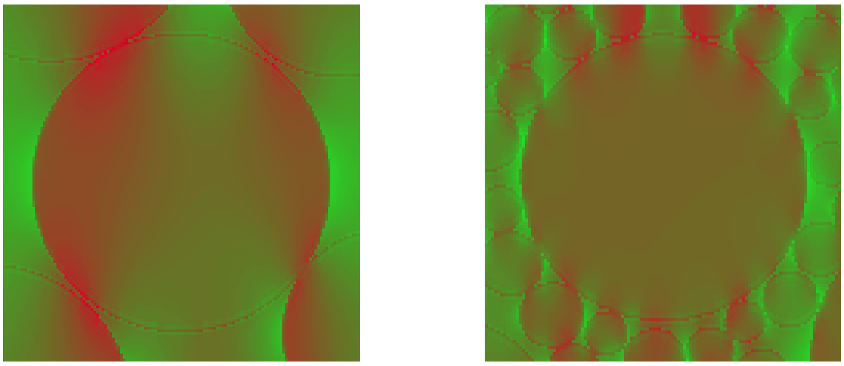

(e) zoom for $\gamma^* = 1.00$ (f) zoom for $\gamma^* = 5.53$

Figure 5.21. – Examples of the stress distributions within the samples are shown for $\theta^* = 1.36$ and selected values of γ^*. Low stress is coloured green, high stress in red.

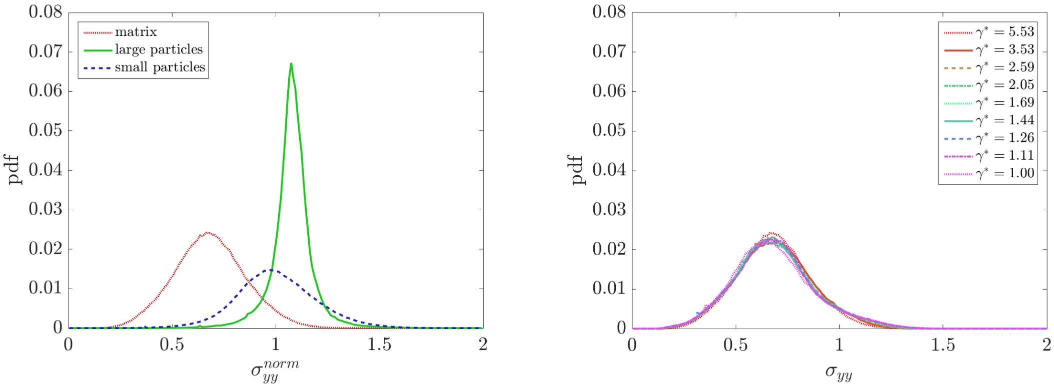

(a) all phases $\gamma^* = 5.53$

(b) matrix

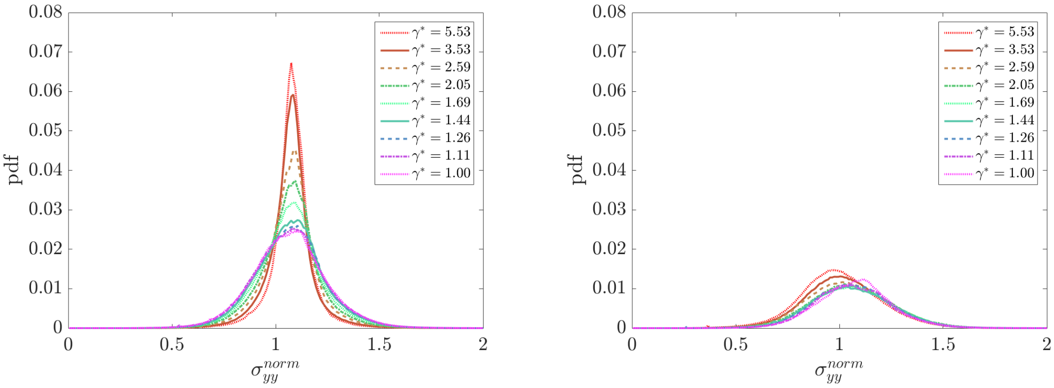

(c) large particles

(d) small particles

Figure 5.22. – Vertical stress distributions $\sigma_{yy}^{norm} = \sigma_{yy}/\overline{\sigma_{yy}}$ in full samples (a) in all three material phases for $\gamma^* = 5.53$, (b) in matrix for different γ^*, (c) in large particles for different γ^*, (d) in small particles for different γ^*. ($\theta^* \approx 1.36$).

5.2.5. Tensile properties of porous samples

The introduction of void spaces into the matrix changes the mechanical behaviour drastically. To highlight the effects of pores, the Young's modulus and yield stress are represented as $E^{rel} = E_{porous}/E_{full}$ and $\sigma_y^{rel} = \sigma_y^{porous}/\sigma_y^{full}$. The dependency of Young's modulus on ρ_p^*, which was observed for full samples, is lost for the porous material. Instead the modulus increases with the matrix saturation S_m (Figure 5.23b on page 117). For very low S_m the modulus tends to go towards 0, which would be expected for a composite without any matrix in tension. This behaviour of modulus in dependency of S_m, and therefore ρ_m^*, is in accordance with the results of Topin et al. [180] and Chichti et al. [135]. Regarding the influence of PSD, we observed that for similar S_m the highest modulus is obtained for samples with the highest γ^*.

The Mori-Tanaka prediction can be used for porous samples, too, assuming that the first type of spherical inclusions are particles and the second type are voids, as was done by Topin et al. [180]. The parameters for Equation 5.18 then become:

$$G_0 = E_m/2(1+\nu) \tag{5.37}$$
$$B_0 = E_m/2(1-\nu) \tag{5.38}$$
$$\rho_0 = \rho_m^* \tag{5.39}$$
$$B_1 = E_p/2(1-\nu) \tag{5.40}$$
$$\rho_1 = \rho_p^* \tag{5.41}$$
$$B_2 = 0 \tag{5.42}$$
$$\rho_2 = \rho_v^* = 1 - \rho_m^* - \rho_p^* \tag{5.43}$$
$$\tag{5.44}$$

This theoretical prediction does however not describe the observed behaviour accurately anymore. The Young's modulus of the porous samples is overestimated (Figure 5.23b) when calculated by Equation 5.18. The reason for this mismatch might be due to the theory assuming inclusions in a continuous matrix, whereas the matrix in our porous samples is discontinuous. Theory and simulations results could be matched, if E_m is lowered (not shown), but further investigation of this point is needed.

The relative yield stress ($\sigma_y^{rel} = \sigma_y^{porous}/\sigma_y^{full}$) of the porous samples was found to be increasing with S_m (Figure 5.23c). If the matrix saturation is $S_m > 0.5$, the value of γ^* becomes more important and for samples with high matrix saturation ($S_m > 0.8$), it is the samples with the highest γ^*, which will have the highest yield stress. This is however not true for smaller values of matrix saturation. The influence of the radius ratio γ^* on the relative yield stress is also visible in Figure 5.23d. It shows that for porous samples it is not only the matrix saturation S_m, but also the PSD, which determines the yield stress. This is likely to be related to the size of pores. For similar S_m but higher γ^* pore size is smaller (Figure 5.16b on page 108). Interestingly, the excess kurtosis is larger for higher γ^*, indicating a more heterogeneous size distribution of the pores. However, this seems to affect the strength of the material less than the average pore size.

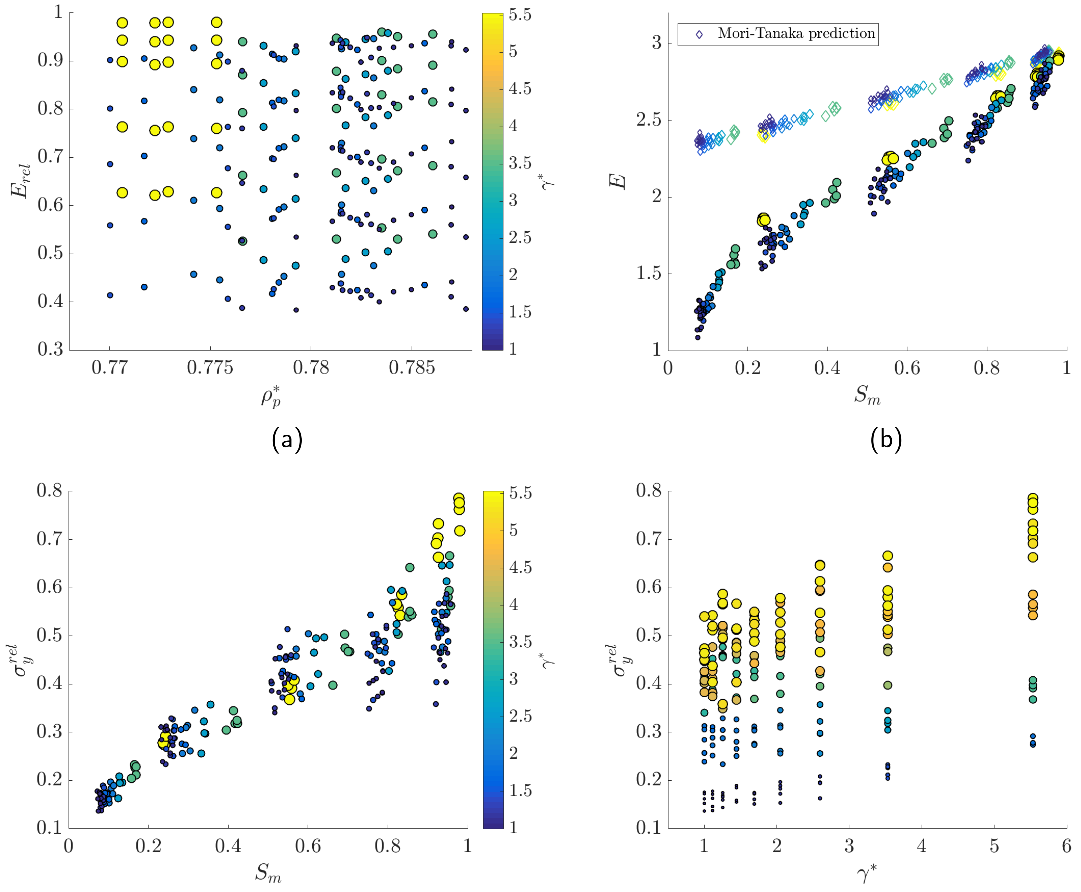

(a) (b)

(c) (d)

Figure 5.23. – The Young's modulus for porous samples is shown in dependence of (a) ρ_p^*; circle size and colour show the value of γ^* and (b) matrix saturation S_m; circle size and colour show the value of γ^*. The yield stress for porous samples is shown in dependence of (c) matrix saturation S_m; circle size and colour show the value of γ^* and (d) γ^*; circle size and colour show the value of S_m. ($E^{rel} = E^{porous}/E^{full}$, $\sigma_y^{rel} = \sigma_y^{porous}/\sigma_y^{full}$)

Stress distributions

In Figure 5.24 on page 119 it is visible that the stresses in all phases change significantly with changing matrix saturation [6]. The stress distribution in matrix and small particles change from exponential to Gaussian with increasing matrix saturation. An exponential stress distribution is typical for granular material, where stresses are distributed heterogeneously and stresses much higher than the average can occur.
In samples with very low matrix saturation S_m, the highest stresses are carried by matrix and small particles (Figure 5.24). These high stresses are found at the grain-grain contact points around the pores [7]. The matrix also has very low stresses, which originate from the horizontally oriented matrix bridges not being stressed [8].
A change of polydispersity does not influence the shape of stress distributions in small particles significantly (Figure 5.25a) [9]. But for lower matrix saturation, the small particles capture more high stresses.
Stress distributions in large particles are always peaked at slightly above average σ_{yy}^{norm} for high γ^*, but become more wide with decreasing matrix saturation (Figure 5.25c). The narrow peak is lost for the monodisperse sample (Figure 5.25d), as was also observed for full samples [10]. As for the full samples, for higher γ^* the number of contacts of small particles around each large particle Z_{ls} is higher. This then leads to rather homogeneously distributed stresses within the large granules. However, with decreasing matrix saturation, the grain-grain contact points themselves become more stressed, leading to the exponential slope towards high stresses.
In porous samples with high matrix saturation S_m small particles therefore reinforce the material in the same way as for full samples: a more spatially homogeneous distribution of stresses. For lower values of matrix saturation this is not true anymore and the origin of that effect needs more investigation.

5.2.6. Effect of interface properties

For a subset of samples, the mechanical parameter of interface toughness K_{pm} was varied (see Table 5.2 on page 99). A reduction in interface toughness K_{pm} resulted in a drastic decrease of yield stress (Figure 5.26a). The decrease in yield stress was found to be related to the change of interface toughness. Yield stress can be scaled by the interface toughness: $\sigma_y^{sc} = \sigma_y^{norm}/K_{pm}$ (Figure 5.26), as was also shown by [300]. This is also in accordance with [180], who showed that the tensile strength increases with increasing interface adhesion. However, the scaling effect of K_{pm} for our study was only verified for full samples. Our results showed a strong change of yield stress with S_m for porous samples and the isovalue lines of yield stress in the parameter space of interface strength and matrix volume fraction reported in [180] are not evolving linearly and therefore suggest that a scaling with K_{pm} only might not be sufficient for porous material. Affes et al. [300] however, showed that the scaling works for a large range of matrix volume fraction (in 3D), except for $\rho^m < 0.10$.

---

[6] Distribution for all six states of matrix saturation can be found in the appendix in Figure A.2 on page 180.

[7] Visible Figure A.7 and Figure A.8 in the appendix on page 186.

[8] Quantitatively visible in Figure A.6 in the appendix.

[9] Stress distributions for all γ^* are shown in Figure A.4 in the appendix.

[10] Stress distributions for all γ^* are shown in Figure A.3 in the appendix.

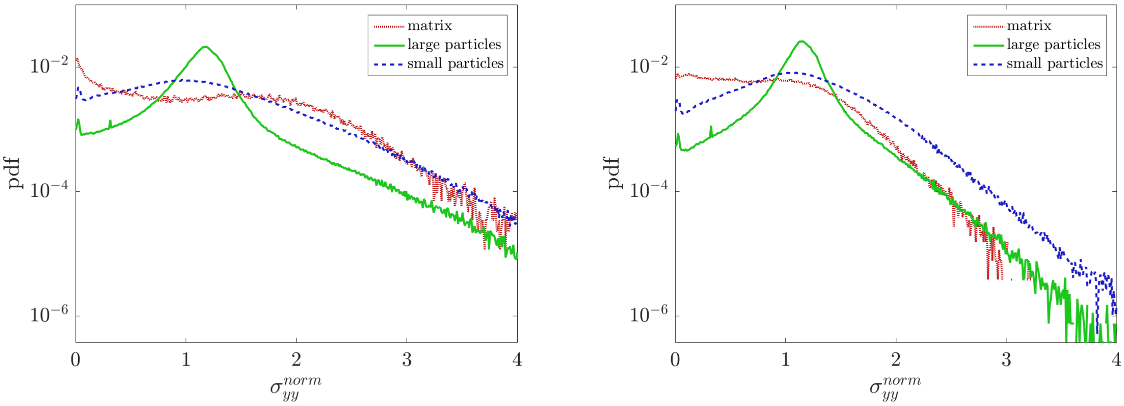

(a) $S_m = 0.03$ (b) $S_m = 0.17$

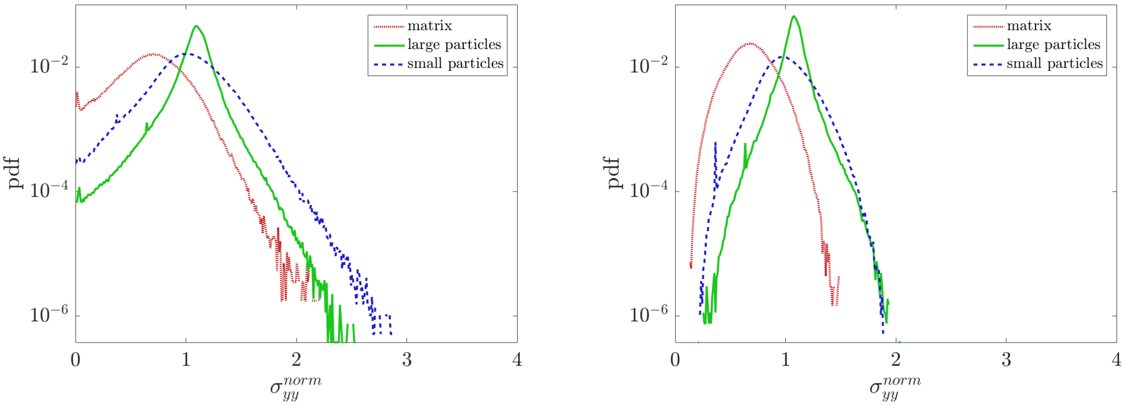

(c) $S_m = 0.73$ (d) $S_m = 1.00$

Figure 5.24. – (a-f) Stress distributions $\sigma_{yy}^{norm} = \sigma_{yy}/\overline{\sigma_{yy}}$ in all phases with increasing matrix saturation ($\gamma^* = 5.53$, $\theta^* \approx 1.36$).

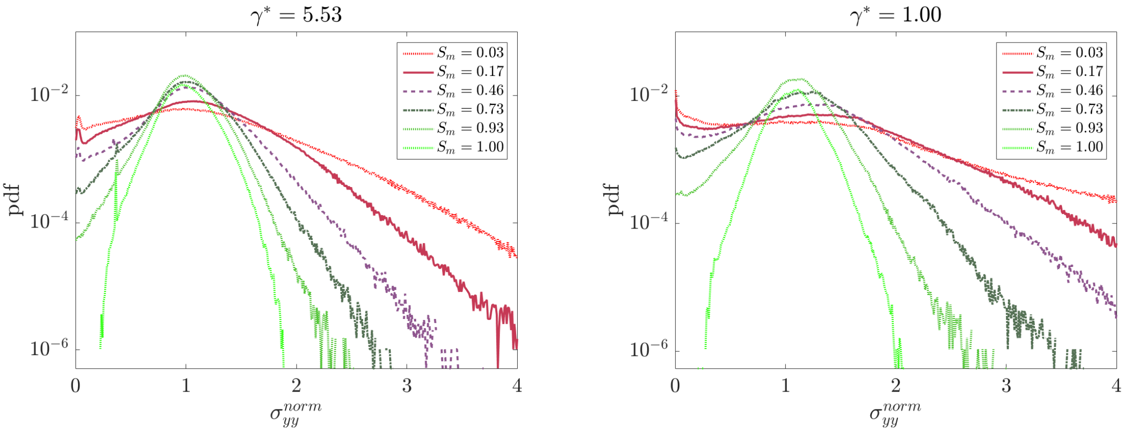

(a) small particles (b) small particles

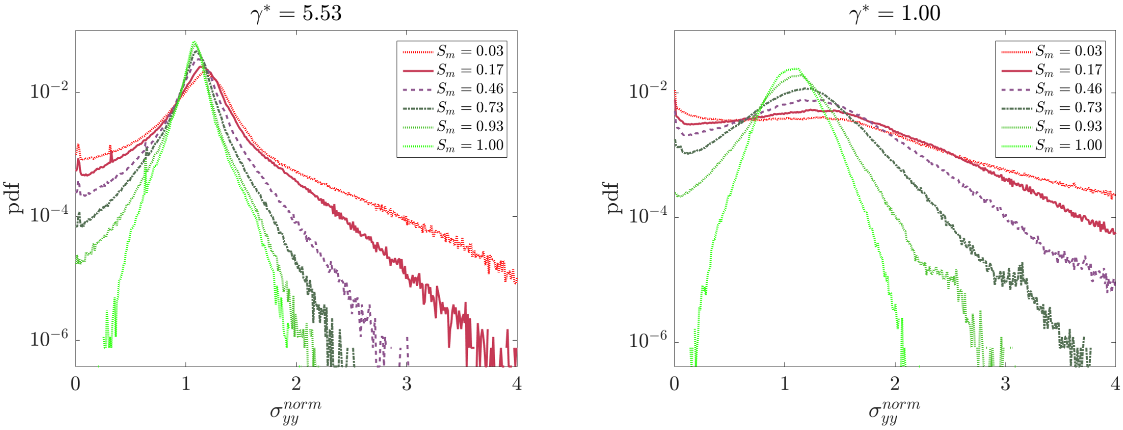

(c) large particles (d) large particles

Figure 5.25. – (a-d) Stress distributions in **large particles** and **small particles** of **porous** samples for the two most extreme values of γ^* ($\theta^* \approx 1.36$).

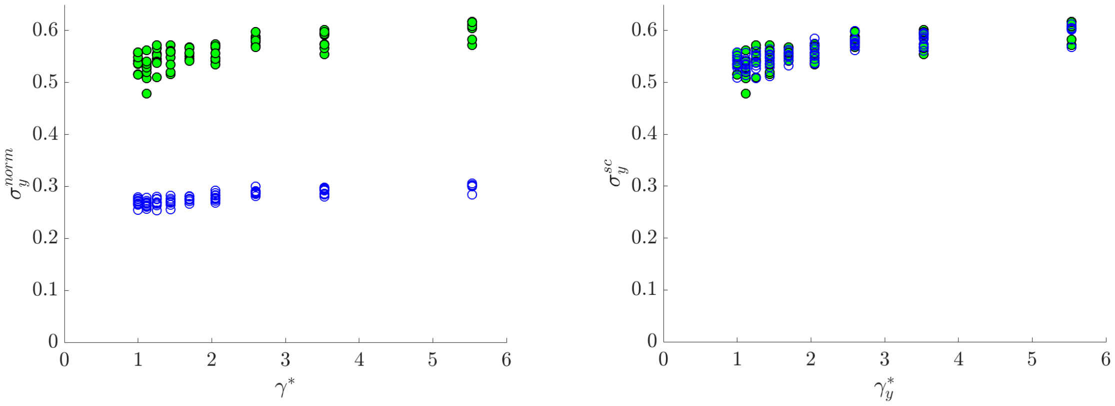

(a) (b)

Figure 5.26. – (a) The yield stress for full samples of $\theta^* \approx [1.74, 2.90]$ and varying γ^* is shown for high interface toughness K_{pm} (red, filled circles) and low interface toughness K_{pm} (blue, empty circles). (b) Values coincide, if yield stress is scaled by interface toughness: $\sigma_y^{sc} = \sigma_y^{norm}/K_{pm}$.

5.2.7. Conclusion

PSD was shown to influence the mechanical properties of a cemented granular material. The particle size distribution influences the particle contacts and consequently the stress distributions within the material, the yield stress and elastic modulus in a non-linear manner. In samples without porosity, an increase of particle size difference and amount of small particles increases the yield stress, by homogenising the contact network and consequently the stress distributions. The Young's modulus increases mostly with the total particle volume, which is higher for larger particle size differences due to a more efficient packing. Additionally, the Young's modulus is slightly higher for samples with larger particle size differences for a given particle volume fraction.

The mechanical properties of porous sample are mostly determined by the matrix saturation. Similarly to non-porous samples, the effect of PSD is limited. Yield stress of only slightly porous samples increases with larger particle size differences, due to the same effect as for full samples. But for lower matrix saturation levels, larger particle size differences do not always result in the largest yield stress, which might be linked to the size and spatial distribution of the pores within the matrix.

Overall, the influence of PSD is less important than other factors, such as the amount of cementing material and the particle-matrix adhesion toughness.

SGSD and wheat milling Correlations between the (mechanical) wheat hardness class and the SGSD were observed [273]. Gaines et al. [161] observed more small granules and smaller granule sizes in (mechanically) hard wheat and larger granules in soft wheat. Softer wheats also had less total starch [161]. On the contrary, Li et al. [48] reported greater B-type granules in (genetically) hard wheat, but also less large granules. A strong genetic component on SGSD was also suggested by Gaines et al. [161]. Due to the number of involved factors it is difficult to directly compare such experimental findings with our simulations. In first instance, our findings agree with less total starch in wheats with larger granules, as was reported by Gaines et al. [161]. The highest particle volume fraction was found for the largest size ratio of large to small granules. A softer texture of such wheats could then be rather the direct result of less total starch and therefore indirectly of the SGSD. However, the porosity of the protein matrix has a significant effect and therefore needs to be considered., However, it complicates the interpretation of experimental results in wheat grains compared to our simulations, since no absolute value of the porosity of wheat grains is measurable so far, even though vitreousness allows for a classification. Predictions on grain fragmentation for non-vitreous grains, where the exact amount of matrix saturation is not known, are therefore difficult. The more complex relationships in porous samples could explain the controversial experimental results.

5.3. Investigation of the governing factors of particle damage in a cemented granular material

Abstract

The particle damage obtained by a cemented granular material under tensile or compressive forces depends on its structure and the mechanical properties of the constituting phases. We performed an extensive parametric of the particle toughness and particle-matrix interface toughness on a cemented granular material with bi-modal granule size distribution. As the mechanical response is known to be greatly influenced by the amount of cementing matrix, two states were analysed: fully cemented and partly cemented with voids. The particle damage is traced separately in the large and small particles. In agreement with previous studies we observe that one parameter is governing the amount of particle, which is the relative toughness of particle to particle-matrix interface.

Table 5.3. – Nomenclature used in this section

ϵ		strain
θ	$= \rho^p_{large}/\rho^p_{small} \approx 1.66$	area ratio
ρ		volume fraction
ρ^p_{large}		volume fraction large discs
ρ^m		volume fraction matrix
ρ^p	$= \rho^p_{large} + \rho^p_{small}$	particle solid fraction
ρ^p_{small}		volume fraction small discs
ρ^v		volume fraction voids
σ		stress
σ_y		yield stress
D^p	$= nb^p/nb_{total}$	total particle damage percentage
D^m	$= nb^m/nb_{total}$	total matrix damage percentage
D^i	$= nb^i/nb_{total}$	total interface damage percentage
DB^i	$= nb^i/n_i$	percent of broken interface bonds
DV^p	$= nb^p/nb_{total} \cdot 1/\rho^p$	scaled damage particle
DV^m	$= nb^m/nb_{total} \cdot 1/\rho^m$	scaled damage matrix
E		Young's modulus
E_p		elastic modulus particle
E_m		elastic modulus matrix
E_i		elastic modulus interface
K		Toughness
K_p		toughness particle
K_m		toughness matrix
K_i		toughness interface
K^r	$= K_p/K_i$	relative particle-interface toughness
K^r_c		critical relative particle-interface toughness
n		number of bonds
nb^p		number of broken bonds particle
nb^m		number of broken bonds matrix
nb^i		number of broken bonds interface)
nb_{total}	$= nb^p + nb^m + nb^i$	total number of broken bonds
r_{equ}	$= r_L + r_S$	perimeter radius
r_L		radius large discs
r_S		radius small discs

5.3.1. Introduction

Different milling behaviour is observed for different types of wheat, in terms of the milling energy, flour yield and starch damage [104]. These differences are related to the macroscopic properties grain hardness and vitreousness [112]. Grain hardness is and important characteristic, because it affects grain milling behaviour. Softer grains require less milling energy, produce more fine flour particles and less damaged starch in the flour [131]. Starch damage is related to the water absorption properties of the flour [301], and therefore important for flour end-uses.

Wheat grain hardness can be seen from a genetic or mechanic viewpoint, which can differ from each other [156]. Genetic hardness is mainly related to the Hardness locus *Ha*, which encodes the proteins puroindolines (PINs) a and b [143]. In common wheat *Triticum aestivum*, PINs can be present in wild-type form, (soft varieties) or in mutated form (hard varieties) [13]. In durum wheat *Triticum durum*, whose grains are harder than common wheat, no PINs are present due to the lack of the corresponding chromosome [13]. Differences between mechanically hard and soft wheat are thought to be related to the genetical properties through the PINs affecting the starch-protein interface in the starchy endosperm [174, 186]. Differences on the interface between a soft and hard variety were only recently measured directly by atomic force microscopy (AFM) [135].

Another important measurable grain scale property is grain vitreousness. It is an optically measured parameter, describing the glassy appearance of the grain's interior [115]. Vitreousness is directly linked to grain density [156]. Lower grain density is caused by the presence of air spaces in the matrix, making it porous and fragmented [177, 302]. Vitreous grains have a more continuous protein matrix [177]. Vitreousness is connected to the genetical hardness and the fracture behaviour, but mainly for (genetically) hard varieties [156].

Because whole grain milling includes different tissues and a combination of forces, a clearer understanding of endosperm mechanical properties can be gained from experiments on blocks or cylinders made only from starchy endosperm tissue. A number of studies investigated the relation between genetical hardness and vitreousness to mechanical properties [170, 171, 14, 156, 155]. Such studies can point out relationships between endosperm properties (i. e. density, vitreousness, genetical hardness) and the mechanical behaviour, characterised by the yield stress or modulus. But unless a large number of samples with different genetic background and from different environments is studied, it is difficult to obtain general predictive relations, because of the ultimately limited diversity of the biological samples.

Numerical modelling can help to investigate the underlying mechanisms that govern endosperm mechanical behaviour. However, information on the mechanical properties of the constituents is necessary for an accurate representation. Such information can be gained from AFM measurements on for example the abrasive hardness of starch and protein [135] or from contact resonance atomic force microscopy (CR-AFM) measurements of the (contact) modulus (section 4.4).

A small number of numerical studies exists, concerned with modelling a cemented granular material in order to gain insight into wheat endosperm fractionation [180, 181, 182, 183]. The effects of particle-matrix interface strength, the amount of protein matrix and voids within that matrix, and the amount of particle fraction were investigated.

The importance of interface adhesion in combination with matrix fraction on the yield stress [180, 181, 183] was shown and an almost linear evolution of effective stiffness with matrix content was observed [182]. Furthermore, the amount of particle damage in dependence of matrix fraction and interface adhesion was investigated and the existence of three different cracking regimes was demonstrated [180, 181, 182]. Starch damage was demonstrated to scale with a single parameter: the relative toughness of starch and the interface K_c^r [180, 181, 182].

Whereas Topin et al. [180, 181, 182] believed the mechanical properties of starch and protein in the wheat endosperm to be indifferent and treated bare particle-particle contacts as cohesionless,

Table 5.4. – Comparison of the parameters used for numerical studies of wheat endosperm as a cemented granular material in 2D.

study	radii	volume fractions			bond elasticity E			bond tensile strength σ or toughness K		
		ρ_m	ρ_p	ρ_v	E_m	E_p	$E_{pp,pm}$	matrix	particle	par.-part., part.-matr.
LEM [181, 182]	$r_A/r_B = 4$ $r_{A,B} = const$	$0.04 \dots 0.2$	0.8		$E_m = E_p = E_{pm}$			$\sigma_m = \sigma_p$		$\sigma_{pm} = 0.3\sigma_p \dots 1.05\sigma_p$ $\sigma_{pp} = 0$
LEM [183]	$r_A/r_B = 4$ $r_{A,B} = const$	$0.03 \dots 0.34$	$0.66 \dots 0.8$	$0 \dots 0.18$	$E_p = 3.5E_m$		$E_{pm} = E_{pp} = E_m$	$\sigma_p = 2.5\sigma_m$		$\sigma_{pp} = \sigma_{pm} = 0.2\sigma_p \dots 1.2\sigma_p$
peridynamics	$r_A/r_B = 5$ normal distr.	0.12; 0.086	0.88	0; 0.035	$E_p = 4E_m$		$E_{pm} = E_{pp} = E_m$	$K_p = K_m \dots 3.5K_m$		$K_{pp} = K_{pm} = 0.5K_m \dots 1.0K_m$

Chichti et al. [183] used different values for starch and protein properties based on nano-mechanical experiments. These authors also changed the bare contacts for particle-matrix-like contact, also based on experimental findings. Chichti et al. [183] demonstrated the strong effect of interface adhesion on the yield stress and that the starch volume fraction is more important in the case of higher particle-matrix adhesion. In accordance with Topin et al. [182], they established that the porosity is the factor with the highest influence on the elastic modulus.

Based on these previous studies, we performed a parametric study of starch toughness and interface adhesion and their effect on particle damage and the strength and elastic properties of the material. Several parameters were changed in comparison to these previous studies. Differences and similarities are compared in Table 5.4. Topin et al. [180, 181, 182] and Chichti et al. [183] used bimodal distributions of constant radii with the smaller discs having a four-times smaller in radius than the large discs. We implement a normal distribution around each disc population and decrease the size of the small discs further. A different numerical method is used, peridynamics, which uses bond toughness and elasticity. The lattice element method (LEM) used by Topin et al. and Chichti et al., used bond elasticity and a critical bond tensile strength. Furthermore, we differentiate the damage between large and small particles within the particle fraction.

5.3.2. Numerical method

Samples

This study used two-dimensional, square sample volumes filled with round discs of a bi-modal size distribution. Samples consisted of three bulk phases: discs of a hard material representing starch granules, a matrix representing the embedding protein network and a void phase that creates porosity in the matrix.

The structure is characterised by the following parameters: the radius of the discs (r_L for large and r_S for small discs), the volume fraction of small discs ρ^p_{small}, large discs ρ^p_{large} and the total particle volume fraction $\rho^p = \rho^p_{large} + \rho^p_{small}$, the void volume fraction ρ^v and the protein volume fraction ρ^m. The condition $\rho^p + \rho^m + \rho^v = 1$ is always fulfilled.

Granule radii The diameter of large A-type starch granules in wheat is up to 30 µm in the long axis of the ellipsoid, while the diameter of small B-type granules is about 2 µm to 3 µm [27]. B-type granules can therefore be up to 10-times smaller than A-type granules in the long axis. In the simulations a trade-off between resolution and computation time is necessary. The largest size difference that could be investigated with reasonable computation time was a size difference of $r_L = 5r_S$, which is what was used in this study. The effect of changing particle size was investigated earlier (section 5.2).

To mimick the variability of a biological system, granule sizes followed a normal distribution for small and large discs, respectively, around the mean radii $r_{L,S}$ with the standard deviations $\sigma_L = 0.25r_L$

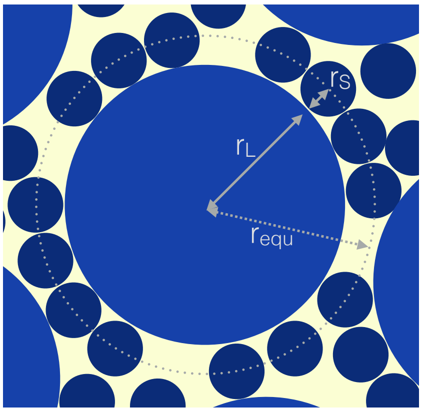

Figure 5.27. – A schematic image of a large granule of radius r_L surrounded by small discs of radius r_S is shown.

and $\sigma_S = 0.25 r_S$. An additional cutoff for discs sizes of $c_L^{+,-} = r_L \pm 1.5\sigma_L$ and $c_S^{+,-} = r_S \pm 1.5\sigma_S$ had to be implied due to the finite resolution of the numerical method.

Large to small granule ratio Another structural parameter is the ratio of small to big granules, which can be expressed as ratio of number, area or volume. Large granules are reported to make up to 60 % to 80 % of the volume of starch granules in the endosperm [49, 166]. For the two-dimensional samples of this study, we assume an ≈80 % "coverage" of large particle by small particles (Figure 5.27). Further, assuming that the small particles are close on the perimeter of the large particle, their number can be estimated as

$$n_S = 0.8 \cdot \frac{2\pi\, r_{equ}}{2 r_S} = 0.8\pi \left(1 + \frac{r_L}{r_S}\right) \tag{5.45}$$

The ratio of volume fractions of small to big granules is given by:

$$\theta = \frac{\rho^p_{large}}{\rho^p_{small}} = n_L \pi r_L^2 \Big/ n_S \pi r_S^2 \tag{5.46}$$

with n_L and n_S being the respective total number of discs per type. Combining Equation 5.46 and Equation 5.45 for $n_L = 1$ it follows that:

$$\theta = \frac{\pi r_L^2}{n_S \pi r_S^2} = \frac{1}{0.8}\frac{r_L^2}{\pi\left(r_L r_S + r_S^2\right)} = 1.66 \tag{5.47}$$

Sample assembly was performed in several steps: fast Poisson disc sampling (FPDS), discrete element method (DEM) compression, matrix filling, cropping and meshing, according to the methods described in subsection 5.2.2.

Two states of matrix filling were investigated: full samples with $\rho^v = 0$ and porous samples with $\rho^v = 0.035$ (Figure 5.28). For $\rho^v = 0$ all free spaces that were not occupied by discs were considered to be filled with matrix ($\rho^m = 1 - \rho^p$). For porous samples, the matrix filling was computed following the procedure described by Topin et al. [180]. Matrix filling resulted from establishing trapezoidal bridges of matrix between neighbouring discs (see previous section, section 5.2.2 on page 96). The sample volumes had an average void volume of 3.5 %.

A square was cropped out of the centre of the box and meshed onto a grid of 1024x1024 nodes. Volume fractions were calculated after meshing as $\rho^p = n^p_{nodes}/n^{total}_{nodes}$, $\rho^m = n^m_{nodes}/n^{total}_{nodes}$ and $\rho^v = n^v_{nodes}/n^{total}_{nodes}$. The averaged volume fraction percent for every phase are summarised in Table 5.5.

Table 5.5. – Volume fractions of the non-porous and porous samples, given as the average and standard deviation of five samples.

Matrix state	ρ^m	ρ^p	ρ^p_{large}	ρ^p_{small}	ρ^v
non-porous	0.122 (0.002)	0.878 (0.002)	0.546 (0.007)	0.332 (0.007)	0 (0)
porous	0.086 (0.001)	0.878 (0.002)	0.546 (0.007)	0.332 (0.007)	0.035 (0.002)

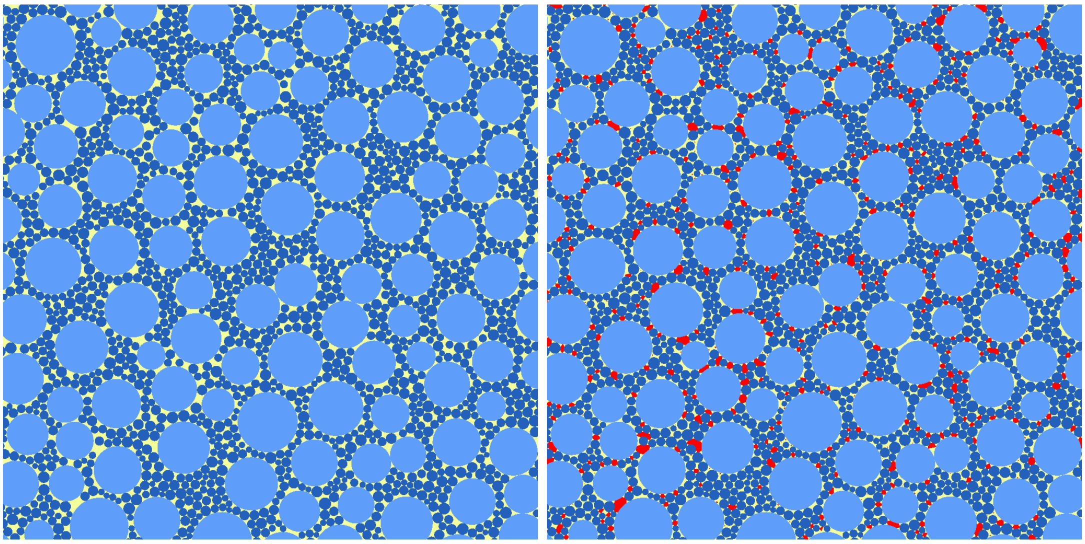

(a) (b)

Figure 5.28. – Samples for both investigated matrix states are shown: (a) full matrix, (b) porous matrix. Large particles are shown in bright blue, small particles in dark blue, matrix in yellow and pores in red.

Sample meshing

The peridynamic approach is an alternative to continuum mechanics. It is based on integral equations and is less sensitive to local anisotropies due to meshing than classical LEM [180, 183]. Peridynamics allows taking into account heterogeneous distributions of mechanical properties using bond-based schemes with brittle linear springs. The stress and strain tensors are computed on a rectilinear grid by integrating long-range interactions over a limited neighbourhood. As the algorithm is based on non-local interactions, failure occurs in the form of damaged zones with a characteristic thickness. A detailed description of peridynamics is given in subsection 5.2.2 on page 90.

The cropped, square samples were meshed onto a rectilinear grid of 1024 × 1024 nodes. Every node is assigned to exactly one of the three phases: granule, matrix or void. Discs were considered as distinct elements, whereas the matrix was considered as one single element. Nodes were connected via brittle, linear springs within a horizon, which was set to be three nodes in each direction. The bonds were classified to three cases: (I) connecting two nodes within the same material phase in the same element (node in ρ^p_{discX} to node in ρ^p_{discX}, all nodes within ρ^m to each other), (II) connecting two nodes within the same material phase in different elements (node in ρ^p_{discX} to node in ρ^p_{discY}) or (III) connecting nodes of different material phases (node in ρ^p to node in ρ^m). Whereas bonds of case (I) belong to either the particle of matrix phase, all bonds of case (II) and (III) represent interfaces. Therefore an interface layer was considered to be present around all discs, even if two discs are in contact with each other. Depending on the cases, the bonds were characterized by an elastic modulus E_p, E_m and E_i and toughness K_p, K_m and K_i (particle, matrix, interface). Large and small discs were assumed to have the same elastic and toughness properties: E_p and K_p.

Parameter choice and parametric study

The parameter values for elasticity E and toughness K of the different phases are summarised in Table 5.6. The parameters were chosen to be similar to the values reported in [183], taking into account nano-mechanical measurements of starch and protein inside wheat endosperm by atomic force microscopy [173].

The aim of this study was to vary two mechanical parameters: the toughness of the starch phase K_p and the toughness of the interface K_i. Starch toughness K_p was varied between $K_m \leq \mathbf{K_p} \leq 3.5K_m$ in steps of $0.5K_m$. Three values for interface toughness were investigated: $\mathbf{K_i} = [0.5K_m, 0.8K_m, 1.0K_m]$. Results are expressed in terms of the relative toughnesses $\mathbf{K_p}/K_m$ and $\mathbf{K_i}/K_m$.

Table 5.6. – The model parameters elasticity E $[Pa]$ and toughness K $[Jm^{-3}10^{-4}]$ for the phases are summarised. The bold parameters $\mathbf{K_p}$ and $\mathbf{K_i}$ were varied for the parametric study.

matrix	particle	interface
E_m	$E_p = 4E_m$	$E_i = E_m$
K_m	$\mathbf{K_p} = K_m \ldots 3.5K_m$	$\mathbf{K_i} = 0.5K_m \ldots K_m$

Mechanical tests and damage Samples were submitted to quasi-static uniaxial tension or compression in the y-direction. The lower boundary was fixed, the side walls were free and the top wall (uppermost line of nodes) was submitted to displacement at constant speed until integrity failure occurred. Yield stress σ^y and Young's modulus E were obtained from the stress-strain curves. Yield stress σ_y was normalised by the yield stress of pure matrix: σ_y^{norm}. Damage was obtained from the number of broken bonds nb^p, nb^m and nb^i (particle, matrix, interface) and is represented either as percent of total damage to show the spread of damage in the different bond types:

$$D^p = \frac{nb^p}{nb_{total}} \tag{5.48}$$

$$D^m = \frac{nb^m}{nb_{total}} \tag{5.49}$$

$$D^i = \frac{nb^i}{nb_{total}} \tag{5.50}$$

Additionally, the damage scaled with volume fraction was calculated for matrix and particle to show the amount of damage relative to the volume of the phase in the sample:

$$DV^p = \frac{nb^p}{nb_{total}} \cdot \frac{1}{\rho_p} \tag{5.51}$$

$$DV^m = \frac{nb^m}{nb_{total}} \cdot \frac{1}{\rho_m} \tag{5.52}$$

$$\tag{5.53}$$

This second representation shows if damage preferably occurs in one phase more than another. As an example, a straight line of damage in the sample would cause $DV \approx 100$ in particles and matrix. Since the interface has no volumetric phase, interphase damage is shown differently. The amount of broken interface bonds relative to the theoretical amount of interface bonds in a straight line damage zone is calculated:

$$DB^i = \frac{nb^i}{(n^i/n^{total}) \cdot nl^{TH}} \tag{5.54}$$

with n^i being the total number of interphase bonds and nl^{TH} the theoretical amount of broken bonds in a straight line (1024 × 36).

5.3.3. Results

Damage distribution into phases

Particle toughness The relative toughness of particles compared to matrix (K_p/K_m) was one of the investigated parameters. Figure 5.29 shows examples of damaged, full sample volumes after tension for different K_p/K_m. In the case of weak interface $K_p/K_m < 1$ (Figure 5.29a to Figure 5.29c), the fracture path goes around the particles, mainly along the interface. If matrix and particles have the same toughness $K_p/K_m = 1$, the fracture can also go through particles. For a stronger interface (Figure 5.29d to Figure 5.29f), the fracture takes a slightly different path, which traverses the particles also for higher K_p/K_m. For the equivalency of all phases ($K_p = K_m = K_i$), the fracture tends to take a straight path. A slight branching occurs, which indicates the limit of the quasistatic regime. If pores are present in the matrix (Figure 5.29g to Figure 5.29i), fracture initiates at a different location.
Figure 5.30 on page 131 shows the influence of this relative toughness on the damage obtained by the three bond types. In Figure 5.30a, for high $K_p/K_m > 2.5$ there is no damage in the particle phase, but most of the damage is located at the interface and only <20 % in the protein matrix. For $K_p/K_m < 2.5$ the damage in the particle phase increases almost linearly with decreasing K_p/K_m, while damage in the interface and protein phase decrease. Two cross-point can be observed: for $K_p/K_m < 2.2$ there is more total damage in the particles than in the protein matrix. And for

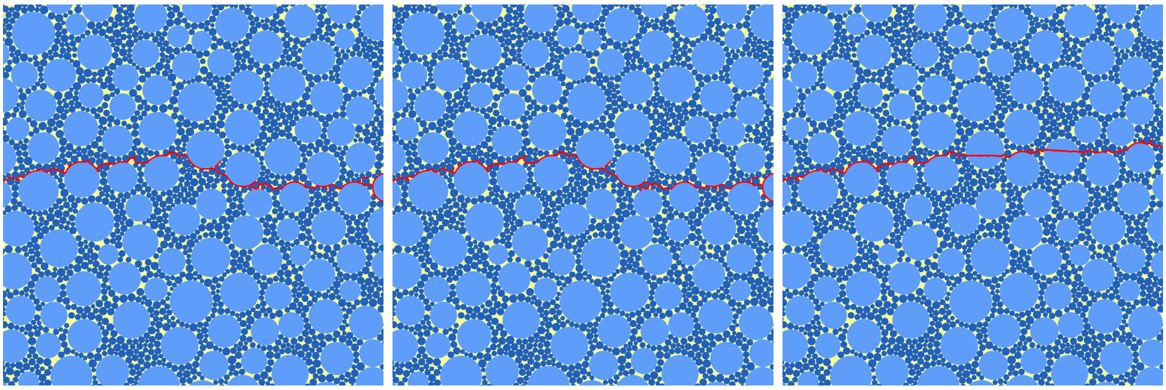

(a) Full, $\frac{\mathbf{K_i}}{K_m} = 0.5$, $\frac{\mathbf{K_p}}{K_m} = 3.5$ (b) Full, $\frac{\mathbf{K_i}}{K_m} = 0.5$, $\frac{\mathbf{K_p}}{K_m} = 2.5$ (c) Full, $\frac{\mathbf{K_i}}{K_m} = 0.5$, $\frac{\mathbf{K_p}}{K_m} = 1.0$

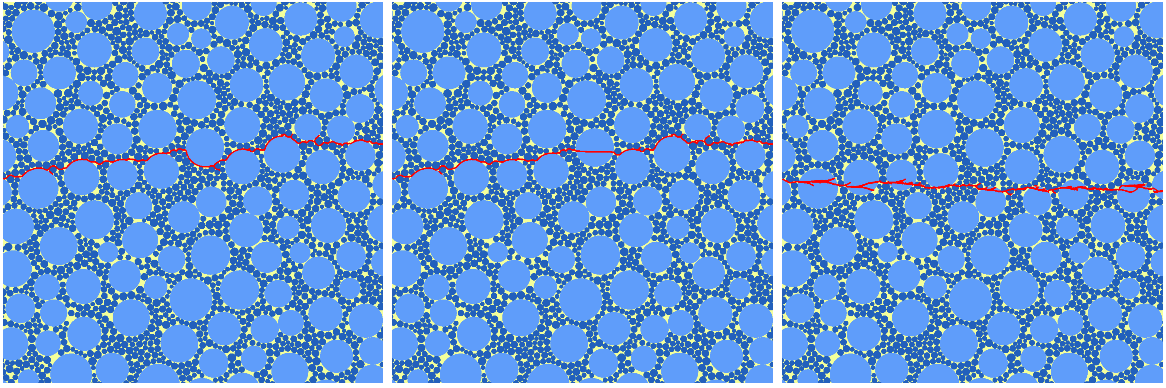

(d) Full, $\frac{\mathbf{K_i}}{K_m} = 1.0$, $\frac{\mathbf{K_p}}{K_m} = 3.5$ (e) Full, $\frac{\mathbf{K_i}}{K_m} = 1.0$, $\frac{\mathbf{K_p}}{K_m} = 2.5$ (f) Full, $\frac{\mathbf{K_i}}{K_m} = 1.0$, $\frac{\mathbf{K_p}}{K_m} = 1.0$

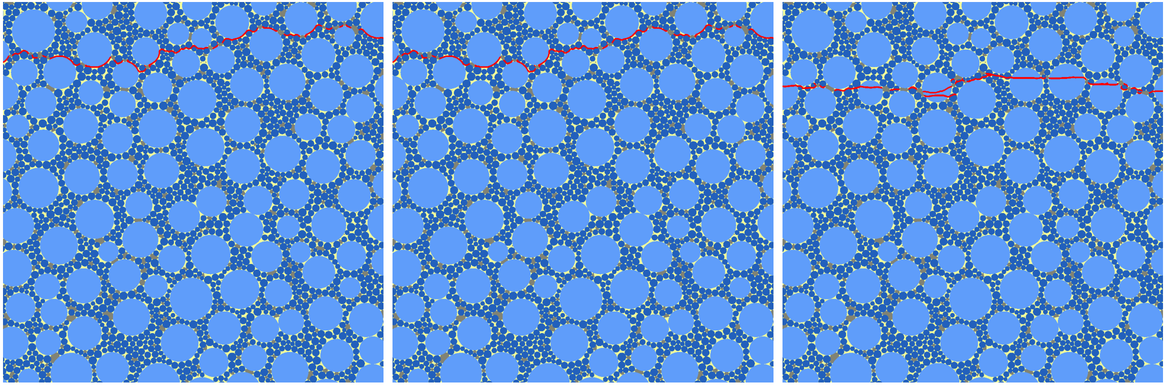

(g) Por., $\frac{\mathbf{K_i}}{K_m} = 1.0$, $\frac{\mathbf{K_p}}{K_m} = 3.5$ (h) Por., $\frac{\mathbf{K_i}}{K_m} = 1.0$, $\frac{\mathbf{K_p}}{K_m} = 2.5$ (i) Por., $\frac{\mathbf{K_i}}{K_m} = 1.0$, $\frac{\mathbf{K_p}}{K_m} = 1.0$

Figure 5.29. – Examples of sample volumes after failure under **tension** for varying particle toughness for (a-c) a weak interface in **full** samples, (d-e) a **strong interface** in **full** samples and (g-i) a **strong interface** in **porous** samples. Damage is shown in red.

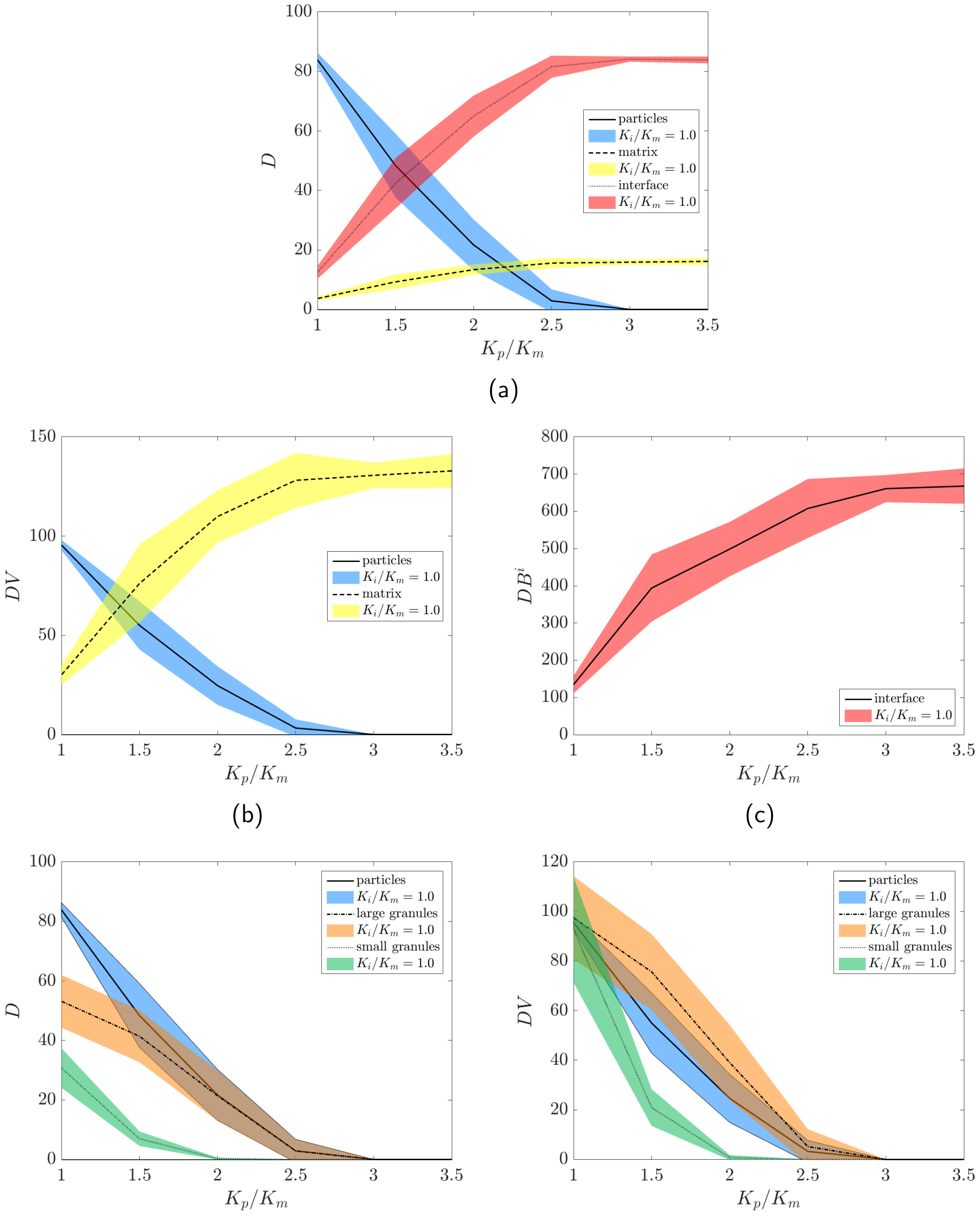

(a)

(b)

(c)

(d)

(e)

Figure 5.30. – (a) The distribution of damage within the three bond phases (starch, matrix, interface) is shown as percentage D of the total damage in **full** samples under **tension**. (b) The damage DV scaled with the respective volume fraction of starch and matrix. (c) The percentage of broken interface bonds is shown. (d) The distribution of damage into large and small granules separately is shown in percentage of the total damage D and (e) as scaled damage DV. Lines connect the averages of five simulations at each point; coloured areas show the standard deviation.

$K_p/K_m < 1.6$ more total damage is obtained in the particle phase than in the interface phase. Most of the damage to the particle phase is peripheral (Figure 5.29c).

Because $\rho^p > \rho^m$ more total damage is observed in the particles. It is therefore interesting to look at the scaled damage DV. Figure 5.30b shows the scaled damage DV in particle and matrix phase and it is visible that for high K_p/K_m the matrix sustains proportionally more damage. After crosspoint at $K_p/K_m \approx 1.4$ relatively more damage is obtained in the particle phase. Similarly, the relative interface damage DB^i shows that the interface always obtains more damage than it would, if the fracture formed a straight line. This is related to the fracture pathway going around the particles, visible i.e. in Figure 5.29a.

We are able to further separate the particle phase into the large and small granules. Figure 5.30d shows the evolution of damage in both starch phases separately, in percent D of the total damage and as scaled damage DV. The amount of damage clearly differs for large and small granules. Large granules, which make up almost twice the volume of small granules in the sample, always obtain more total damage and are getting damaged for $K_p/K_m < 3.0$. For $2.0 < K_p/K_m < 3.0$ damage in the particle phase proceeds exclusively through the large granules. Small granules obtain damage only for $K_p/K_m < 2.0$. This is not only related to the higher volume of large granules, since proportionally more damage proceeds though large granules (Figure 5.30e).

Interface toughness The second parameter that was investigated was the relative interface toughness K_i/K_m. The trends observed before with varying K_p/K_m are maintained also for different interface toughness (Figure 5.31 on page 133), but the curves and consequently the cross-points are shifted to lower values of K_p/K_m. Interestingly, for $K_i/K_m = 0.5$ this shift resulted in the fact, that the total damage in particle and matrix phase is always <24 %, even for $K_p = K_m$. Additionally, the maximum relative damage in the matrix phase is lowered for lower interface toughness and accordingly, the relative damage in the interface phase is higher (Figure 5.31b).

A very weak interface therefore limits damage to the matrix and particle phase (maximum <24 % for this specific case). Furthermore, only the large granules are damaged, whereas there is no damage at all to small granules (Figure 5.31c).

One particle damage controlling parameter: $\mathbf{K_p/K_i}$ In accordance with Topin et al. [180, 181, 182] we were able to extract a single parameter that controls starch damage: the relative particle-interface toughness (the ratio of particle to interface toughness):

$$K^r = \frac{K_p}{K_i} \tag{5.55}$$

If particle damage D and DV is expressed as a function of K^r, all particle damage curves collapse to form one curve only (Figure 5.32a on page 134), which is also true for the damage in small and large granules (Figure 5.32b). K^r does however not merge the damage curves of matrix and interface phase, indicating the maintained strong effect of interface toughness K_i/K_m (Figure 5.32a and Figure 5.32c).

The critical value K^r_c for which no particle damage is obtained, was found to be $K^r_c = 3.0$. Topin et al. found a lower critical relative toughness of $K^r_{c,Topin} = 2$ [181, 182]. The differences are most likely due to the differences in the elastic parameters (Table 5.4 on page 125) and indicates a possible influence of K_m.

Matrix porosity We investigated samples with a void fraction $\rho_v > 0$. Some examples of damaged samples are shown in Figure 5.29g to Figure 5.29i on page Figure 5.29g. Figure 5.33 shows the differences in damaged fractions between the porous and full samples in tension. The critical value

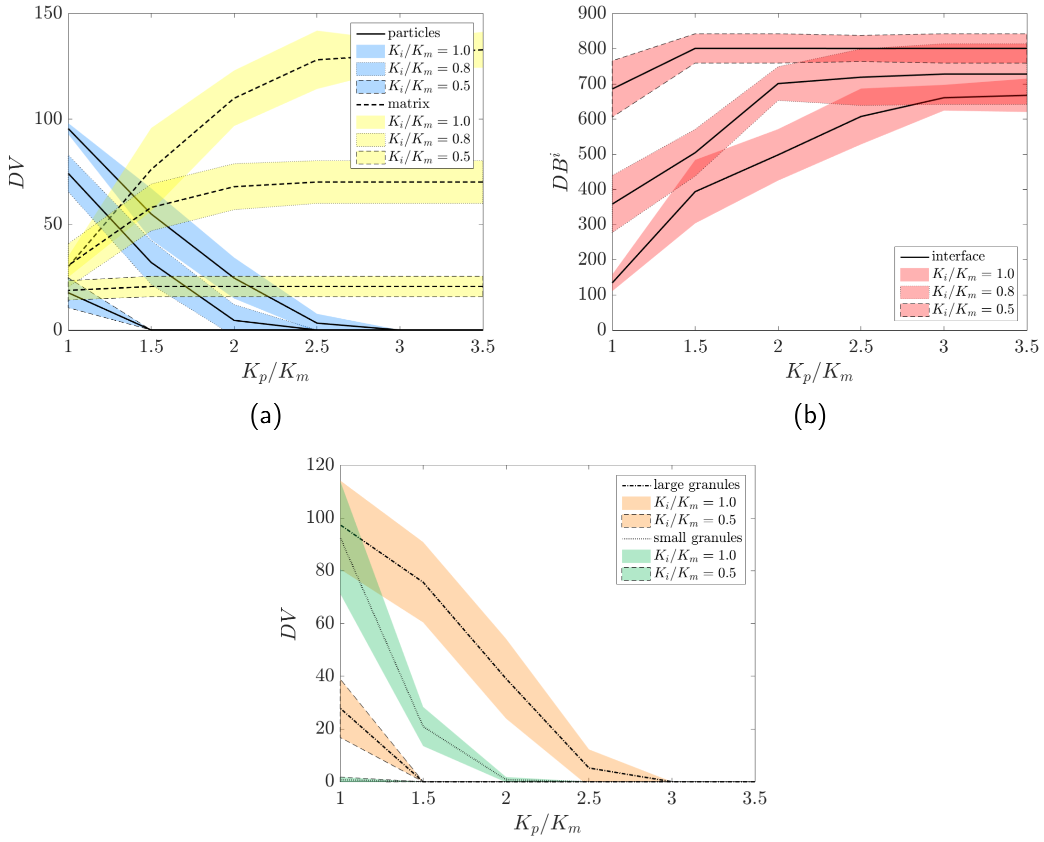

(a) (b)

(c)

Figure 5.31. – (a) The scaled damage DV in particles and matrix is shown in **full** samples under **tension** for different values of **interface toughness** K_i/K_m. (b) The percentage of broken interface bonds is shown for different interface toughness K_i/K_m. (c) The relative damage in large and small granules is shown for the highest and lowest investigated interface toughness.

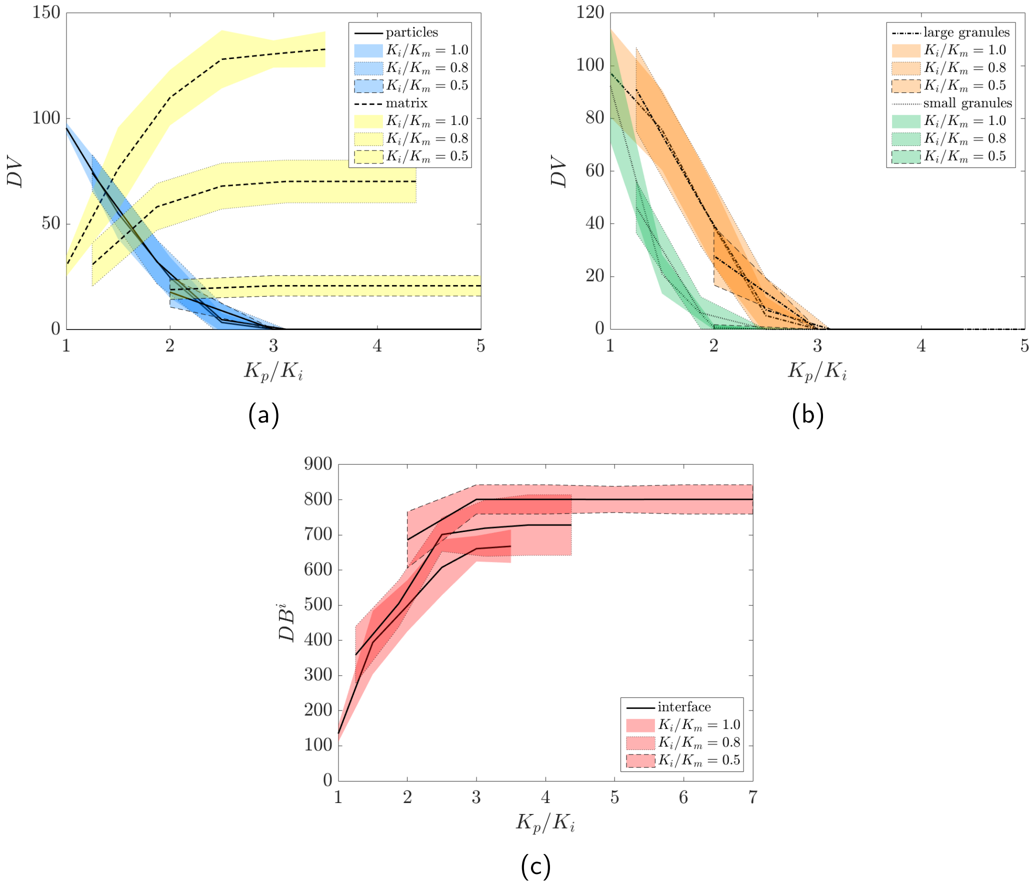

(a)

(b)

(c)

Figure 5.32. – (a) The scaled damage DV in **full** samples under **tension** in particles and matrix, (b) in large and small granules, and (c) the percentage of broken interface bonds is shown versus the **relative starch toughness** K_p/K_i.

K_c^r for particle damage is lower for the porous sample at $K_c^r = 2.5$, which is in agreement with the findings of Topin et al. [180]. Particle damage is slightly lower for the porous sample in the range of $1.5 \lessapprox K_p/K_i < 3.0$ in general. The relative particle-interface toughness K_p/K_i still merges the total particle damage curves and the large and small particle damage curves, shown in Figure 5.33d. In porous samples the damage in large and small granules is slightly more equivalent than in full samples, with lower damage in large granules and higher damage in small granules.

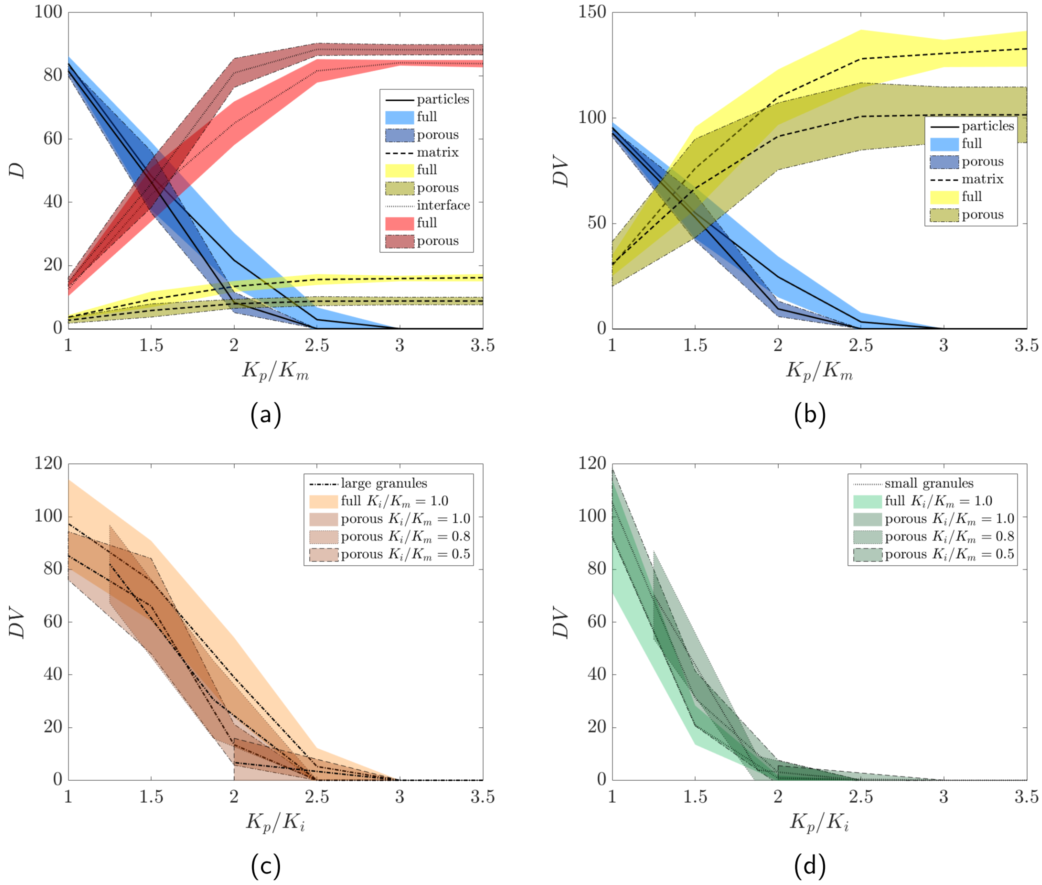

(a) (b)

(c) (d)

Figure 5.33. – In **full** and **porous** samples under **tension** for **strong interface** of $K_i/K_m = 1.0$ and high particle toughness $K_p/K_m = 3.5$ (a) the distribution of total damage into the phases D and (b) the scaled damage DV for particles and matrix is shown. For **porous** samples the damage into (c) large and (d) small granules is shown separately versus the **relative starch toughness** K_p/K_i in comparison with full samples with strong interface ($K_i/K_m = 1.0$.)

Testing direction (tension vs compression)

The same samples were tested in compression. Some examples of damaged samples are shown in Figure 5.34. The general trends, which were observed for tension are also observed for compression. The evolution of particle damage with K_p/K_m is similar to the one observed in tension (comparison Figure 5.35). The particle damage in compression is on the lower border of particle damage in tension for lower particle toughness, but higher in compression than in tension for higher particle toughness $K_p/K_m > 2.5$ (Figure 5.35a). For the tested range of particle toughness until K_p/K_m, the particle damage in compression is always above 0. The matrix phase obtains more damage in compression, whereas the opposite can be observed for the interface phase (Figure 5.35a).
Interestingly, the distribution of damage into small and large granules is opposite in compression to tension. Whereas in tension most particle damage was obtained in the large granules, the small granules obtain more total damage than large ones in compression and small granules also sustain relatively more damage than large ones (Figure 5.35c on page Figure 5.35c). Inter-sample variance is also found to be smaller in compression than in tension.
Whereas the relative particle-interface toughness K^r merges the damage curves in large particles, the collapse is less clear for small granules (Figure 5.35e), but inter-sample variance is also smaller in compression than in tension (Figure 5.32b on page 134).

Matrix porosity In tension, matrix porosity slightly loweres the relative particle and matrix damage. In compression, matrix porosity has less effect on the particle damage, but increases the relative damage to the matrix phase (Figure 5.36a and Figure 5.36b on page 139).

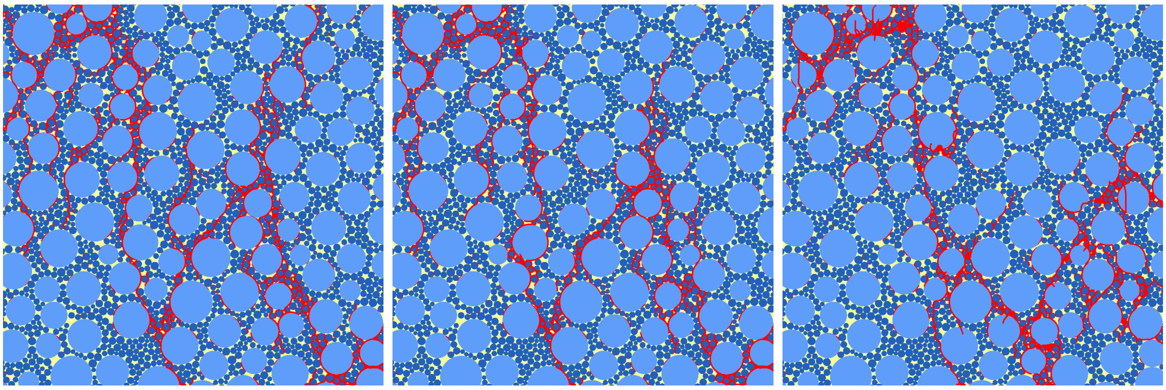

(a) Full, $\frac{\mathbf{K_i}}{K_m} = 0.5$, $\frac{\mathbf{K_p}}{K_m} = 3.5$ (b) Full, $\frac{\mathbf{K_i}}{K_m} = 0.5$, $\frac{\mathbf{K_p}}{K_m} = 2.5$ (c) Full, $\frac{\mathbf{K_i}}{K_m} = 0.5$, $\frac{\mathbf{K_p}}{K_m} = 1.0$

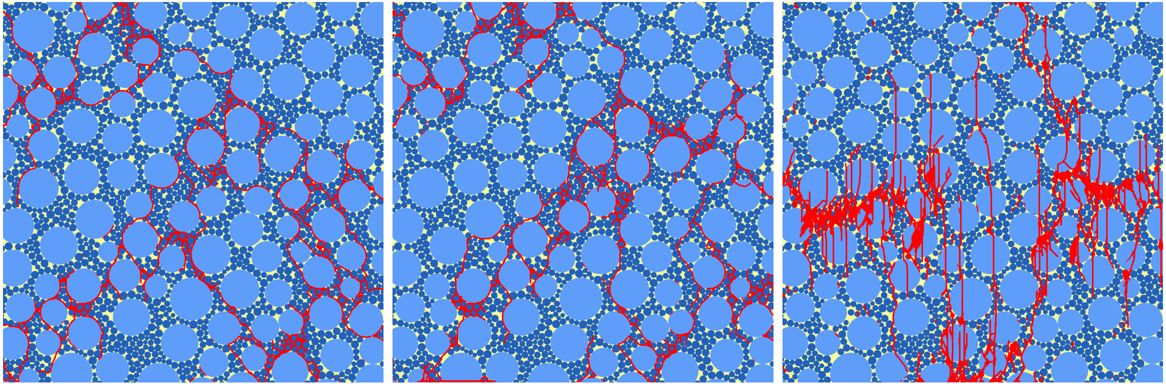

(d) Full, $\frac{\mathbf{K_i}}{K_m} = 1.0$, $\frac{\mathbf{K_p}}{K_m} = 3.5$ (e) Full, $\frac{\mathbf{K_i}}{K_m} = 1.0$, $\frac{\mathbf{K_p}}{K_m} = 2.5$ (f) Full, $\frac{\mathbf{K_i}}{K_m} = 1.0$, $\frac{\mathbf{K_p}}{K_m} = 1.0$

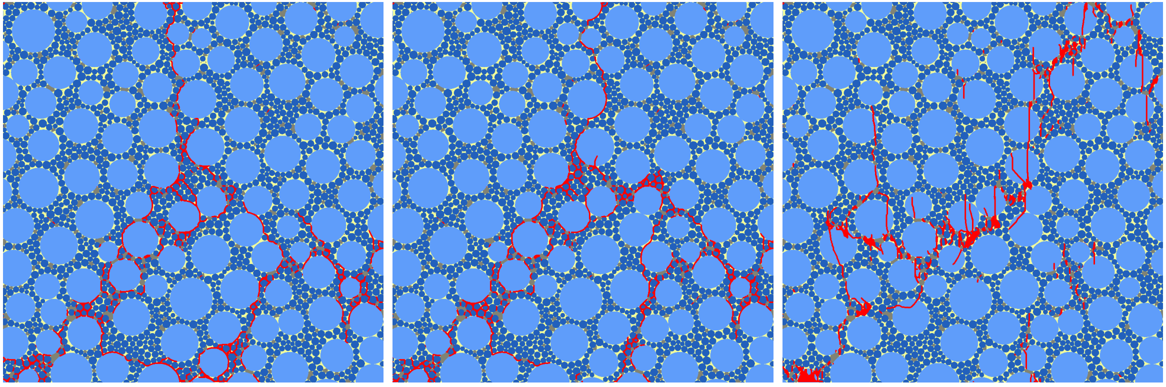

(g) Por., $\frac{\mathbf{K_i}}{K_m} = 1.0$, $\frac{\mathbf{K_p}}{K_m} = 3.5$ (h) Por., $\frac{\mathbf{K_i}}{K_m} = 1.0$, $\frac{\mathbf{K_p}}{K_m} = 2.5$ (i) Por., $\frac{\mathbf{K_i}}{K_m} = 1.0$, $\frac{\mathbf{K_p}}{K_m} = 1.0$

Figure 5.34. – Examples of sample volumes after failure under **compression** for varying particle toughness for (a-c) a **weak interface** in **full** samples, (d-e) a **strong interface** in **full** samples and (g-i) a **strong interface** in **porous** samples. Damage is shown in red.

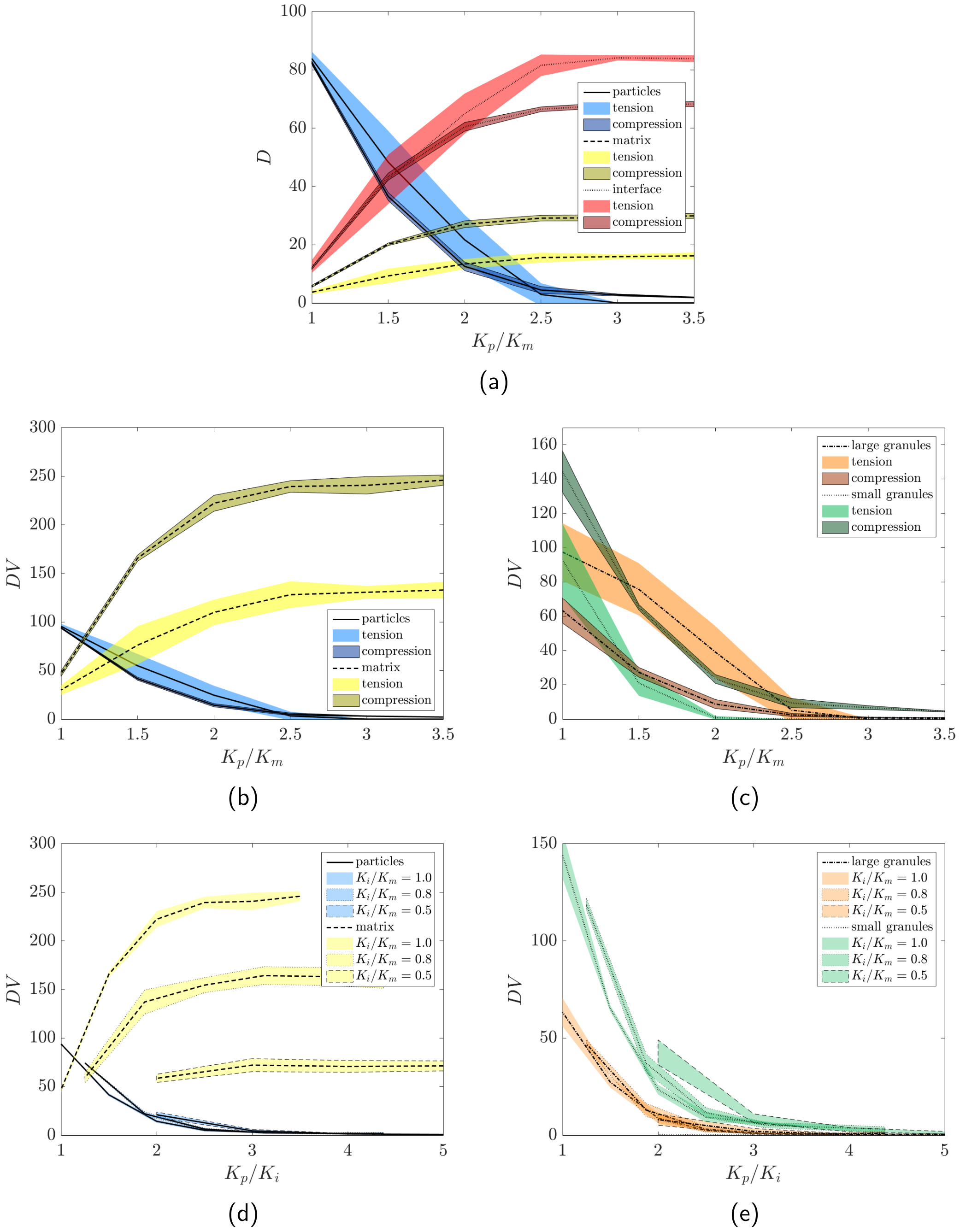

(a)

(b) (c)

(d) (e)

Figure 5.35. – For **full** samples in **compressive** and **tension** with **strong interface** the (a) distribution of damage within the three bond phases is shown in percentage of the total damage D, (b) the damage scaled DV, and (c) the distribution of scaled damage into large and small granules. For **full** samples after **compressive** failure the (d) scaled damage DV versus the **relative starch toughness** in particles and matrix is shown for different values of interface toughness K_i/K_m. (e) the scaled damage DV in large and small granules.

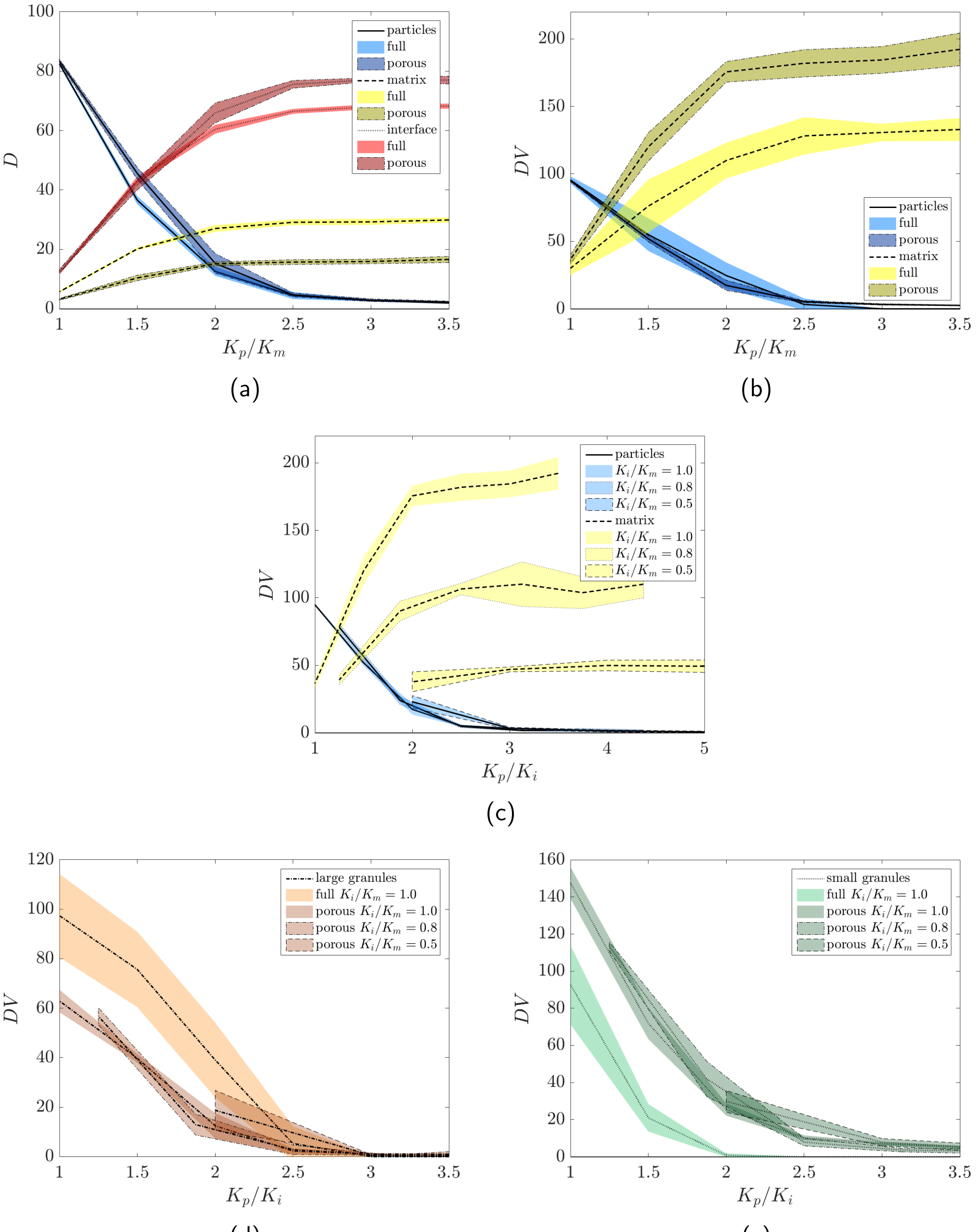

(a) (b)

(c)

(d) (e)

Figure 5.36. – For **porous** samples after **compressive** failure the (a) distribution of total damage within the three bond phases D is shown in percentage of the total damage is shown in comparison to full samples under compression, and (b) the damage scaled DV in large and small particles. For **porous** samples after **compressive** failure the (c) scaled damage DV versus **relative particle toughness** in particles and matrix is shown for different values of interface toughness K_i/K_m, (d) the scaled damage DV in large granules and (d) the scaled damage DV in small granules.

Overall comparison

The overall particle damage does not vary greatly with the testing direction or matrix state (Figure 5.37a), though damage tends to be higher in tension. However, the distribution of the damage into large and small granules varies. More damage is obtained in large granules in tension than in compression (Figure 5.37b), whereas more damage is found in small granules in compression (Figure 5.37c).

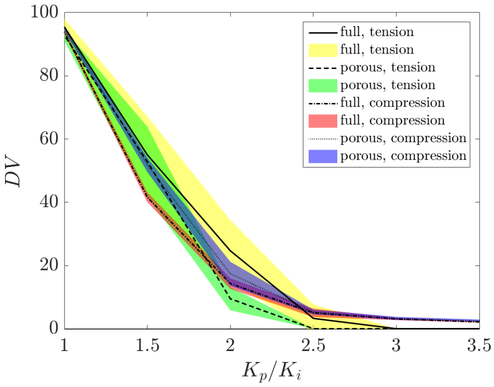

(a) All particle damage

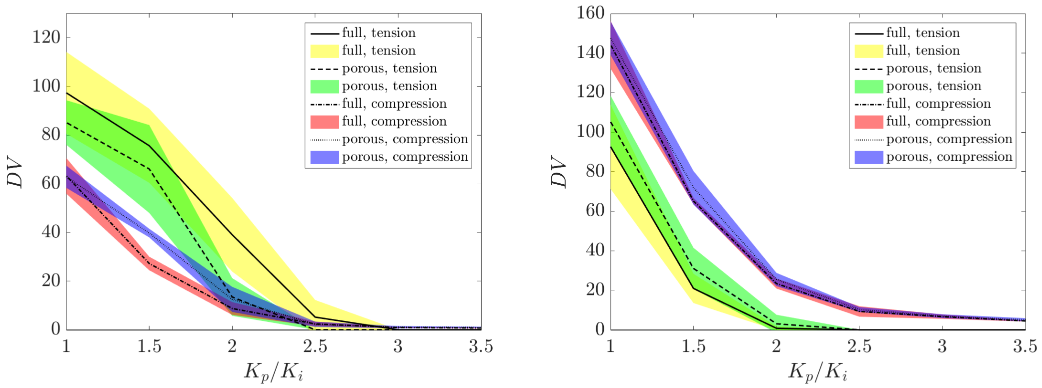

(b) Large particle damage (c) Small particle damage

Figure 5.37. – The (a) particle damage, (b) large granule damage and (c) small granule damage versus **relative particle toughness** is compared for the **tension** and **compression** and **full** and **porous** samples.

Strength properties

For each set of mechanical parameters the Young's modulus E and yield stress σ_y^{norm} were calculated as the average of all five different disc arrangements. Young's modulus and yield stress for different interface toughness, matrix state and testing direction are summarised in Table 5.7 and Table 5.8.

It was shown earlier that the yield stress scales with K_i (see section 5.2), which is confirmed by our findings for both testing directions.

A strong effect of voids on the modulus was already observed in other studies [180, 182, 183] and in the previous section (section 5.2). Yield stress is also affected by the presence of voids, resulting in a reduction of 48 %. The relationship of σ_y^{norm} to the amount of voids was studied in detail in [183, 181] and in section 5.2.

Table 5.7. – The Young's modulus E is summarised for different matrix states (full, porous), testing directions (tension, compression) and interface toughness $\mathbf{K_i}$.

	$\mathbf{K_i}$	E
Full	$1.0K_m$	$3.01\ (0.01)$
	$0.8K_m$	$2.99\ (0.01)$
	$0.5K_m$	$2.99\ (0.01)$
Porous	$1.0K_m$	$2.67\ (0.03)$
	$0.8K_m$	$2.66\ (0.03)$
	$0.5K_m$	$2.66\ (0.03)$

Table 5.8. – The yield stress σ_y^{norm} is summarised for different matrix states (full, porous), testing directions (tension, compression) and interface toughness $\mathbf{K_i}$.

	$\mathbf{K_i}$	σ_y^{norm}
Full, tension	$1.0K_m$	$0.58\ (0.04)$
	$0.8K_m$	$0.48\ (0.01)$
	$0.5K_m$	$0.30\ (0.01)$
Porous, tension	$1.0K_m$	$0.30\ (0.03)$
	$0.8K_m$	$0.25\ (0.02)$
	$0.5K_m$	$0.16\ (0.01)$
Full, compression	$1.0K_m$	$-1.90\ (0.07)$
	$0.8K_m$	$-1.42\ (0.03)$
	$0.5K_m$	$-1.03\ (0.02)$
porous, compression	$1.0K_m$	$-0.88\ (0.07)$
	$0.8K_m$	$-0.76\ (0.04)$
	$0.5K_m$	$-0.55\ (0.03)$

5.3.4. Conclusion

Particle damage is mostly affected by the relative particle-interface toughness $K^r = K_p/K_i$, leading to more damage for higher K_i and/or lower K_p. Young's modulus can be lowered only by the presence of voids in the matrix and particle volume fraction (see also section 5.2) and is not affected by K_i or K_p. Yield stress on the other hand is lower for lower K_i and/or more voids. The lowest yield stress is therefore obtained for samples with voids and low interface toughness.

It is difficult to relate our findings on particle damage to experimental data, because starch damage on endosperm bricks or cylinders is only qualitatively observed by scanning electron microscopy (SEM) on the fracture surfaces (examples shown in Figure 5.38) [170, 171]. Starch damage is however frequently measured in flour after milling, showing that harder wheats produce more starch damage during milling. The starch damage in flour from a durum wheat with PINs was for example about four-times lower than the starch damage in a unmodified durum wheat (section 3.1). These differences are believed to be caused by higher adhesion between protein matrix and starch granules in the starchy endosperm. In accordance with Topin et al. [181] and Chichti et al. [183], we prove the great significance of interface adhesion on starch damage. More precisely, the important factor

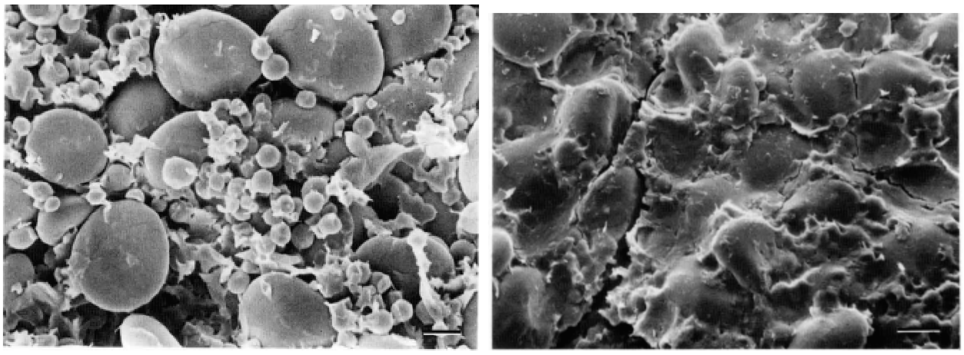

(a) Soft, non-vitreous common wheat after compressive failure

(b) Soft, vitreous common wheat after compressive failure

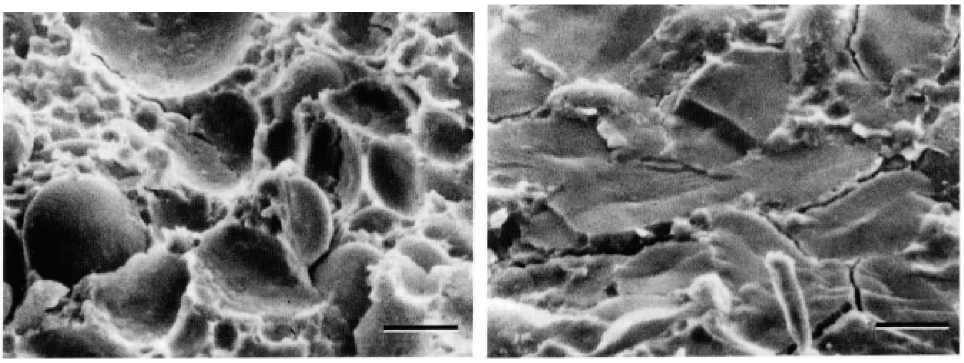

(c) Soft, non-vitreous common wheat after tensile failure

(d) Soft, vitreous common wheat after tensile failure

Figure 5.38. – SEM images of fractured surfaces of endosperm blocks after tension and compression tests from [170]. Scale bar: 10 µm

is the ratio of particle to interface toughness. Depending on that ratio we observed the relative particle damage to vary between 0 and almost 100 percent. The model therefore confirms that a four-times reduced amount of starch damage could be explained by differences in interface toughness. The porosity of the wheat samples also differed, but according to the simulations porosity has less of an effect than interface adhesion.

We demonstrated differences in the damage obtained by small and large particles in a bimodal granular material, mainly due to the testing direction. We also observed that low porosity (3.5 % of voids) has little effect on the total particle damage and the influence of porosity for the large and small particle damage is less than the influence of the testing direction.

Glenn et al. [303] observed in SEM images of fracture surfaces of the same wheat cultivar (Figure 5.38) strikingly more starch damage in vitreous than non-vitreous grains. According to our results, such a large difference would indicate a change in interface toughness, which is unlikely, since interface adhesion is believed to be controlled genetically and should therefore not change for the same cultivar. However, such SEM images only show a very small region of the fracture surface and do therefore not supply quantitative information. Additionally, one should keep in mind that the simulation results report the particle damage in percent of all damage and not the absolute damage.

A change of the mechanical properties of starch could also change the breaking behaviour as it was shown in this study. But the mechanical properties of starch still require further experimental investigation, as was demonstrated in chapter 4. The effect of a change of matrix properties is also still open for investigation, but, according to the Mori-Tanaka prediction, could also influence the

Young's modulus.

We highlighted the governing relationships of particle damage in a cemented granular material. The main factor influencing particle damage is the relative toughness of particles to interface, which is able to bundle particle damage for different matrix states and testing direction and therefore to predict particle damage. These results are in agreement with [180, 181, 300], even though differences in the critical toughness for the onset of starch damage are observed. Such differences are likely to be caused by the different parameters used for elasticity and toughness, since differences in matrix volume fraction were found to have little to no effect [300]. We observed that overall particle damage varies only slightly for different testing direction and matrix states, but that the spread of damage into large and small particles differs between compression and tension.

5.4. General discussion on modelling

Numerical results vs endosperm bricks

Numerical simulations of cemented granular material are undertaken with the goal to provide insight into the fracture behaviour of wheat during milling. The milling process is however complex, with different forces acting simultaneously on the grains (compression, shear and tension) and a direct comparison to meso-scale model samples would therefore be too simplistic. However, in order to investigate the starchy endosperm's mechanical properties a number of studies tested the mechanics of endosperm bricks or cylinders, which are simpler than the whole grain and closer to the numerical samples. Such experiments can measure the yield stress and Young's modulus of the starchy endosperm, which gives direct mechanical information and could therefore more easily related to numerical simulation results. A summary of the ratios of yield stress and modulus obtained from the literature for different wheat types by micro-mechanical experimental measurements is given in Figure 5.39.

The compressive yield stress of hard non-vitreous wheat was observed to be 55 % of the one of hard vitreous wheat. This correlates well with the results from the model of full to porous (3.5 % voids) samples of the same interface toughness (46 % to 54 %). In soft wheat, this ratio is lower. Since the (tensile) strength of porous samples was shown to largely depend on the porosity (section 5.2), this lower ratio is an indicator of either more porosity in soft non-vitreous wheat or a lower interface toughness than the one used in the model. The ratio of yield stress between non-vitreous hard to non-vitreous soft wheat was experimentally found to be between 0.49. This is also lower than what was found in the simulations between samples with the same porosity, but two-fold difference of interface toughness. Again, this would indicate either an even higher difference of interface toughness or a higher porosity in the soft samples.

From the little data on tensile strength it can be observed that soft vitreous wheat has 58 % of the tensile strength of durum or hard vitreous wheat. It was shown in section 5.2 that the tensile yield stress scales with the interface adhesion. The experimentally observed ratio could therefore be an indicator that the starch-protein adhesion is reduced by about half by puroindolines.

Experimental measurements of the Young's modulus resulted in more spread values. The simulations showed that any ratio between 0.4 and 1 is possible, depending on the porosity of the samples. For soft wheat, the experimentally observed ratio between vitreous and non-vitreous is lower than for hard wheat, which is indicating different ranges of porosity of the soft non-vitreous samples. The interface adhesion does however not influence the Young's modulus of the samples.

All of these observations combined indicate that the porosity of soft non-vitreous grains might be higher than the one of hard non-vitreous grains. This was also proposed by Dobraszczyk et al. [156].

Numerical results vs grain scale hardness measurements

It is interesting to confront the numerical results not only to the endosperm mechanical measurements, but also to grain-scale hardness measurements. The two most commonly used grain-scale hardness measurements are near infrared reflectance spectroscopy (NIRS) and the single kernel characterisation system (SKCS). NIRS evaluates the particle size after grinding [108], whereas SKCS measures the force necessary to crush individual kernels [110]. It is known that both methods do not measure the same grain properties [112]. NIRS hardness is very dependent on the genotype, which is believed to influence the protein-starch adhesion [112]. SKCS hardness was found to depend on genetics and vitreousness [112], which is an indicator of grain porosity. Mechanically, observations on SKCS hardness can be explained by observations on the yield stress from the simulations. SKCS

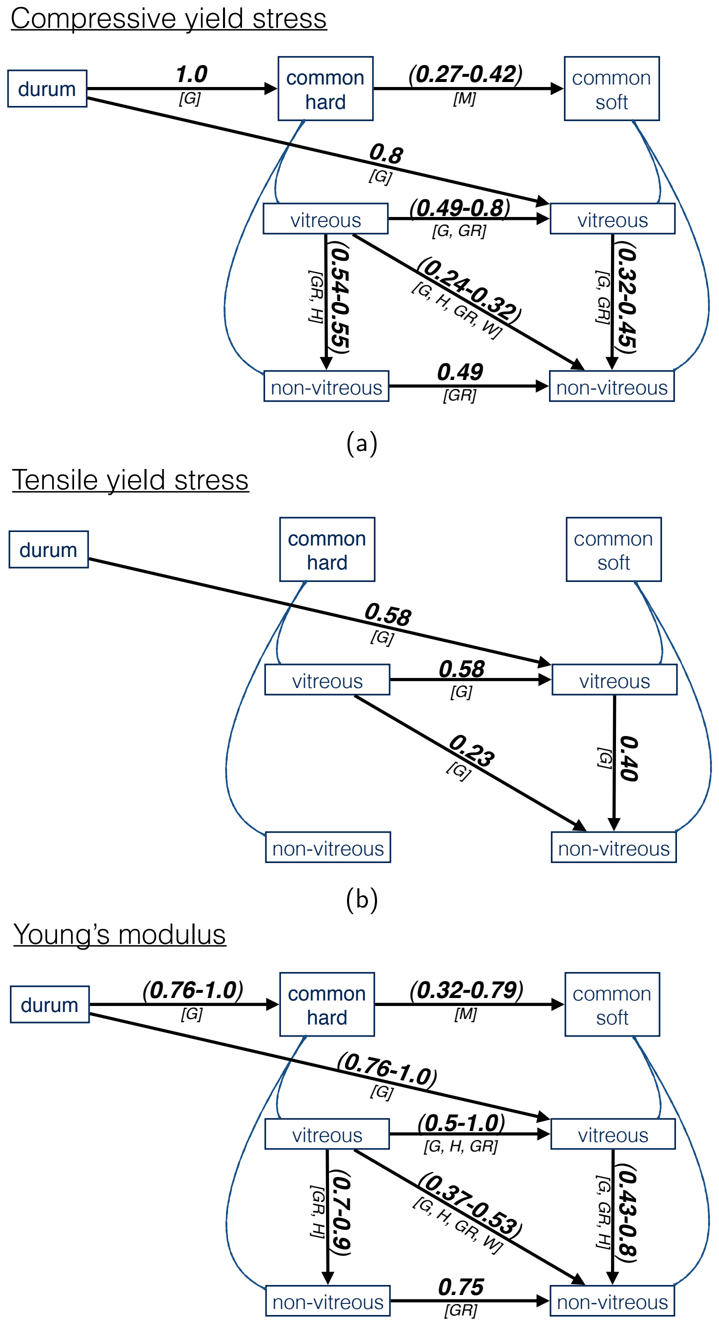

(a)

(b)

(c)

Figure 5.39. – Summary of yield stress and Young's modulus measured on endosperm bricks or cylinders from the data in the literature. Numbers mark the ratios: arrow head/ arrow tail. Reading example: The compressive yield stress of soft vitreous common wheat is 0.8 times the one of durum wheat. The sources are marked as: [G]-[170], [GR]-[131], [H]-[155], [M]-[14], [W]-[171].

hardness increases with vitreousness and a shift to lower values is observed for the soft genotype, while the slope is maintained (Figure 5.40a). This is very similar to our observations on the yields stress versus matrix saturation and the reduction of yield stress with reduced interface toughness. NIRS hardness measurements are known to depend mostly on the genotype, with a clear separation between (genetically) soft and hard wheats (Figure 5.40b). The particle size after grinding is related to the created surface, which can potentially be related to the total damage measured in the numerical simulations. We did not focus our observations on the total damage after failure, but an indication of created surface can be taken for example from the interface damage, because more damage on the interfaces implies more created surface. The simulations show that the interface obtains more absolute damage, if interface toughness is low, and slightly more, if the sample is porous. A slight trend of increase of NIRS hardness is observed for soft wheat (Figure 5.40b). Topin et al. [181, 182] showed an increase in the number of broken with a decrease of porosity, but only if the tensile strength of the interface is above a certain threshold. This would indicate that the protein-starch adhesion in soft wheat is not very low, which is however unlikely due to other results from different experiments and simulations (i.e. SEM images of fracture surfaces). Additionally, no clear trend between vitreousness and NIRS hardness can be observed for hard wheat, where it would be expected according to the results of Topin et al. [181, 182]. This might point towards a still unknown, additional factor involved in the fragmentation of wheat. Based on the results of our simulations, the spread in grains of hard genotype could be caused by different levels of interface adhesion, which could be the result of the different alleles possible for genetically hard wheat. Another possibility could be differences in starch hardness (connected to particle toughness in the model). So far, only one experimental study on the hardness of starch in wheat grains was done by Chichti et al. [135]. Though no clear differences were observed between the soft and hard NILs, a spread of starch hardness between ≈1.7 GPa to 3.0 GPa is present in the results. According to the simulation results, a two-fold difference of starch hardness could cause significant differences in the damage pathway.

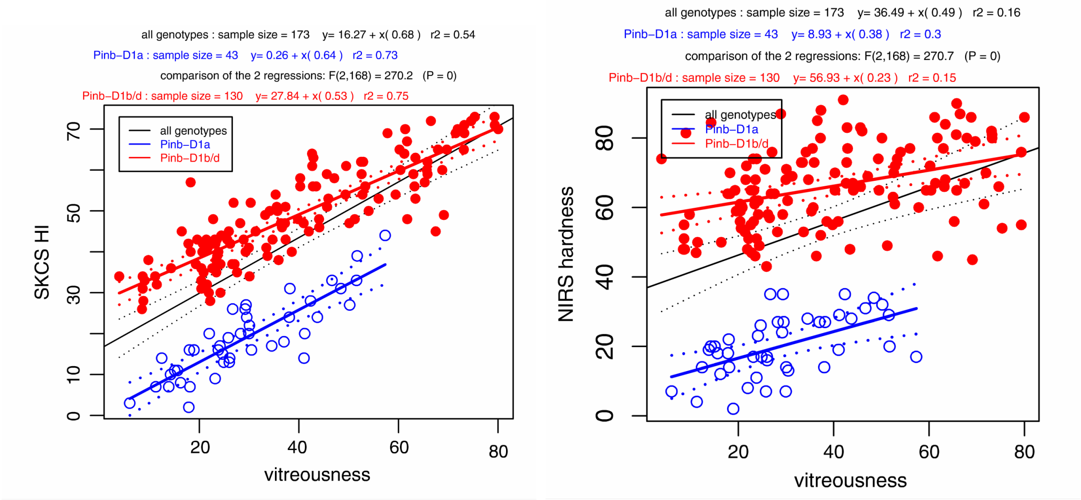

(a) (b)

Figure 5.40. – Results on the relationship of different hardness measurements with vitreousness from Oury et al. [112].

6. Conclusion

In this thesis the biomechanics of grain fragmentation were investigated with a combination of three approaches: experimental milling, atomic force microscopy nanomechanics experiments and numerical simulations.

With grain-scale milling experiments, it was shown that the introduction of puroindoline (PIN) genes results in changes of starchy endosperm structure, grain-scale hardness and milling behaviour. Of the grain scale characteristics, puroindolines affected the vitreousness and grain hardness, but not the protein content or the grain size. Concerning the milling behaviour, the presence of puroindolines lead to higher break flour yield, lower starch damage in flour, lower milling energy and different flour particle size distribution and tissue separation (Figure 6.1). These effects are also observed for genetically soft versus genetically hard wheat [131]. These results therefore suggest a general mechanism, by which puroindolines change grain hardness, independently of the genetic background in which they are introduced.
The structural changes are directly observable by changes in grain vitreousness. Whereas numerical simulations indicate that changes in porosity could account for changes in grain hardness and milling energy, certain observed milling characteristics (i.e. starch damage, flour particle size) imply an additional element determining the grain fragmentation. All our findings are in agreement with the hypothesis that puroindolines change the adhesion between starch and protein. A lower adhesion could also indirectly be responsible for the change of vitreousness. However, further research on the cause of the vitreousness changes observed in the presence or absence of puroindolines is required. All observed changes in grain characteristics and milling behaviour can be explained by a combination of reduced adhesion and reduced vitreousness.

The milling behaviour of the whole grain is caused by a combination of factors. To understand the underlying biomechanical mechanism, these factors and the properties of the grain's components need to be investigated separately. One possibility are nano-mechanical measurements by atomic force microscopy (AFM). In this thesis, the method of choice was contact resonance atomic force microscopy (CR-AFM), which was used to record maps of the contact modulus *in situ* in grains. The focus of these experiments was put on the starch granule.
AFM has great potential for applications in the biomechanical field, but it comes with certain limitations, which need to be kept in mind when interpreting the results. A source of artefacts was discovered for the chosen CR-AFM approach - the local surface slope - which greatly limited the interpretation of the measurements. Therefore, a correction approach was developed, based on the theory of CR-AFM.
The CR-AFM method with correction procedure was then applied to grain sections. For the first time, the mechanical properties of starches from a range of different botanical origin were investigated. No large differences in (micro-metre scale) contact modulus were found between most starch origins, except for starch granules in sorghum grains. These results trigger the questions, which components of starch determine the mechanical properties and what the underlying mechanism is. Answers would to be sought in the nano-metre scale mechanical and the biochemical properties of starch and its components. However, further investigation is needed to verify these

first results obtained by CR-AFM and to determine the sources of variation (between grains, imaging regions, granules). For future lines of investigation, CR-AFM experiments are potentially very interesting, for example to examine differences between large and small granules in bi-modal granule size distributions or the effects of grain pre-treatment.

The last approach was to numerically simulate the fragmentation behaviour of wheat endosperm. Numerical simulations serve two causes: to link the observed starch mechanical properties and grain fragmentation behaviour, but also to investigate, which other factors can explain grain-scale fragmentation behaviour. Numerical simulations of two-dimensional cemented granular samples samples were performed, which mimic the intermediary scale between grain and grain components.Such investigations are interesting for the understanding of wheat fragmentation, but also of any other cemented granular material. To predict the fragmentation behaviour of wheat endosperm as close to reality as possible, the mechanical properties of the components need to be known. These were based on previous nano-mechanical studies [135] and the CR-AFM results.
The simulation showed a number of relations between structural and mechanical properties of the material (Figure 6.1). The particle size distribution (PSD) of a non-porous cemented granular material was found to have an indirect effect on the sample's Young's modulus through the increasing particle volume fraction with higher polydispersity [1]. A slight increase of yield stress with increasing polydispersity could be attributed to the more homogeneous spatially distribution of stresses. Young's modulus and yield stress of porous samples are mainly governed by the degree of porosity. The influence of PSD varies with the degree of porosity. Correlations between wheat grain hardness and the starch granule size distribution (SGSD) are therefore difficult to predict and SGSD is expected to be only of minor influence compared to grain vitreousness.
In agreement with other studies, particle damage was found to be governed by the ratio of toughness between particles and interface. For the first time, particle damage in large and small granules was analysed separately. It was demonstrated that the testing direction has an impact not on the overall particle damage, but on the spread of damage within small and large particles.

A word on moisture One parameter, which potentially affects the results of all three approaches used in this thesis is moisture. Starch is a biological sample, which is known to change its structure, when wetted and heated [266]. Even without heat, some authors observed a significant swelling of starch granules by AFM, when wetted with cold water [212, 213]. It is not clear yet, to which extent the swelling changes the mechanical properties. For CR-AFM measurements this implies that measurement conditions (room temperature and humidity) should be controlled by performing measurements in an environmentally enclosed box. For the setup used in our experiments unfortunately no environmental enclosure was available. An attempt was made to keep conditions similar for all samples, by performing the experiments on the same day and therefore to allow for inter-sample comparisons, but a detailed investigation of the changes in the measured mechanical properties with increasing moisture would be beneficial.
Interestingly, moisture was reported to have a significant effect on the strength of endosperm cylinders, regardless of the wheat variety and therefore genotype [303]. Following the previous line of thought, it could be expected that the moisture changes the mechanical properties of the starch. Our simulation result indicate, that a decrease in particle toughness would not change the material modulus or yield strength, if the interface properties were unaffected. Potentially a decrease in starch modulus could affect the mechanical behaviour. The modulus of non-hydrated and hydrated starch could potentially be investigated by CR-AFM.
Starch is also known to swell, when hydrated. However, a swelling of starch granules would cause a

---

[1] in terms of size difference between large and small particles

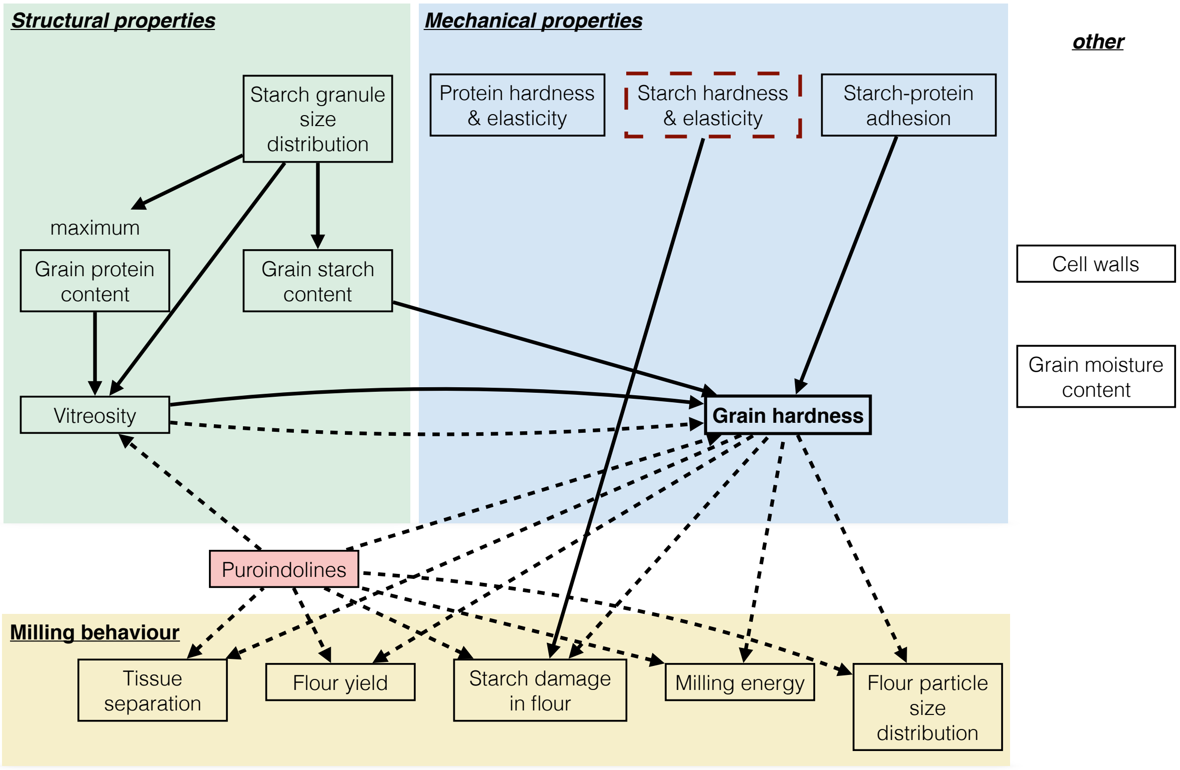

Figure 6.1. – The mechanisms underlying grain hardness and milling behaviour. Dashed arrows indicate relationships concluded from grain-scale milling experiments. Full arrows indicate relationships that could be pointed out by numerical simulations. The red dashed box shows the property investigated by the nano-mechanical AFM method. Other factors, such as cell walls and moisture content are possible perspectives for this line of study.

more dense structure (higher particle volume fraction), which should increase the modulus, opposite to what was observed by Glenn et al. [303]. Other non-starch mechanism could also be involved: changes of the protein hardness, starch-protein adhesion or cell walls.

6.1. Perspectives

Based on the results presented in this thesis, interests and needs for future research can be pointed out.

AFM

- The CR-AFM correction approach should prove to be useful not only for our object of study, but for any nano-mechanical AFM measurements based on tip-sample contact.
- In the light of the limitations of AFM, a re-consideration of what is described in the literature about starch blocklet and growth ring structure seems necessary.
- Our CR-AFM measurements on starch from different origin should be further verified. An investigation determining the variation between grains, between regions in the same grain and between granules in the same region should be performed, collecting enough data to be statistically relevant for each case.
- CR-AFM measurements in starch under controlled humidity would be of interest to investigate possible changes in modulus due to humidity.
- In the same sense, an extensive study of starch hardness of different wheats would be of interest, because it could explain differences in fragmentation behaviour, as was discussed in section 5.4.

Simulations The simulations approach can be improved in several ways.

- The model used in this thesis does not take into account the cell walls in the endosperm. Piot et al. [304] found no significant differences of cell wall composition between wheats of different (mechanical) hardness levels, which suggests that cell wall composition is not an important factor in grain hardness. However, cell walls and the development of endosperm components within cells, compartmentalise the endosperm. This can be expected to have an influence on the fragmentation behaviour and would therefore be an interesting aspect to investigate with the here presented modelling approach.
- One problem with relating the numerical findings to experiments is certainly the difference in dimensions between the 2D model and 3D experiments. It was stated by Joliff et al. [305] that a 2D model of a material with spherical inclusions does not accurately predict the mechanical behaviour. It was overpredicting the modulus for fully cohesive case and underprediciting the modulus in the non-cohesive case. However, Affes et al. [300] confirmed the main findings of a 2D model [180] in a 3D model. Performing all simulations in 3D would be preferable, but it comes with a high computational cost. A small number of 3D simulations could investigate, if the trends we observed for 2D are maintained in 3D.
- In the simulations the particle shape is assumed to be spherical for large and small particles. While this is rather the case for small wheat starch granules, the large wheat starch granules have more of an ellipsoidal shape. To simulate the endosperm more accurately, the effect of shape should be investigated.

- The current compressive simulations do not take into account friction at the grain-grain contacts after bond failure. This could be implemented for a more accurate depiction of grinding.
- All simulation were performed in quasi-static conditions. Wheat grinding is however a highly dynamic process. The peridynamics code allows for the investigation of fracture in dynamic conditions, which would be of great interest. Additionally, the sample shape could be adapted to be spherical instead of square (Figure 6.2a).
- The size of fragments after failure could be determined in the fractured samples (Figure 6.2b). Such a parameter could be better related to grain-scale measurements of near infrared reflectance spectroscopy (NIRS) hardness. This would be especially interesting after dynamic tests.
- Finally, the starch damage on fracture surfaces of endosperm bricks could be evaluated quantitatively from scanning electron microscopy (SEM) images (Figure 6.3), which would be better relatable to results from simulations.
- It is possible to obtain balls of starchy endosperm by debranning wheat grains and to investigate their milling behaviour. Such balls could be well resembled by spherical, 3D numerical samples. A direct comparison of milling of endosperm balls to dynamic numerical simulations of spherical 3D samples, possibly with cell walls, would provide interesting information on how accurate the simulations can predict the milling behaviour.

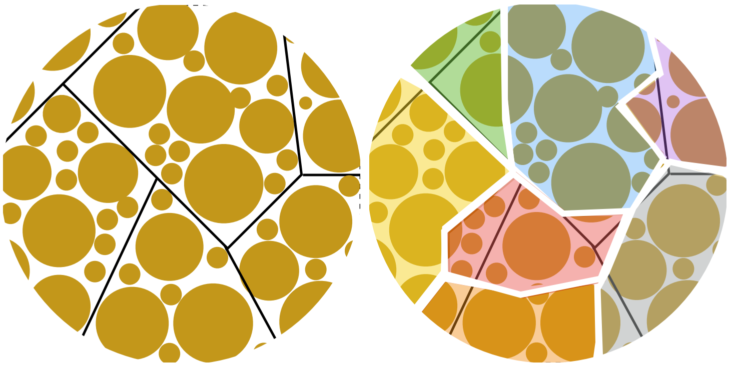

(a) (b)

Figure 6.2. – (a) Schematic idea of simulations on round samples with cells walls (black lines). (b) The fragment size after (dynamic) failure could be determined with floodfill algorithms.

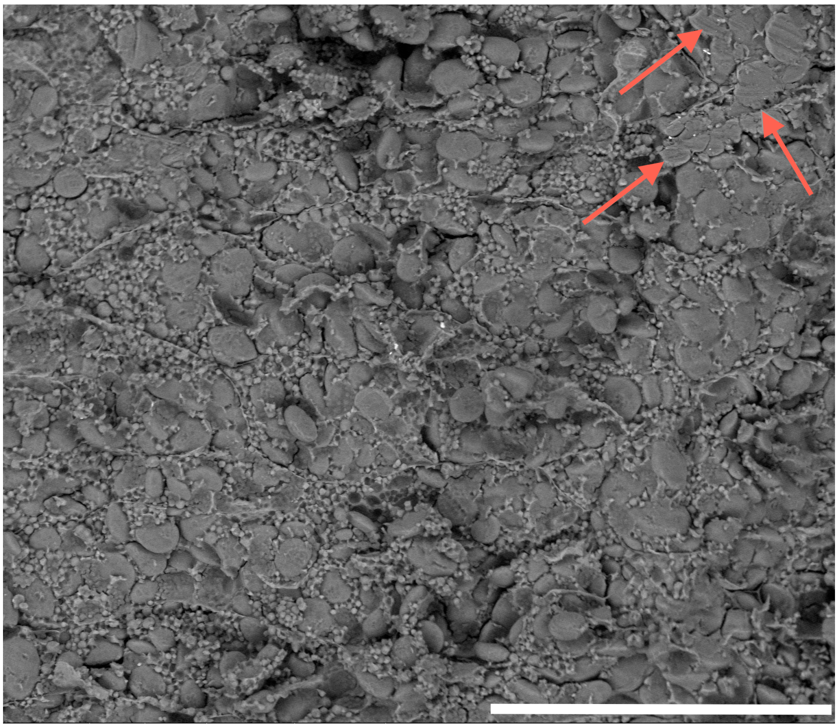

Figure 6.3. – A SEM image of a fracture surface after grain fracture is shown (unpublished data provided by V. Lullien-Pellerin). Damaged starch can be seen in the upper right corner (arrows). The percentage of damage starch could possibly be evaluated by image analysis. Scale bar: 200 µm

Résumé en français

Le blé est l'une des cultures céréalières les plus importantes au monde, utilisée pour l'alimentation humaine et animale mais aussi pour des applications non alimentaires. L'utilisation du blé sous formes de fractions telles que la farine ou la semoule met en jeu des opérations complexes qui nécessitent l'utilisation de différents broyeurs ou meules puis la séparation des particules engendrées pour séparer notamment le coeur du grain (ou albumen) des parties périphériques (germe et enveloppes). L'amélioration des processus impliqués dans le broyage du blé nécessite une meilleure compréhension des mécanismes de fragmentation. Le grain de blé est une structure biologique complexe dont la biomécanique dépend intimement de l'agencement de différentes phases et interfaces. L'albumen amylacé représente la majeure partie du grain en volume et ses caractéristiques sont le principal déterminant du comportement au broyage.

L'albumen amylacé des céréales en général et celui du blé en particulier sont des matériaux composites [9] contenant une phase dense d'inclusions sous forme de particules relativement sphériques enchâssées dans une matrice protéique. Le comportement mécaniques de ce type de composite relève de celui des matériaux granulaires cohésifs ou cimentés et est proche de matériaux tels que les bétons ou les enrobés bitumineux. Toutefois, du fait de la nature biologique et de la faible taille des hétérogénéités de structures (inférieures au micromètre) présentes dans l'albumen, l'étude de ses propriétés mécaniques reste une tâche complexe.

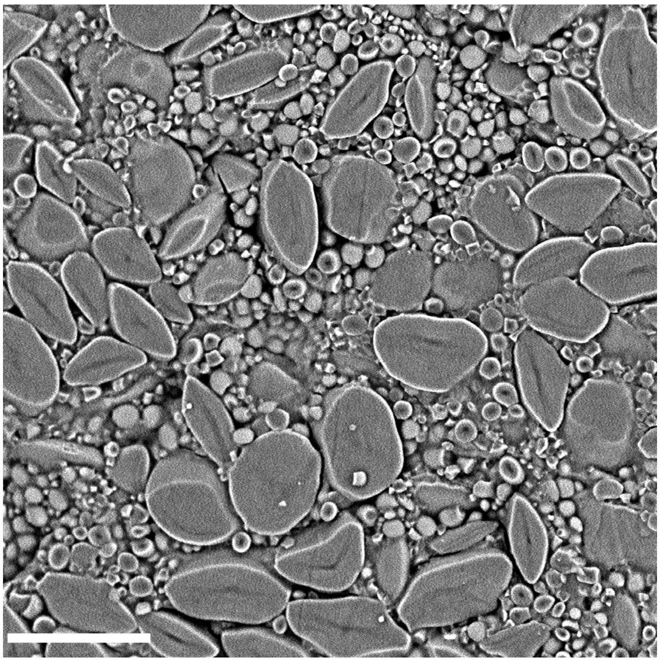

FIGURE 6.4. – MEB d'albumen du blé. Barre d'échelle : 30 µm.

Le broyage est une opération qui met en jeu des grandes déformations et une multi-fissuration du matériau. Néanmoins il a été montré qu'il existe de fortes corrélations entre le comportement au broyage et la mécanique de la rupture des grains. Celles-ci dépendent de la structure du grain et des propriétés de ses composants. Le comportement de l'albumen peut être étudié à partir de milieux modèles dont les propriétés sont bien maitrisées à l'échelle des constituants. Une autre approche, qui a l'intérêt de faciliter les études paramétriques extensives est la mise en oeuvre d'un modèle numérique représentant les caractéristiques les plus importantes de l'albumen. Ce type de modèle permet de tester des hypothèses sur la structure du matériau (qui dépend de la génétique et des conditions de culture) sur le comportement au broyage.

La structure de l'albumen est complexe et implique l'agencement de nombreuses molécules et polymères. Au sein de l'albumen, on considère généralement deux principaux composants qui sont l'amidon et le gluten. Les protéines de réserves présentes dans l'albumen sont en effet capables de former un réseau de très haut poids moléculaire appelé gluten dont la structure complexe est loin d'être résolue, il sera considéré ici comme une phase homogène. L'amidon est composé essentiellement de deux types de polysaccharides, l'un d'entre eux étant fortement ramifié, qui forment à plus grande échelle des granules de structure organisée de taille micrométrique.

Un grand nombre de connaissances pratiques sur le broyage du blé ont été capitalisées et on peut faire remonter l'origine de certains savoirs à plusieurs milliers d'années. Plus récemment, la recherche expérimentale dans le domaine de la meunerie a permis d'obtenir de plus en plus de résultats sur des lots de grains bien identifiés et sur des lignées aux caractéristiques génétiques de mieux en mieux maitrisées. Cependant, les études paramétriques étendues du blé sont coûteuses en temps de recherche pour aboutir à la sélection de variétés contrastées, la mise en culture, et la récolte dans différentes conditions culturales. En outre, les processus physiques impliquant la micro-mécanique du broyage à l'échelle des meules se passent en des temps caractéristiques de quelques millisecondes les rendant difficilement observables. Des test efficaces et systématiques de nouvelles hypothèses à grande échelle sur le comportement à la mouture reste toujours difficile a mettre en oeuvre.

Une étude approfondie du broyage du blé (ou des céréales en général) doit intégrer à terme des résultats issus de domaines scientifiques variés tels que la biomécanique mais aussi l'agronomie, la génétique, la biochimie, la botanique, l'ingénierie alimentaire, la bioinformatique. Il est évident qu'une compréhension globale du comportement au broyage et de ses enjeux en terme de production de produits finis n'est possible qu'avec une telle approche multidisciplinaire. Le travail présenté dans cette thèse de doctorat vise à accroître la connaissance de la biomécanique du fractionnement du blé en se concentrant sur un petit nombre de questions et de méthodes. Trois approches majeures sont mises en oeuvre et s'appuient sur : le broyage expérimental de grains de blés, des essais au Microscope à Force Atomique (AFM) et des simulations numériques du comportement mécanique et de la rupture. Dans ce qui suit, un bref aperçu des principaux est donné en suivant la chronologie des chapitres de la thèse.

Les puroindolines sont des protéines du grain de blé qui jouent un rôle important dans la résistance mécanique des grains. Il semble que leur présence fragilise les grains en générant une adhérence faible entre les granules d'amidon et la matrice de gluten [12]. Les puroindolines sont codées sur un locus spécifique au chromosome 5D dans le blé tendre Triticum aestivum [13]. Lorsqu'elles sont présentes sous forme sauvage dans le blé tendre les grains sont friables et qualifiés de "soft" alors que les mutations sur les allèles de puroindolines conduisent à un blé plus dur appelé "hard" [13]. Le blé dur (ou Triticum durum) qui ne possède pas le chromosome sur lequel se trouvent les allèles de puroindolines présente des grains encore plus durs que le blé tendre [13]. Des manipulations génétiques ont permis une translocation des gènes codant les puroindolines dans le blé dur [14], affectant considérablement les propriétés au broyage [14].

Les caractéristiques physiques du grain et le comportement au broyage d'une lignée de blé dur dans lequel les gènes de puroindolines de type sauvage ont été transloquées (Svevo-Pin) ont été comparés à une lignée parente (Svevo). Les seules différences observées ont été leur résistance mécanique et la porosité de l'albumen amylacé (révélée par la mesure de vitrosité ; mesure optique qui est corrélée à la présence de pores). Une augmentation significative du taux de farine produite et une diminution du rendement en semoule et de l'énergie de broyage ont été observées pour le Svevo-Pin. En outre, la distribution granulométrique obtenue pour la farine de Svevo-Pin est cohérente avec la tendance générale des courbes granulométriques obtenues pour des blés de type soft comportant une adhérence inférieure entre granules d'amidon et matrice protéique attribuée à la présence de puroindolines de type sauvage. La fraction de sons grossiers est plus importante pour le Svevo-Pin, qui traduit une proportion plus élevée d'albumen amylacé qui se retrouve intimement lié à la fraction de son et qui est donc difficilement récupérable. Par ailleurs, la farine provenant de la lignée de blé dur (durum) se trouve être inversement enrichie en acide phytique, un marqueur cellulaire de la couche à aleurone. Le taux d'amidon endommagé est également inférieurs dans les farines Svevo-Pin par rapport à celui des les farines Svevo, du fait de la plus grande fragilité de l'albumen.

L'amidon est l'un des principaux composants de l'albumen de blé [16] et est présent dans le blé sous la forme de granules d'amidon de tailles micrométriques. La détermination des propriétés mécaniques de l'amidon à petite échelle est précieuse pour une meilleure compréhension du comportement mécanique de l'albumen. La microscopie à force atomique (AFM) est un outil de plus en plus utilisé pour les mesures mécaniques. Celle-ci peut fournir la résolution requise pour cartographier les propriétés à l'échelle des phases et a été utilisé dans cette thèse pour l'étude in situ de la structure de granules d'amidon. Une brève revue de la littérature sur l'imagerie AFM concernant l'amidon est présentée. Cette revue met l'accent sur les avantages et les limites des techniques AFM. Les différences structurelles d'amidons qui ont un effet potentiel sur la mécanique sont ensuite discutées. Dans cette thèse, une méthode AFM basée sur la résonance de contact a été mise au point. Cette méthode a été choisie pour cartographier les propriétés mécaniques de granules d'amidon à l'échelle de la centaine de nanomètre. Ces granules sont observés dans des coupes de grains préparées par des techniques peu invasives sans incorporation de résine. Cependant, les surfaces obtenues restent entachées de fortes variations topographiques qui ont des répercussion sur l'interprétation directe des résultats. En effet, du fait de pentes importantes l'angle local de la pointe AFM avec la surface peut atteindre des angles de ± 50 degree. La corrélation non triviale entre cette pente et la fréquence de résonance au contact (CR) rend complexe l'interprétation directe des mesures de module sur ces échantillons. L'influence significative de l'angle de contact sur la fréquence CR est étudiée en détail et une méthode pratique est développée pour corriger les mesures. Cette méthode s'appuie sur des modèles analytiques permettant de prendre en compte les effets de l'inclinaison et de déduire la variation non linéaire des deux premiers modes de fréquence CR pour une large gamme d'angles. Les calculs sont ensuite confirmés par des expériences CR-AFM effectuées sur une surface bien définie, incurvée et dont les propriétés mécaniques sont homogènes. Enfin, le modèle est appliqué pour cartographier le module de contact à l'intérieur d'un granule d'amidon de blé. Finalement cette approche se révèle être prometteuse pour l'étude de l'élasticité des matériaux biologiques à petite échelle dans une gamme de modules de quelques GPa.

L'amidon constitue une forme de stockage du carbone et est une ressource en énergie pour les premier moments de la vie de la plante. Il est composé de deux polymères de glucose : l'amylose et l'amylopectine dont la proportion varie respectivement entre 15 % to 30 % et 70 % to 85 %. Des mutants de type "waxy" (<15 %) ou "high amylose" (>15 %) permettent de faire varier plus largement la concentration en amylose. Les propriétés de l'amidon sont exploitées pour l'alimentation animale et humaine au travers de produits transformés ou après extraction en papeterie, textiles, plastiques, biocarburant' Du fait de l'importance de l'amidon, de nombreuses caractéristiques physicochimiques associées aux granules ont été étudiées dans la littérature en fonction l'origine botanique des grain(e)s. Il peut s'agir par exemple de la forme, du nombre, de la répartition des granules d'amidon, de leur pourcentage de cristallinité, de l'aptitude à l'hydrolyse par les enzymes de digestion' Pourtant, très peu d'études concernent la caractérisation des propriétés mécaniques in situ qui jouent un rôle central sur le comportement au broyage des grain(e)s et sur le taux d'amidon endommagé lors des étapes de transformation. Pour préciser le comportement mécanique à petite échelle, une première approche basée sur des essais de type "scratch test" a été développée dans une précédente thèse. Elle utilise une pointe de microscope à force atomique (AFM) pour endommager en surface le granule au sein d'un grain de blé. Cette approche a permis de mettre en évidence des duretés du même ordre de grandeur que celle d'un autre matériau biologique, la dentine, alors que la matrice protéique entourant les granules présentaient une dureté moindre de l'ordre de celle du talc. Dans la continuité de ces travaux la méthode de résonance de contact mise en ¡uvre a été utilisée pour mesurer le module de contact des granules d'amidon de grain(e)s de différente d'origines botaniques (céréales de type C3 ou C4, légumineuses). Les résultats de cette campagne d'essais ainsi que la capacité de l'AFM à rendre compte des propriétés mécaniques de l'amidon sont discutés au regard des connaissances actuelles sur sa structure et ses propriétés physicochimiques.

La modélisation numérique est une approche complémentaire à la recherche expérimentale qui permet de tester et valider certaines hypothèses, notamment dans le cadre d'études paramétriques. L'albumen de blé peut être considéré comme un matériau granulaire cimenté et des simulations sur le fractionnement du blé peuvent donc être effectuées dans le cadre de la recherche sur les matériaux granulaires. Une question qui relève de la mécanique est dans quelle mesure les propriétés de l'albumen de blé sont influencées par la distribution granulométrique des granules et leur assemblage. Pour préciser cette question une étude paramétrique a été réalisée. On considère l'albumen de blé comme un assemblage compact bidisperse de granules (particules) collés entre eux par une matrice. Il a été fait varier le rapport de taille des petit et gros granules, ainsi que la fraction volumétrique des petits par rapport aux gros, sur des plages importantes. Les deux paramètres montrent qu'ils influencent la compacité de l'assemblage granulaire, ainsi que le nombre de points de contact par particule et la taille des pores dans la matrice. Une étude de la distribution des contraintes montre que ces facteurs influent directement ou indirectement les concentrations de contraintes dans le composite, ainsi que le module d'élasticité. Les relations entre la répartition de la taille des particules, la structure géométrique de l'échantillon et le comportement mécanique sont analysés en détail et les résultats numériques sont comparés à la prédiction théorique du modèle Mori-Tanaka valable pour les composites chargés dilués.

Dans un matériau granulaire cimenté, l'endommagement des particules lors d'une sollicitation de traction ou de compression dépend de la microstructure et des propriétés mécaniques des phases constitutives. Une étude paramétrique étendu a été réalisée pour mettre en évidence l'effet de la ténacité des particules et de la dureté de l'interface matrice-particules sur la fracture, en fonction de la distribution granulométrique des grains. Le comportement mécanique étant connu pour être fortement influencée par la quantité de matrice cimentaire, deux états ont été analysés : le cas où la matrice occupe complètement l'espace poral entre les vides et le cas où il rempli partiellement les pores. Finalement, l'endommagement des particules a été étudié en considérant indépendamment les petits et les gros granules. En accord avec des études antérieures, nous observons qu'un seul paramètre, la ténacité de l'interface particule-matrice relative à celle de la particule, régit la surface de particules endommagés.

Bibliography

[1] M. Allaby, ed., *A Dictionary of Plant Sciences*. Oxford University Press, 3 ed., 2006.

[2] B. Moulia, "Plant biomechanics and mechanobiology are convergent paths to flourishing interdisciplinary research," *Journal of Experimental Botany*, vol. 64, no. 15, pp. 4617–4633, 2013.

[3] D. Voet, J. G. Voet, and C. V. Pratt, *Fundamentals of Biochemistry*. John Wiley & Sons, Inc., 5 ed., 2016.

[4] J. lin Jane, "Chapter 6 - Structural Features of Starch Granules {II}," in *Starch (Third Edition)* (J. BeMiller and R. Whistler, eds.), Food Science and Technology, pp. 193 – 236, San Diego: Academic Press, third edition ed., 2009.

[5] T. Fulton and R. Koebner, "Marker Assisted Breeding, a Learning Module."

[6] G. Prelich, "Gene Overexpression: Uses, Mechanisms, and Interpretation," *Genetics*, vol. 190, no. 3, pp. 841–854, 2012.

[7] http://www.iapt-taxon.org/nomen/main.php?page=art4.

[8] G. M. Campbell, "Roller Milling of Wheat," in *Particle Breakage* (A. D. Salman, M. Ghadiri, and M. J. Hounslow, eds.), vol. 12 of *Handbook of Powder Technology*, ch. 7, pp. 383 – 419, Elsevier, 2007.

[9] K.-M. Turnbull and S. Rahman, "Endosperm Texture in Wheat," *Journal of Cereal Science*, vol. 36, no. 3, pp. 327 – 337, 2002.

[10] D. Skylas, J. Mackintosh, S. Cordwell, D. Basseal, B. Walsh, J. Harry, C. Blumenthal, L. Copeland, C. Wrigley, and W. Rathmell, "Proteome Approach to the Characterisation of Protein Composition in the Developing and Mature Wheat-grain Endosperm," *Journal of Cereal Science*, vol. 32, no. 2, pp. 169 – 188, 2000.

[11] C. W. Wrigley, "Giant proteins with flour power," *Nature*, vol. 381, no. 6585, pp. 738–739, 1996.

[12] A. Pauly, B. Pareyt, E. Fierens, and J. A. Delcour, "Wheat (Triticum aestivum L. and T. turgidum L. ssp. durum) Kernel Hardness: I. Current View on the Role of Puroindolines and Polar Lipids," *Comprehensive Reviews in Food Science and Food Safety*, vol. 12, no. 4, pp. 413–426, 2013.

[13] C. F. Morris, "Puroindolines: the molecular genetic basis of wheat grain hardness," *Plant Molecular Biology*, vol. 48, no. 5, pp. 633–647, 2002.

[14] C. F. Morris, S. R. Delwiche, A. D. Bettge, F. Mabille, J. Abécassis, M. J. Pitts, F. E. Dowell, C. Deroo, and T. Pearson, "Collaborative Analysis of Wheat Endosperm Compressive Material Properties," *Cereal Chemistry Journal*, vol. 88, no. 4, pp. 391–396, 2011.

[15] K. Heinze, A. Kiszonas, J. Murray, C. Morris, and V. Lullien-Pellerin, "Puroindoline genes introduced into durum wheat reduce milling energy and change milling behavior similar to soft common wheats," *Journal of Cereal Science*, vol. 71, pp. 183 – 189, 2016.

[16] E. S. Posner and A. N. Hibbs, *Wheat Flour Milling*. AACC International, Inc., 2 ed., 2005.

[17] C. W. Wrigley, *Wheat: A Unique Grain for the World*, ch. 1, pp. 1–17. AACC International, Inc., 2009.

[18] W. D. Teague, *Flour for Man's Bread*. University of Minnesota Press, 1952.

[19] P. R. Shewry, "Wheat," *Journal of Experimental Botany*, vol. 60, no. 6, pp. 1537–1553, 2009.

[20] F. Salamini, H. Ozkan, A. Brandolini, R. Schafer-Pregl, and W. Martin, "Genetics and geography of wild cereal domestication in the near east," *Natutre Reviews Genetics*, vol. 3, no. 6, pp. 429–441, 2002.

[21] Y. Matsuoka, "Evolution of Polyploid Triticum Wheats under Cultivation: The Role of Domestication, Natural Hybridization and Allopolyploid Speciation in their Diversification," *Plant and Cell Physiology*, vol. 52, no. 5, pp. 750–764, 2011.

[22] Food and Agriculture Organization of the United Nations.

[23] A. Surget and C. Barron, "Histologie du grain de blé," *Industries des céréales*, pp. 3–7, 2005.

[24] F. Brouns, Y. Hemery, R. Price, and N. M. Anson, "Wheat Aleurone: Separation, Composition, Health Aspects, and Potential Food Use," *Critical Reviews in Food Science and Nutrition*, vol. 52, no. 6, pp. 553–568, 2012. PMID: 22452734.

[25] L. Saulnier, F. Guillon, and A.-L. Chateigner-Boutin, "Cell wall deposition and metabolism in wheat grain," *Journal of Cereal Science*, vol. 56, no. 1, pp. 91 – 108, 2012. Cereal Grain Development: Molecular Mechanisms and Impacts on Grain Composition and Functionality.

[26] S. Pérez and E. Bertoft, "The molecular structures of starch components and their contribution to the architecture of starch granules: A comprehensive review," *Starch - Stärke*, vol. 62, no. 8, pp. 389–420, 2010.

[27] A. Buléon, P. Colonna, V. Planchot, and S. Ball, "Starch granules: structure and biosynthesis," *International Journal of Biological Macromolecules*, vol. 23, no. 2, pp. 85 – 112, 1998.

[28] R. F. Tester, J. Karkalas, and X. Qi, "Starch–composition, fine structure and architecture," *Journal of Cereal Science*, vol. 39, no. 2, pp. 151 – 165, 2004.

[29] K. Shibanuma, Y. Takeda, S. Hizukuri, and S. Shibata, "Molecular structures of some wheat starches," *Carbohydrate Polymers*, vol. 25, no. 2, pp. 111 – 116, 1994.

[30] F. Zia, K. M. Zia, M. Zuber, S. Kamal, and N. Aslam, "Starch based polyurethanes: A critical review updating recent literature," *Carbohydrate Polymers*, vol. 134, no. Supplement C, pp. 784 – 798, 2015.

[31] J. P. Robin, C. Mercier, R. Charbonniere, and A. Guilbot, "Lintnerized starches. gel filtration and enzymatic studies of insoluble residues from prolonged acid treatment of potato starch," *Cereal Chemistry Journal*, vol. 51, no. 3, pp. 389–406, 1974.

[32] W. Morrison, T. Milligan, and M. Azudin, "A relationship between the amylose and lipid contents of starches from diploid cereals," *Journal of Cereal Science*, vol. 2, no. 4, pp. 257 – 271, 1984.

[33] P. J. Jenkins, R. E. Cameron, and A. M. Donald, "A Universal Feature in the Structure of Starch Granules from Different Botanical Sources," *Starch - Stärke*, vol. 45, no. 12, pp. 417–420, 1993.

[34] T. A. Waigh, I. Hopkinson, A. M. Donald, M. F. Butler, F. Heidelbach, and C. Riekel, "Analysis of the Native Structure of Starch Granules with X-ray Microfocus Diffraction," *Macromolecules*, vol. 30, no. 13, pp. 3813–3820, 1997.

[35] A. M. Donald, K. L. Kato, P. A. Perry, and T. A. Waigh, "Scattering Studies of the Internal Structure of Starch Granules," *Starch - Stärke*, vol. 53, no. 10, pp. 504–512, 2001.

[36] B. Zhang, X. Li, J. Liu, F. Xie, and L. Chen, "Supramolecular structure of A- and B-type granules of wheat starch," *Food Hydrocolloids*, vol. 31, no. 1, pp. 68 – 73, 2013.

[37] D. French, "Fine Structure of Starch and its Relationship to the Organization of Starch Granules," *Journal of the Japanese Society of Starch Science*, vol. 19, no. 1, pp. 8–25, 1972.

[38] G. T. Oostergetel and E. F. van Bruggen, "The crystalline domains in potato starch granules are arranged in a helical fashion," *Carbohydrate Polymers*, vol. 21, no. 1, pp. 7 – 12, 1993.

[39] M. B. Cardoso and H. Westfahl, "On the lamellar width distributions of starch," *Carbohydrate Polymers*, vol. 81, no. 1, pp. 21 – 28, 2010.

[40] D. J. Gallant, B. Bouchet, and P. M. Baldwin, "Microscopy of starch: evidence of a new level of granule organization," *Carbohydrate Polymers*, vol. 32, no. 3, pp. 177 – 191, 1997.

[41] R. Waduge, S. Xu, and K. Seetharaman, "Iodine absorption properties and its effect on the crystallinity of developing wheat starch granules," *Carbohydrate Polymers*, vol. 82, no. 3, pp. 786 – 794, 2010.

[42] R. N. Waduge, S. Xu, E. Bertoft, and K. Seetharaman, "Exploring the surface morphology of developing wheat starch granules by using Atomic Force Microscopy," *Starch - Stärke*, vol. 65, no. 5-6, pp. 398–409, 2013.

[43] G. N. Barrera, G. Calderon-Dominguez, J. Chanona-Perez, G. F. Gutierrez-Lopez, A. E. Leon, and P. D. Ribotta, "Evaluation of the mechanical damage on wheat starch granules by SEM, ESEM, AFM and texture image analysis.," *Carbohydrate Polymers*, vol. 98, no. 2, pp. 1449–1457, 2013.

[44] M. Salerno, A. Żukowska, S. Thorat, R. Ruffilli, M. Stasiak, and M. Molenda, "High resolution imaging of native wheat and potato starch granules based on local mechanical contrast," *Journal of Food Engineering*, vol. 128, pp. 96 – 102, 2014.

[45] D. Bechtel, I. Zayas, L. Kaleikau, and Y. Pomeranz, "Size-Distribution of Wheat Starch Granules During Endosperm Development," *Cereal Chemistry Journal*, vol. 67, no. 1, pp. 59–63, 1990.

[46] C. Wei, J. Zhang, Y. Chen, W. Zhou, B. Xu, Y. Wang, and J. Chen, "Physicochemical properties and development of wheat large and small starch granules during endosperm development," *Acta Physiologiae Plantarum*, vol. 32, no. 5, pp. 905–916, 2010.

[47] H. Dengate and P. Meredith, "Variation in size distribution of starch granules from wheat grain," *Journal of Cereal Science*, vol. 2, no. 2, pp. 83 – 90, 1984.

[48] W.-y. Li, S.-h. Yan, Y.-p. Yin, Y. Li, T.-b. Liang, F. Gu, Z.-m. Dai, and Z.-l. Wang, "Comparison of Starch Granule Size Distribution Between Hard and Soft Wheat Cultivars in Eastern China," *Agricultural Sciences in China*, vol. 7, no. 8, pp. 907 – 914, 2008.

[49] M. Ö. Raeker, C. S. Gaines, P. L. Finney, and T. Donelson, "Granule Size Distribution and Chemical Composition of Starches from 12 Soft Wheat Cultivars," *Cereal Chemistry Journal*, vol. 75, no. 5, pp. 721–728, 1998.

[50] A. B. Soulaka and W. R. Morrison, "The amylose and lipid contents, dimensions, and gelatinisation characteristics of some wheat starches and their A- and B-granule fractions," *Journal of the Science of Food and Agriculture*, vol. 36, no. 8, pp. 709–718, 1985.

[51] H. Salman, J. Blazek, A. Lopez-Rubio, E. P. Gilbert, T. Hanley, and L. Copeland, "Structure–function relationships in A and B granules from wheat starches of similar amylose content," *Carbohydrate Polymers*, vol. 75, no. 3, pp. 420 – 427, 2009.

[52] Z. Ao and J. lin Jane, "Characterization and modeling of the A- and B-granule starches of wheat, triticale, and barley," *Carbohydrate Polymers*, vol. 67, no. 1, pp. 46 – 55, 2007.

[53] J. lin Jane, "Current Understanding on Starch Granule Structures," *Journal of Applied Glycoscience*, vol. 53, no. 3, pp. 205–213, 2006.

[54] R. Kumar, A. Kumar, N. K. Sharma, N. Kaur, V. Chunduri, M. Chawla, S. Sharma, K. Singh, and M. Garg, "Soft and Hard Textured Wheat Differ in Starch Properties as Indicated by Trimodal Distribution, Morphology, Thermal and Crystalline Properties," *PLoS ONE*, vol. 11, no. 1, p. e0147622, 2016.

[55] X. Yu, B. Li, L. Wang, X. Chen, W. Wang, Y. Gu, Z. Wang, and F. Xiong, "Effect of drought stress on the development of endosperm starch granules and the composition and physicochemical properties of starches from soft and hard wheat," *Journal of the Science of Food and Agriculture*, vol. 96, no. 8, pp. 2746–2754, 2016.

[56] W. Li, Y. Shan, X. Xiao, Q. Luo, J. Zheng, S. Ouyang, and G. Zhang, "Physicochemical Properties of A- and B-Starch Granules Isolated from Hard Red and Soft Red Winter Wheat," *Journal of Agricultural and Food Chemistry*, vol. 61, no. 26, pp. 6477–6484, 2013. PMID: 23756853.

[57] N. Singh, N. Kaur, M. Katyal, A. Kaur, and K. Shevkani, "Characteristics of starch separated from coarse and fine flour fractions obtained from hard, medium-hard, and soft Indian wheat cultivars," *Starch - Stärke*, vol. 69, no. 1-2, 2017.

[58] S. S. Kozlov, A. V. Krivandin, O. V. Shatalova, T. Noda, E. Bertoft, J. Fornal, and V. P. Yuryev, "Structureof starches extracted from near-isogenic wheat lines," *Journal of Thermal Analysis and Calorimetry*, vol. 87, no. 2, pp. 575–584, 2007.

[59] J. E. Fannon, R. J. Hauber, and J. N. BeMiller, "Surface Pores of Starch Granules," *Cereal Chemistry Journal*, vol. 69, no. 3, pp. 284–288, 1992.

[60] J. E. Fannon, J. M. Shull, and J. N. BeMiller, "NOTE: Interior Channels of Starch Granules," *Cereal Chemistry Journal*, vol. 70, pp. 611–613, 1993.

[61] X.-Z. Han, M. Benmoussa, J. A. Gray, J. N. BeMiller, and B. R. Hamaker, "Detection of Proteins in Starch Granule Channels," *Cereal Chemistry Journal*, vol. 82, no. 4, pp. 351–355, 2005.

[62] H.-S. Kim and K. C. Huber, "Channels within soft wheat starch A- and B-type granules," *Journal of Cereal Science*, vol. 48, no. 1, pp. 159 – 172, 2008.

[63] S. Naguleswaran, J. Li, T. Vasanthan, and D. Bressler, "Distribution of Granule Channels, Protein, and Phospholipid in Triticale and Corn Starches as Revealed by Confocal Laser Scanning Microscopy," *Cereal Chemistry Journal*, vol. 88, no. 1, pp. 87–94, 2010.

[64] P. R. Shewry and N. G. Halford, "Cereal seed storage proteins: structures, properties and role in grain utilization," *Journal of Experimental Botany*, vol. 53, no. 370, pp. 947–958, 2002.

[65] J. D. Schofield, "Wheat proteins: structure and functionality in milling and breadmaking," in *Wheat: Production, Properties and Quality* (W. Bushuk and V. F. Rasper, eds.), ch. 7, pp. 73–106, Boston, MA: Springer US, 1994.

[66] P. Greenwell and J. D. Schofield, "A starch granule protein associated with endosperm softness in wheat," *Cereal Chemistry Journal*, vol. 63, no. 4, pp. 379–380, 1986.

[67] M.-F. Gautier, M.-E. Aleman, A. Guirao, D. Marion, and P. Joudrier, "Triticum aestivum puroindolines, two basic cystine-rich seed proteins: cDNA sequence analysis and developmental gene expression," *Plant Molecular Biology*, vol. 25, no. 1, pp. 43–57, 1994.

[68] M. Kooijman, R. Orsel, M. Hessing, R. Hamer, and A. Bekkers, "Spectroscopic Characterisation of the Lipid-binding Properties of Wheat Puroindolines," *Journal of Cereal Science*, vol. 26, no. 2, pp. 145 – 159, 1997.

[69] C. F. Morris and M. Bhave, "Reconciliation of D-genome puroindoline allele designations with current DNA sequence data," *Journal of Cereal Science*, vol. 48, no. 2, pp. 277 – 287, 2008.

[70] R. Capparelli, M. G. Amoroso, D. Palumbo, M. Iannaccone, C. Faleri, and M. Cresti, "Two Plant Puroindolines Colocalize in Wheat Seed and in vitro Synergistically Fight Against Pathogens," *Plant Molecular Biology*, vol. 58, no. 6, pp. 857–867, 2005.

[71] L. Dubreil, T. Gaborit, B. Bouchet, D. J. Gallant, W. F. Broekaert, L. Quillien, and D. Marion, "Spatial and temporal distribution of the major isoforms of puroindolines (puroindoline-a and puroindoline-b) and non specific lipid transfer protein (ns-LTP1e1) of Triticum aestivum seeds. Relationships with their in vitro antifungal properties," *Plant Science*, vol. 138, no. 2, pp. 121 – 135, 1998.

[72] V. S. Lesage, B. Bouchet, L. Rhazi, K. Elmorjani, G. Branlard, and D. Marion, "New insight into puroindoline function inferred from their subcellular localization in developing hard and soft near-isogenic endosperm and their relationship with polymer size of storage proteins," *Journal of Cereal Science*, vol. 53, no. 2, pp. 231 – 238, 2011.

[73] L. Feiz, H. Wanjugi, C. Melnyk, I. Altosaar, J. Martin, and M. Giroux, "Puroindolines co-localize to the starch granule surface and increase seed bound polar lipid content," *Journal of Cereal Science*, vol. 50, no. 1, pp. 91 – 98, 2009.

[74] M. Fujiwara, G. Suzuki, D. Kudo, H. Oba, Y. Wada, H. Wada, N. Wada, S. Rahman, K. Fukui, and Y. Mukai, "Localization of transgene-derived friabilins in rice endosperm cells," *Plant Biotechnology*, vol. 31, no. 1, pp. 67–70, 2014.

[75] M. L. Wall, H. L. Wheeler, J. Smith, D. Figeys, and I. Altosaar, "Mass Spectrometric Analysis Reveals Remnants of Host–Pathogen Molecular Interactions at the Starch Granule Surface in Wheat Endosperm," *Phytopathology*, vol. 100, no. 9, pp. 848–854, 2010.

[76] R. Capparelli, G. Borriello, M. J. Giroux, and M. G. Amoroso, "Puroindoline A-gene expression is involved in association of puroindolines to starch," *Theoretical and Applied Genetics*, vol. 107, no. 8, pp. 1463–1468, 2003.

[77] C. Swan, F. Meyer, A. Hogg, J. Martin, and M. Giroux, "Puroindoline B limits binding of puroindoline A to starch and grain softness," *Crop Science*, vol. 46, no. 4, pp. 1656–1665, 2006.

[78] Y. Li, X. Mao, Q. Wang, J. Zhang, X. Li, F. Ma, F. Sun, J. Chang, M. Chen, Y. Wang, K. Li, G. Yang, and G. He, "Overexpression of Puroindoline a gene in transgenic durum wheat (Triticum turgidum ssp. durum) leads to a medium–hard kernel texture," *Molecular Breeding*, vol. 33, no. 3, pp. 545–554, 2014.

[79] H. Wanjugi, A. Hogg, J. Martin, and M. Giroux, "The role of puroindoline A and B individually and in combination on grain hardness and starch association," *Crop Science*, vol. 47, no. 1, pp. 67–76, 2007.

[80] M. Ziemann, A. Ramalingam, and M. Bhave, "Evidence of physical interactions of puroindoline proteins using the yeast two-hybrid system," *Plant Science*, vol. 175, no. 3, pp. 307 – 311, 2008.

[81] R. L. Phillips, E. A. Palombo, J. F. Panozzo, and M. Bhave, "Puroindolines, Pin alleles, hordoindolines and grain softness proteins are sources of bactericidal and fungicidal peptides," *Journal of Cereal Science*, vol. 53, no. 1, pp. 112 – 117, 2011.

[82] K. Krishnamurthy and M. J. Giroux, "Expression of wheat puroindoline genes in transgenic rice enhances grain softness," *Nat Biotech*, vol. 19, no. 2, pp. 162–166, 2001.

[83] R. L. Alfred, E. A. Palombo, J. F. Panozzo, and M. Bhave, "The Antimicrobial Domains of Wheat Puroindolines Are Cell-Penetrating Peptides with Possible Intracellular Mechanisms of Action," *PLOS ONE*, vol. 8, no. 10, pp. 1–11, 2013.

[84] M. J. Giroux, T. Sripo, S. Gerhardt, and J. Sherwood, "Puroindolines: Their Role in Grain Hardness and Plant Defence," *Biotechnology & genetic engineering reviews*, vol. 20, no. 1, pp. 277–290, 2003.

[85] C. L. Guernevé, M. Seigneuret, and D. Marion, "Interaction of the Wheat Endosperm Lipid-Binding Protein Puroindoline-a with Phospholipids," *Archives of Biochemistry and Biophysics*, vol. 360, no. 2, pp. 179 – 186, 1998.

[86] J. Rosicka-Kaczmarek, M. Stasiuk, E. Nebesny, and A. Komisarczyk, "Fluorimetric studies of the interactions of wheat puroindolines with polar lipids on the surface starch granules," *Journal of Cereal Science*, vol. 66, no. Supplement C, pp. 53 – 58, 2015.

[87] S. C. Biswas and D. Marion, "Interaction between puroindolines and the major polar lipids of wheat seed endosperm at the air–water interface," *Colloids and Surfaces B: Biointerfaces*, vol. 53, no. 2, pp. 167 – 174, 2006.

[88] K.-H. Kim, L. Feiz, J. Martin, and M. Giroux, "Puroindolines are associated with decreased polar lipid breakdown during wheat seed development," *Journal of Cereal Science*, vol. 56, no. 2, pp. 142 – 146, 2012.

[89] L. A. Clifton, M. D. Lad, R. J. Green, and R. A. Frazier, "Single Amino Acid Substitutions in Puroindoline-b Mutants Influence Lipid Binding Properties," *Biochemistry*, vol. 46, no. 8, pp. 2260–2266, 2007. PMID: 17274601.

[90] A. Pauly, B. Pareyt, N. De Brier, and J. A. Delcour, "Incubation of Isolated Wheat Starch with Proteolytic or Lipolytic Enzymes and Different Extraction Media Reveals a Tight Interaction Between Puroindolines and Lipids at Its Granule Surface," *Cereal Chemistry Journal*, vol. 91, no. 3, pp. 240–246, 2014.

[91] D. Ma, H. Qin, H. Ding, J. Zhang, C. Wang, and T. Guo, "Surface Lipids Play a Role in the Interaction of Puroindolines with Wheat Starch and Kernel Hardness," *Cereal Chemistry Journal*, vol. 93, no. 5, pp. 523–528, 2016.

[92] K. Elmorjani, N. Geneix, M. Dalgalarrondo, G. Branlard, and D. Marion, "Wheat grain softness protein (Gsp1) is a puroindoline-like protein that displays a specific post-translational maturation and does not interact with lipids," *Journal of Cereal Science*, vol. 58, no. 1, pp. 117 – 122, 2013.

[93] G. Tranquilli, J. Heaton, O. Chicaiza, and J. Dubcovsky, "Substitutions and Deletions of Genes Related to Grain Hardness in Wheat and Their Effect on Grain Texture," *Crop Science*, vol. 42, pp. 1812–1817, 2002.

[94] W. R. Morrison, "Wheat Lipid Composition," *Cereal Chemistry Journal*, vol. 55, no. 5, pp. 548–558, 1978.

[95] W. R. Morrison, "Lipids in cereal starches: A review," *Journal of Cereal Science*, vol. 8, no. 1, pp. 1 – 15, 1988.

[96] K. D. Hargin and W. R. Morrison, "The distribution of acyl lipids in the germ, aleurone, starch and non-starch endosperm of four wheat varieties," *Journal of the Science of Food and Agriculture*, vol. 31, no. 9, pp. 877–888, 1980.

[97] G. Greenblatt, A. Bettge, and C. Morris, "Relationship between endosperm texture and the occurrence of friabilin and bound polar lipids on wheat starch," *Cereal Chemistry Journal*, vol. 72, no. 2, pp. 172–175, 1995.

[98] P. R. Shewry, R. A. Mitchell, P. Tosi, Y. Wan, C. Underwood, A. Lovegrove, J. Freeman, G. A. Toole, E. C. Mills, and J. L. Ward, "An integrated study of grain development of wheat (cv. Hereward)," *Journal of Cereal Science*, vol. 56, no. 1, pp. 21 – 30, 2012. Cereal Grain Development: Molecular Mechanisms and Impacts on Grain Composition and Functionality.

[99] T. E. Young and D. R. Gallie, *Programmed cell death during endosperm development*, pp. 39–57. Dordrecht: Springer Netherlands, 2000.

[100] D. Bechtel, R. Gaines, and Y. Pomeranz, "Protein secretion in wheat endosperm—formation of the matrix protein," *Cereal Chemistry Journal*, vol. 59, no. 5, pp. 336–343, 1982.

[101] F. Dupont and S. Altenbach, "Molecular and biochemical impacts of environmental factors on wheat grain development and protein synthesis," *Journal of Cereal Science*, vol. 38, no. 2, pp. 133 – 146, 2003.

[102] C. M. Hazel and S. Patel, "Influence of processing on trichothecene levels," *Toxicology Letters*, vol. 153, no. 1, pp. 51 – 59, 2004. Trichothecenes with a special focus on DON.

[103] R. J. Peña, R. Trethowan, W. H. Pfeiffer, and M. V. Ginkel, "Quality (End-Use) Improvement in Wheat," *Journal of Crop Production*, vol. 5, no. 1-2, pp. 1–37, 2002.

[104] A. Pauly, B. Pareyt, E. Fierens, and J. A. Delcour, "Wheat (Triticum aestivum L. and T. turgidum L. ssp. durum) Kernel Hardness: II. Implications for End-Product Quality and Role of Puroindolines Therein," *Comprehensive Reviews in Food Science and Food Safety*, vol. 12, no. 4, pp. 427–438, 2013.

[105] W. T. Greenaway, "A wheat hardness index," *Cereal Science Today*, vol. 14, no. 2, 1969.

[106] W. Worzella and G. Cutler, "A critical study of technique for measuring granulation in wheat meal," *Journal of Agricultural Research*, vol. 58, pp. 329–341, 1939.

[107] P. C. Williams and D. C. Sobering, "Attempts at standardization of hardness testing of wheat. i. the grinding/sieving (particle size index) method," *Cereal Foods World*, 1986.

[108] P. C. Williams, S. G. Stevenson, P. M. Starkey, and G. C. Hawtin, "The application of near infrared reflectance spectroscopy to protein-testing in pulse breeding programmes," *Journal of the Science of Food and Agriculture*, vol. 29, no. 3, pp. 285–292, 1978.

[109] W. Saurer, "Use of infra-red reflectance measurement for determination of protein and water content and grain hardness in wheat," *Getreide, Mehl und Brot*, vol. 32, pp. 272–276, 1978.

[110] C. R. Martin, R. Rousser, and D. L. Brabec, "Development of a single-kernel wheat characterization system," *Transactions of the ASAE*, vol. 36, no. 5, pp. 1399–1404, 1993.

[111] C. S. Gaines, P. F. Finney, L. M. Fleege, and L. C. Andrews, "Predicting a hardness measurement using the single-kernel characterization system," *Cereal Chemistry Journal*, vol. 73, no. 2, pp. 278–283, 1996.

[112] F.-X. Oury, P. Lasme, C. Michelet, M. Rousset, J. Abecassis, and V. Lullien-Pellerin, "Relationships between wheat grain physical characteristics studied through near-isogenic lines with distinct puroindoline-b allele," *Theoretical and Applied Genetics*, vol. 128, no. 5, pp. 913–929, 2015.

[113] Y. Haddad, J. C. Benet, and J. Abecassis, "A Rapid General Method for Appraising the Rheological Properties of the Starchy Endosperm of Cereal Grains," *Cereal Chemistry Journal*, vol. 75, no. 5, pp. 673–676, 1998.

[114] J. A. Delcour, I. J. Joye, B. Pareyt, E. Wilderjans, K. Brijs, and B. Lagrain, "Wheat Gluten Functionality as a Quality Determinant in Cereal-Based Food Products," *Annual Review of Food Science and Technology*, vol. 3, no. 1, pp. 469–492, 2012. PMID: 22224557.

[115] J. Dexter, P. Williams, N. Edwards, and D. Martin, "The relationships between durum wheat vitreousness, kernel hardness and processing quality," *Journal of Cereal Science*, vol. 7, no. 2, pp. 169 – 181, 1988.

[116] M. F. Samson, F. Mabille, R. Chéret, J. Abécassis, and M. H. Morel, "Mechanical and Physicochemical Characterization of Vitreous and Mealy Durum Wheat Endosperm," *Cereal Chemistry Journal*, vol. 82, no. 1, pp. 81–87, 2005.

[117] A.-N. Sieber, T. Würschum, and C. F. H. Longin, "Vitreosity, its stability and relationship to protein content in durum wheat," *Journal of Cereal Science*, vol. 61, pp. 71 – 77, 2015.

[118] C. F. Morris and B. S. Beecher, "The distal portion of the short arm of wheat (Triticum aestivum L.) chromosome 5D controls endosperm vitreosity and grain hardness," *Theoretical and Applied Genetics*, vol. 125, no. 2, pp. 247–254, 2012.

[119] S. F. Schuler, R. K. Bacon, P. L. Finney, and E. E. Gbur, "Relationship of test weight and kernel properties to milling and baking quality in soft red winter wheat," *Crop Science*, vol. 35, no. 4, pp. 949–953, 1995.

[120] F.-X. Oury, P. Lasme, C. Michelet, A. Dubat, O. Gardet, E. Heumez, B. Rolland, M. Rousset, J. Abecassis, C. Bar L'Helgouac'h, and V. Lullien-Pellerin, "Bread wheat milling behavior: effects of genetic and environmental factors, and modeling using grain mechanical resistance traits," *Theoretical and Applied Genetics*, vol. 130, no. 5, pp. 929–950, 2017.

[121] C. M. Brites, C. A. L. d. Santos, A. S. Bagulho, and M. L. Beirão-da Costa, "Effect of wheat puroindoline alleles on functional properties of starch," *European Food Research and Technology*, vol. 226, no. 5, pp. 1205–1212, 2008.

[122] B. Beecher, A. Bettge, E. Smidansky, and M. Giroux, "Expression of wild-type pinB sequence in transgenic wheat complements a hard phenotype," *Theoretical and Applied Genetics*, vol. 105, no. 6, pp. 870–877, 2002.

[123] J. Lelievre, "Starch Damage," *Starch - Stärke*, vol. 26, no. 3, pp. 85–88, 1974.

[124] C. S. Gaines, J. R. Donelson, and P. L. Finney, "Effects of Damaged Starch, Chlorine Gas, Flour Particle Size, and Dough Holding Time and Temperature on Cookie Dough Handling Properties and Cookie Size.," *Cereal Chemistry Journal*, vol. 65, no. 5, pp. 384–389, 1988.

[125] K. H. Tipples, R. H. Kilborn, and K. R. Preston, "Bread-wheat quality defined," in *Wheat: Production, Properties and Quality* (W. Bushuk and V. F. Rasper, eds.), pp. 25–36, Boston, MA: Springer US, 1994.

[126] R. Pujol, C. Létang, I. Lempereur, M. Chaurand, F. Mabille, and J. Abecassis, "Description of a Micromill with Instrumentation for Measuring Grinding Characteristics of Wheat Grain," *Cereal Chemistry Journal*, vol. 77, no. 4, pp. 421–427, 2000.

[127] G. Campbell, C. Fang, and I. Muhamad, "On Predicting Roller Milling Performance VI," *Food and Bioproducts Processing*, vol. 85, no. 1, pp. 7 – 23, 2007.

[128] G. M. Campbell, C. Sharp, K. Wall, F. Mateos-Salvador, S. Gubatz, A. Huttly, and P. Shewry, "Modelling wheat breakage during roller milling using the Double Normalised Kumaraswamy Breakage Function: Effects of kernel shape and hardness," *Journal of Cereal Science*, vol. 55, no. 3, pp. 415 – 425, 2012.

[129] P. R. Shewry and H. Jones, "Transgenic wheat: where do we stand after the first 12 years?," *Annals of Applied Biology*, vol. 147, no. 1, pp. 1–14, 2005.

[130] M. J. Giroux and C. F. Morris, "Wheat grain hardness results from highly conserved mutations in the friabilin components puroindoline a and b," *Proceedings of the National Academy of Sciences*, vol. 95, no. 11, pp. 6262–6266, 1998.

[131] V. Greffeuille, J. Abecassis, M. Rousset, F.-X. Oury, A. Faye, C. B. L'Helgouac'h, and V. Lullien-Pellerin, "Grain characterization and milling behaviour of near-isogenic lines differing by hardness," *Theoretical and Applied Genetics*, vol. 114, no. 1, pp. 1–12, 2006.

[132] K. Takata, T. M. Ikeda, M. Yanaka, H. Matsunaka, M. Seki, N. Ishikawa, and H. Yamauchi, "Comparison of five puroindoline alleles on grain hardness and flour properties using near isogenic wheat lines," *Breeding Science*, vol. 60, no. 3, pp. 228–232, 2010.

[133] V. S. Lesage, M. Merlino, C. Chambon, B. Bouchet, D. Marion, and G. Branlard, "Proteomes of hard and soft near-isogenic wheat lines reveal that kernel hardness is related to the amplification of a stress response during endosperm development," *Journal of Experimental Botany*, vol. 63, no. 2, pp. 1001–1011, 2012.

[134] P. Lasme, F.-X. Oury, C. Michelet, J. Abécassis, F. Mabille, C. B. L'Helgouac'h, and V. Lullien-Pellerin, "A Study of Puroindoline b Gene Involvement in the Milling Behavior of Hard-Type Common Wheats," *Cereal Chemistry Journal*, vol. 89, no. 1, pp. 44–51, 2011.

[135] E. Chichti, M. George, J.-Y. Delenne, and V. Lullien-Pellerin, "Changes in the starch-protein interface depending on common wheat grain hardness revealed using atomic force microscopy," *Plant Science*, vol. 239, pp. 1 – 8, 2015.

[136] N. Wada, S. Kajiyama, J. A. Cartagena, L. Lin, Y. Akiyama, M. Otani, G. Suzuki, Y. Mukai, N. Aoki, and K. Fukui, "The effects of puroindoline b on the ultrastructure of endosperm cells and physicochemical properties of transgenic rice plant," *Journal of Cereal Science*, vol. 51, no. 2, pp. 182 – 188, 2010.

[137] L. Zhang, M. D'Acunzi, M. Kappl, G. K. Auernhammer, D. Vollmer, C. M. van Kats, and A. van Blaaderen, "Hollow Silica Spheres: Synthesis and Mechanical Properties," *Langmuir*, vol. 25, no. 5, pp. 2711–2717, 2009.

[138] A. Gennaro, P. Forte, D. Panichi, D. Lafiandra, M. A. Pagnotta, M. G. D'Egidio, and C. Ceoloni, "Stacking small segments of the 1D chromosome of bread wheat containing major gluten quality genes into durum wheat: transfer strategy and breeding prospects," *Molecular Breeding*, vol. 30, no. 1, pp. 149–167, 2012.

[139] J. M. Martin, F. D. Meyer, E. D. Smidansky, H. Wanjugi, A. E. Blechl, and M. J. Giroux, "Complementation of the pina (null) allele with the wild type Pina sequence restores a soft phenotype in transgenic wheat," *Theoretical and Applied Genetics*, vol. 113, no. 8, pp. 1563–1570, 2006.

[140] L. Xia, H. Geng, X. Chen, Z. He, M. Lillemo, and C. F. Morris, "Silencing of puroindoline a alters the kernel texture in transgenic bread wheat," *Journal of Cereal Science*, vol. 47, no. 2, pp. 331 – 338, 2008.

[141] C. F. Morris, J. Casper, A. M. Kiszonas, E. P. Fuerst, J. Murray, M. C. Simeone, and D. Lafiandra, "Soft Kernel Durum Wheat—A New Bakery Ingredient?," *Cereal Foods World*, vol. 60, no. 2, pp. 76–83, 2015.

[142] L. Gazza, D. Sgrulletta, A. Cammerata, G. Gazzelloni, M. Perenzin, and N. E. Pogna, "Pastamaking and breadmaking quality of soft-textured durum wheat lines," *Journal of Cereal Science*, vol. 54, no. 3, pp. 481 – 487, 2011.

[143] M. Bhave and C. F. Morris, "Molecular genetics of puroindolines and related genes: regulation of expression, membrane binding properties and applications," *Plant Molecular Biology*, vol. 66, no. 3, pp. 221–231, 2008.

[144] G. Branlard, M. Dardevet, R. Saccomano, F. Lagoutte, and J. Gourdon, "Genetic diversity of wheat storage proteins and bread wheat quality," *Euphytica*, vol. 119, no. 1, pp. 59–67, 2001.

[145] A. Y. Novoselskaya-Dragovich, "Genetics and genomics of wheat: Storage proteins, ecological plasticity, and immunity," *Russian Journal of Genetics*, vol. 51, no. 5, pp. 476–490, 2015.

[146] G. Igrejas, B. Faucher, D. Bertrand, D. Guibert, P. Leroy, and G. Branlard, "Genetic Analysis of the Size of Endosperm Starch Granules in a Mapped Segregating Wheat Population," *Journal of Cereal Science*, vol. 35, no. 1, pp. 103 – 107, 2002.

[147] A. Turner, R. Bradburne, L. Fish, and J. Snape, "New quantitative trait loci influencing grain texture and protein content in bread wheat," *Journal of Cereal Science*, vol. 40, no. 1, pp. 51 – 60, 2004.

[148] Y. Mak, D. J. Skylas, R. Willows, A. Connolly, S. J. Cordwell, C. W. Wrigley, P. J. Sharp, and L. Copeland, "A proteomic approach to the identification and characterisation of protein composition in wheat germ," *Functional & Integrative Genomics*, vol. 6, no. 4, pp. 322–337, 2006.

[149] S. Meziani, I. Nadaud, B. Gaillard-Martinie, C. Chambon, M. Benali, and G. Branlard, "Proteomic analysis of the mature kernel aleurone layer in common and durum wheat," *Journal of Cereal Science*, vol. 55, no. 3, pp. 323 – 330, 2012.

[150] M. Pompa, M. M. Giuliani, C. Palermo, F. Agriesti, D. Centonze, and Z. Flagella, "Comparative Analysis of Gluten Proteins in Three Durum Wheat Cultivars by a Proteomic Approach," *Journal of Agricultural and Food Chemistry*, vol. 61, no. 11, pp. 2606–2617, 2013. PMID: 23414385.

[151] G.-X. Chen, J.-W. Zhou, Y.-L. Liu, X.-B. Lu, C.-X. Han, W.-Y. Zhang, Y.-H. Xu, and Y.-M. Yan, "Biosynthesis and Regulation of Wheat Amylose and Amylopectin from Proteomic and Phosphoproteomic Characterization of Granule-binding Proteins," *Scientific Reports*, vol. 6, pp. 33111 EP –, 2016.

[152] S. Barak, D. Mudgil, and B. S. Khatkar, "Biochemical and Functional Properties of Wheat Gliadins: A Review," *Critical Reviews in Food Science and Nutrition*, vol. 55, no. 3, pp. 357–368, 2015. PMID: 24915383.

[153] O. Chung, J. Ohm, M. Ram, S. Park, and C. Howitt, *Wheat Lipids*, ch. 10, pp. 363–390. AACC International, Inc., 4th ed., 2009.

[154] J.-P. Douliez, T. Michon, K. Elmorjani, and D. Marion, "Mini Review: Structure, Biological and Technological Functions of Lipid Transfer Proteins and Indolines, the Major Lipid Binding Proteins from Cereal Kernels," *Journal of Cereal Science*, vol. 32, no. 1, pp. 1 – 20, 2000.

[155] Y. Haddad, F. Mabille, A. Mermet, J. Abecassis, and J. Benet, "Rheological properties of wheat endosperm with a view on grinding behaviour," *Powder Technology*, vol. 105, no. 1–3, pp. 89 – 94, 1999.

[156] B. Dobraszczyk, M. Whitworth, J. Vincent, and A. Khan, "Single Kernel Wheat Hardness and Fracture Properties in Relation to Density and the Modelling of Fracture in Wheat Endosperm," *Journal of Cereal Science*, vol. 35, no. 3, pp. 245 – 263, 2002.

[157] C. F. Morris, M. J. Pitts, A. D. Bettge, K. Pecka, G. E. King, and P. J. McCluskey, "Compressive Strength of Wheat Endosperm: Analysis of Endosperm Bricks," *Cereal Chemistry Journal*, vol. 85, no. 3, pp. 351–358, 2008.

[158] A. Nadolska-Orczyk, S. Gasparis, and W. Orczyk, "The determinants of grain texture in cereals," *Journal of Applied Genetics*, vol. 50, no. 3, pp. 185–197, 2009.

[159] R. C. Nirmal, A. Furtado, C. Wrigley, and R. J. Henry, "Influence of Gene Expression on Hardness in Wheat," *PLoS ONE*, vol. 11, no. 10, p. e0164746, 2016.

[160] P. P. Lasme, F.-X. F.-X. Oury, C. C. Michelet, J. J. Abecassis, F. F. Mabille, C. C. Bar L'Helgouac'H, and V. V. Lullien-Pellerin, "A study of puroindoline b gene involvement in the milling behavior of hard-type common wheats," *Cereal Chemistry Journal*, vol. 89, no. 1, pp. 44–51, 2012.

[161] C. S. Gaines, M. Ö. Raeker, M. Tilley, P. L. Finney, J. D. Wilson, D. B. Bechtel, R. J. Martin, P. A. Seib, G. L. Lookhart, and T. Donelson, "Associations of Starch Gel Hardness, Granule Size, Waxy Allelic Expression, Thermal Pasting, Milling Quality, and Kernel Texture of 12 Soft Wheat Cultivars," *Cereal Chemistry Journal*, vol. 77, no. 2, pp. 163–168, 2000.

[162] J. Martin, R. Frohberg, C. Morris, L. Talbert, and M. J. Giroux, "Milling and bread baking traits associated with puroindoline sequence type in hard red spring wheat," *Crop Science*, vol. 41, pp. 228–234, 2001.

[163] A. C. Hogg, B. Beecher, J. M. Martin, F. Meyer, L. Talbert, S. Lanning, and M. J. Giroux, "Hard Wheat Milling and Bread Baking Traits Affected by the Seed-Specific Overexpression of Puroindolines," *Crop Science*, vol. 45, no. 3, pp. 871–878, 2005.

[164] J. M. Martin, F. D. Meyer, C. F. Morris, and M. J. Giroux, "Pilot Scale Milling Characteristics of Transgenic Isolines of a Hard Wheat Over-Expressing Puroindolines," *Crop Science*, vol. 47, pp. 497–504, 2007.

[165] A.-L. Choy, C. K. Walker, and J. F. Panozzo, "Investigation of Wheat Milling Yield Based on Grain Hardness Parameters," *Cereal Chemistry Journal*, vol. 92, no. 6, pp. 544–550, 2015.

[166] M. Edwards, B. Osborne, and R. Henry, "Effect of endosperm starch granule size distribution on milling yield in hard wheat," *Journal of Cereal Science*, vol. 48, no. 1, pp. 180 – 192, 2008.

[167] M. Edwards, B. Osborne, and R. Henry, "Puroindoline genotype, starch granule size distribution and milling quality of wheat," *Journal of Cereal Science*, vol. 52, no. 2, pp. 314 – 320, 2010.

[168] Y. Hemery, V. Lullien-Pellerin, X. Rouau, J. Abecassis, M. F. Samson, P. Çžman, W. v. Reding, C. Spoerndli, and C. Barron, "Biochemical markers: efficient tools for the assessment of wheat grain tissue proportions in milling fractions.," *Journal of Cereal Science*, vol. 49, no. 1, pp. 55–64, 2009.

[169] V. Greffeuille, J. Abecassis, C. B. L'Helgouac'h, and V. Lullien-Pellerin, "Differences in the Aleurone Layer Fate Between Hard and Soft Common Wheats at Grain Milling," *Cereal Chemistry Journal*, vol. 82, no. 2, pp. 138–143, 2005.

[170] G. Glenn and R. Johnston, "Mechanical properties of starch, protein and endosperm and their relationship to hardness in wheat," *Food Structure*, vol. 11, pp. 187–199, 1992.

[171] L. Wang and G. Jeronimidis, "Investigation of the fracture mode for hard and soft wheat endosperm using the loading–unloading bending test," *Journal of Cereal Science*, vol. 48, no. 1, pp. 193 – 202, 2008.

[172] S. R. Delwiche, C. F. Morris, F. Mabille, and J. Abécassis, "Influence of Instrument Rigidity and Specimen Geometry on Calculations of Compressive Strength Properties of Wheat Endosperm," *Cereal Chemistry Journal*, vol. 89, no. 1, pp. 24–29, 2011.

[173] E. Chichti, M. George, J.-Y. Delenne, F. Radjai, and V. Lullien-Pellerin, "Nano-mechanical properties of starch and gluten biopolymers from atomic force microscopy," *European Polymer Journal*, vol. 49, no. 12, pp. 3788 – 3795, 2013.

[174] K. Barlow, M. Buttrose, D. Simmonds, and M. Vesk, "The nature of starch-protein interface in wheat endosperm," *Cereal Chemistry Journal*, vol. 50, pp. 443–454, 1973.

[175] S. Arena, C. D'Ambrosio, M. Vitale, F. Mazzeo, G. Mamone, L. D. Stasio, M. Maccaferri, P. L. Curci, G. Sonnante, N. Zambrano, and A. Scaloni, "Differential representation of albumins and globulins during grain development in durum wheat and its possible functional consequences," *Journal of Proteomics*, vol. 162, pp. 86 – 98, 2017.

[176] K.-M. Turnbull, D. Marion, T. Gaborit, R. Appels, and S. Rahman, "Early expression of grain hardness in the developing wheat endosperm," *Planta*, vol. 216, no. 4, pp. 699–706, 2003.

[177] N. L. Stenvert and K. Kingswood, "The influence of the physical structure of the protein matrix on wheat hardness," *Journal of the Science of Food and Agriculture*, vol. 28, no. 1, pp. 11–19, 1977.

[178] J. Budny, J. Fornal, and W. Obuchowski, "Analysis of correlations between contents of protein fractions in wheat endosperm models and their mechanical resistance," *Journal of Cereal Science*, vol. 71, no. Supplement C, pp. 10 – 18, 2016.

[179] W. Yu, X. Tan, W. Zou, Z. Hu, G. P. Fox, M. J. Gidley, and R. G. Gilbert, "Relationships between protein content, starch molecular structure and grain size in barley," *Carbohydrate Polymers*, vol. 155, no. Supplement C, pp. 271 – 279, 2017.

[180] V. Topin, J. Y. Delenne, F. Radjaï, L. Brendel, and F. Mabille, "Strength and failure of cemented granular matter," *The European Physical Journal E*, vol. 23, no. 4, pp. 413–429, 2007.

[181] V. Topin, F. Radjaï, J.-Y. Delenne, A. Sadoudi, and F. Mabille, "Wheat endosperm as a cohesive granular material," *Journal of Cereal Science*, vol. 47, no. 2, pp. 347 – 356, 2008.

[182] V. Topin, F. Radjaï, J.-Y. Delenne, and F. Mabille, "Mechanical modeling of wheat hardness and fragmentation," *Powder Technology*, vol. 190, no. 1–2, pp. 215 – 220, 2009.

[183] E. Chichti, V. Lullien-Pellerin, M. George, F. Radjai, R. Affès, and J.-Y. Delenne, "Bottom-up model for understanding the effects of wheat endosperm microstructure on its mechanical strength," *Journal of Food Engineering*, vol. 190, pp. 40 – 47, 2016.

[184] J. Delenne, Y. Haddad, J. Bénet, and J. Abecassis, "Use of mechanics of cohesive granular media for analysis of hardness and vitreousness of wheat endosperm," *Journal of Cereal Science*, vol. 47, no. 3, pp. 438 – 444, 2008.

[185] Y. Haddad, J. Benet, J. Delenne, A. Mermet, and J. Abecassis, "Rheological Behaviour of Wheat Endosperm—Proposal for Classification Basedon the Rheological Characteristics of EndospermTest Samples," *Journal of Cereal Science*, vol. 34, no. 1, pp. 105 – 113, 2001.

[186] C. W. W. D. H. Simmonds, K. K. Barlow, "The biochemical basis of grain hardness in wheat," *Cereal Chemistry Journal*, vol. 50, no. 4, pp. 252–258, 1973.

[187] S. Gasparis, W. Orczyk, W. Zalewski, and A. Nadolska-Orczyk, "The RNA-mediated silencing of one of the Pin genes in allohexaploid wheat simultaneously decreases the expression of the other, and increases grain hardness," *Journal of Experimental Botany*, vol. 62, no. 11, pp. 4025–4036, 2011.

[188] V. Greffeuille, F. Mabille, M. Rousset, F.-X. Oury, J. Abecassis, and V. Lullien-Pellerin, "Mechanical properties of outer layers from near-isogenic lines of common wheat differing in hardness," *Journal of Cereal Science*, vol. 45, no. 2, pp. 227 – 235, 2007.

[189] C. F. Morris and S. P. Rose, *Wheat*, pp. 3–54. Dordrecht: Springer Netherlands, 1996.

[190] J. C. Murray, A. M. Kiszonas, J. Wilson, and C. F. Morris, "Effect of Soft Kernel Texture on the Milling Properties of Soft Durum Wheat," *Cereal Chemistry Journal*, vol. 93, no. 5, pp. 513–517, 2016.

[191] F. Mabille and J. Abecassis, "Parametric Modelling of Wheat Grain Morphology: a New Perspective," *Journal of Cereal Science*, vol. 37, no. 1, pp. 43 – 53, 2003.

[192] E. T. Quayson, W. Atwell, C. F. Morris, and A. Marti, "Empirical rheology and pasting properties of soft-textured durum wheat (Triticum turgidum ssp. durum) and hard-textured common wheat (T. aestivum)," *Journal of Cereal Science*, vol. 69, pp. 252 – 258, 2016.

[193] V. Greffeuille, J. Abecassis, N. Barouh, P. Villeneuve, F. Mabille, C. B. L'Helgouac'h, and V. Lullien-Pellerin, "Analysis of the milling reduction of bread wheat farina: Physical and biochemical characterisation," *Journal of Cereal Science*, vol. 45, no. 1, pp. 97 – 105, 2007.

[194] H. Yang, Y. Wang, S. Lai, H. An, Y. Li, and F. Chen, "Application of Atomic Force Microscopy as a Nanotechnology Tool in Food Science," *Journal of Food Science*, vol. 72, no. 4, pp. R65–R75, 2007.

[195] K. D. Jandt, "Atomic force microscopy of biomaterials surfaces and interfaces," *Surface Science*, vol. 491, no. 3, pp. 303 – 332, 2001.

[196] D. P. Allison, N. P. Mortensen, C. J. Sullivan, and M. J. Doktycz, "Atomic force microscopy of biological samples," *Wiley Interdisciplinary Reviews: Nanomedicine and Nanobiotechnology*, vol. 2, no. 6, pp. 618–634, 2010.

[197] M. Gaczynska and P. A. Osmulski, "AFM of biological complexes: what can we learn?," *Current opinion in colloid & interface science*, vol. 13, no. 5, pp. 351–367, 2008.

[198] G. Binnig, C. F. Quate, and C. Gerber, "Atomic Force Microscope," *Physical Review Letters*, vol. 56, pp. 930–933, 1986.

[199] N. Jalili and K. Laxminarayana, "A review of atomic force microscopy imaging systems: application to molecular metrology and biological sciences," *Mechatronics*, vol. 14, no. 8, pp. 907 – 945, 2004.

[200] R. García, *Amplitude Modulation Atomic Force Microscopy*. Wiley-VCH Verlag GmbH & Co. KGaA, 2010.

[201] H.-J. Butt, B. Cappella, and M. Kappl, "Force measurements with the atomic force microscope: Technique, interpretation and applications," *Surface Science Reports*, vol. 59, no. 1–6, pp. 1 – 152, 2005.

[202] H. Dvir, J. Jopp, and M. Gottlieb, "Estimation of polymer–surface interfacial interaction strength by a contact AFM technique," *Journal of Colloid and Interface Science*, vol. 304, no. 1, pp. 58 – 66, 2006.

[203] F. Ahimou, M. J. Semmens, P. J. Novak, and G. Haugstad, "Biofilm Cohesiveness Measurement Using a Novel Atomic Force Microscopy Methodology," *Applied and Environmental Microbiology*, vol. 73, no. 9, pp. 2897–2904, 2007.

[204] U. Rabe, *Atomic Force Acoustic Microscopy*, pp. 37–90. Berlin, Heidelberg: Springer Berlin Heidelberg, 2006.

[205] D. C. Hurley, *Contact Resonance Force Microscopy Techniques for Nanomechanical Measurements*, pp. 97–138. Berlin, Heidelberg: Springer Berlin Heidelberg, 2009.

[206] J. S. Villarrubia, "Algorithms for Scanned Probe Microscope Image Simulation, Surface Reconstruction, and Tip Estimation," *Journal of Research of the National Institute of Standards and Technology*, vol. 102, no. 4, pp. 425–454, 1997.

[207] G. Stan and R. F. Cook, "Mapping the elastic properties of granular Au films by contact resonance atomic force microscopy," *Nanotechnology*, vol. 19, no. 23, p. 235701, 2008.

[208] S. Magonov, V. Elings, and M.-H. Whangbo, "Phase imaging and stiffness in tapping-mode atomic force microscopy," *Surface Science*, vol. 375, no. 2, pp. L385 – L391, 1997.

[209] P.-E. Mazeran, L. Odoni, and J.-L. Loubet, "Curvature radius analysis for scanning probe microscopy," *Surface Science*, vol. 585, no. 1-2, pp. 25–37, 2005.

[210] J.-L. Jane, T. Kasemsuwan, S. Leas, H. Zobel, and J. F. Robyt, "Anthology of Starch Granule Morphology by Scanning Electron Microscopy," *Starch - Stärke*, vol. 46, no. 4, pp. 121–129, 1994.

[211] S. Perez, P. M. Baldwin, and D. J. Gallant, "Structural features of starch granules I," in *Starch* (J. BeMiller and R. Whistler, eds.), Food Sciences and Technology, pp. 142–192, Academic Press, 3 ed., 2009.

[212] M. L. Parker, A. R. Kirby, and V. J. Morris, "In situ Imaging of Pea Starch in Seeds," *Food Biophysics*, vol. 3, no. 1, pp. 66–76, 2008.

[213] M. J. Ridout, M. L. Parker, C. L. Hedley, T. Y. Bogracheva, and V. J. Morris, "Atomic Force Microscopy of Pea Starch - Origins of Image Contrast," *Biomacromolecules*, vol. 5, no. 4, pp. 1519–1527, 2004.

[214] K. Tsukamoto, T. Ohtani, and S. Sugiyama, "Effect of sectioning and water on resin-embedded sections of corn starch granules to analyze inner structure," *Carbohydrate Polymers*, vol. 89, no. 4, pp. 1138 – 1149, 2012.

[215] A. A. Baker, M. J. Miles, and W. Helbert, "Internal structure of the starch granule revealed by AFM," *Carbohydrate Research*, vol. 330, no. 2, pp. 249 – 256, 2001.

[216] M. J. Ridout, M. L. Parker, C. L. Hedley, T. Y. Bogracheva, and V. J. Morris, "Atomic force microscopy of pea starch granules - granule architecture of wild-type parent, r and rb single mutants, and the rrb double mutant," *Carbohydrate Research*, vol. 338, no. 20, pp. 2135 – 2147, 2003.

[217] J. Dang and L. Copeland, "Imaging Rice Grains Using Atomic Force Microscopy," *Journal of Cereal Science*, vol. 37, no. 2, pp. 165 – 170, 2003.

[218] F. H. G. Peroni-Okita, A. P. Gunning, A. Kirby, R. A. Simao, C. A. Soares, and B. R. Cordenunsi, "Visualization of internal structure of banana starch granule through AFM.," *Carbohydrate Polymers*, vol. 128, pp. 32–40, 2015.

[219] T. Ohtani, T. Yoshino, T. Ushiki, S. Hagiwara, and T. Maekawa, "Structure of rice starch granules in nanometre scale as revealed by atomic force microscopy.," *Journal of Electron Microscopy*, vol. 49, no. 3, pp. 487–489, 2000.

[220] M. Ridout, A. Gunning, M. Parker, R. Wilson, and V. Morris, "Using {AFM} to image the internal structure of starch granules," *Carbohydrate Polymers*, vol. 50, no. 2, pp. 123 – 132, 2002.

[221] M. J. Ridout, M. L. Parker, C. L. Hedley, T. Y. Bogracheva, and V. J. Morris, "Atomic force microscopy of pea starch: Granule architecture of the rug3-a, rug4-b, rug5-a and lam-c mutants," *Carbohydrate Polymers*, vol. 65, no. 1, pp. 64 – 74, 2006.

[222] S. Neethirajan, D. J. Thomson, D. S. Jayas, and N. D. G. White, "Characterization of the surface morphology of durum wheat starch granules using atomic force microscopy.," *Microscopy Research & Technique*, vol. 71, no. 2, pp. 125–132, 2008.

[223] S. Neethirajan, K. Tsukamoto, H. Kanahara, and S. Sugiyama, "Ultrastructural Analysis of Buckwheat Starch Components Using Atomic Force Microscopy," *Journal of Food Science*, vol. 77, no. 1, pp. N2–N7, 2012.

[224] D. J. Gallant, B. Bouchet, A. Buleon, and S. Perez, "Physical characteristics of starch granules and susceptibility to enzymatic degradation.," *European Journal of Clinicial Nutrition*, vol. 46 Suppl 2, pp. S3–16, 1992.

[225] P. Baldwin, J. Adler, M. Davies, and C. Melia, "High Resolution Imaging of Starch Granule Surfaces by Atomic Force Microscopy," *Journal of Cereal Science*, vol. 27, no. 3, pp. 255 – 265, 1998.

[226] P. Baldwin, M. Davies, and C. Melia, "Starch granule surface imaging using low-voltage scanning electron microscopy and atomic force microscopy," *International Journal of Biological Macromolecules*, vol. 21, no. 1–2, pp. 103 – 107, 1997.

[227] N. P. Badenhuizen, "Untersuchungen über die sogenannte Blöckchenstruktur der Stärkekörner," *Protoplasma*, vol. 29, no. 1, pp. 246–260, 1938.

[228] M. Sujka and J. Jamroz, "Îś-Amylolysis of native potato and corn starches – SEM, AFM, nitrogen and iodine sorption investigations," *{LWT} - Food Science and Technology*, vol. 42, no. 7, pp. 1219 – 1224, 2009.

[229] H. Park, S. Xu, and K. Seetharaman, "A novel in situ atomic force microscopy imaging technique to probe surface morphological features of starch granules.," *Carbohydr Res*, vol. 346, no. 6, pp. 847–853, 2011.

[230] L. Juszczak, T. Fortuna, and F. Krok, "Non-contact Atomic Force Microscopy of Starch Granules Surface. Part I. Potato and Tapioca Starches," *Starch - Stärke*, vol. 55, no. 1, pp. 1–7, 2003.

[231] L. Juszczak, T. Fortuna, and F. Krok, "Non-contact Atomic Force Microscopy of Starch Granules Surface. Part II. Selected Cereal Starches," *Starch - Stärke*, vol. 55, no. 1, pp. 8–16, 2003.

[232] J. Szymonska and F. Krok, "Potato starch granule nanostructure studied by high resolution non-contact AFM.," *International Journal of Biological Macromolecules*, vol. 33, no. 1-3, pp. 1–7, 2003.

[233] R. A. Simao, A. P. F. B. Silva, F. H. G. Peroni, J. R. O. do Nascimento, R. P. Louro, F. M. Lajolo, and B. R. Cordenunsi, "Mango starch degradation. I. A microscopic view of the granule during ripening.," *Journal of Agricultural and Food Chemistry*, vol. 56, no. 16, pp. 7410–7415, 2008.

[234] W. Jiranuntakul, S. Sugiyama, K. Tsukamoto, C. Puttanlek, V. Rungsardthong, S. Puncha-arnon, and D. Uttapap, "Nano-structure of heat–moisture treated waxy and normal starches," *Carbohydrate Polymers*, vol. 97, no. 1, pp. 1 – 8, 2013.

[235] J. Hong, X.-A. Zeng, R. Buckow, Z. Han, and M. sheng Wang, "Nanostructure, morphology and functionality of cassava starch after pulsed electric fields assisted acetylation," *Food Hydrocolloids*, vol. 54, Part A, pp. 139 – 150, 2016.

[236] K. Radotić, C. Roduit, J. Simonović, P. Hornitschek, C. Fankhauser, D. Mutavdžić, G. Steinbach, G. Dietler, and S. Kasas, "Atomic Force Microscopy Stiffness Tomography on Living Arabidopsis thaliana Cells Reveals the Mechanical Properties of Surface and Deep Cell-Wall Layers during Growth," *Biophysical Journal*, vol. 103, no. 3, pp. 386 – 394, 2012.

[237] P. Milani, M. Gholamirad, J. Traas, A. Arnéodo, A. Boudaoud, F. Argoul, and O. Hamant, "In vivo analysis of local wall stiffness at the shoot apical meristem in Arabidopsis using atomic force microscopy," *The Plant Journal*, vol. 67, no. 6, pp. 1116–1123, 2011.

[238] O. Arnould and R. Arinero, "Towards a better understanding of wood cell wall characterisation with contact resonance atomic force microscopy," *Composites Part A: Applied Science and Manufacturing*, vol. 74, pp. 69 – 76, 2015.

[239] S. S. Nair, S. Wang, and D. C. Hurley, "Nanoscale characterization of natural fibers and their composites using contact-resonance force microscopy," *Composites Part A: Applied Science and Manufacturing*, vol. 41, no. 5, pp. 624 – 631, 2010.

[240] W. Rodríguez-Castellanos, F. J. Flores-Ruiz, F. Martínez-Bustos, F. Chiñas-Castillo, and F. J. Espinoza-Beltrán, "Nanomechanical properties and thermal stability of recycled cellulose reinforced starch–gelatin polymer composite," *Journal of Applied Polymer Science*, vol. 132, no. 14, 2015.

[241] O. Arnould, D. Siniscalco, A. Bourmaud, A. L. Duigou, and C. Baley, "Better insight into the nano-mechanical properties of flax fibre cell walls," *Industrial Crops and Products*, vol. 97, pp. 224 – 228, 2017.

[242] J. A. Turner and J. S. Wiehn, "Sensitivity of flexural and torsional vibration modes of atomic force microscope cantilevers to surface stiffness variations," *Nanotechnology*, vol. 12, no. 3, p. 322, 2001.

[243] D. Passeri, M. Rossi, and J. Vlassak, "On the tip calibration for accurate modulus measurement by contact resonance atomic force microscopy," *Ultramicroscopy*, vol. 128, pp. 32 – 41, 2013.

[244] B. D. Huey, "AFM and Acoustics: Fast, Quantitative Nanomechanical Mapping," *Annual Review of Materials Science*, vol. 37, pp. 351–385, 2007.

[245] K. Yamanaka, A. Noguchi, T. Tsuji, T. Koike, and T. Goto, "Quantitative material characterization by ultrasonic AFM," *Surface and Interface Analysis*, vol. 27, no. 5-6, pp. 600–606, 1999.

[246] U. Rabe, S. Amelio, E. Kester, V. Scherer, S. Hirsekorn, and W. Arnold, "Quantitative determination of contact stiffness using atomic force acoustic microscopy," *Ultrasonics*, vol. 38, no. 1–8, pp. 430 – 437, 2000.

[247] P. A. Yuya, D. C. Hurley, and J. A. Turner, "Contact-resonance atomic force microscopy for viscoelasticity," *Journal of Applied Physics*, vol. 104, no. 7, p. 074916, 2008.

[248] J. P. Killgore, D. G. Yablon, A. H. Tsou, A. Gannepalli, P. A. Yuya, J. A. Turner, R. Proksch, and D. C. Hurley, "Viscoelastic Property Mapping with Contact Resonance Force Microscopy," *Langmuir*, vol. 27, no. 23, pp. 13983–13987, 2011.

[249] F. Dinelli, M. R. Castell, D. A. Ritchie, N. J. Mason, G. A. D. Briggs, and O. V. Kolosov, "Mapping surface elastic properties of stiff and compliant materials on the nanoscale using ultrasonic force microscopy," *Philosophical Magazine A*, vol. 80, no. 10, pp. 2299–2323, 2000.

[250] T. J. Young, M. A. Monclus, T. L. Burnett, W. R. Broughton, S. L. Ogin, and P. A. Smith, "The use of the PeakForce TM quantitative nanomechanical mapping AFM-based method for high-resolution Young's modulus measurement of polymers," *Measurement Science and Technology*, vol. 22, no. 12, p. 125703, 2011.

[251] G. Smolyakov, C. Formosa-Dague, C. Severac, R. Duval, and E. Dague, "High speed indentation measures by FV, QI and QNM introduce a new understanding of bionanomechanical experiments," *Micron*, vol. 85, pp. 8 – 14, 2016.

[252] M. Radmacher, R. Tillmann, and H. Gaub, "Imaging viscoelasticity by force modulation with the atomic force microscope," *Biophysical Journal*, vol. 64, no. 3, pp. 735 – 742, 1993.

[253] E. Barthel, "Adhesive elastic contacts: JKR and more," *Journal of Physics D: Applied Physics*, vol. 41, no. 16, p. 163001, 2008.

[254] K. L. Johnson, *Contact Mechanics*. Cambridge University Press, 1985.

[255] J. E. Sader, J. W. M. Chon, and P. Mulvaney, "Calibration of rectangular atomic force microscope cantilevers," *Review of Scientific Instruments*, vol. 70, no. 10, pp. 3967–3969, 1999.

[256] B. J. Rodriguez, C. Callahan, S. V. Kalinin, and R. Proksch, "Dual-frequency resonance-tracking atomic force microscopy," *Nanotechnology*, vol. 18, no. 47, p. 475504, 2007.

[257] D. C. Hurley, *Quantitative Measurements of Elastic Properties with Ultrasonic-Based AFM and Conventional Techniques*, pp. 351–373. Berlin, Heidelberg: Springer Berlin Heidelberg, 2013.

[258] A. Delafargue and F.-J. Ulm, "Explicit approximations of the indentation modulus of elastically orthotropic solids for conical indenters," *International Journal of Solids and Structures*, vol. 41, no. 26, pp. 7351 – 7360, 2004.

[259] J. Jumel, G. Bresson, O. Arnould, W. Bou Mjahed, N. Ben Salem, and M. E. Shanahan, "Hysol ea9394 strength under multiaxial proportional loading statistical analysis in relation with microstructural analysis," in *5th International Symposium on Advanced Science and Technology in Experimental Mechanics*, 2010.

[260] R. Arinero, *Microscopie à force atomique en mode contact vibrant et application à l'étude des propriétés élastiques à l'échelle nanométrique*. PhD thesis, Université de Montpellier 2, 2003.

[261] J. P. Killgore and D. C. Hurley, "Low-force AFM nanomechanics with higher-eigenmode contact resonance spectroscopy," *Nanotechnology*, vol. 23, no. 5, p. 055702, 2012.

[262] F. Dinelli, S. K. Biswas, G. A. D. Briggs, and O. V. Kolosov, "Ultrasound induced lubricity in microscopic contact," *Applied Physics Letters*, vol. 71, no. 9, pp. 1177–1179, 1997.

[263] A. Socoliuc, E. Gnecco, S. Maier, O. Pfeiffer, A. Baratoff, R. Bennewitz, and E. Meyer, "Atomic-Scale Control of Friction by Actuation of Nanometer-Sized Contacts," *Science*, vol. 313, no. 5784, pp. 207–210, 2006.

[264] M. T. Cuberes, *Nanoscale Friction and Ultrasonics*, pp. 35–55. Cham: Springer International Publishing, 2015.

[265] T. Swift and M. U. D. of Botany, *Histology of the Wheat Grain*. Monash University, 1969.

[266] Y. Ai and J.-L. Jane, "Gelatinization and rheological properties of starch," *Starch - Stärke*, vol. 67, no. 3-4, pp. 213–224, 2015.

[267] V. Vamadevan and E. Bertoft, "Structure-function relationships of starch components," *Starch - Stärke*, vol. 67, no. 1-2, pp. 55–68, 2015.

[268] C. Barron, U. Holopainen-Mantila, S. Sahlstrom, A. K. Hotekjolen, and V. Lullien-Pellerin, "Assessment of biochemical markers identified in wheat for monitoring barley grain tissue," *Journal of Cereal Science*, vol. 74, pp. 11 – 18, 2017.

[269] L. W. Rooney and R. L. Pflugfelder, "Factors Affecting Starch Digestibility with Special Emphasis on Sorghum and Corn1," *Journal of Animal Science*, vol. 63, pp. 1607–1623, 1986.

[270] F. Zhu, "Structure, Physicochemical Properties, Modifications, and Uses of Sorghum Starch," *Comprehensive Reviews in Food Science and Food Safety*, vol. 13, no. 4, pp. 597–610, 2014.

[271] G. A. Annor, C. Tyl, M. Marcone, S. Ragaee, and A. Marti, "Why do millets have slower starch and protein digestibility than other cereals?," *Trends in Food Science & Technology*, vol. 66, no. Supplement C, pp. 73 – 83, 2017.

[272] W. Gindl and T. Schöberl, "The significance of the elastic modulus of wood cell walls obtained from nanoindentation measurements," *Composites Part A: Applied Science and Manufacturing*, vol. 35, no. 11, pp. 1345 – 1349, 2004.

[273] D. Bechtel, I. Zayas, R. Dempster, and J. Wilson, "NOTE: Size-Distribution of Starch Granules Isolated from Hard Red Winter and Soft Red Winter Wheats," *Cereal Chemistry Journal*, vol. 70, no. 2, pp. 238–240, 1993.

[274] P. Lade, C. Liggio, and J. Yamamuro, "Effects of Non-Plastic Fines on Minimum and Maximum Void Ratios of Sand," *International Journal for Numerical and Analytical Methods in Geomechanics*, 1998.

[275] T. Wichtmann and T. Triantafyllidis, "On the influence of the grain size distribution curve on P-wave velocity, constrained elastic modulus Mmax and Poisson's ratio of quartz sands," *Soil Dynamics and Earthquake Engineering*, vol. 30, no. 8, pp. 757 – 766, 2010.

[276] M. S. Meddah, S. Zitouni, and S. Belâabes, "Effect of content and particle size distribution of coarse aggregate on the compressive strength of concrete," *Construction and Building Materials*, vol. 24, no. 4, pp. 505 – 512, 2010.

[277] Y. Zhang and T. Napier-Munn, "Effects of particle size distribution, surface area and chemical composition on Portland cement strength," *Powder Technology*, vol. 83, no. 3, pp. 245 – 252, 1995.

[278] S.-Y. Fu, X.-Q. Feng, B. Lauke, and Y.-W. Mai, "Effects of particle size, particle/matrix interface adhesion and particle loading on mechanical properties of particulate–polymer composites," *Composites Part B: Engineering*, vol. 39, no. 6, pp. 933–961, 2008.

[279] A. Hemmerle, M. Schröter, and L. Goehring, "A cohesive granular material with tunable elasticity," *Scientific Reports*, vol. 6, pp. 35650 EP –, 2016.

[280] J. Wiącek, "Geometrical parameters of binary granular mixtures with size ratio and volume fraction: experiments and DEM simulations," *Granular Matter*, vol. 18, no. 3, p. 42, 2016.

[281] T. Shire, K. Hanley, and C. O'Sullivan, *The influence of finer fraction and size-ratio on the micro-scale properties of dense bimodal materials*, pp. 231–236. CRC press, 2014.

[282] S. Silling and E. Askari, "A meshfree method based on the peridynamic model of solid mechanics," *Computers and Structures*, vol. 83, no. 17, pp. 1526 – 1535, 2005. Advances in Meshfree Methods.

[283] X. Frank, J.-Y. Delenne, S. Nezamabadi, and F. Radjaï, "Strength and failure of heterogeneous materials using a peridynamic approach." unpublished.

[284] Y. D. Ha and F. Bobaru, "Characteristics of dynamic brittle fracture captured with peridynamics," *Engineering Fracture Mechanics*, vol. 78, no. 6, pp. 1156 – 1168, 2011.

[285] M. Allen and D. Tildesley, *Computer Simulation of Liquids*. Oxford University Press, Oxford, 1986.

[286] R. Bridson, "Fast Poisson Disk Sampling in Arbitrary Dimensions," in *ACM SIGGRAPH 2007 Sketches*, SIGGRAPH '07, (New York, NY, USA), ACM, 2007.

[287] J.-N. Roux and G. Combe, "Quasistatic rheology and the origins of strain," *Comptes Rendus Physique*, vol. 3, no. 2, pp. 131 – 140, 2002.

[288] L. Vandevenne, "Floodfill algorithm."

[289] R. K. McGEARY, "Mechanical Packing of Spherical Particles," *Journal of the American Ceramic Society*, vol. 44, no. 10, pp. 513–522, 1961.

[290] R. P. Dias, J. A. Teixeira, M. G. Mota, and A. I. Yelshin, "Particulate Binary Mixtures:âĂĽ Dependence of Packing Porosity on Particle Size Ratio," *Industrial & Engineering Chemistry Research*, vol. 43, no. 24, pp. 7912–7919, 2004.

[291] P. Jalali and M. Li, "Model for estimation of critical packing density in polydisperse hard-disk packings," *Physica A: Statistical Mechanics and its Applications*, vol. 381, pp. 230 – 238, 2007.

[292] L. Meng, P. Lu, and S. Li, "Packing properties of binary mixtures in disordered sphere systems," *Particuology*, vol. 16, pp. 155 – 166, 2014.

[293] J. Sánchez, G. Auvinet, and B. Cambou, *Coordination number and geometric anisotropy in binary sphere mixtures*, pp. 225–230. CRC Press, 2014.

[294] J. Dodds, "The porosity and contact points in multicomponent random sphere packings calculated by a simple statistical geometric model," *Journal of Colloid and Interface Science*, vol. 77, no. 2, pp. 317 – 327, 1980.

[295] K. P. Balanda and H. L. MacGillivray, "Kurtosis: A Critical Review," *The American Statistician*, vol. 42, no. 2, pp. 111–119, 1988.

[296] T. Mori and K. Tanaka, "Average stress in matrix and average elastic energy of materials with misfitting inclusions," *Acta Metallurgica*, vol. 21, no. 5, pp. 571 – 574, 1973.

[297] G. Hu, G. Guo, and D. Baptiste, "A micromechanical model of influence of particle fracture and particle cluster on mechanical properties of metal matrix composites," *Computational Materials Science*, vol. 9, no. 3, pp. 420 – 430, 1998.

[298] I. Jasiuk, J. Chen, and M. F. Thorpe, "Elastic Moduli of Two Dimensional Materials With Polygonal and Elliptical Holes," *Applied Mechanics Reviews*, vol. 47, no. 1S, pp. S18–S28, 1994.

[299] S. Thevanayagam, T. Shenthan, S. Mohan, and J. J. Liang, "Undrained Fragility of Clean Sands, Silty Sands, and Sandy Silts," *Journal of Geotechnical and Geoenvironmental Engineering*, vol. 128, no. 10, pp. 849–859, 2002.

[300] R. Affes, J. Y. Delenne, Y. Monerie, F. Radjaï, and V. Topin, "Tensile strength and fracture of cemented granular aggregates," *The European Physical Journal E*, vol. 35, no. 11, p. 117, 2012.

[301] G. N. Barrera, G. T. Pérez, P. D. Ribotta, and A. E. León, "Influence of damaged starch on cookie and bread-making quality," *European Food Research and Technology*, vol. 225, no. 1, pp. 1–7, 2007.

[302] R. Moss, N. Stenvert, K. Kingswood, and G. Pointing, "The relationship between wheat microstructure and flourmilling.," *Scanning Electron Microscope*, 1980.

[303] G. Glenn, F. Younce, and M. Pitts, "Fundamental physical properties characterizing the hardness of wheat endosperm," *Journal of Cereal Science*, vol. 13, no. 2, pp. 179 – 194, 1991.

[304] O. Piot, J.-C. Autran, and M. Manfait, "Investigation by Confocal Raman Microspectroscopy of the Molecular Factors Responsible for Grain Cohesion in theTriticum aestivum Bread Wheat. Role of the Cell Walls in the Starchy Endosperm," *Journal of Cereal Science*, vol. 34, no. 2, pp. 191 – 205, 2001.

[305] Y. Joliff, J. Absi, M. Huger, and J. Glandus, "Experimental and numerical study of the room temperature elastic modulus of model materials with partly bonded matrix/particles interfaces," *Computational Materials Science*, vol. 39, no. 2, pp. 267 – 273, 2007.

List of Publications

- K. Heinze, X. Frank, V. Lullien-Pellerin, M. George, F. Radjai and J.-Y. Delenne, "Numerical modeling of the tensile strength of a biological granular aggregate: Effect of the particle size distribution", *EPJ Web Conf. 140 08013*, 2017, DOI: 10.1051/epjconf/201714008013. (part of section 5.2)
- K. Heinze, A.M. Kiszonas, J.C. Murray, C.F. Morris, V. Lullien-Pellerin, "Puroindoline genes introduced into durum wheat reduce milling energy and change milling behavior similar to soft common wheats", *Journal of Cereal Science*, Volume 71, September 2016, Pages 183-189, DOI: 10.1016/j.jcs.2016.08.016. (section 3.1)
- K. Heinze, E. Sasaki, N. P. King, D. Baker, D. Hilvert, G. J. L. Wuite, and W. H. Roos, "Protein Nanocontainers from Nonviral Origin: Testing the Mechanics of Artificial and Natural Protein Cages by AFM", *The Journal of Physical Chemistry B*, 120 (26), 5945-5952, 2016, DOI: 10.1021/acs.jpcb.6b01464. (not in this thesis)
- J. Costi, K. Heinze, I. Lawless, R. Stanley, and B. Freeman, "Do combined compression, flexion and axial rotation place degenerated discs at risk of posterolateral herniation? Measurement of 3D lumbar intervertebral disc internal strains during repetitive loading", *Bone Joint J*, 96-B(SUPP 11), 219, 2014. (not in this thesis)

Other media

- K. Heinze, X. Frank, V. Lullien-Pellerin, M. George, F. Radjai and J.-Y. Delenne, "Insights into the mechanics of wheat fractionation by numerical simulations", video abstract, 2017.

Conference presentations (2014-2017)

- Poster presentation at Graines (2017, France)
- Poster and video abstract presentation at Powders and Grains (8th International Conference on Micromechanics of Granular Media, 2017, France)
- Oral presentation at Forum des Microscopies à Sonde Locale (2017, France)
- Oral and poster presentation at Nanostruc (3rd International Conference on Structural Nano Composites, 2016, UK)

A. Appendix 1

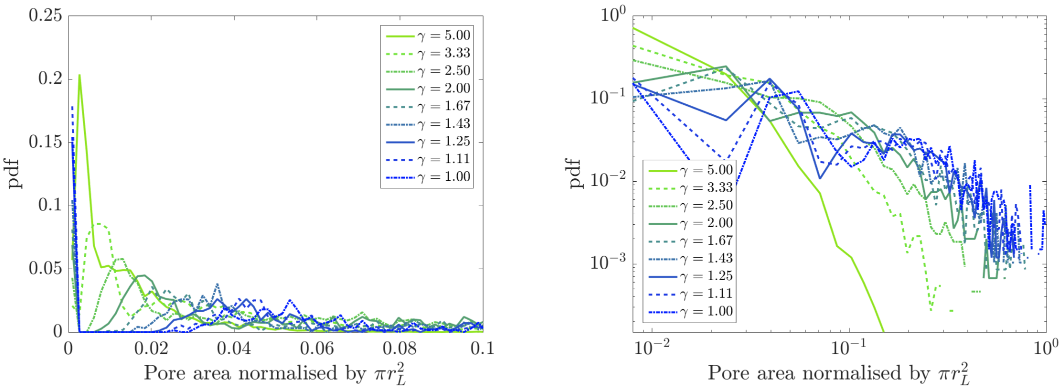

(a) (b)

Figure A.1. – The size distribution of the inter-grain spaces without any matrix for samples of $\theta \approx 1.36$ and varying γ is shown for (a) small sizes (b) all sizes in a log-log plot.

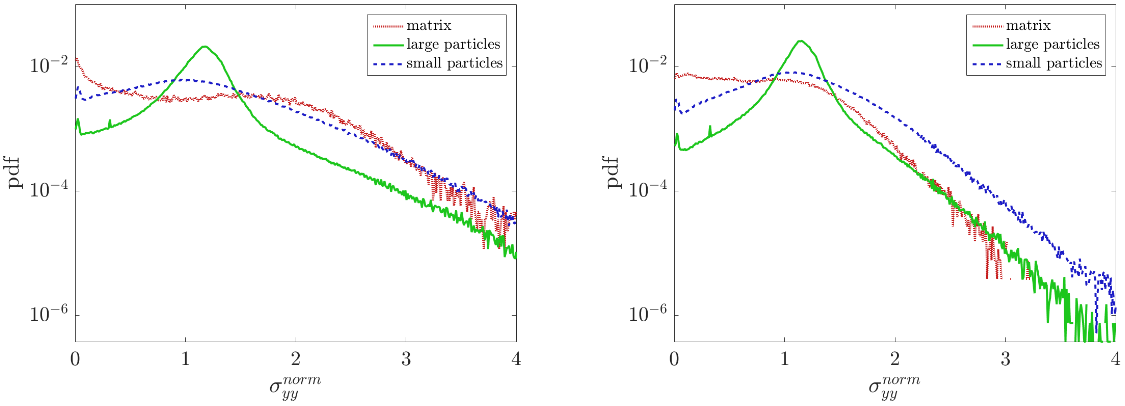

(a) $S_m = 0.03$ (b) $S_m = 0.17$

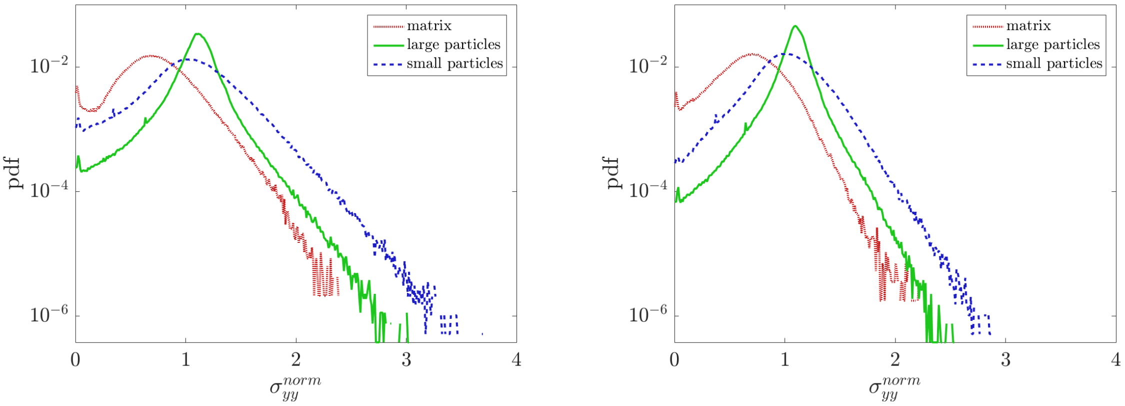

(c) $S_m = 0.46$ (d) $S_m = 0.73$

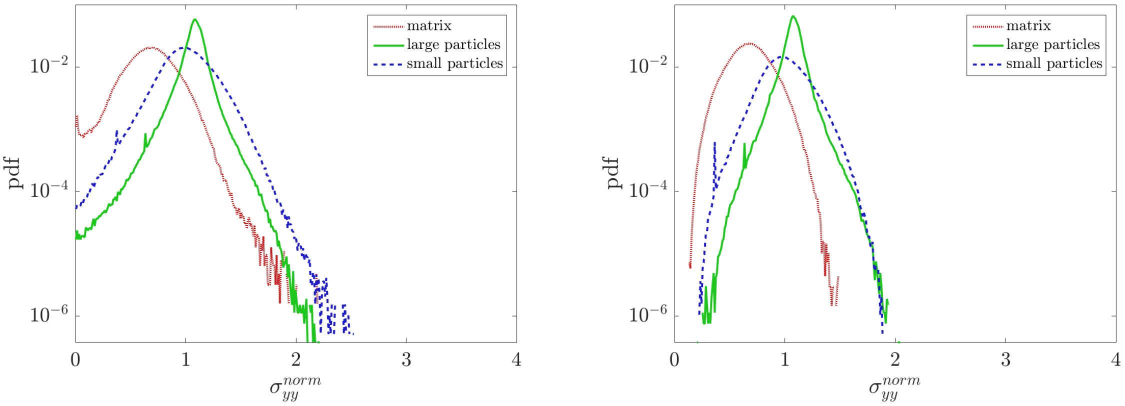

(e) $S_m = 0.93$ (f) $S_m = 1.00$

Figure A.2. – (a-f) Stress distributions $\sigma_{yy}^{norm} = \sigma_{yy}/\overline{\sigma_{yy}}$ in all phases with increasing matrix saturation ($\gamma^* = 5.53$, $\theta^* \approx 1.36$).

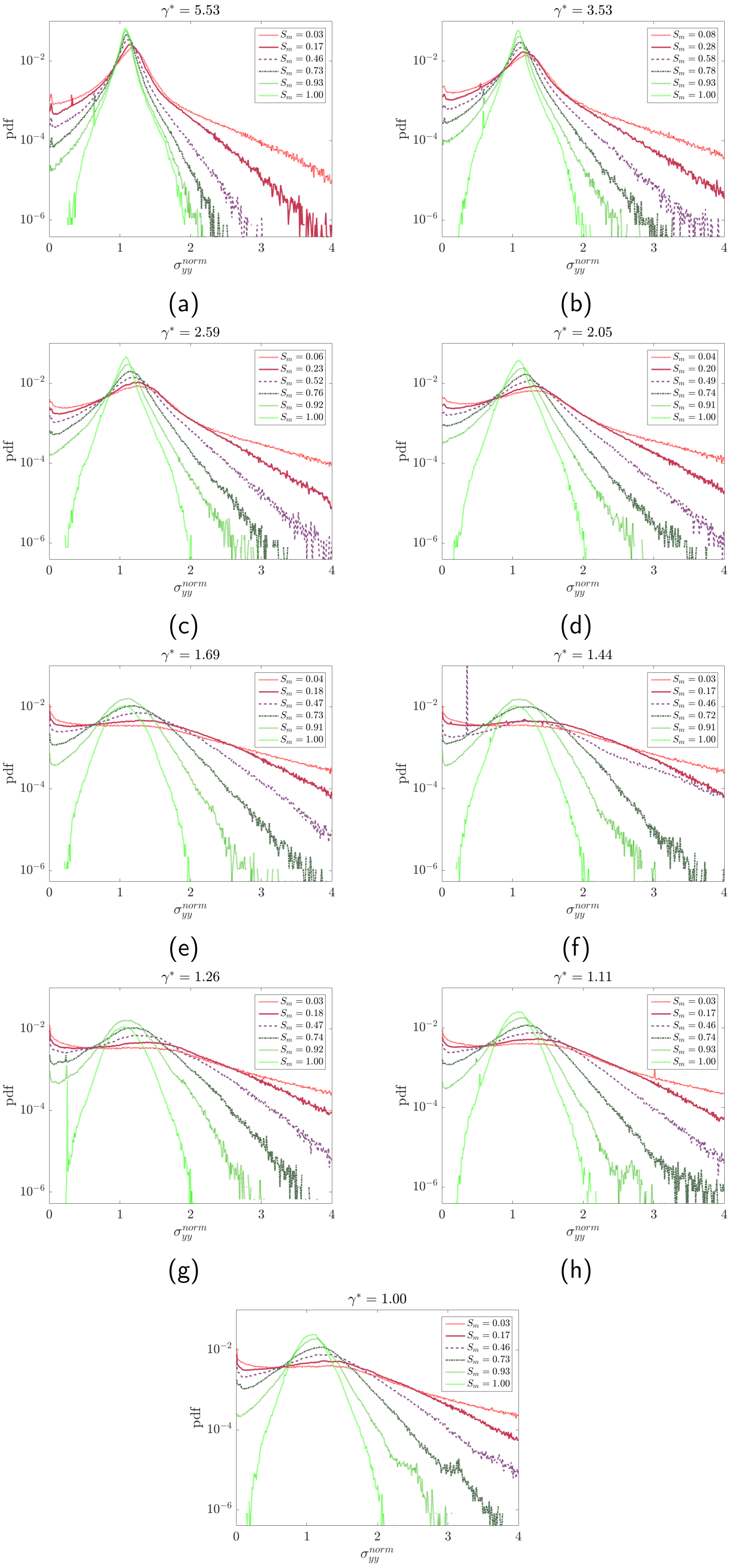

(a) (b) (c) (d) (e) (f) (g) (h) (i)

Figure A.3. – Stress distributions in large granules of porous samples with increasing γ^* ($\theta^* \approx 1.36$).

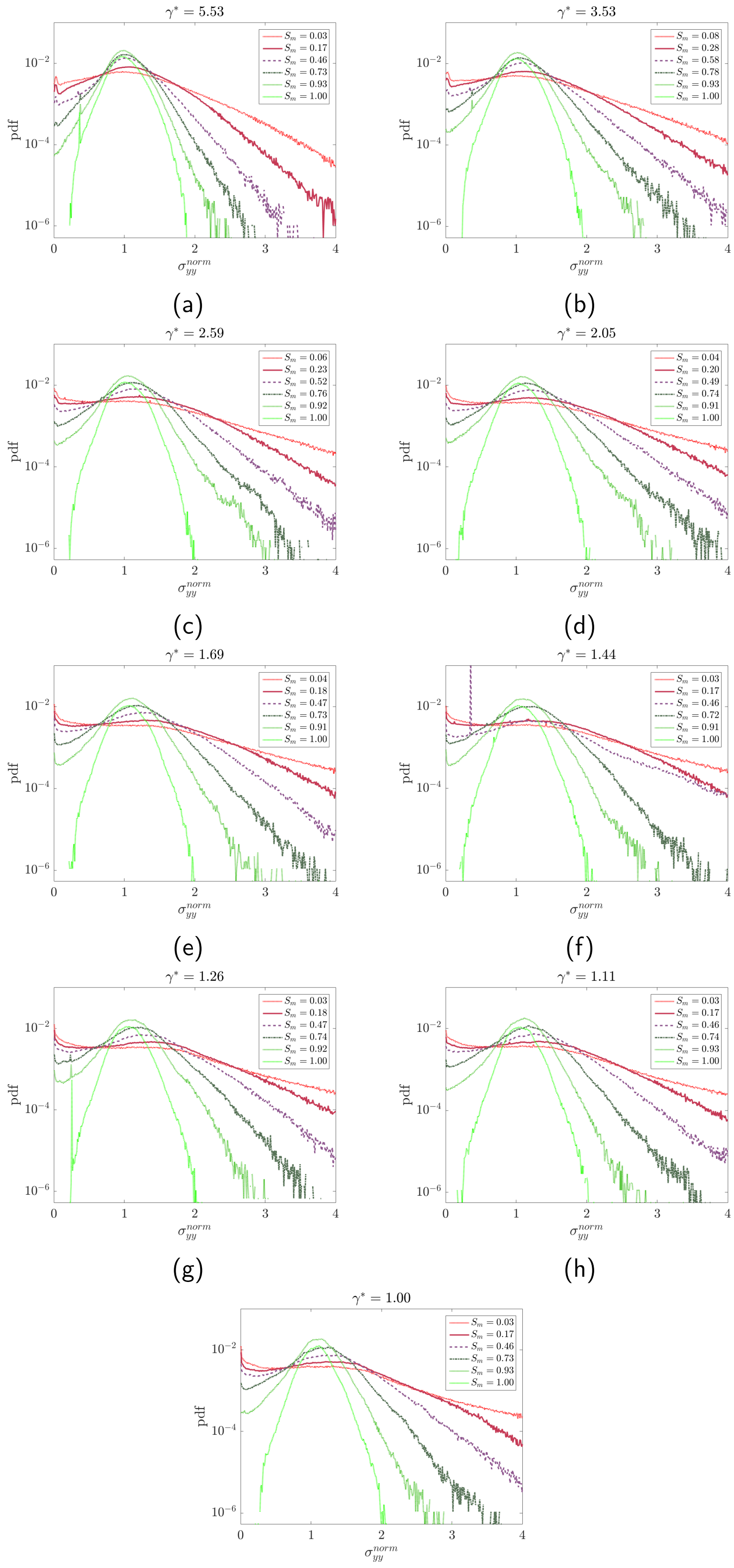

(a) (b)

(c) (d)

(e) (f)

(g) (h)

(i)

Figure A.4. – (a-f) Stress distributions in small granules of porous samples with increasing γ^* ($\theta^* \approx 1.36$).

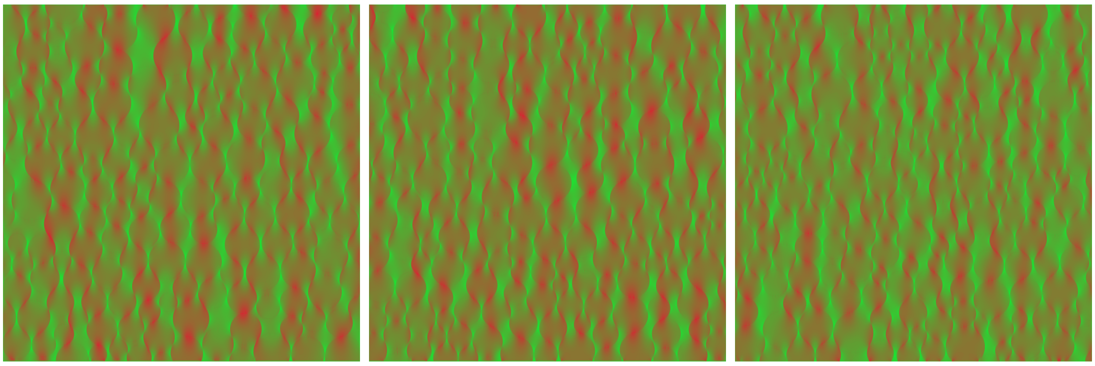

(a) $\gamma^* = 1.00$ (b) $\Gamma = 1.11$ (c) $\Gamma = 1.26$

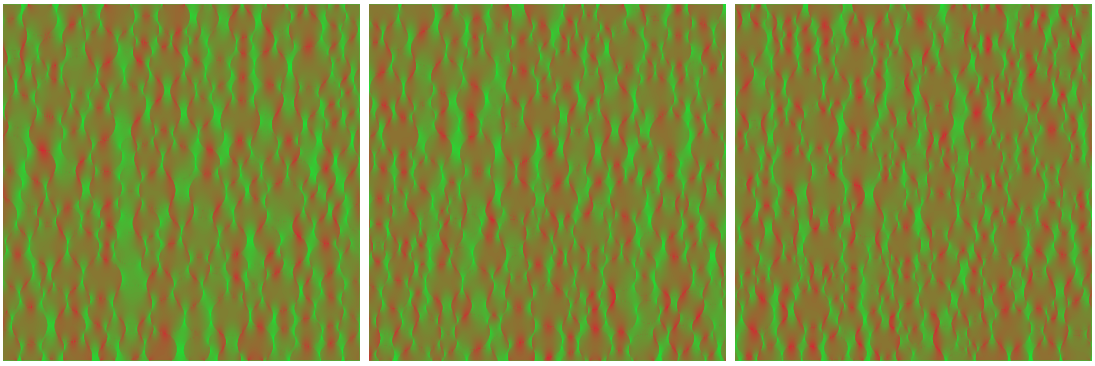

(d) $\Gamma = 1.44$ (e) $\gamma^* = 1.69$ (f) $\gamma^* = 2.05$

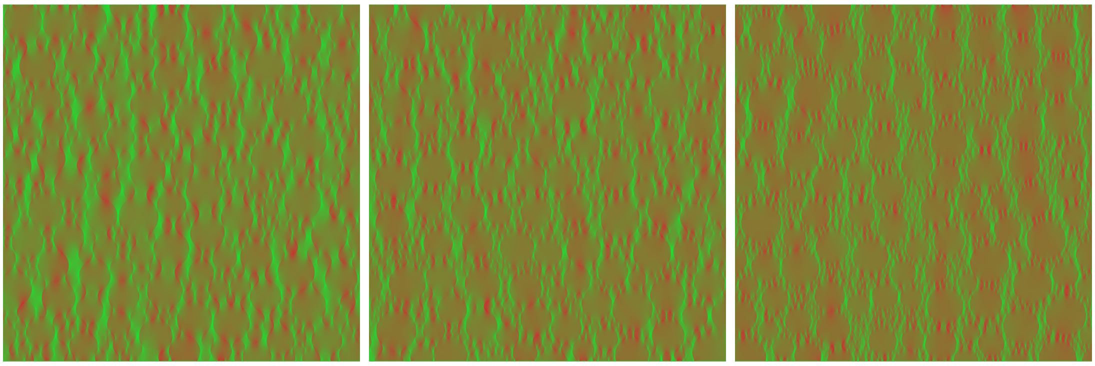

(g) $\gamma^* = 2.59$ (h) $\gamma^* = 3.53$ (i) $\gamma^* = 5.53$

Figure A.5. – Examples of the stress distributions within the samples are shown for $\theta^* = 1.36$ and increasing γ^*. Low stress is coloured green, high stress in red.

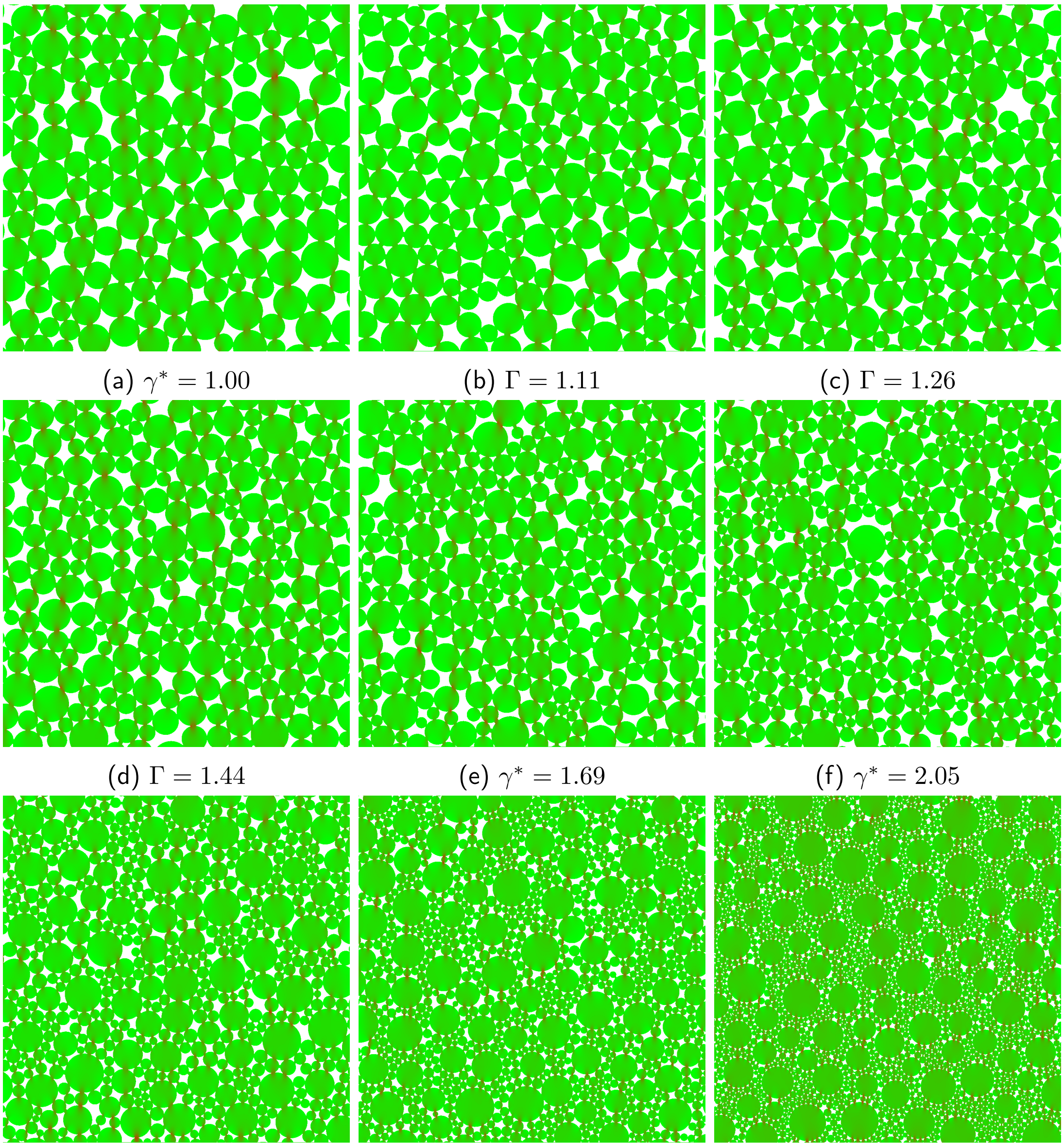

(a) $\gamma^* = 1.00$

(b) $\Gamma = 1.11$

(c) $\Gamma = 1.26$

(d) $\Gamma = 1.44$

(e) $\gamma^* = 1.69$

(f) $\gamma^* = 2.05$

(g) $\gamma^* = 2.59$

(h) $\gamma^* = 3.53$

(i) $\gamma^* = 5.53$

Figure A.6. – Examples of the stress distributions within porous samples are shown for $\theta^* = 1.36$ and increasing γ^*. Low stress is coloured green, high stress in red. Images are scaled by maximum stress.

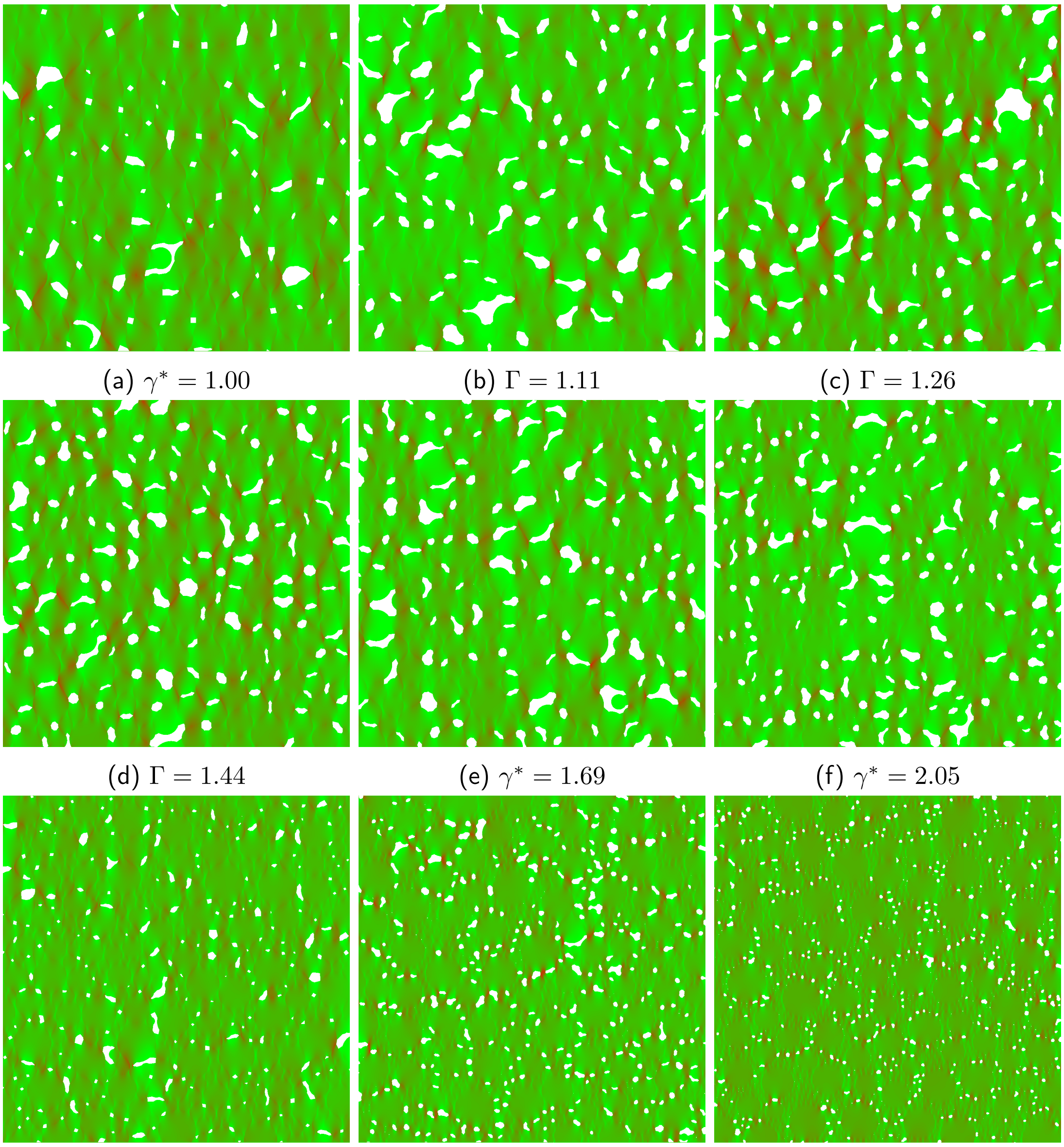

(a) $\gamma^* = 1.00$

(b) $\Gamma = 1.11$

(c) $\Gamma = 1.26$

(d) $\Gamma = 1.44$

(e) $\gamma^* = 1.69$

(f) $\gamma^* = 2.05$

(g) $\gamma^* = 2.59$

(h) $\gamma^* = 3.53$

(i) $\gamma^* = 5.53$

Figure A.7. – Examples of the stress distributions within porous samples are shown for $\theta^* = 1.36$ and increasing γ^*. Low stress is coloured green, high stress in red. Images are scaled by maximum stress.

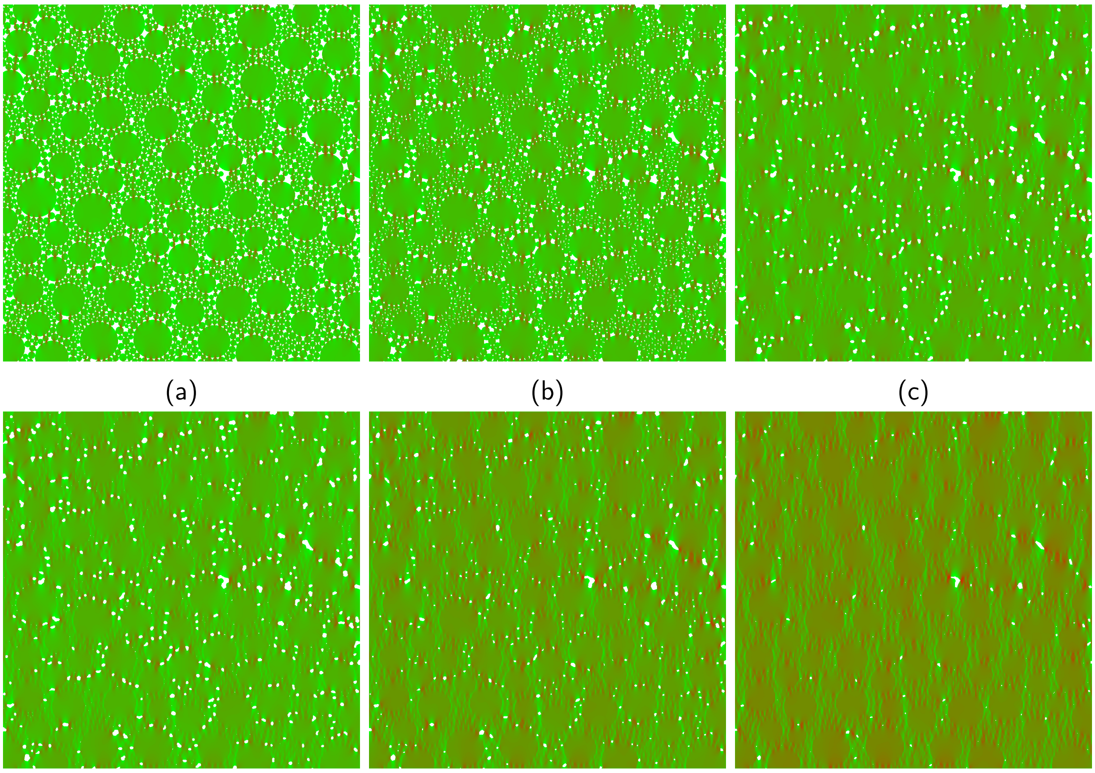

(a) (b) (c)

(d) (e) (f)

Figure A.8. – Examples of the stress distributions within porous samples of $\gamma^* = 5.53$ with increasing matrix saturation S_m. Low stress is coloured green, high stress in red. Images are scaled by maximum stress.

Du grain aux granules : Biomécanique de la fragmentation du blé et rôle des granules d'amidon

La culture du blé est l'une des plus importantes au monde. Le grain de blé est un matériau composite naturel dont la majeure partie est constituée d'albumen amylacé formé d'un assemblage compact de granules d'amidons (glucides) enchâssés dans une matrice protéique (gluten). Pour obtenir des produits comme la farine, la structure de l'albumen doit être fragmentée en broyant les grains sous des fortes contraintes. La quantité et la qualité des produits obtenus dépendent du comportement de l'albumen à la fragmentation.

En raison de sa nature composite, le comportement rhéologique du grain est tributaires des propriétés mécaniques des phases qui le composent (granules, gluten, pores), de leurs interactions, ainsi que de leur distribution spatiale. Les granules d'amidons sont de formes relativement sphériques et de tailles micrométriques, tandis que les protéines sont organisées en un réseau entourant les granules. L'interaction entre l'amidon et ce réseau protéique est influencée par certaines protéines, les puroindolines, dont la présence et le type d'allèle sont contrôlées génétiquement. Si les gènes codant pour les puroindolines sont présents sous forme sauvages, la dureté meunière, c'est à dire l'aptitude à la fragmentation du grain est faible. L'origine de ce comportement est liée à une adhérence limitée entre matrice protéique et amidon. L'absence totale de puroindolines chez le blé dur conduit au contraire à une dureté très élevée des grains et à une forte adhérence.

L'objectif de cette thèse est d'étudier, à partir d'une approche multidisciplinaire, la biomécanique du fractionnement du grain de blé en mettant l'accent sur le rôle des granules d'amidon. Des échelles de taille différentes sont considéréesă : échelle micrométrique du granule et de la matrice protéique ; agencement complexe de ces composants dans l'albumen et échelle millimétrique du grain. Ainsi, des expériences de broyage à l'échelle du grain ont été combinées avec des mesures nano-mécaniques par microscopie à force atomique (AFM) et des simulations numériques.

Le comportement au broyage a été étudié en utilisant un micro-moulin instrumenté. Une comparaison a été effectuée entre des essais réalisés sur une variété de blé dur et sur la même variété dans laquelle ont été introduits les gènes codant pour les puroindolines. Un changement significatif du comportement mécanique des grains transformés, attribuable uniquement à la présence de puroindolines, a été observé - en termes d'énergie consommée, - de productivité en farine et - de taux d'amidon endommagé. Ces changements sont compatibles avec l'hypothèse d'une faible adhérence, entre granules d'amidon et matrice protéique, induite par la présence des puroindolines et montrent l'effet significatif de celles-ci sur le comportement à la fragmentation. Ces modifications de comportement mécanique peuvent être étudiées par des mesures AFM nano-mécaniques. Pour compléter des travaux antérieurs ayant permis la mesure des propriétés de l'amidon et du gluten, une méthode basée sur des mesures AFM en mode résonance de contact (CR-AFM) a été développée. Celle-ci permet de cartographier les propriétés directement à l'intérieur des granules d'amidon et prend en compte à travers un modèle théorique les variations importantes de topographie observées dans les sections de grains. Ces études CR-AFM de l'albumen ont ensuite porté sur les propriétés mécaniques des granules d'amidon d'origines botaniques différentes (céréales et légumineuses).

Enfin, le rôle de la distribution bimodale en taille des granules d'amidon sur la fragmentation de l'albumen a été précisé à partir d'une étude numérique paramétrique détaillée. Les propriétés mécaniques élastiques et à la rupture ont été analysées en détail, ainsi que le rôle dominant de la ténacité des granules et de l'adhérence à l'interface sur l'endommagement de l'amidon.

From grain to granule: Biomechanics of wheat grain fractionation with a focus on the role of starch granules

The wheat grain is a natural composite material of worldwide importance. The major part of the grain is the starchy endosperm. To obtain food products, such as flour, the endosperm's compact structure needs to be disintegrated, which is achieved by milling the grains under high forces. The quantity and quality of the milling products notably depend on the fragmentation behaviour of the endosperm.

Due to the endosperm's composite nature, this behaviour depends strongly on the mechanical properties of its components and their interaction. The main components of the endosperm are carbohydrates and proteins. The carbohydrates are deposited as starch in the form of granules of micro-meter size, whereas proteins form a network (gluten), which surrounds the starch granules. The interactions between starch and proteins is believed to be influenced by certain non-gluten proteins (puroindolines), whose presence and allelic state are genetically controlled. If puroindoline genes are present in the wild-type form, grain hardness is low, which has been related to low starch-protein adhesion. The complete absence of puroindolines in the durum wheat species leads to very high grain hardness and indicates a strong adhesion.

The aim of this thesis was to investigate the biomechanics of wheat grain fractionation with a focus on the role of the starch granules therein, which was pursued with a multi-disciplinary approach. Different size scales were considered, from the micro meter-sized structures of starch and protein, the complexity of their arrangement in the endosperm, up to the millimetre-sized grains. In this work, grain-scale milling experiments were combined with nano-mechanical measurements by atomic force microscopy (AFM) and numerical simulations. The milling behaviour of a transgenic durum wheat line, which contained puroindoline genes, was determined by grain scale milling experiments and compared to the milling behavior of non-modified durum wheat. A significant change of milling behavior of the transformed durum wheat grains was observed in terms of milling energy, flour yield and starch damage, which was solely attributable to the presence of puroindolines. The observed changes were consistent with the hypothesis of a lower adhesion between starch granules and protein matrix due to the presence of puroindolines and confirmed the significant effect of puroindolines on the fragmentation behaviour, independent of the grain's genetic background.

The change of fragmentation behaviour is a result of modifications of the mechanical properties of the endosperm's components and/ or their interaction. Such modifications can be investigated by AFM nano-mechanical measurements. Based on previous work illuminating the global nano-mechanical properties of starch and gluten, contact-resonance AFM (CR-AFM) was applied to obtain maps of the nano-mechanical properties inside the grains. Due to the high topography variations of grain section surfaces and the non-trivial correlation between surface slope and contact resonance-frequency, which hindered a straight-forward interpretation of CR-AFM measurements, a practical method based on existing analytical models of the cantilever vibration was developed to correct the measurements. CR-AFM studies of the endosperm were then focused specifically on the mechanical properties of starch granules and the link to starch structure, and applied to the study of starches from wheat in comparison to plants from different botanical origin (other cereals and legumes).

Finally, the role of starch granules, their size distribution, and mechanical properties on endosperm fragmentation was analysed by parametric numerical studies. The influence of the bi-modal size distribution of granules on the mesoscale mechanical properties was shown, as well as the governing role of granule toughness and interface adhesion on the granule damage.